STUDY OF IMPROVING PERFORMANCE OF CARBON FIBER-REINFORCED POLYMER (CFRP) COMPOSITES BY INCORPORATING NANO-MATERIALS IN THE MANUFACTURING PROCESS

OR KING HEI

PhD

The Hong Kong Polytechnic University

2026

The Hong Kong Polytechnic University

School of Fashion and Textiles

Study of improving performance of carbon fiber-reinforced polymer (CFRP) composites by incorporating nano-materials in the manufacturing process

OR King Hei

A thesis submitted in partial fulfillment of the requirement for the degree of Doctor of Philosophy

August 2025

CERTIFICATE OF ORIGINALITY

I hereby declare that this thesis is my own work and that, to the best of my knowledge and belief, it reproduces no material previously published or written, nor material that has been accepted for the award of any other degree or diploma, except where due acknowledgement has been made in the text.

____

OR King Hei

Abstract

Carbon fiber-reinforced polymer (CFRP) composites have found widespread applications across various industries such as aviation and marine. Their high specific strength and stiffness make them an ideal choice for constructing aircraft and vessels in order to reduce the structural weight. However, the performance of composites is significantly compromised under specific usage conditions, particularly in high-temperature environments. This limitation restricts their applicability to certain locations, such as turbine blades in aircraft engines. As a result, there is an increasing demand for improving the properties of composites, including strength and thermal stability. Recent research suggested that carbon nanotubes (CNTs) may serve as a suitable medium for enhancing the performance of composites. In this study, composites were fabricated using the Vacuum-assisted Resin Infusion Molding (VARIM) method. The impact of various configurations of constituents and CNT additive was evaluated. Tensile property evaluations were conducted in accordance with ASTM standards. Ply stack configurations, matrix viscosities, and reinforcement weave patterns were compared to establish a baseline for assessing the performance of CNT additive. An eight-ply twill-weaved composite with WS105/209 resin system was found to have the most consistent results across different fabrication conditions and was subsequently used as the base sample for incorporating CNT additive. Improvements were observed in both tensile and thermal aspects of the composites with CNT additive.

Publication arising from the thesis

Journal paper:

Or, I. K.-H., Lo, C. K.-Y., & Kan, C.-W. (2023). A systematic literature network analysis: Development of manufacturing, enhancement and sustainability of fiber-reinforced polymer composites (1998–2020) and future research agenda. *Fibers and Polymers, 24*(3), 789-800.

Acknowledgements

First and foremost, I would like to express my special gratitude and appreciation to my Chief Supervisor Prof. Kan Chi Wai (Professor of the School of Fashion and Textiles, The Hong Kong Polytechnic University) for his trust and guidance. He taught me the knowledge of matrix and inspired me to explore more on this area. His mentorship and support are indispensable for the completion of this research study.

I would like to express my gratitude to the staffs and technicians of the School of Fashion and Textiles. I am deeply grateful for the help and assistance from FYP students Miss Wong Kei Yau Janice and Miss Wong Sin Yi Phoebe.

I would like to acknowledge the School of Fashion and Textiles for their financial support of this research study under departmental grant.

Last but not least, I must acknowledge the help and support from the Productisation and Manufacturing Team, Industrial Centre. I wish to extend my special thanks to Mr. Pang Man Kit Peter (Engineering Manager), Mr. Leung Hoi Cheung (Senior Engineer) and Mr. Shum Pak Wo Gary (Assistant Engineer) for their professional advice and expertise in the field of composites.

Table of contents

List of Figures

List of Tables

List of Equations

Chapter 1 Introduction

1.1 Background

Throughout human history, materials have been a vital key in developing and building civilization. From the Stone Age all the way to the Silicon Age, numerous natural resources have been discovered and utilized, and thanks to the advancements of science and technology, many synthetic materials are being innovated. However, every material has limitations and is difficult to apply in modern applications with specific demands on material properties (Balasubramanian, 2014). Composite materials have been developed to combine the strength of multiple materials in order to suit the required properties that no single material can fulfill. Composite materials have been extensively utilized in various industries, including aviation and marine, over the past few decades. With their extraordinary characteristics in both physical and chemical aspects, composite materials enable many groundbreaking designs and the realization of innovative products, for example, the latest generation of aircraft, automobiles, and vessels (Aamir, Tolouei-Rad, Giasin, & Nosrati, 2019; Goren & Atas, 2008). The adoption of composite materials in vehicle designs offers a more energy-efficient operation in vehicles by reducing the structural weight without compromising the structural robustness when compared to traditional designs with metallic materials (Chen, Arakawa, & Xu, 2015). Despite the fact that composites have relatively higher mechanical performance than other materials, the mechanical properties of composites vary significantly based on the selection of weave patterns in reinforcements and the nature of resins. Furthermore, the integrity of composites is severely compromised under specific operation environments, such as high temperatures, which limits their utilization in certain applications, such as turbine blades within aircraft engines (Guo, Zhuang, Li, & Chen, 2021).

To overcome these inherent limitations, incorporating additional elements during the fabrication process appears to be a viable approach to broaden the applicability of composites. Recent researches have suggested that nanomaterials are suitable candidates to serve as the additional element in order to enhance the performance of composites without compromising their mechanical strength (Ayatollahi, Isfahani, & Monfared, 2017; Liu, Deng, & Zhang, 2017). Researchers have been investigating the impact of incorporating nanomaterials into different fiber-reinforced polymer composites, including silica nanoparticles in E-glass fiber epoxy composites. Notably, some research outcomes have indicated an enhancement in both the target properties and tensile properties of these composites (Georgakilas et al., 2012; Monfared, Ayatollahi, & Isfahani, 2018; Uddin & Sun, 2008). Despite the encouraging results obtained in recent research, numerous combinations of a wide range of reinforcements, resins, and nanomaterials will yield distinct profiles and characteristics of the resulting composites, creating a substantial research gap for researchers to explore.

1.2 Scope of research

Composite materials are formed by combining reinforcement phase material and matrix phase material (Akovali, 2001). Reinforcement phase materials can be in the form of 0D (particle), 1D (filament), 2D (textile) or 3D (spacer) such as carbon fiber, glass fiber and aramid fiber. Matrix phase materials can be ceramics, metals or polymers. (Balasubramanian, 2014). In recent decades, composites with carbon fiber reinforcements and polymer matrices have demonstrated outstanding specific mechanical performance compared to conventional metallic alloys and particulate-reinforced composites (Kaw, 1997). Therefore, in the initial phase of this research study, carbon fiber-reinforced polymer (CFRP) composites with different configurations of carbon fiber fabric weave patterns and epoxy resin viscosities are fabricated and investigated. In the second phase, nanomaterials are added into CFRP composites for further investigation. In recent research, carbon nanotube (CNT) is stated as a potential candidate for nanomaterials based on its inherent properties and promising results. Therefore, in this study, CNT is the primary subject employed to incorporate as a nanomaterial during the matrix infusion process. To assess the influence of the weave pattern of reinforcement and the viscosity of the matrix on the resulting composites in the initial phase, and to evaluate the impact of nanomaterial in the second phase, the mechanical performance of all composites fabricated in this research study is evaluated in accordance with the corresponding ASTM International Standard Testing Methods (ASTM International, 2018).

1.3 Research objectives

This research study aims to enhance CFRP composites by incorporating nanomaterials. To gain a comprehensive understanding of CFRP composites, a systematic literature network analysis of existing articles on the subject has been conducted. This systematic literature network analysis has identified the current trends in CFRP composites development and collected information on the latest technology regarding materials and fabrication methods in order to further improve the quality and overcome the limitations of CFRP composites. The initial phase of this research study is a pilot study aimed at investigating how the configuration of composite constituents, such as the weave pattern of carbon fiber fabric and the viscosity of epoxy resin, influences the mechanical properties of the resulting CFRP composites. The second phase of this research study is to investigate how the incorporation of carbon nanotube affects the properties of the resulting CFRP composites. The mechanical performance of CFRP composites fabricated in this research study is evaluated through the comparison of their tensile properties. The consistency of the results obtained from specimens with identical experimental conditions can assess the fabrication quality. As a result, the following objectives are setup for this research study:

- To investigate the properties of CFRP composites and identify the challenges associated with their application in various environments or conditions
- To identify the potential approaches for enhancing CFRP composites through a systematic literature network analysis of current available articles
- To investigate and evaluate the influence of weave pattern and viscosity of composite constituents on the mechanical performance of the resulting composites
- To investigate and evaluate the mechanical performance of carbon nanotube incorporated CFRP composites

1.4 Significance and value

The systematic literature network analysis conducted in this research study provides an overview of the current research trends in the field of fiber-reinforced polymer (FRP) composites (Or, Lo, & Kan, 2023). Articles related to FRP composites are categorized into research clusters based on their bibliographic data which indicate different research directions. The topic of nano-filler enhancing FRP composites has gained significant attention and emerged as an emerging area of research in the past decade. However, there are limited articles investigating the effects of incorporating CNT into FRP composites, particularly carbon fiber-reinforced polymer composites. Therefore, this research study can contribute in investigating the tensile properties on incorporating non-functionalized CNT into CFRP composites with an over-curing analysis.

Among FRP composites, CFRP composites have been widely utilized in various industries to develop economically designed products, such as the recent generation aircraft, which employs carbon fiber composites in its fuselage skin (Takeda et al., 2005). High specific strength of CFRP composites allows the reduction in aircraft structural weight so as to lower the energy consumption during operation. However, not all aircraft components are suitable for the application of composite materials, particularly those located near the aircraft engines, which are required to withstand high temperature. High operation temperature may lead to thermal degradation of matrix phase which severely compromise the mechanical performance of the composites (Ravikovich, Arkhipov, Shakhov, & Erofeev, 2021). To broaden the range of applications of CFRP composites, this research study focuses on introducing nanomaterials into the composites in order to facilitate the continuous development of innovative designs. Increase in operating temperature range of composites can eliminate the necessity of using metal or ceramic around scorching environment and help further reduce the structural weight by replacing the components with composite materials. The ability to withstand high temperature also enables composites to provide fire prevention features and facilitates the application of composite materials in products that require specific fire prevention certifications. Furthermore, the composites with this ability can effectively mitigate the spread of fire during emergency situations and facilitate the evacuation of civilians from the scene of fire.

Chapter 2 Literature review

2.1 Background of composite materials

A composite material is commonly known as the combination of two or more materials with distinct phases, and their own phases are retained after the formation processes of the composite. The constituents of a composite material are typically categorized into two phases: the reinforcement phase and the matrix phase (Balasubramanian, 2014). Reinforcements are materials with superior mechanical properties that are utilized for load-bearing purposes, while matrices have good processability and are distributed as a continuous medium. The ratio, arrangement, and orientation of the constituent materials significantly influence the properties of the resulting composite (Mallick, 2008; Ullah, Palevicius, Vilutis, Fangueiro, & Janusas, 2026).

2.2 Reinforcement of composite materials

Composites reinforcements can be classified into fiber-reinforced or particulate-reinforced. Fiber-reinforced composites can further be divided into continuous fiber or short fiber. Continuous fiber allows loading to be transferred throughout the composites, and the fibers are typically weaved into fabric form, which makes continuous fiber-reinforced composites suitable for substantial load-bearing applications. Reinforcement fabric can be constructed with various weave patterns, such as unidirectional, plain-weaved, and twill-weaved, which different weave patterns will affect the direction and distribution of loading within the composite. Continuous fiber-reinforced composites demonstrate superior load-bearing capability along the fiber direction due to the inherent mechanical properties of the reinforcement phase. Composites with reinforcement phases involving reinforcement fibers in a single direction, such as unidirectional fiber-reinforced composites, are susceptible to lateral forces which are perpendicular to the fiber direction. In contrast, composites with reinforcement phases involving reinforcement fabrics with warp and weft fiber yarns, such as plain-weaved fiber composites, are capable of withstanding forces from both longitudinal and lateral directions. However, the interlacing of warp and weft yarns generates gaps between fibers as the warp yarns and weft yarns alternate over and under each other. Variations in yarn spacing can influence the performance of matrix phase and subsequently increase the void content of composites which may affect the integrity of the composite. Additionally, there are numerous types of fibers that can be utilized as reinforcements, including glass fiber, aramid fibers, and carbon fibers. Among these fibers, carbon fiber stands out as a commonly utilized reinforcement in fiber-reinforced polymer composites (Carraher, 2018).

Carbon fiber is a fiber with a carbon content of at least 92 wt% (Dér et al., 2021; Morgan, 2005). Therefore, carbon fiber precursors should possess a high carbon content to minimize the mass loss incurred during production. Furthermore, precursors should exhibit good mechanical stretchability, allowing them to spin into thin yarns (Lengsfeld, 2020). Three types of precursors are employed in the carbon fiber manufacturing process: acrylic precursors such as Polyacrylonitrile (PAN), cellulosic precursors such as Rayon, and pitch-based precursors derived from petroleum or coal tar (Jones, 1994; Park, 2015). Over 90 % of carbon fiber currently in the commercial market is fabricated using PAN-based precursors, while the remaining approximately 10% is produced using pitch-based precursors (Lengsfeld, 2020). PAN-based precursors have a higher carbon yield compared to cellulosic precursors, with PAN-based precursors containing approximately 60% carbon and cellulosic precursors containing only 44 % (Lengsfeld, 2020; Park, 2015). Although pitch-based precursors contain over 85% carbon, their manufacturing cost is significantly higher than PAN-based precursors (Rahaman, Ismail, & Mustafa, 2007). Furthermore, the availability of PAN is considerably higher than other precursors, and the carbon fiber generated from PAN has relatively consistent quality (Lengsfeld, 2020). Therefore, the majority of carbon fibers available in the market are manufactured from PAN-based precursors.

2.2.1 *Fabrication process of carbon fiber*

Polyacrylonitrile (PAN) is a thermoplastic polymer derived from the polymerization of acrylonitrile monomers. However, PAN-based precursors are not directly obtained from homopolymer PAN, as the latter undergoes challenging processing during the oxidation stage. The high initiation temperature and rapid heat changes during oxidation generate thermal shock, leading to the scission of polymer chains. Therefore, precursors typically contain over 85% acrylonitrile monomers along with some co-monomers to control the exothermic reaction during oxidation (Park, 2015). The composition of co-monomers and the selection of solvents employed in the synthesis of precursors significantly influence the properties of the precursor and the efficiency of polymerization. Polymerization methods, such as solution polymerization, bulk polymerization, emulsion polymerization, and aqueous dispersion polymerization, are employed to fabricate PAN-based precursors (Park, 2015). The chemical compositions and fabrication methods of precursors are typically proprietary information which closely guarded by manufacturers (Lengsfeld, 2020).

PAN-based precursors are fibers optimized for carbon fiber production. PAN-based fibers are textile fibers developed by DuPont in the 1940s (Park, 2015). Shindo, Fujii, and Sengoku (1962) further developed carbonization and graphitization processes to create carbon products from PAN-based fibers at the Agency of Industrial Science and Technology in Japan. Shindo, Fujii, and Sengoku (1962) also proposed that a low-temperature heat pre-treatment at approximately 200°C with an oxidizing atmosphere can facilitate carbonization and graphitization processes. The post-treatment of carbon fiber after carbonization and graphitization involves surface treatment, washing, drying, and sizing (Lengsfeld, 2020).

Figure 2.1 shows the sequence of manufacturing stages involved in producing PAN-based carbon fiber.

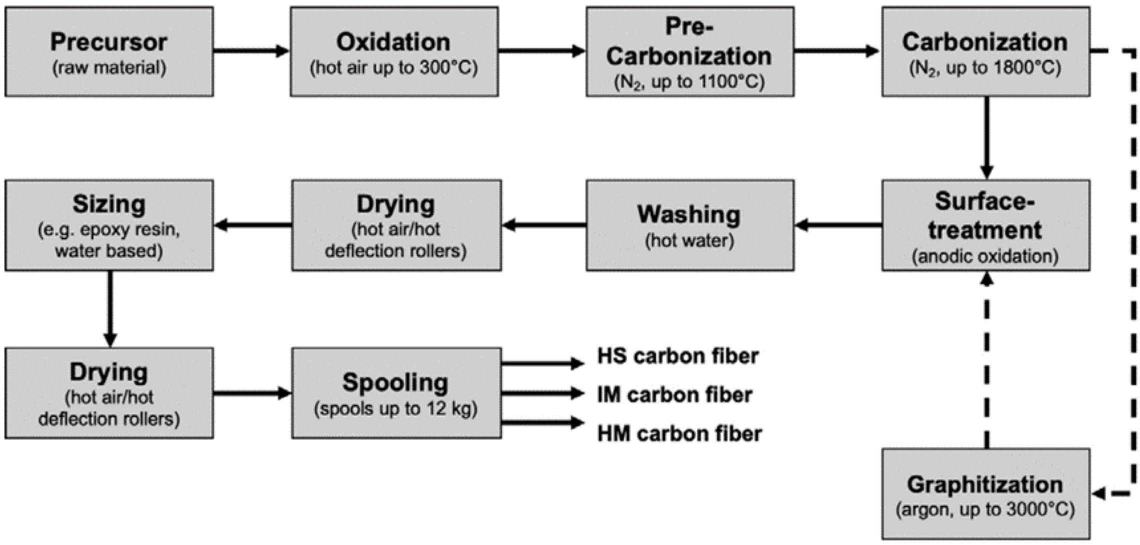

Figure 2.1. Sequence of manufacturing stages of PAN-based carbon fiber (Lengsfeld, 2020)

Oxidation, or thermal stabilization, is a process that stabilizes PAN-based precursors thermally by converting linear molecules into ladder polymers. PAN-based precursors are subjected to an oxygen atmosphere at approximately 200 °C to undergo cyclization and form a planar aromatic structure (Jones, 1994). The cyclization reaction is catalyzed by a co-monomer incorporated within PAN-based precursors, which serves as an initiator to induce thermal polymerization. The pendant nitrile groups in PAN-based precursors absorb oxygen from the atmosphere, and water molecules are eliminated from the precursors during the cyclization process, resulting in the formation of rings during the polymerization reaction. Other co-monomers incorporated within PAN-based precursors are employed to reduce the minimum temperature required for cyclization and the glass transition temperature of the precursor which facilitate the diffusion of oxygen (Jones, 1994). During the oxidation process, PAN-based precursors are also stretched to enhance the orientation of molecular structures and promote structural alignment (Lengsfeld, 2020). The oxidation process stabilizes the structure of PAN-based precursors, enabling them to withstand elevated temperatures in future treatment without melting and maintain their fiber form (Park, 2015). Furthermore, oxidation transforms the color of PAN-based precursors from white to black and facilitates the formation of graphite structures during carbonization and graphitization (Jones, 1994). Despite the exothermic nature of the reaction, it is a crucial process for producing high-quality carbon fiber (Lengsfeld, 2020). Figure 2.2 illustrates the transformations in chemical structures of PAN-based precursors from linear molecules to ladder polymers with cyclic aromatic structures.

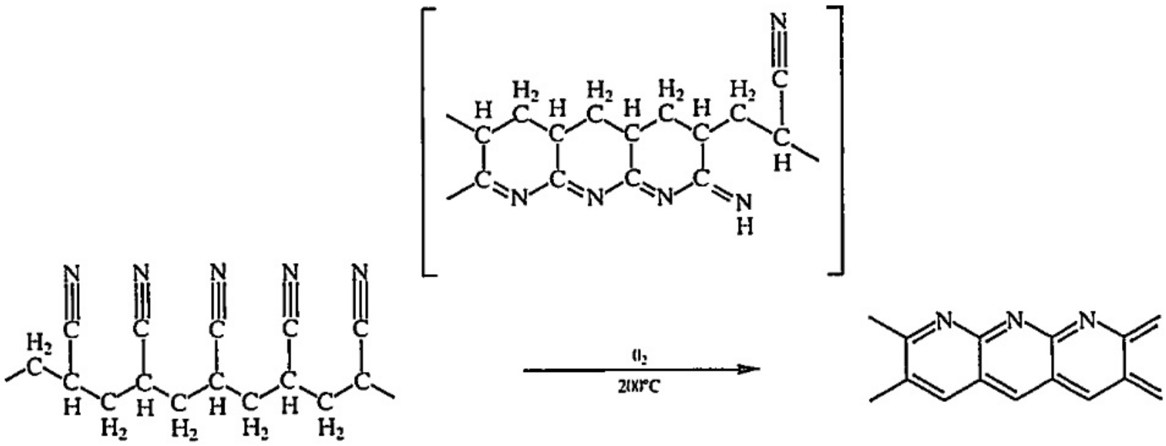

Figure 2.2. Changes in chemical structural of PAN-based precursors during oxidation (Jones, 1994)

Carbonization is a relatively low-temperature heating stage employed to remove all non-carbon elements from the precursors and condense the ladder polymer into carbon fiber filament. This process takes place in an inert environment to prevent material being combusted during high-temperature operations (Lengsfeld, 2020). Typically, nitrogen is utilized to establish the inert atmosphere due to its cost-effectiveness and high natural abundance. Stabilized PAN-based precursors obtained through oxidation are then placed in a furnace for carbonization. With approximately 60 % carbon content, the precursors are condensed or polymerized into a form of graphene-like ribbons through the elimination of hydrogen (H_2) and the formation of covalent bonds between carbon atoms. Subsequently, after dehydrogenation, the ribbons are further condensed into graphene-like sheet structures by eliminating nitrogen (N2). Dehydrogenation and denitrogenation are took place at different operating temperatures ranging from 400 to 600 °C and from 600 to 1300 °C respectively during the carbonization process (Park, 2015). Figure 2.3 illustrates the chemical structures of the precursor and processing stages at various operating temperatures. In addition to hydrogen and nitrogen, hydrogen cyanide and any oxygen products are also removed during the process. Therefore approximately half of the original precursor weight is lost, resulting in a fiber with over 90 % carbon content (Dér et al., 2021; Jones, 1994). Carbon fiber with graphite structure is obtained at the end of denitrogenation. At the final phase of carbonization, with the escalating treatment temperature, the orientation and alignment of the chemical structure are progressively improved along the fiber direction, subsequently enhancing the mechanical properties of carbon fiber (Lengsfeld, 2020).

Graphitization, a high-temperature heating process, is employed to further enhance the alignment and orientation of carbon atoms, resulting in the production of high-modulus carbon fiber (Lengsfeld, 2020). Graphitization can be regarded as an extended heating process of carbonization conducted in a continuous furnace which facilitates the growth of graphite structure within carbon fiber (Park, 2015). Similar to carbonization, graphitization takes place in an inert environment with argon being the inert gas used to fill the atmosphere instead of nitrogen. As the operation temperature of graphitization can reach up to 3000 °C, at which point nitrogen may react with carbon to form cyanogen, a hazardous gas. Therefore, nitrogen is not suitable for use in graphitization. Despite the higher cost of argon compared to nitrogen, its higher density and viscosity enable it to promote the quality and strength of carbon fiber (Park, 2015). Graphitization further refines the graphene layers and develops the graphite structure within the fiber. As graphene layers align along the fiber direction and reduce inter-layer space, the graphite structure expands in thickness, resulting in increased crystallinity and enhanced modulus of elasticity when the treatment temperature approaches 3000 °C (Lengsfeld, 2020; Park, 2015).

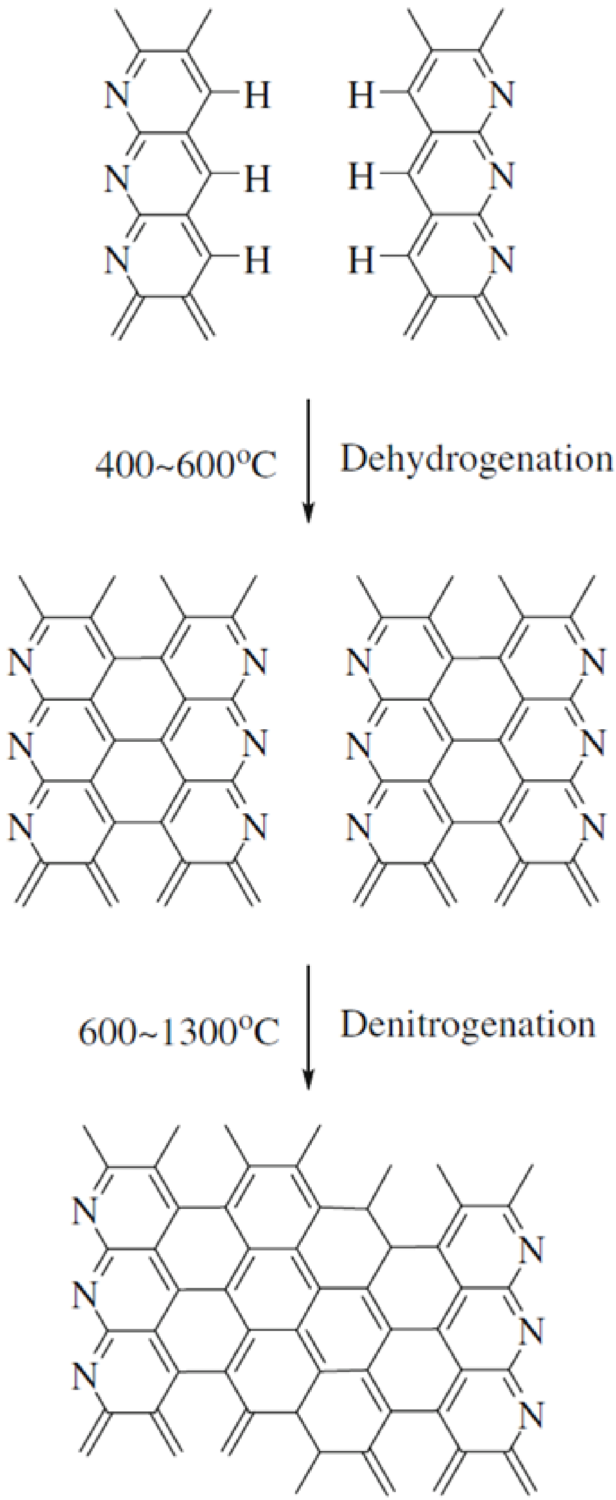

Figure 2.3. Chemical structure and processing stages at different operation temperature (Park, 2015)

Throughout the carbonization and graphitization processes, carbon fiber can be extracted from the furnace at various treatment temperatures, resulting in distinct mechanical properties (Lengsfeld, 2020). Both tensile strength and modulus of elasticity of carbon fiber show an upward trend with increasing treatment temperature, commencing at 1000 °C. Carbon fiber attains its maximum tensile strength when the treatment temperature falls within the range of 1500-1600°C, and tensile strength decreases as the treatment temperature exceeds 1600 °C (Park, 2015). On the other hand, the modulus of elasticity of carbon fiber continues to increase, reaching a peak of 500 GPa at 3000 °C. Figure 2.4 shows the correlation between the final heat treatment temperature and the mechanical properties of carbon fiber.

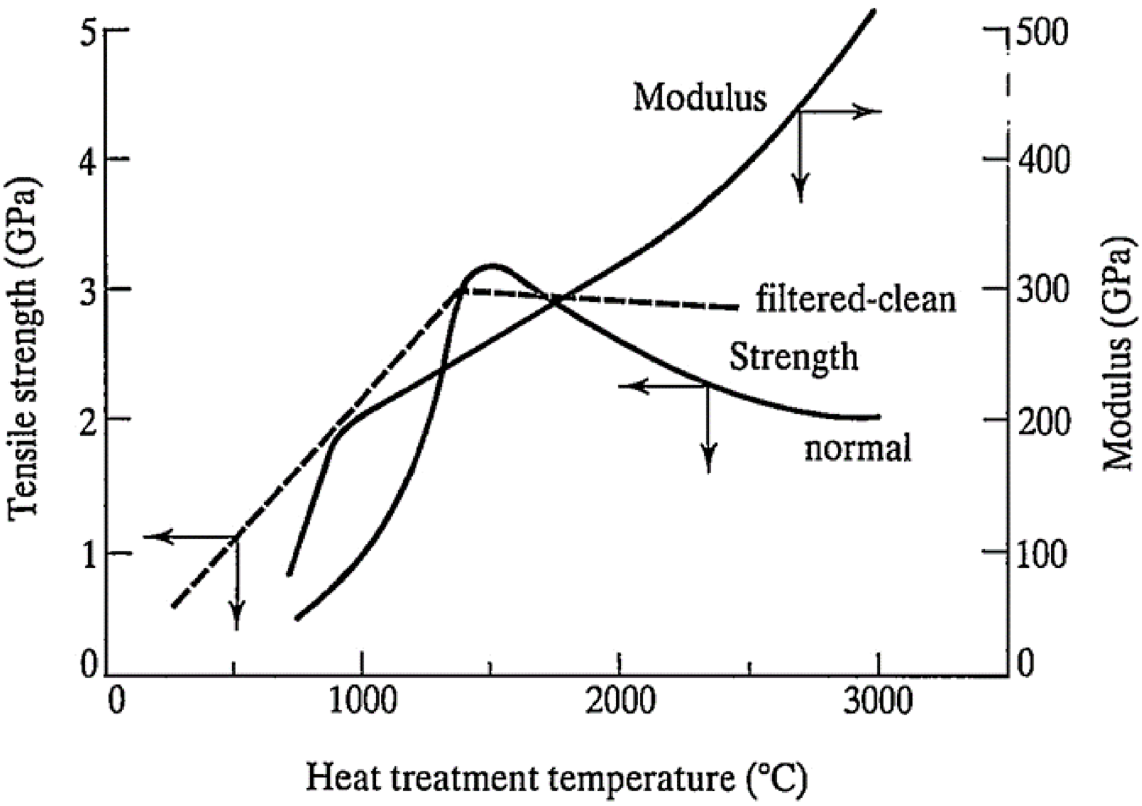

Figure 2.4. Effect of heat treatment temperature on the strength and modulus of carbon fibers (Jones, 1994)

2.2.2 *Classification of carbon fiber*

Carbon fiber is being categorized according to its mechanical properties at different treatment temperatures (Jones, 1994). The orientation of crystalline structures within the fiber at a specific treatment temperature serves as the primary determinant in classifying carbon fiber into categories: Ultra-High Modulus (UHM), High Modulus (HM), Intermediate Modulus (IM), High Tensile Strength (HT), and isotropic. These categories can also group into Type I, Type II, and Type III. Carbon fibers subjected to heat treatment temperatures exceeding 2000°C with the crystalline structures oriented along the fiber direction are classified as Type I – high modulus carbon fiber. Type I carbon fibers include the UHM and HM categories with modulus of elasticity exceeding 300GPa. The tensile strength of UHM and HM carbon fiber is typically less than 1% of its modulus of elasticity. Carbon fibers subjected to heat treatment temperatures at approximately 1500°C with the crystalline structures oriented along the fiber direction are classified as Type II – high strength carbon fiber. Type II carbon fibers include the IM and HT categories with modulus of elasticity ranging from 300GPa to 3GPa. The tensile strength of IM carbon fiber is typically greater than 1% of its modulus of elasticity, while HT carbon fiber has a tensile strength between 1.5% and 2%. Carbon fibers subjected to heat treatment temperatures below 1000°C with the crystalline structures oriented randomly are classified as Type III – isotropic carbon fiber. Type III carbon fibers include the isotropic categories with modulus of elasticity ranging not less than 100GPa with low tensile strength. Type III carbon fiber has the lowest production cost among all types, as it requires the lowest treatment temperature (Park, 2015). Table 2.1 provides a detailed specification of the aforementioned three types of carbon fiber and their corresponding categories.

Table 2.1. Classification of carbon fibers (Park, 2015)

Carbon fiber type	Heat treatment temperature (°C)	Crystallite orientation	Long-distance order	
Type I high modulus	>2,000	Mainly parallel to the fiber axis	High	UHM HM
Type II high strength	≈1,500	Mainly parallel to the fiber axis	Low	IM HT
Type III isotropic	<1,000	Random	Very low	Isotropic

2.3 Matrix of composite materials

Another constituent of composites is the matrix phase. Matrices used in composite materials can be categorized into polymer matrices, metal matrices, or ceramic matrices. Among these three types of matrices, polymer matrix composites are most frequently utilized in industrial applications. Polymer resin systems are primarily classified into thermoplastic and thermosetting polymer. Thermoplastic resin systems are commonly employed in composites fabricated through injection molding and prepreg while thermosetting resin systems are typically utilized in composites manufactured through resin infusion or resin transfer molding processes (Mazumdar, 2002). The selection of resin system depends on the intended application. Epoxy resins, a type of thermosetting resin system, are commonly employed as matrix phase materials in composites utilized for structural applications. Epoxy resins enhance the structural integrity of composites by achieving high crystallinity upon curing (Fried, 2014). The high crystalline structure in the matrix phase combined with fabric form of continuous fiber reinforcement enables the resulting composites to attain high specific mechanical properties comparable to those of high-performance metallic alloys utilized in various industries, such as the 6061-aluminum alloy employed in the construction of aircraft monocoque structures. Epoxy resins have better thermal stability, chemical resistance, and low molecular weight compared to other matrix (Strong, 2006). However, brittle properties, long fabrication cycle, as well as limited storage life are the limitation of epoxy resins. Any resin systems containing epoxides functional groups are classified as epoxy resins, Figure 2.5 shows the chemical structure of the epoxide group (Park, 2015).

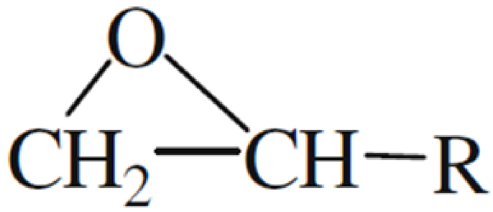

Figure 2.5. Chemical structure of epoxide group (Park, 2015)

Several important properties such as viscosity, gelation time, curing time, curing temperature and wettability should be considered when selecting a resin system for the production of a composite material. Typically, some of these parameters are controlled by the catalyst employed to initiate the crosslink reaction which serves as the hardener of the resin system (Young, 2011). The shrinkage effect may become noticeable when producing resin objects in massive size. During the curing process, exothermic reactions generate heat which can accumulate within the resin with a large volume, particularly in regions with greater thickness. The elevated temperature in these areas accelerates the curing process of the resin which potentially results in uneven curing of the object (Atkins, 2016). Therefore, the overall shrinkage effect on the object may become more obvious. The mechanical properties of these resins after curing can vary significantly depending on the curing conditions and the process of infusing the resin into reinforcement (Bag, 2013). The variation in epoxy resin, coupled with different weave pattern of reinforcement, may results in large discrepancy in the mechanical properties of composites.

2.4 Nanomaterials

Nanomaterials, such as carbon nanotube, are incorporated into carbon fiber-reinforced polymer (CFRP) composite during the matrix infusion process to enhance the mechanical performance and broaden the range of applications for the resulting composites. Carbon nanotubes (CNTs) are the most widely utilized material within the carbon nanomaterials. Carbon atoms are typically arranged in three distinct structures: graphite, diamond, and fullerenes, each showing unique characteristics. Single-walled carbon nanotubes (SWCNTs) consist of a single layer of graphene wrapped into tubular form with buckyball structure just like fullerenes at both ends of the tube. Multi-walled carbon nanotubes (MWCNTs) comprise multiple layers of graphene wrapped into a tubular form, similar to a SWCNT enclosing a smaller SWCNT and so on. CNTs show a structural similarity to graphene which grants them semi-conductor properties akin to those of graphene (Huang, Qi, Boey, & Zhang, 2012). CNTs have a negative coefficient of thermal expansion, which has led to the assumption that they have the ability to increase the thermal stability within polymer matrices and composites (Najmi & Hu, 2023; Zhang, Fan, & Shen, 2023).

However, CNTs cannot disperse uniformly within a polymer matrix due to their high aspect ratio and inherent van der Waals forces. Therefore, they tend to entangle with each other, forming bundles and ropes. Furthermore, the presence of CNTs may affect the crosslink reactions of the polymer matrix during the curing stage of manufacturing. CNTs treated with surfactants prior to incorporation into polymer matrix may alleviate the entanglement problem and reduce the impact on crosslink reactions. Surfactants disperse CNTs into a polymer matrix by enhancing the chemical interaction between CNTs and the matrix which facilitating their bonding (Wang et al., 2007). Pre-treated CNTs enhance their stability during the incorporation process. Ultrasound and centrifugation can facilitate the separation of CNTs from entanglement (Allaoui & El Bounia, 2009).

2.5 Fabrication methods of composite materials

Fiber-reinforced polymer composite can be manufactured using a variety of methods according to the design specification of the product. Composites with thermosetting resin system as matrix phase materials are typically manufactured through resin transfer molding. Resin Transfer Molding (RTM) is a closed mold process that has evolved from liquid molding technology (Yalcinkaya et al., 2019). Over the past decade, RTM has advanced significantly, with the development of low-viscosity thermosetting resin systems and automated fiber laminates production. This has led to the emergence of various RTM variants, such as vacuum-assisted RTM (VARTM), Seeman's Composite Resin Infusion Molding Process (SCRIMP), and resin film infusion (RFI), each with its own advantages and applications (Beckwith & Hyland, 1998).

RTM involves filling a mold with resin to saturate fiber laminates, resulting in a composite part with excellent surface finish and near-net shape. The process offers advantages such as short cycle times, low injection pressure, and the ability to incorporate molded-in inserts, but tooling design and laminates placement are critical considerations (Chen, Arakawa, & Uchino, 2016). The utilization of conventional RTM process has grown significantly across various industries. This growth has led to the development of numerous RTM variants, each with unique aspects, but all involving the movement of resin through reinforcement laminates to create a composite structure. Examples of RTM applications include aerospace components, marine rudders, and sports equipment, showcasing its ability to produce complex parts with high fiber volume fractions and attractive surface finishes (Heider & Gillespie, 2004). Bill Seemann's SCRIMP™ process uses hard tooling, a vacuum bag, and a resin distribution system to rapidly infuse resin into large composite structures. This process successfully used with various resins and has been particularly successful in fabricating large composite structures, such as yacht hulls, marine deck structures, refrigerated railcars, and submarine bow sections. The SCRIMP^{TM} process can easily attain a fiber volume ratio of 50%, but it shows significant challenges when attempting to further increasing it to 55-60% (Seemann, 1991). The Boeing Company developed the Resin Film Infusion (RFI) process to enable the use of high-viscosity resins in RTM. The RFI process involves laying up a resin film in the lower tool half, placing a stitched laminate on top, and applying vacuum and autoclave pressure during a cure cycle. This process, coupled with stitched laminates technology, improves damage tolerance and fatigue resistance, making it suitable for large-scale aerospace applications. Key factors of RFI process include laminates design, tooling optimization, and a tailored viscosity-temperature-time profile for complete saturation (Berg & Higgins, 2008).

VARIM was developed to inherit the advantages of different RTM variants. It is the most widely used manufacturing technique due to its low tooling costs, minimal emission of volatile organic compounds (VOCs) and scalability to the size and shape of the product (Rudd, Long, Kendall, & Mangin, 1997; Williams, Summerscales, & Grove, 1996). VARIM also generates significantly less scrap compared to other methods by effectively reducing the void content within the composite (Goren & Atas, 2008). Void content directly impacts the fiber volume fraction and, hence, the mechanical properties of the composite. A high-quality composite should demonstrate a low void content and only the composite with less than 1% void content are suitable for aerospace applications (Li, Krehl, Gillespie, & Heider, 2004).

The VARIM process comprises various components, including vacuum bagging films, sealant tapes, peel plies, liquid release agents, resin distribution mediums, and breather fabrics (Amirkhosravi, Pishvar, & Altan, 2018). Vacuum bagging films are utilized to establish a closed system by sealing the mold edge with sealant tape. Double-sided sealant tapes are applied between the bag and the mold surface to ensure a vacuum-tight seal. Resin distribution medium can facilitate the resin to spread laterally and are placed on the top of the entire molding layup. Breather fabrics allow the air and volatiles to escape from the vacuum environment within the mold throughout the cure cycle and absorb any excessive resin from the fiber laminates. Peel plies are placed against fiber laminates to provide a clean and uncontaminated surface for post-processing with excellent heat resistance. Liquid release agents are utilized to facilitate the release of the composite from the mold and impart a glossy finish on the cured composite. In certain instances, liquid release agents can temporarily address tool porosity issues. These components collaborate to establish a closed system, effectively remove trapped air, and ensure the production of a high-quality composite (Polowick, 2013). Resin systems employed in the VARIM process should have a prolonged pot life and low viscosity. A prolonged pot life enables the resin to fully penetrate the reinforcement of a large and complex product, and low viscosity facilitates the resin's rapid filling of all mold cavities. Thermosetting polymers, such as polyester and epoxy resins, are commonly utilized in the VARIM process (Simacek, Eksik, Heider, Gillespie, & Advani, 2012). These resins typically have low viscosity value ranging from 100 to 400 mPa·s which facilitates effortless flow through the densely packed fiber laminates. Additionally, they have low peak exotherms to prevent excessive heat accumulation during infusion and curing process. Furthermore, these resins have low reactivity but short gelation and curing time which ensure adequate mold filling time and short molding cycle (Zhang, Gu, Li, & Zhang, 2014).

2.6 Systematic Literature Network Analysis (SLNA) of CFRP composites

Systematic literature network analysis (SLNA) is a literature review methodology that comprises with Systematic Literature Review (SLR) and Citation Network Analysis (CNA).

SLR selects the most relevant articles for CNA to analyze. CNA makes use of the bibliographic information from the selected articles, including publication details, citation, and keywords, to analyze the evolution of knowledge. Researchers often cite each other which leads to the development of a citation network (Colicchia & Strozzi, 2012; Wong et al., 2020).

Citation data for articles is retrieved from the Institute for Scientific Information (ISI) Citation Database via a web-based client called Web of Science (WoS). Keywords and phrases related to this research study, along with their synonyms and abbreviations, are inputted into WoS for searching articles within the same research field. The analysis was conducted and 269 articles were returned. Conference papers, theses, early access articles, and any other articles that fall outside the scope of this research study were excluded as researchers typically reference to historical viewpoints from journal articles to support their new discoveries (Colicchia & Strozzi, 2012; Ngai, Moon, Riggins, & Yi, 2008). Irrelevant articles were eliminated based on their titles, abstracts, and bibliographic information through WoS database to minimize any bias from subjective judgment. The search result was subsequently refined to 151 articles for further analysis.

A citation matrix document containing the complete bibliographic profile of each selected article was exported from the WoS database. Selected articles were statistically analyzed with their publication journal, year, locations, and research areas. CNA was conducted using CitNet Explorer, a bibliometric analysis software, with the citation links, abstracts, authors, and keywords of the selected articles from the citation matrix document. Articles were grouped into clusters through clustering analysis based on their citation linkages as researchers tend to cite articles with closely related topics (Colicchia & Strozzi, 2012; Tam et al., 2020). CitNet Explorer also provided a visualization diagram for each cluster formed to reveal the knowledge transfer and development patterns within the research field. The clustering results were validated using another bibliometric analysis software called VOS Viewer (van Eck & Waltman, 2014).

2.6.1 *Clustering of SLNA reviewed articles*

CitNet Explorer clusters the shortlisted 151 articles into large and small clusters. With the specified minimum cluster size, CitNet Explorer will discards or combines the clusters that does not meet the specified size as they may not be significant (van Eck & Waltman, 2014). The minimum cluster size was set to 4 publications, which resulted in 7 principal clusters containing a total of 94 articles. The remaining 48 clusters, comprising 57 articles, were discarded. Notably, 3 principal clusters formed with 4 articles are mostly published within the last decade, suggesting that these 3 clusters are emerging topics.

The principal clusters are named after the research direction of the articles within them. The first cluster focuses on improving the VARIM method (Bodaghi et al., 2020; Gajjar, Shah, Joshi, & Patel, 2020; Yalcinkaya, Sozer, & Altan, 2017). The second cluster focuses on the mechanical properties of composites (Dean, Obore, Richmond, & Nyairo, 2006; Kochan, 2020; Volponi, Spena, De Nicola, & Guadagno, 2019). The third cluster focuses on the dynamic responses of composites (Hossain et al., 2014; Hosur et al., 2003; Hosur, Chowdhury, & Jeelani, 2007). The fourth cluster focuses on natural fiber composites (Garcia et al., 2020; O'Donnell, Dweib, & Wool, 2004; Tafur, Mora, & Baracaldo, 2018). The last three clusters focus on rapid curing in VARIM (Gu, Qin, Li, Zhang, & Zhang, 2015; Zhang, Gu, Wang, Li, & Zhang, 2014; Zhang et al., 2016), nano-filler enhancement (Liu, Deng, & Zhang, 2017; Monfared, Ayatollahi, & Isfahani, 2018; Uddin & Sun, 2008), and hydrothermal aging (Dogan & Arman, 2018; Dogan, Arman, & Ozdemir, 2019; Dogan & Atas, 2016). Therefore, rapid curing, nano-filler enhancement and hydrothermal aging are considered as emerging research directions in field of composite materials. Table 2.2 lists the themes and number of articles in each cluster. Figure

2.6 visualizes the networks and clustering of the 151 shortlisted articles. Figure 2.7 provide further drilldown to each cluster, with the cluster color corresponding to Figure 2.6.

Table 2.2 Principal clusters of CNA analysis (Or, Lo, & Kan, 2023)

Themes of Principal Clusters		
Cluster 1	Fabrication and molding methods of composites – (e.g. VARIM)	41 articles
Cluster 2	Properties and performance of multiscale composites – (e.g. static and dynamic mechanical properties)	29 articles
Cluster 3	Dynamic responses of CFRP composites	6 articles
Cluster 4	Fabrication and performance of natural fiber-reinforced polymer composites	6 articles
Cluster 5	Rapid curing in CFRP composites fabrications	4 articles
Cluster 6	Nano-filler enhanced FRP composites	4 articles
Cluster 7	Hydrothermal aging effect on FRP composites	4 articles

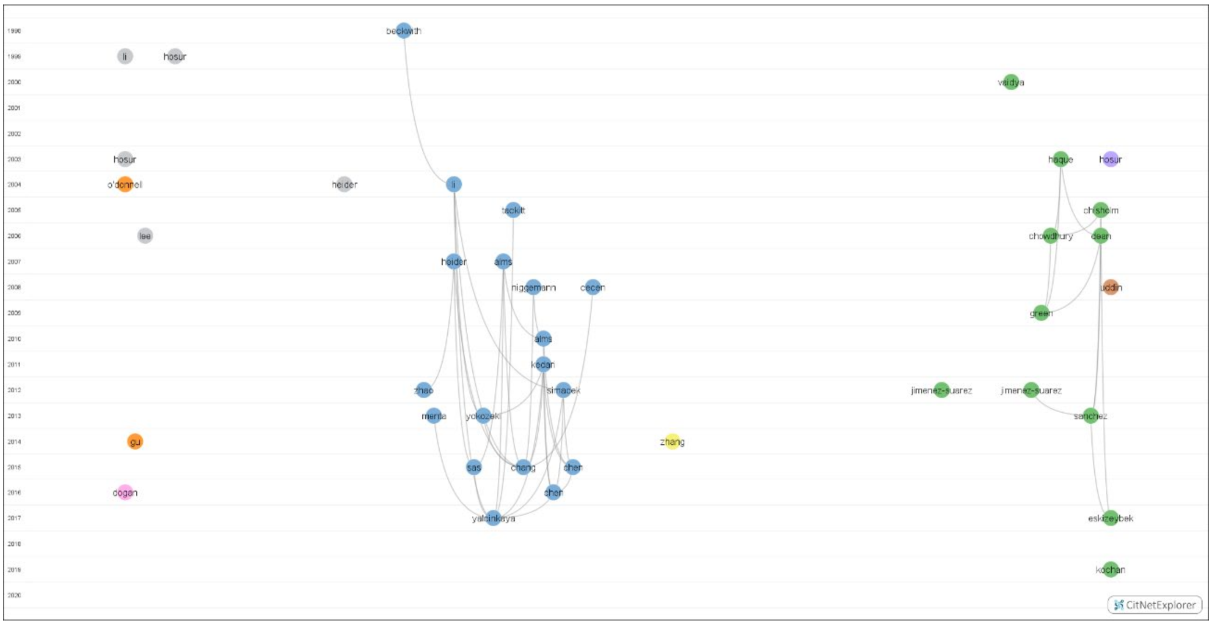

Figure 2.6 Visualization of CNA clustering (Or, Lo, & Kan, 2023)

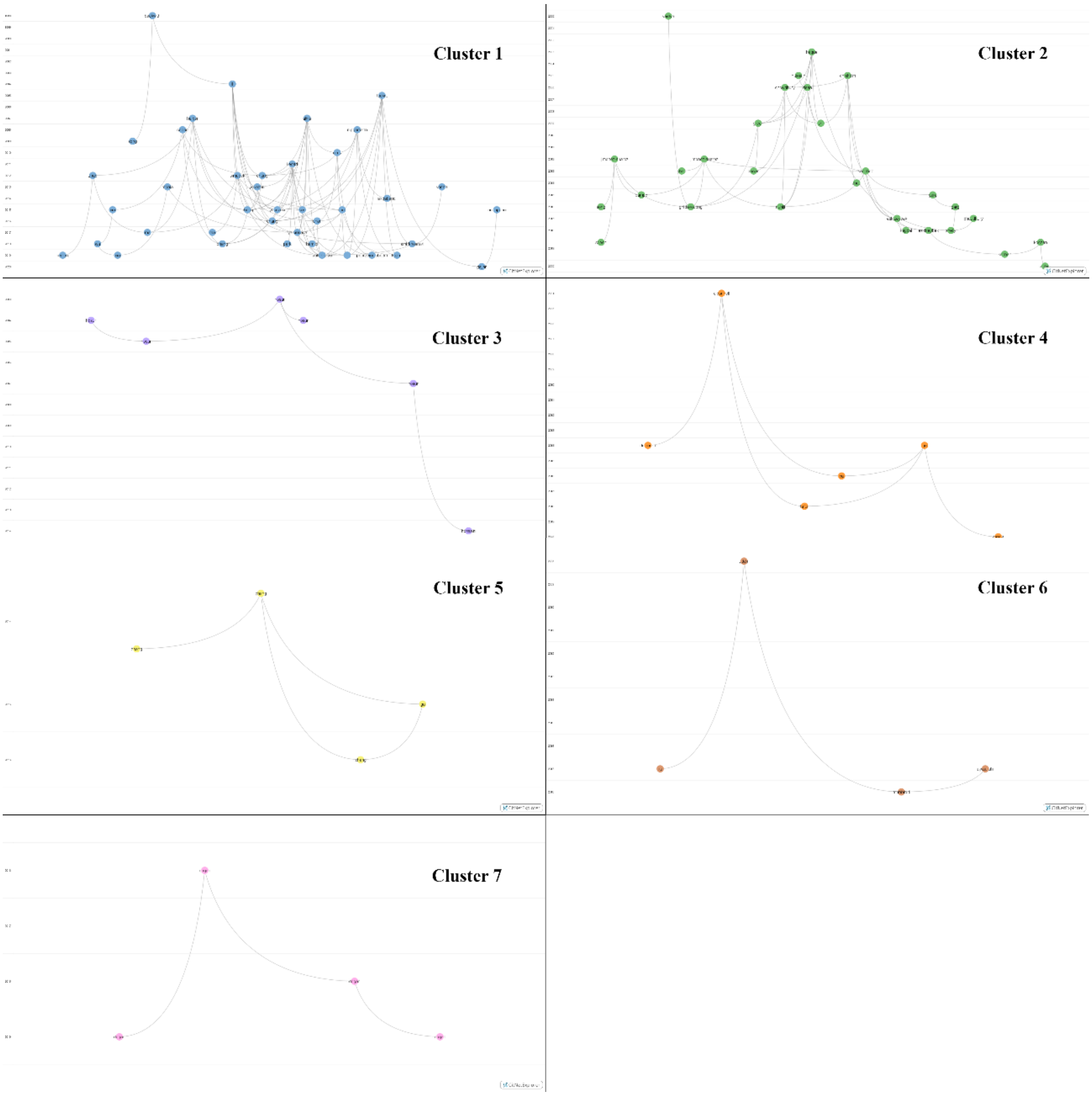

Figure 2.7 Visualization of 7 principal clusters (Or, Lo, & Kan, 2023)

2.7 Chapter Summary

In order to understand the current research direction and the knowledge transfer and development of CFRP composites, Citation Network Analysis and Main Path Analysis were conducted. Articles are formed into 7 principal clusters with 4 or more articles in each cluster. There are two large clusters dominating the research field: “fabrication and molding methods of composites” and “properties and performance of multiscale composites”. The SLNA and clustering analysis results are published as a journal article in the journal of Fibers and Polymers (Or, Lo, & Kan, 2023).

Among all fabrication methods, VARIM (or VARTM or SCRIM) is the most common used molding method. VARIM is a cost effective fabrication method as it only uses one-sided mold with low cost operating materials. Thus, most of the modified fabrication methods are based on VARIM. Materials used in VARIM processes, such as vacuum bagging films, peel plies and resin distribution medium, were clearly explained. Constituents of CFRP composite were reviewed. Manufacturing process of carbon fiber was explained in detail. The processes include oxidation, carbonization and graphitization. Classification of carbon fibers were identified, they are Type I with high modulus, Type II with high strength and Type III with isotropic. They are derived from different heat treatment temperature throughout the manufacturing process. The characteristics and chemical structure of epoxy resin were mentioned. Structure of carbon nanotube were also introduced.

Chapter 3 Methodology

3.1 Constituent specification for CFRP composite specimens

3.1.1 *Carbon fiber reinforcement*

The carbon fiber fabrics employed in this research study were 2/2 balanced twill-weaved 3K carbon fiber fabric (TI-3711) and plain-weaved 3K carbon fiber fabric (TI-3101) with a fabric weight of 208 gsm and 200 gsm respectively. TI-3711 has a fabric count of 13 PPI and 13 EPI while TI-3101 has a fabric count of 12.5 PPI and 12.5 EPI. Both fabrics were sourced from TEi Composites Corporation and weaved with TORAYCA T300 carbon fiber from Toray Composite Materials America, Inc. TORAYCA carbon fiber is a PAN-based carbon fiber with T300 as a standard modulus carbon fiber commonly used in aerospace application. The T300 carbon fiber used in TI-3101 and TI-3711 has a filament count of 3,000 and the diameter of each filament is 7μm. The carbon fiber density is 1.76 g/cm^3 with carbon content over 93 %. The sizing resin of T300 carbon fiber is compatible with epoxy, phenolic, bismaleimide (BMI), polyester, and vinyl ester resin system.

3.1.2 *Epoxy resin matrix*

Three epoxy resin systems were used in this research study: (1) WEST SYSTEM 105 Epoxy Resin (WS105) with WEST SYSTEM 209 Extra Slow Hardener (WS209) from Gougeon Brothers Inc. (WS105/209); (2) ML-812 A-LV Resin (ML812A) with ML-812 B-LV Hardener (ML812B) from Wells Advanced Materials Co., Ltd. (ML812A/B); and (3) IN2 Epoxy Infusion Resin (IN2) with AT30 Slow Hardener (AT30S) from Easy Composites Ltd (IN2/AT30S).

The WS105 resin and WS209 hardener have a viscosity of 1000 and 85 mPa·s respectively. The mix ratio of WS105/209 resin system is 3.68 : 1 by weight and a mixed viscosity of 650 mPa·s with a pot life of 40 minutes at 22 °C. The ML812A resin and ML812B hardener have a viscosity of 1500 and 30 mPa·s respectively. The mix ratio of ML812A/B resin system is 2.5 : 1 by weight and a mixed viscosity of 400 mPa·s with a pot life of 120 minutes at 25 °C. The IN2 resin and AT30S hardener have a viscosity of 500 and 10 mPa·s respectively. The mix ratio of IN2/AT30S resin system is 3.33 : 1 by weight and a mixed viscosity of 200 mPa·s with a pot life of 80 minutes at 25 °C. Table 3.1 summarizes the mixing parameters various resin systems.

Table 3.1 Mixing parameters of various resin systems

Resin system	Mix ratio (by weight) Resin : Hardener	Mixed viscosity (mPa·s)	Pot life
WS105/209	3.68 : 1	650	40 mins @ 22 °C
ML812A/B	2.5 : 1	400	120 mins @ 25 °C
IN2/AT30S	3.33 : 1	200	80 mins @ 25 °C

3.1.3 *Carbon nanotubes*

Carbon nanotubes used in this research study are multi-walled carbon nanotubes (MWCNTs) from Jiangsu XFNANO Materials Tech Co., Ltd. The MWCNTs have an outer diameter between 5 to 15 nm and a length between 10 to 30 μm. The purity of the MWCNTs is over 95 %. The MWCNTs have a specific surface area over 200 m^2/g. Figure 3.1 shows the information of the carbon nanotubes.

Figure 3.1 Carbon nanotubes used in this study

3.2 Fabrication of CFRP composite specimens

Figure 3.2 illustrates the fabrication flow of the CFRP composite specimens. The details of each fabrication process will be discussed in the following sections. A route card was developed to standardize the fabrication processes. Parameters for each process have been recorded for monitoring the quality of the specimen. If the parameters of a batch of specimens deviate from the standard, that batch will be discarded and the fabrication process will be restarted. Figure 3.3 shows the route card for specimens fabrication.

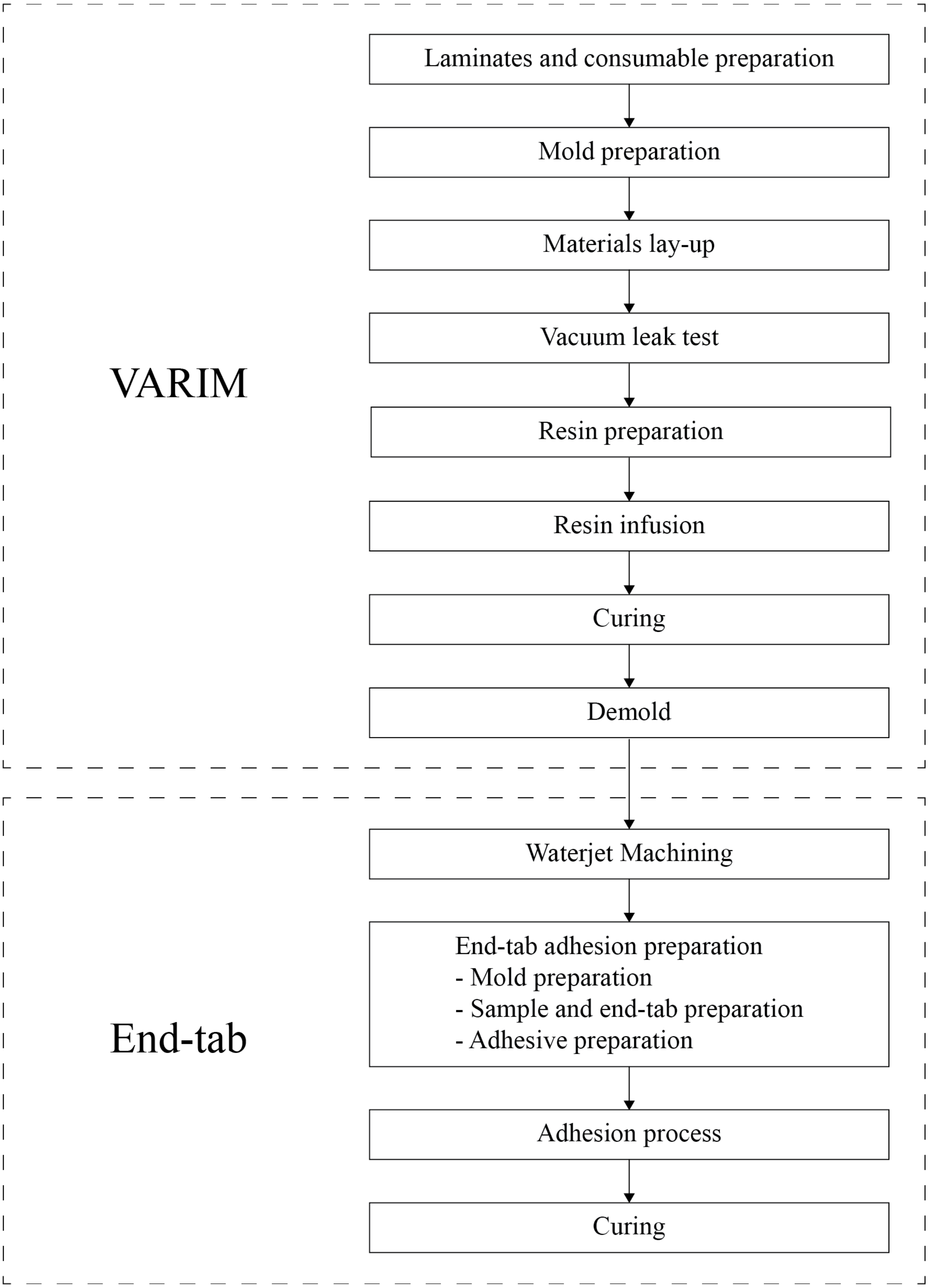

Figure 3.2 Flow chart of CFRP composite specimen fabrication

Route Card

THE HONG KONG POLYTECHNIC UNIVERSITY 香港理工大學
INDUSTRIAL CENTRE 工業中心
Composites & Fabrication

Route Card Number:	RC.00083R0	Issue:	01
Part Number:	CF TW panel 8plies		
Description:	Open mold + infusion process		
Drawing / Model No.:	NA	Issue:	0
Material Spec.:	- CF fibre TW 208gsm - WS105/209	P/O or Project Reference:	

Important Note: Any deviations to the process documented on this route card must be recorded in writing on the sheet, including: reason for deviation, dated and signed by the Project Engineer.

Op. No.	Operation Description	Tools / Time (As required)	Sign and Date
010	**Mould Release Preparation** - In accordance with ICFC.SOP.mould releasing procedure, ensure that the tooling plate is cleaned, sealed and released. - Use Table 1 below to track progress.	- Gloves - Safety Specks - Solvent - 2x2ft glass tool plate - 1" Masking Tape - Releaser - Paper Towel *Mould Release Preparation* ____h____min	

Part	Cleaned / C	Sealed / S	Released R
Layers applied			
Tick when complete			

Above: Table 1

Type of solvent used: ________________
Type of sealant used: ________________
Type of releasing agent used: ________________

Note: tape off the tooling edge with masking tape to avoid over releasing if sealing tape is to be applied onto the mould edge.

Op. No.	Operation Description	Tools / Time (As required)	Sign and Date
020	**Check-out Fibre** - Log-out material from dry storage. - Record material data in Table 2 below.	- Gloves ____h____min	

Data	Description
Material ID no.	
Batch no. (if any)	

Above: Table 2

Op. No.	Operation Description	Tools / Time (As required)	Sign and Date
030	**Ply Cutting** Cut out plies to their required dimensions. Use Table 3 to track progress.	- Gloves - Tape measure - PE Ruler - PE Set square - Masking tape ____h____min	

No. of Plies	Required Dimension	Fibre Direction	Tick when complete
A1	310 x 310mm	0/90	
A2	310 x 310mm	±45	
A3	310 x 310mm	±45	
A4	310 x 310mm	0/90	
B1	310 x 310mm	0/90	
B2	310 x 310mm	±45	
B3	310 x 310mm	±45	
B4	310 x 310mm	0/90	

Above: Table 3

Write down the total weight of the plies: ________grams

Issue	Date	Author	Quality Review	Technical Authorisation	Reason for Change
1	04/07/2022	HC Leung			1st Issue

Doc Ref: RC.00000.R0 – Route Card Template   Page 1 of 7

Figure 3.3 Route card for specimens fabrication

3.2.1 *Laminates preparation*

During the initial phase of this research study, carbon fiber-reinforced polymer (CFRP) composites were fabricated to evaluate the mechanical performance of various reinforcement weave patterns and matrix viscosities. Carbon fiber laminates with dimensions of 310 mm by 310 mm were cut from both twill-weaved and plain-weaved carbon fiber fabrics. Each weave pattern required two sets of carbon fiber laminates, with one set having the warp and weft tows oriented at 0 and 90 degrees (0/90), and the other set having the warp and weft tows oriented at 45 and -45 degrees (45/-45). Carbon fiber laminates were stacked with the fibers oriented in a symmetric manner which means the upper half of the laminates stack has a fiber orientation order mirroring that of the lower half. For example, 0/90 laminates are placed on top and bottom of the stack, followed by two 45/-45 laminates in between, that is [0/90, 45/-45, 45/-45, 0/90] which can be denoted as [0/90, 45/-45]s. A symmetric fiber orientation stack requires a minimum of four plies of laminates and results in a quasi-isotropic composite with isotropic in-plane properties. The weight of the laminates was measured and would be utilized in the resin preparation process.

3.2.2 *Mold preparation*

Vacuum-assisted resin infusion molding (VARIM) was employed to fabricate all composite specimens being tested in this research study. A flat and thick 600 mm by 600 mm square metal plate served as the mold for fabricating the composite plate. Acetone was applied to the mold surface from various directions so as to remove the dirt or residue that had been left from previous fabrication, as shown in Figure 3.4. Masking tape was then applied along the edges of the mold. Pressing the masking tape firmly was crucial to prevent any liquid seepage. LOCTITE FREKOTE 770-NC epoxy mold release agent from Henkel AG & Co. KGaA was applied to the mold surface to facilitate the separation of the composite plate from the mold at the end of fabrication cycle. Three layers of mold release agent were applied to ensure complete coverage, with each layer thoroughly dried before application of the next layer. The masking tape previously applied to the mold edges was then removed, and double-sided sealant tape was applied to the masked areas of the mold edges.

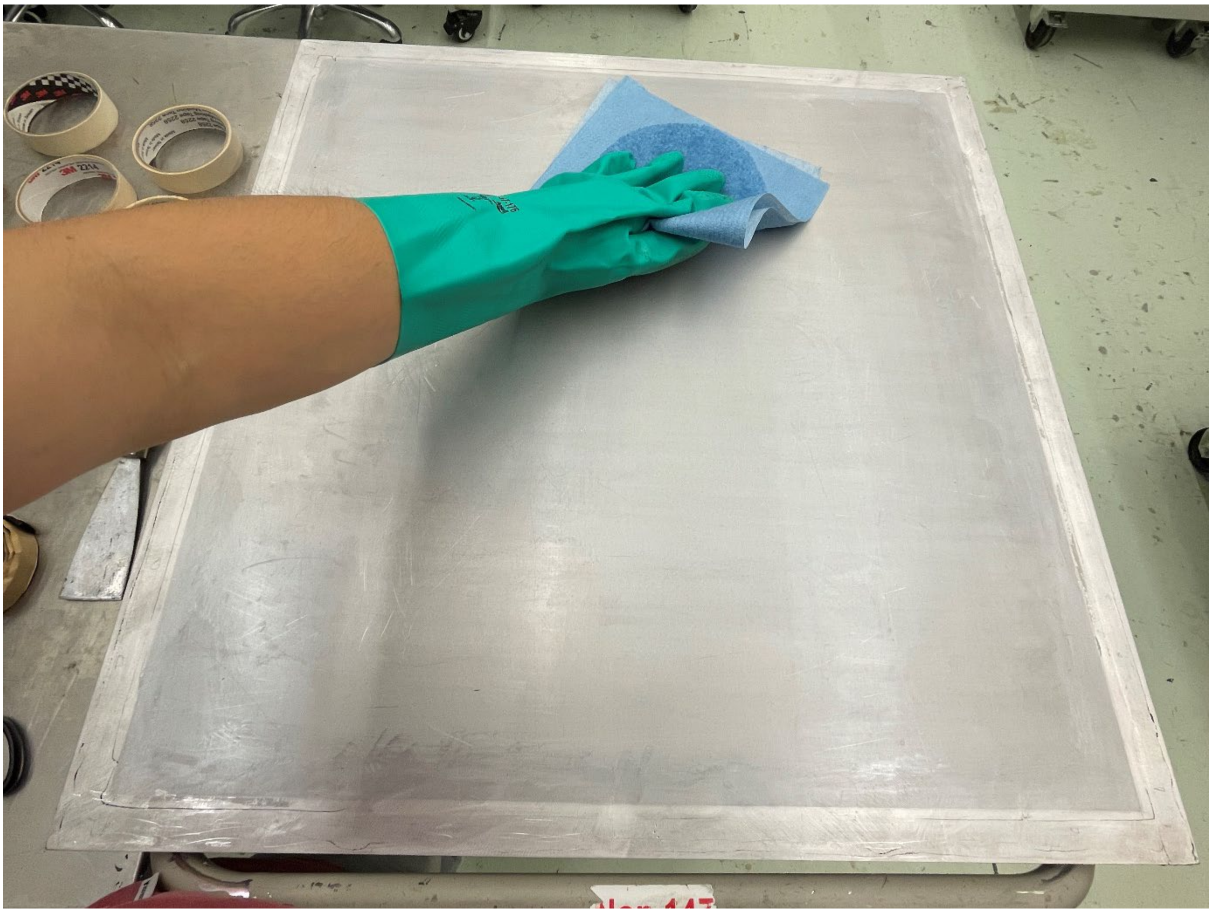

Figure 3.4 Mold surface cleaning using acetone

3.2.3 *Consumable preparation*

Consumables and laminates were positioned in the center of the mold surface which had been coated with a mold release agent, as shown in Figure 3.5. The consumables include peel plies, resin distribution mediums, and spiral tubes. Spiral tubes were employed to facilitate the spread of resin by transforming a point source of resin from the infusion inlet into a line source of resin on the mold surface. Two resin distribution mediums (or flow media) and two peel plies were cut to the same width as the carbon fiber laminates, which was 310 mm. The two resin infusion mediums were cut to the lengths of 50 mm and 320 mm, while the two peel plies were cut to lengths of 75 mm and 350 mm. Two spiral tubes with a length of 270 mm, and a 700 mm by 700 mm vacuum bag were also prepared.

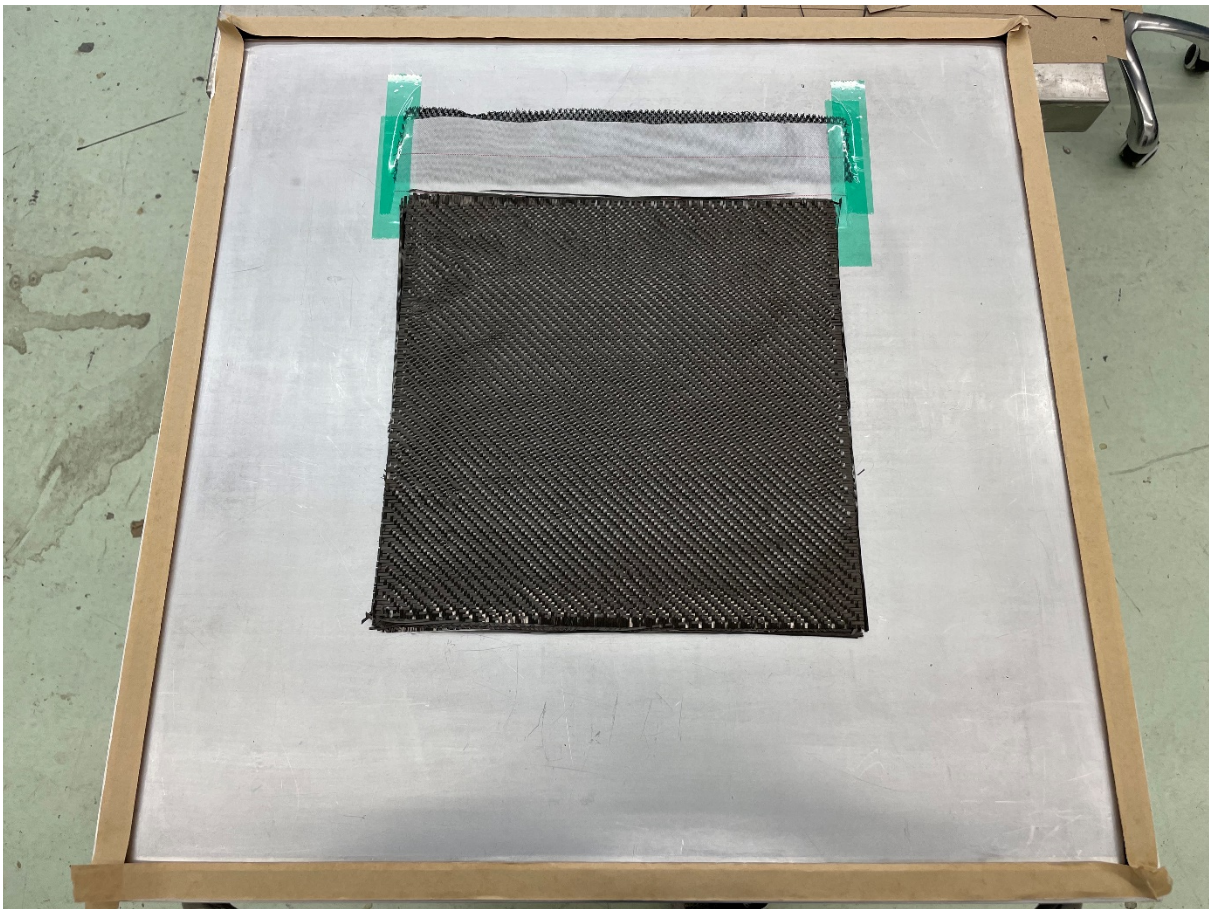

Figure 3.5 Consumables and laminates placed on the mold surface

3.2.4 *Materials lay-up*

The short resin distribution medium was positioned at the side of the resin infusion inlet, followed by the short peel ply. A fully stretched spiral tube was placed on top of the short peel ply. The laminates stack was then placed at the center of the mold, with some overlap with the short peel ply, but not the short resin distribution medium. The long peel ply was then covered over the laminates stack with a portion of the peel ply protruding from the laminates stack for resin infusion outlet. The resin infusion inlet and outlet should be positioned at opposite sides of the laminates stack to facilitate the permeation of resin throughout the laminates. The long resin distribution medium was placed on the long peel ply in alignment with the protruding edge of the peel ply. Finally, another fully stretched spiral tube was placed on top of the long resin distribution medium and positioned at the side of the protruding edge. Figure 3.6 illustrates the lay-up of the consumables and laminates stack on the mold surface.

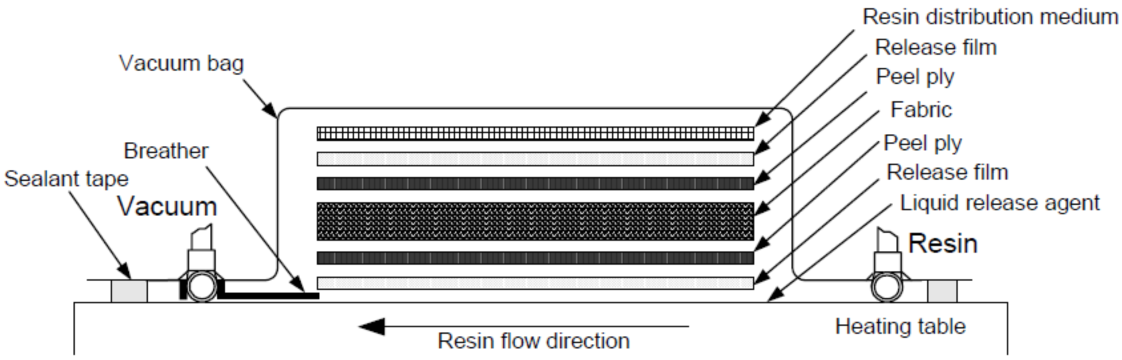

Figure 3.6 Schematic illustration of the VARIM setup (Goren & Atas, 2008)

All consumables were affixed to the mold surface with heat-resistant adhesive tapes. A resin infusion connector was positioned at the center of each spiral tube. A vacuum bag was used to cover the entire lay-up and the mold was sealed with the double-sided sealant tapes that had been previously applied to the mold edges. Pressing the vacuum bag and sealant tape firmly was crucial to prevent air leakage during the resin infusion and curing process, which could result in the production of high-quality composites. Vacuum bag was then perforated with a hole above each resin infusion connector, and a silicone tube was inserted into each connector. Sealant tapes were applied around the holes on the vacuum bag to complete the vacuum seal.

3.2.5 *Vacuum leak test*

One silicone tube was sealed with a clamp to prevent air from entering the mold. Another silicone tube was connected to a vacuum pump for removing air from the mold. The vacuum pump was turned on and the vacuum level within the mold was maintained at at least 25 inHg for a minimum of 15 minutes. The vacuum pump was then turned off and the vacuum level inside the mold was recorded. After 10 minutes, the current vacuum level was checked and compared with the previously recorded vacuum level. If the vacuum level difference was less than or equal to 1 inHg, the mold was airtight and ready for the resin infusion process. If the vacuum level difference was greater than 1 inHg, all the sealant tapes had to be firmly pressed again and the vacuum leak test was repeated until the vacuum level difference is less than or equal to 1 inHg.

3.2.6 *Resin preparation*

Resin and hardener were prepared according to the ratio provided by the manufacturer. The required amount of matrix for resin infusion was 1.5 times the weight of the reinforcement. For example, twill-weaved carbon fiber laminates have a fabric weight of 208 gsm and each laminate has an area of 0.0961 m^2 $(0.31\ m \times 0.31\ m)$. A four-ply twill-weaved carbon fiber laminates stack weighs 80.0 g $(0.0961\ m^2 \times 208\ gsm \times 4\ plies)$, and the required weight of matrix is 120 g $(80.0\ g \times 1.5)$. For using WS105/209 resin system as matrix, the mixing ratio between resin and hardener is 3.68 : 1 by weight. Therefore, the required weight of resin is 76.9 g $(120\ g\ \times\ \frac{3.68}{3.68+1})$ while the hardener is 25.6 g $(120\ g\ \times\ \frac{1}{3.68+1})$. Similar calculations can be applied to other composite configurations by multiplying the corresponding fabric weight, number of plies, and resin system mixing ratio.

The precise quantities of resin and hardener were weighed using an analytical balance with a resolution of at least 0.01 g, as shown in Figure 3.8, and subsequently placed into the vacuum chamber for degassing. This process eliminated any air pockets trapped within the resin and hardener. Resin and hardener were degassed separately to prevent cross-contamination which could potentially initiate the curing process of the resin. Both resin and hardener must degas for at least 15 minutes under a full vacuum level of approximately 30 inHg. During degassing, the resin and hardener may overflow due to the pressure difference between the interior and exterior of the liquid generated by the vacuum. Therefore, an emergency pressure relief valve was essential to prevent the liquids from overflowing. The sudden release of vacuum pressure by the emergency pressure relief valve ruptured the air bubble of the overflowing liquid and released the trapped air.

After degassing, the resin and hardener were weighed again and the actual weight of resin and hardener, which would be mixed, was recorded. The hardener was then mixed with the resin and the pot life started to count down, which is 40 minutes for the WS105/209 resin system. The resin mixture was thoroughly stirred with a spatula as illustrated in Figure 3.7. The resin mixture was then placed back into the vacuum chamber for degassing under a full vacuum level as air pockets were created during the mixing process.

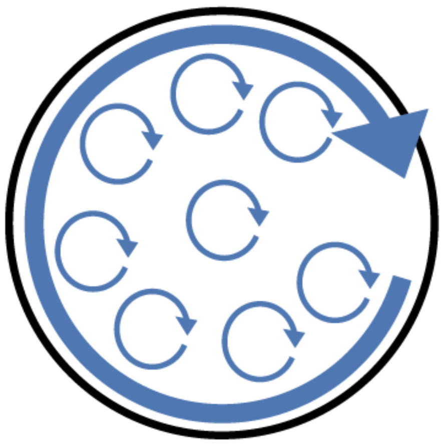

Figure 3.7 Stirring directions for mixing resin and hardener

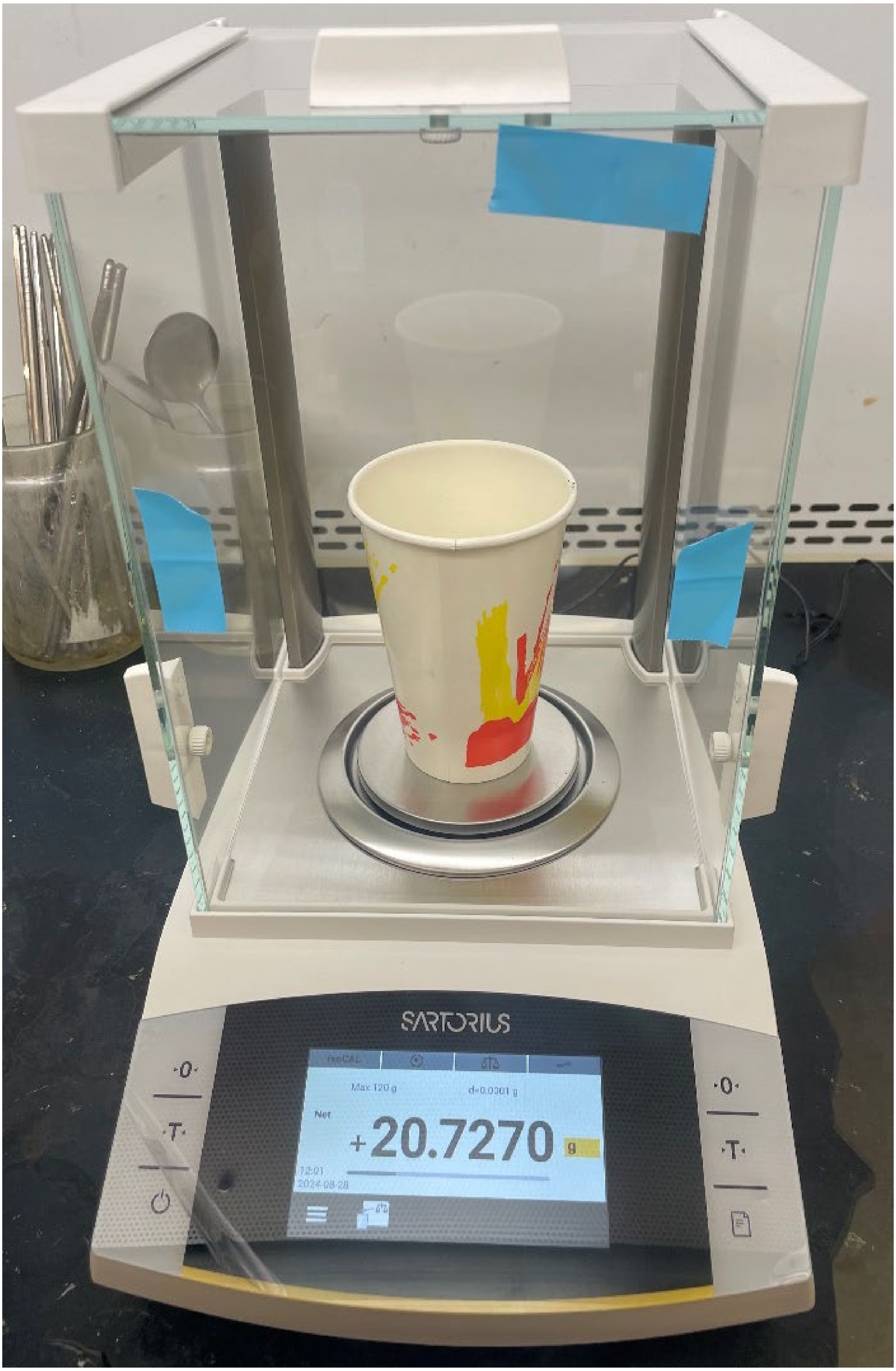

Figure 3.8 Resin and hardener weighed with analytical balance (with accuracy up to 0.0001g)

3.2.7 *Resin infusion*

Upon completion of the resin mixture preparation, the resin infusion outlet silicone tube was securely connected to a resin infusion catch-pot. This device served as a safety measure to prevent resin being drawn accidentally into the vacuum pump. The resin infusion catch-pot was then connected to the vacuum pump, and the resin infusion inlet silicone tube was immersed in the resin mixture. Once the setup was ready for the resin infusion process, the vacuum pump was switched on and the time was recorded. The resin infusion inlet silicone tube remained immersed in the resin mixture throughout the resin infusion process to avoid any air being drawn into the lay-up. The resin should permeate through the lay-up and fully saturate all the carbon fiber laminates as shown in Figure 3.9. As the resin mixture propagated and reached the resin infusion outlet, continue drawing of resin mixture for a few more minutes would be carried out if sufficient resin mixture was available in the inlet container. The resin infusion inlet silicone tube was sealed with a clamp before the resin entered the resin infusion catch-pot. The vacuum pump remained operational for at least 15 minutes to facilitate the evacuation of air pockets from the mold. The vacuum pump was then switched off and the time of the end of the resin infusion process was recorded.

Figure 3.9 Resin permeated through the lay-up with resin infusion inlet and outlet silicone tube positioned at two sides

The resin infusion process should be completed prior to the expiration of the resin pot life. In the case of WS105/209 resin system, the interval between the start of hardener mixing with the resin and the shutdown of the vacuum pump should not exceed the pot life of the resin system, which is 40 minutes in this case. The inlet container with residue resin mixture was weighed and recorded for calculating the amount of resin infused into the mold.

3.2.8 *Curing and demold*

Each resin system has its own curing profile, and some resin systems even have multiple profiles to achieve different mechanical performance. For instance, the curing profile of WS105/209 resin system to achieve its maximum strength is curing for nine days at 21 °C. The expected tensile strength of cured WS105/209 epoxy matrix is 50.3 MPa with a glass transition temperature at 54 °C. The curing profile of ML812A/B resin system to achieve its maximum strength is curing for either 24 hours at 25 °C or 4 hours at 50 °C, followed by 3 hours at 170 °C. The expected tensile strength of cured ML812A/B epoxy matrix is 60 MPa with a glass transition temperature at 164 °C. The curing profile of IN2/AT30S resin system to achieve its maximum strength is curing for 24 hours at 25 °C, followed by 2 hours at every 10 °C from 40 °C to 70 °C, and finally 4 hours at 80 °C. The expected tensile strength of cured IN2/AT30S epoxy matrix is 65.5 MPa with a glass transition temperature at 92 °C. Table 3.2 summarize the curing condition of various resin system.

Most of the resin systems remain at room temperature for 24 hours to solidify the resin before placing them in an oven. In some cases, the resin may require higher temperatures before solidification. Therefore, an autoclave is required to apply vacuum and heat simultaneously. Upon the complete curing of the matrix, all consumables were removed. The composite plate was then separated from the mold and peel plies, and marked with a unique part number for specimen identification. Figure 3.10 shows a demolded composite plate after curing and Figure 3.11 shows the composite plate after the removal of all consumables.

Table 3.2 Curing conditions of various resin systems

Resin system	**Curing condition**	**Glass transition temperature**
WS105/209	9 days @ 21 °C	54 °C
ML812A/B	24 hrs @ 25 °C + 3 hrs @ 170 °C	164 °C
IN2/AT30S	24 hrs @ 25 °C + 2 hrs @ 40 °C + 2 hrs @ 50 °C + 2 hrs @ 60 °C + 2 hrs @ 70 °C + 4 hrs @ 80 °C	92 °C

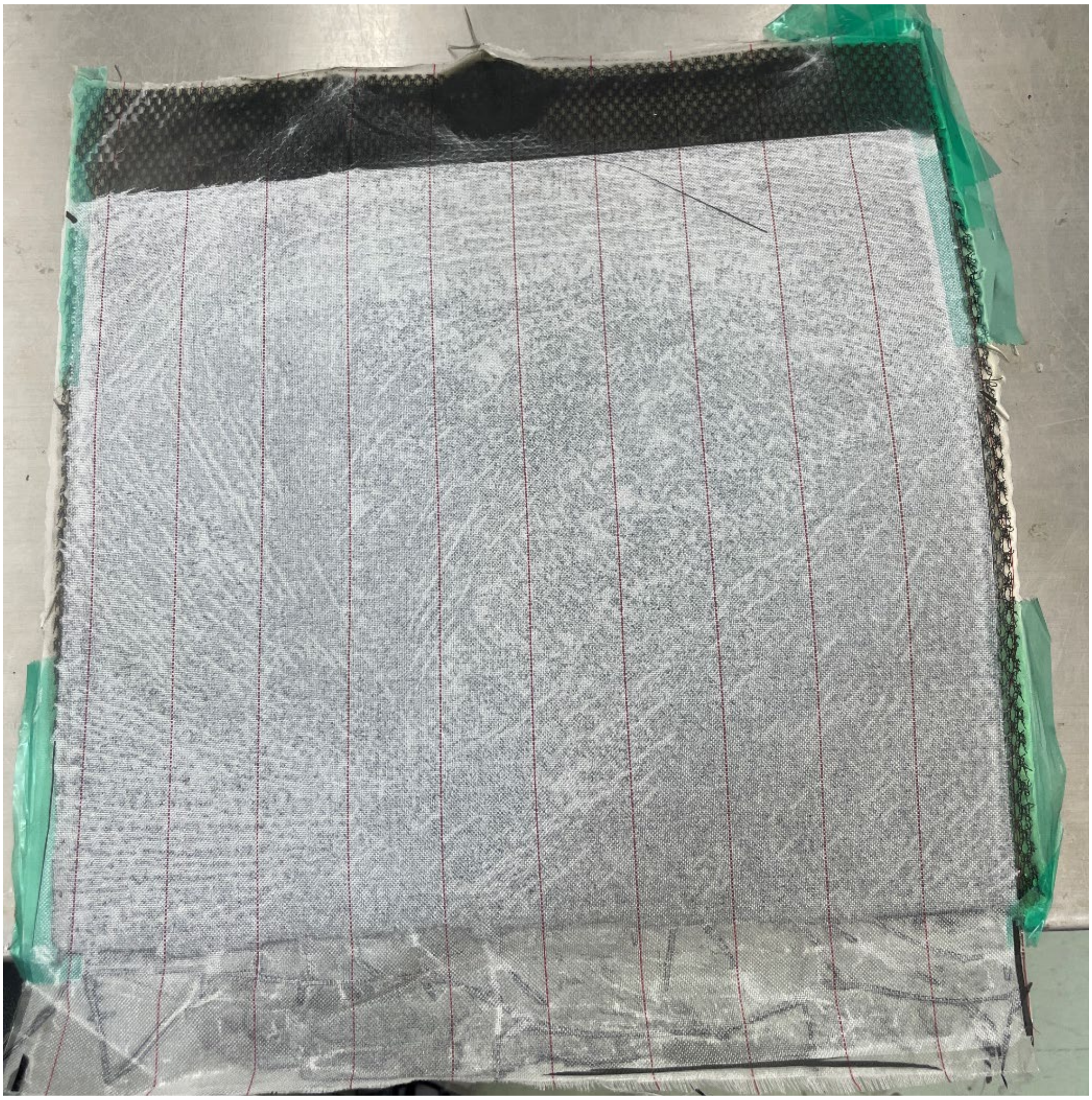

Figure 3.10 Demolded composite plate after curing


Figure 3.11 Composite plate after the removal of all consumables

3.2.9 *Waterjet Machining*

Composite plates were cut into specimens for various property evaluations. The specimen size for each evaluation experiment is specified in the corresponding ASTM international standard. ASTM D3039 and ASTM D2344 were used to evaluate the composites fabricated in this research study. For balanced and symmetrically oriented fiber composites, ASTM D3039 requires a specimen size of 25 mm in width and 250 mm in length for tensile properties evaluation. ASTM D2344 requires a specimen size of 12 mm in width and 40 mm in length for short beam properties evaluation. The composite plates fabricated in this research study had a dimension of 310 mm by 310 mm. However, the edges of the composite plate may not be suitable for creating specimens for properties evaluation as laminates may not align perfectly at each edge. Therefore, approximately 30 mm of composite materials were discarded from each edge to ensure the quality of the specimens. Eight tensile specimens and eight short beam specimens were cut from each composite plate by abrasive waterjet machining, as shown in Figure 3.12. Abrasive waterjet machining involved a high-pressure water stream which carried abrasive particles. The particles were accelerated and impacted the work piece at high velocity to effectively remove the unwanted materials. Each specimen was then be clearly labeled, as shown in Figure 3.13. The specimens were then placed in a dehydration chamber to eliminate the moisture that had been absorbed during the waterjet machining process.

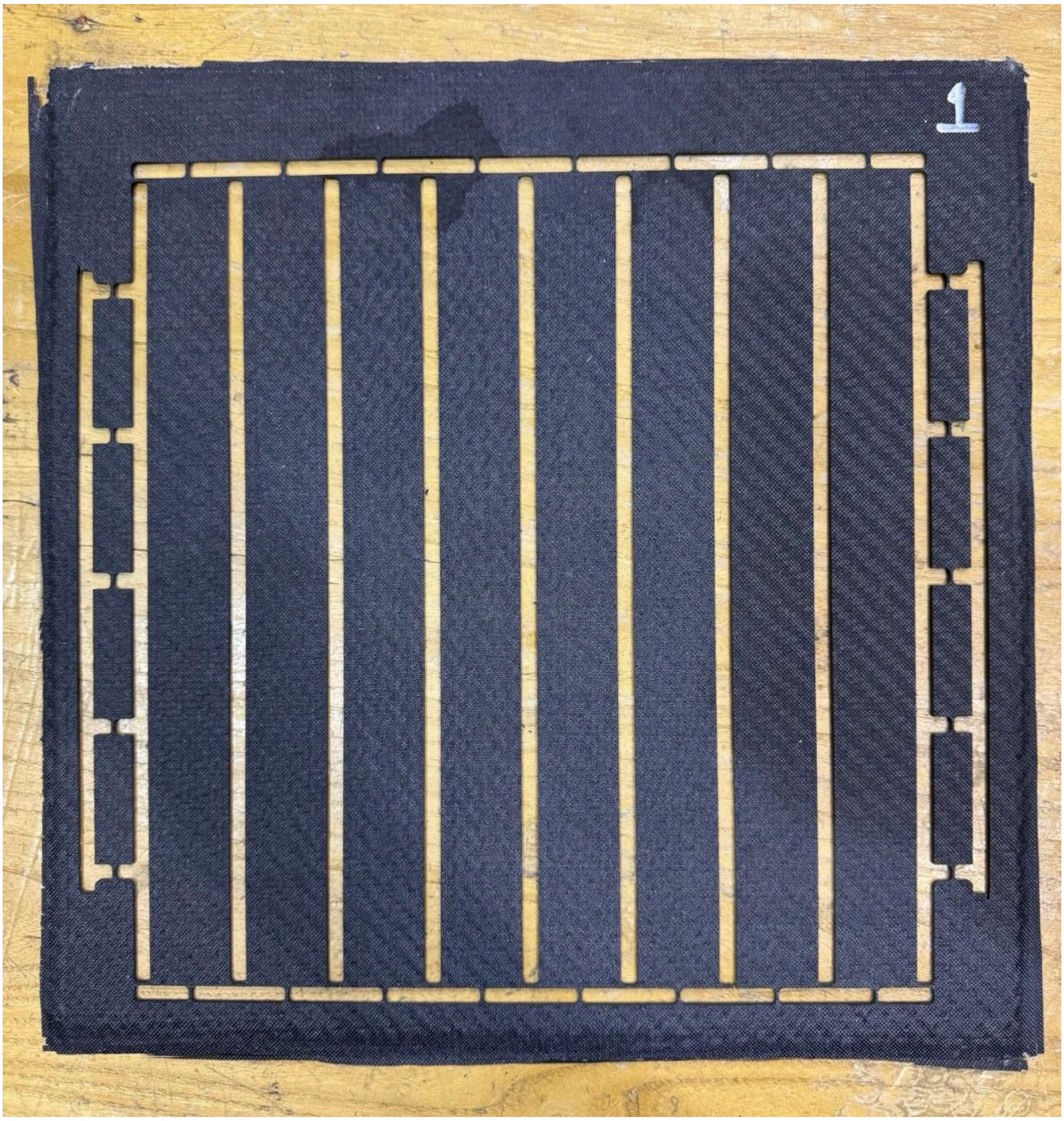

Figure 3.12 Composite plate with eight tensile specimens and eight short beam specimens cut by abrasive waterjet machining

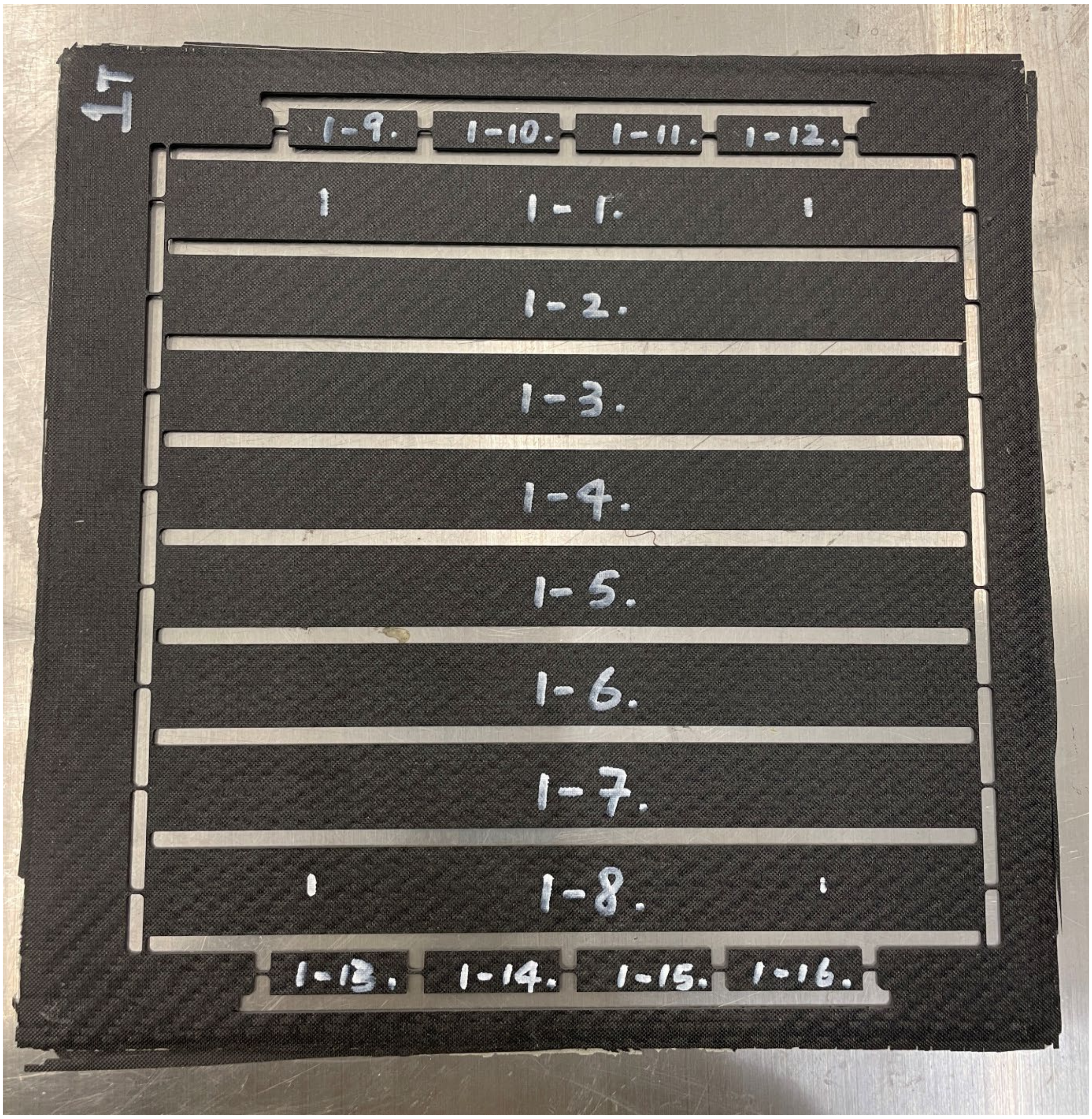

Figure 3.13 Composite plate with all specimens clearly labelled

3.2.10 *End-tab adhesion preparation*

ASTM D3039 tensile properties evaluation requires the specimen being securely held by the grip of the testing machine. The serrated surface of these grips effectively prevents slippage between the grip surface and the specimen, which facilitates the efficient transfer of force from the testing machine to the specimen. However, serrated grip surfaces can potentially induce damage to the matrix and fiber reinforcement, and this may lead to a tensile failure in an unforeseen location on the specimen during the evaluation. Therefore, tabs are recommended in ASTM D3039 for preventing the tensile specimens from gripping damage. In this study, all tensile specimens were bonded with aluminum tabs before their tensile performance evaluation. The aluminum tab was designed with a width equal to the width of the tensile specimen and a length of 50 mm. Both ends and both sides of each tensile specimen were bonded to aluminum tabs using 3M Scotch-Weld epoxy adhesive 2216.

The end-tab adhesion process was similar to composite plate fabrication. A 600 mm by 600 mm flat metal plate served as the base for the end-tab adhesion process. The metal plate was cleaned with acetone to eliminate any dirt or residue. Masking tape was applied and firmly pressed along the edges of the metal plate to prevent any liquid seepage. Three layers of LOCTITE FREKOTE 770-NC epoxy mold release agent were applied to the unmasked area of the metal plate to facilitate the separation in the event of excessive adhesive spillage. The masking tape was removed, and the double-sided sealant tape was applied along the edges of the metal plate that were previously masked. A piece of vacuum bag with dimensions of 700 mm by 700 mm and a piece of peel ply with dimensions of 400 mm by 350 mm were also prepared. All the above preparations should be done before mixing the epoxy adhesive.

An oxide layer on the surface of the aluminum tab reduces its bond strength. Therefore, sanding the bond surface of aluminum tab is necessary to remove the oxide and facilitate proper bonding. A sanding machine, as shown in Figure 3.14, was used to sand the materials surfaces. It is crucial to perform the abrasion process shortly before the adhesive preparation as the oxide layer on aluminum surfaces can rapidly regrow within a few hours. Figure 3.15 shows the before and after sanding condition of the aluminum tab surfaces. Similarly, the areas on each end and each side of the tensile specimen that would bond to the aluminum tab were sanded to remove the matrix phase materials and expose the reinforcement. Figure 3.16 shows the sanded areas at the ends of the specimens. These surface preparations enhance the adhesion quality and ensure that the force acting on the aluminum tab is effectively transferred to the tensile specimen. All surfaces that underwent abrasion were thoroughly cleaned with acetone to remove the debris generated during the abrasion process.

3M Scotch-Weld epoxy adhesive 2216 is a two-part adhesive consisting of Part A resin and Part B hardener. The adhesive was prepared by mixing the two parts in a weighed ratio of 1.4 : 1 and thoroughly stirred with a spatula. Once the mixing process was initiated, the adhesive mixture had a pot life of 90 minutes. The total amount of adhesive mixture required per aluminum tab was approximately 1 g. Four aluminum tabs were necessary to cover each end and each side of a tensile specimen. Eight tensile specimens were considered as one batch of specimens, as they were cut from the same composite plate. Therefore, one batch of tensile specimens required 32 g of adhesive mixture. The adhesive mixture was prepared by mixing 13.3 g ($32g \times \frac{1}{1.4+1}$) of Part B hardener with 18.7 g ($32g \times \frac{1.4}{1.4+1}$) of Part A resin.

Figure 3.14 Sanding machine used to sand the materials surfaces

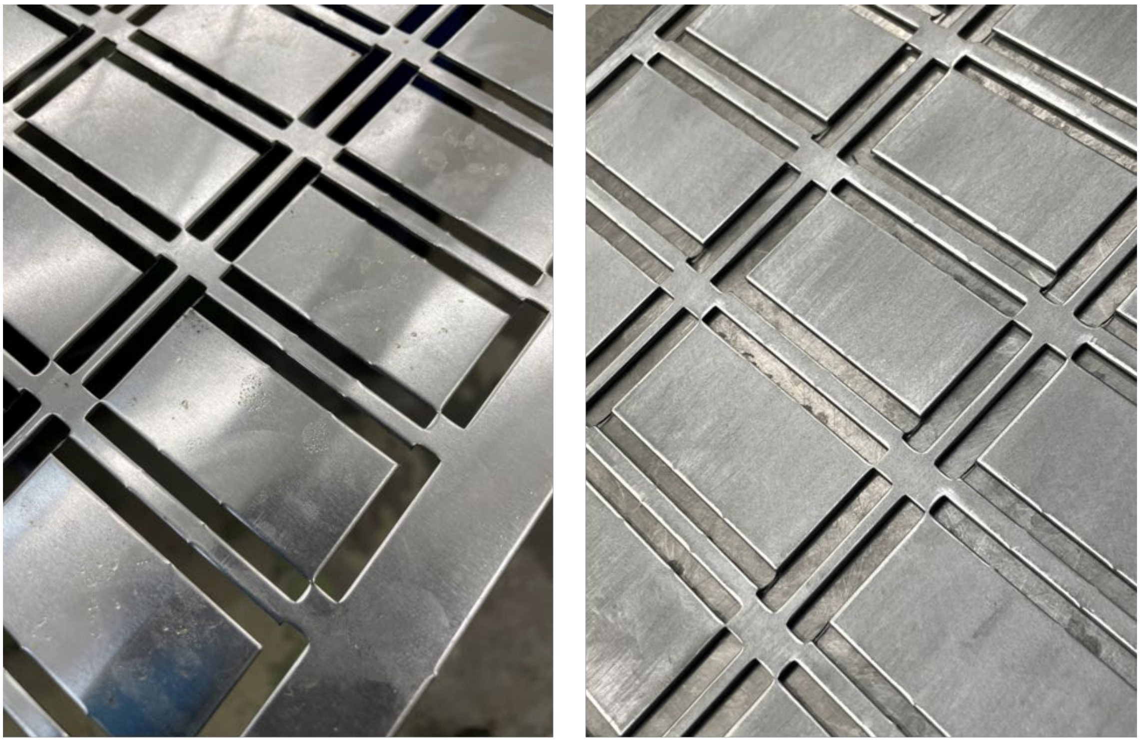

Before Sanding　　After Sanding

Figure 3.15 Aluminum tab before and after sanding

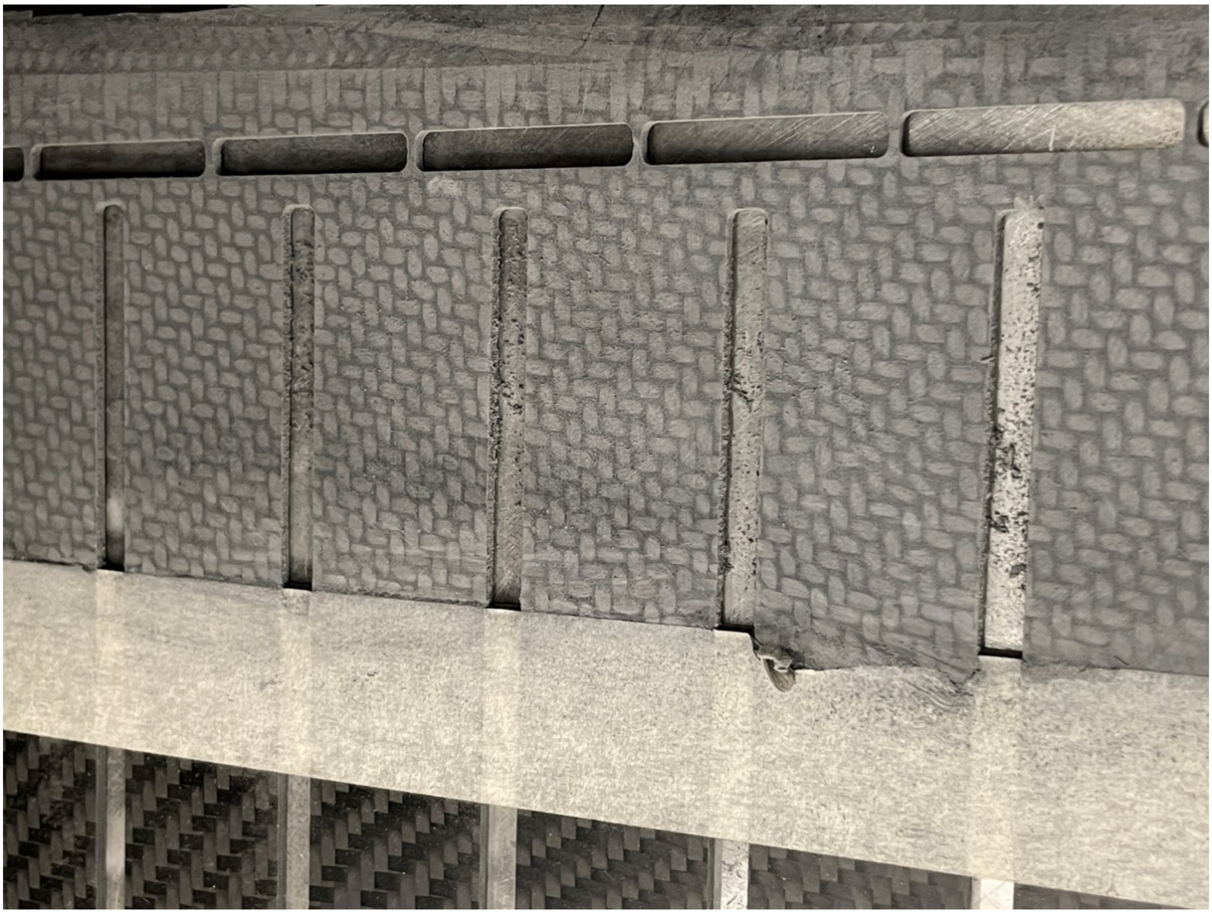
Figure 3.16 The sanded areas at the ends of the specimens

3.2.11 *End-tab adhesion and curing*

The sanded surface of the aluminum tab was completely and evenly coated with the well-blended adhesive. The coated aluminum tab was then positioned against one end of a side of the tensile specimen. This process was repeated until all aluminum tabs had been glued to the tensile specimens. This process should be done before the end of the adhesive pot life. The midsection of the tensile specimen was elevated by the aluminum tab at both ends when they are horizontally placed. Therefore, a fixture was placed on the metal plate, as shown in Figure 3.17, to support the midsection of the tensile specimens which prevented the vacuum force from stressing the midsection and eliminated unnecessary bending motion.

After all aluminum tabs were properly glued in place, as shown in Figure 3.18, and all specimens were horizontally positioned on the fixture, peel ply was applied over the entire surface of the specimens to absorb any remaining adhesive. Two vacuum connector bases were positioned at the corners of the metal plate in a diagonal manner, as shown in Figure 3.19. A vacuum bag was then sealed with double-sided sealant tape that had been previously applied to the edges of the metal plate. The vacuum bag was firmly pressed against the sealant tape to prevent air leakage during the adhesive curing process. The vacuum bag was then perforated with a hole above each vacuum connector base and the vacuum connector was secured from outside the vacuum bag. The vacuum connector and its base became airtight once they were securely locked with each other. Figure 3.20 shows the vacuum connector and the vacuum connector base.

Figure 3.17 Fixture supporting the midsection of the tensile specimen

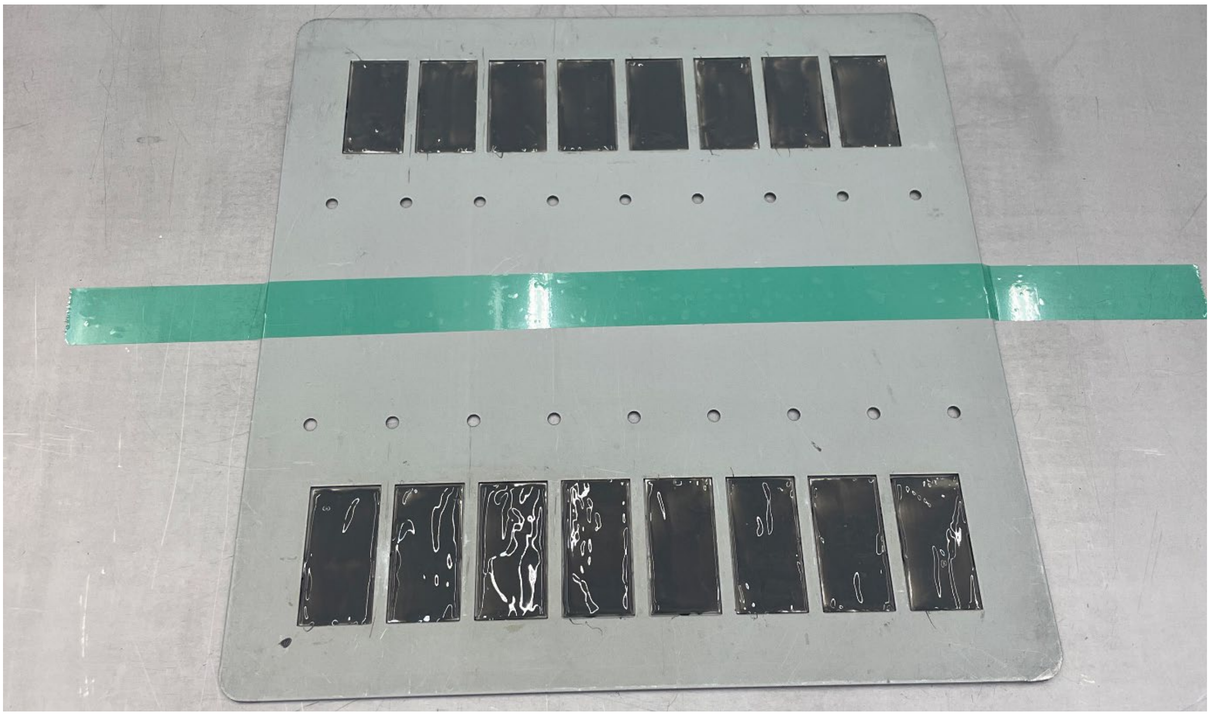

Figure 3.18 Evenly glued aluminum tab place in the fixture

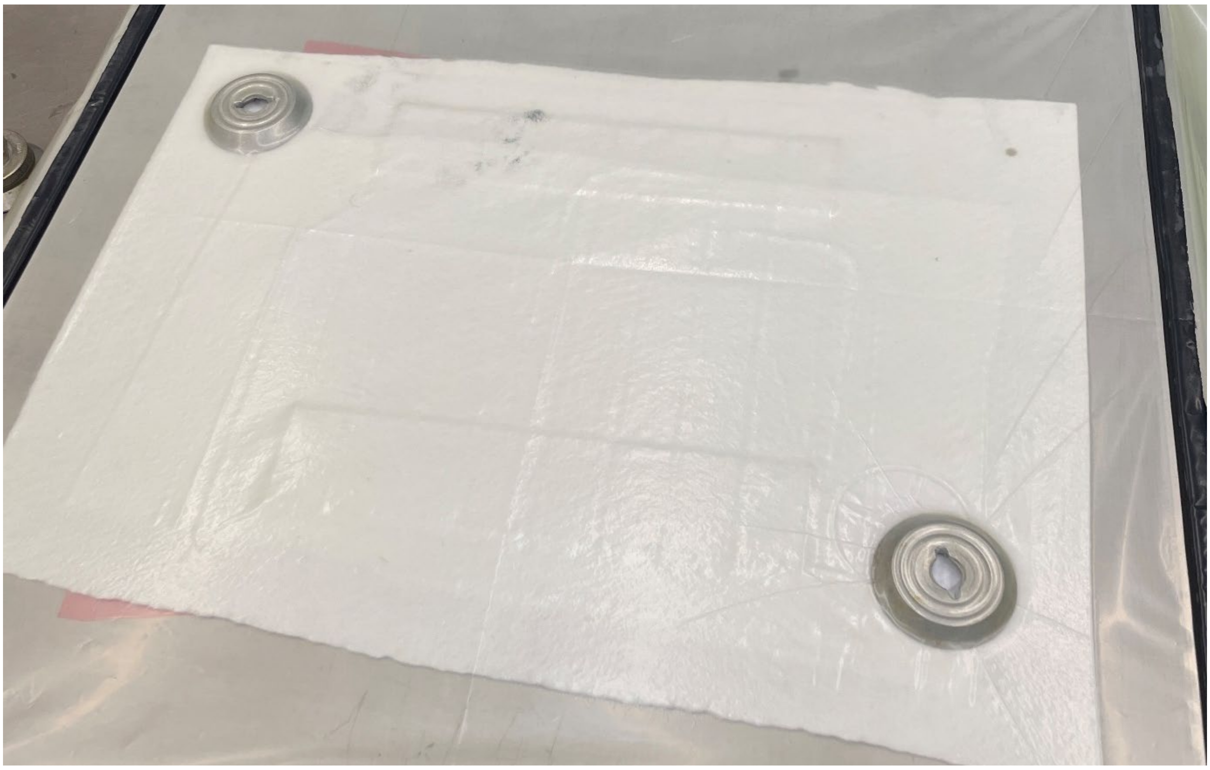

Figure 3.19 Two vacuum connector bases positioned at the corners of the metal plate in a diagonal manner

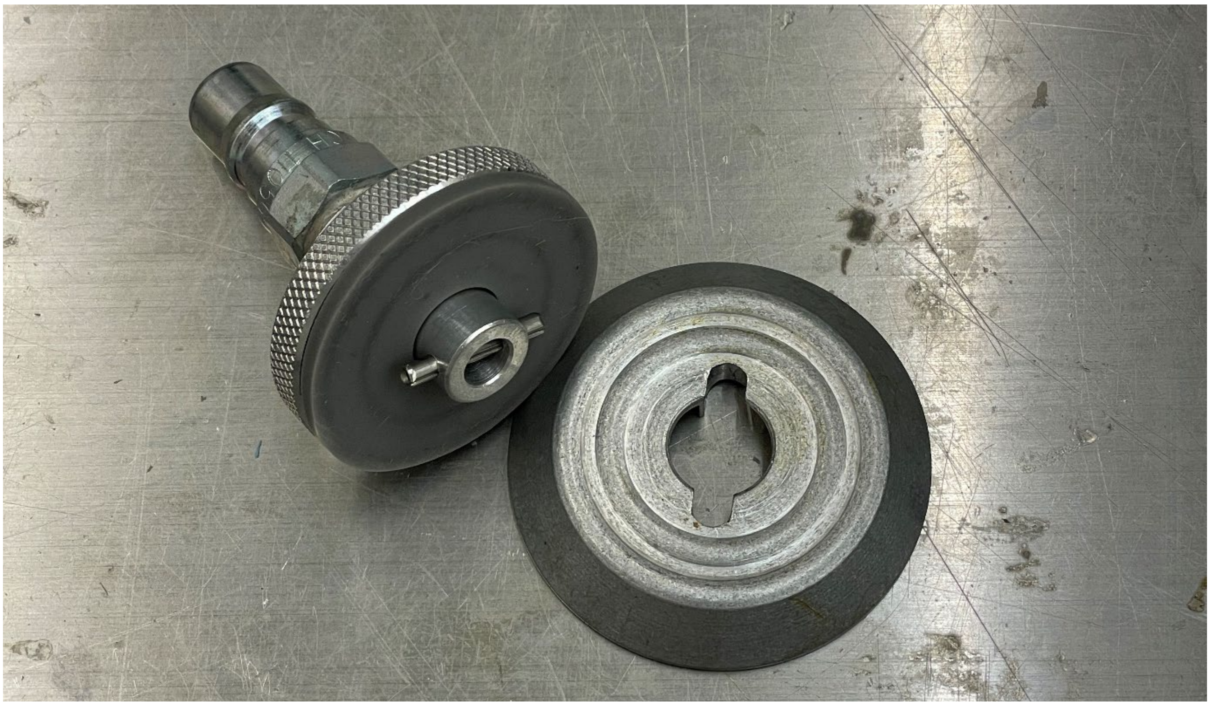

Figure 3.20 Vacuum connector and the connector base

One of the vacuum connectors was connected to a vacuum pump, while the other was connected to a pressure gauge, as shown in Figure 3.21. Figure 3.22 shows the pressure gauge. In contrast to the previous vacuum condition, the vacuum level required for the adhesive curing process was not as high as the resin infusion process during composite plate fabrication. The vacuum provided uniform compression force to hold everything in place during the curing process and to ensure the adhesive was evenly distributed which allowed the aluminum tab surfaces to be parallel to the testing direction of the composite specimen. The adhesive began to solidify after its 90-minute pot life and gradually cured over seven days at room temperature (approximately 24 °C). The curing time could be shortened by elevating the curing temperature.

After the adhesive had fully cured, all consumables, including vacuum bags, peel ply, and double-sided sealant tape were removed. The specimens were then separated from the metal plate and marked with a specimen coupon number. Excessive adhesive may bonded the specimens together which may require additional effort to separate them individually. Figure 3.23 shows the bonded specimens and the specimens after separation. Excessive adhesive around the end tab had to be trimmed off, as shown in Figure 3.24. The specimens were ready for evaluation once the end-tab adhesion process had been completed.

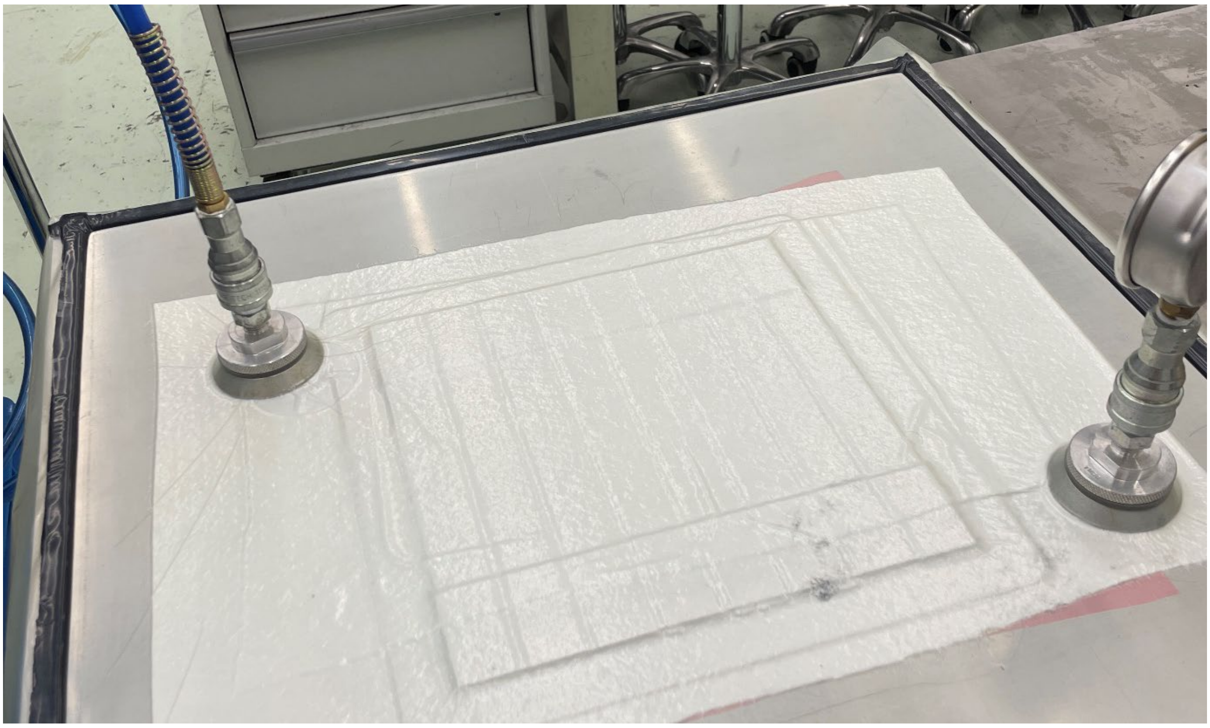

Figure 3.21 Vacuum connectors connected to vacuum pump (left) and pressure gauge (right)

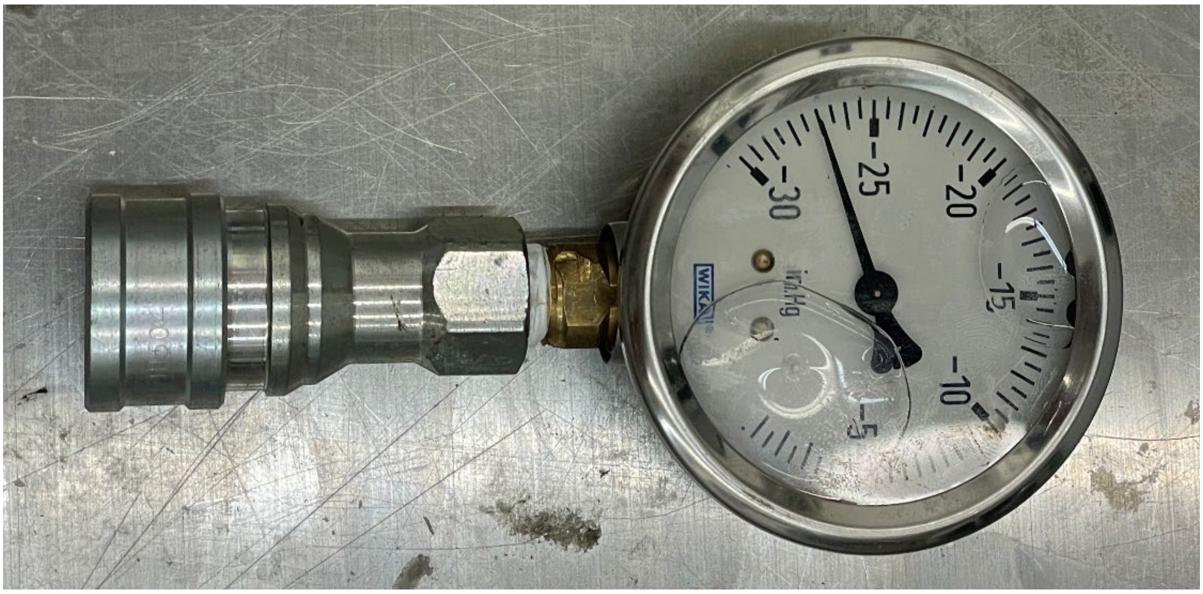

Figure 3.22 Pressure gauge in inHg

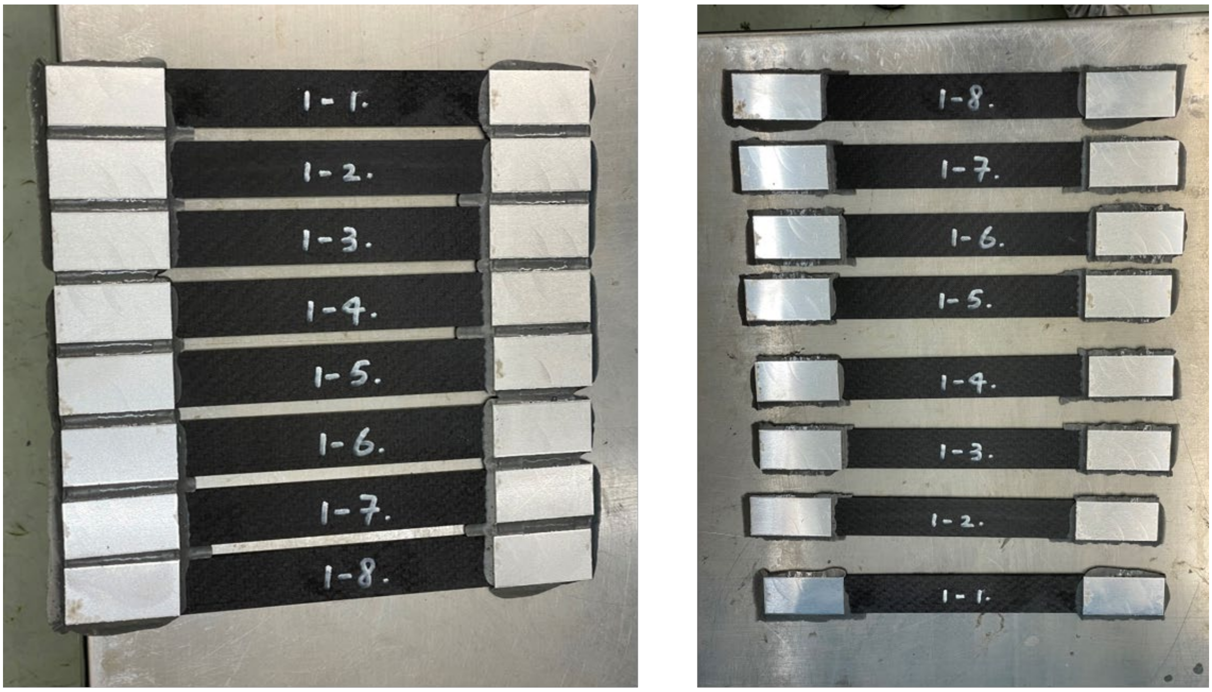

Bonded Specimens

Separated Specimens

Figure 3.23 Separation of bonded specimens due to excessive adhesive

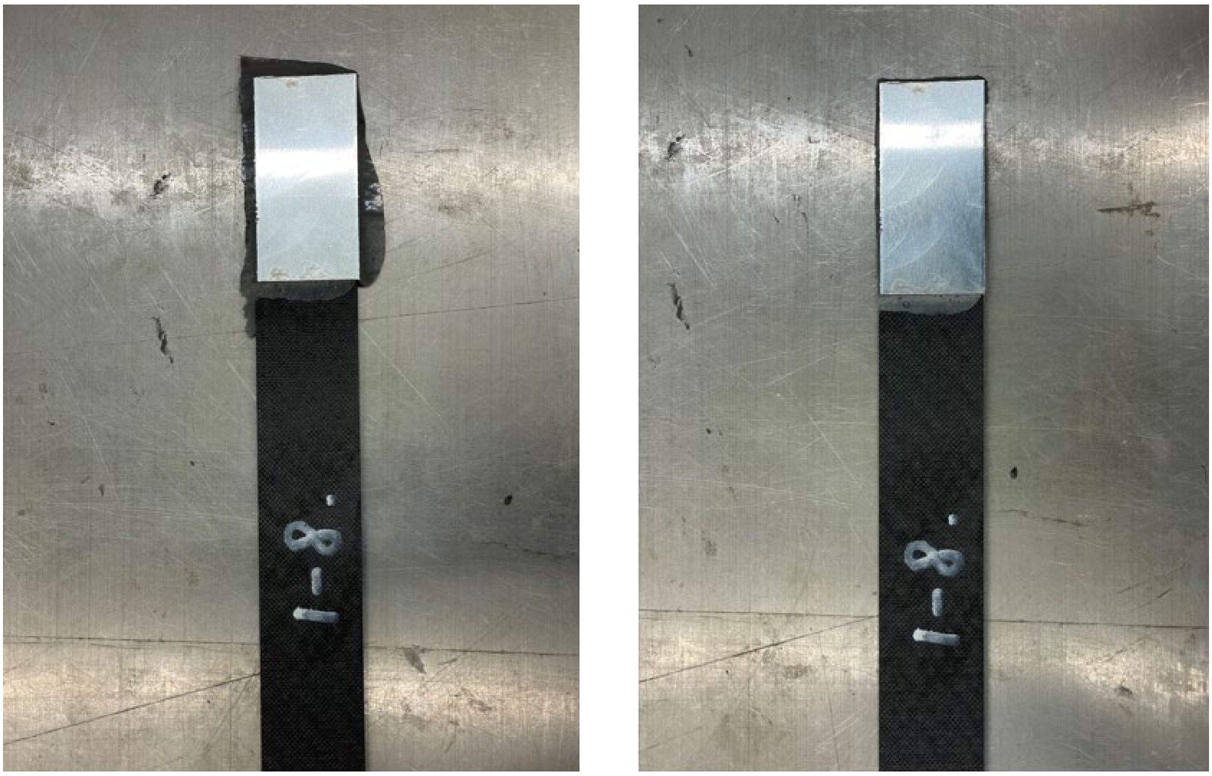

End tab with excessive adhesive

End tab after trimming off the excessive adhesive

Figure 3.24 Trimming of excessive adhesive

3.3 Evaluation of CFRP composite specimens

All composite specimens fabricated in this research study were tested in accordance with the testing standards published by ASTM International. ASTM International is an international organization that develops and publishes standard guides, test methods, and practices for evaluating the properties of various materials. ASTM International standard guides provide comprehensive information on evaluating a material with its corresponding standard test methods. Standard guides are being developed to summarize standards for testing different properties of a specific material type. ASTM International standard test methods provide standardized procedures and detailed specifications, including specimen specification, specimen conditioning criteria, sampling methods, data collection methods, result calculation, apparatus specification, evaluation parameters, report preparation, data precision, and post-test specimen analysis for testing a specific property of a material type. Standard test methods are being developed to summarize relevant information for establishing an objective evaluation to characterize a material.

ASTM D4762 is the Standard Guide for Testing Polymer Matrix Composite Materials which provides comprehensive guidelines for evaluating continuous-fiber reinforced polymer matrix composites (ASTM International, 2018). As CFRP composite falls under the category of continuous-fiber reinforced polymer matrix composites, the standard test methods outlined in ASTM D4762 can be effectively utilized to assess the specimens fabricated in this study. The standard test methods listed in ASTM D4762 are primarily categorized into six distinct sections, and each section is dedicated to evaluating a specific aspect of composite material properties. The six sections include static tests, dynamic tests, structural tests, sandwich construction tests, constituent-related tests, and environmental conditioning tests (ASTM International, 2018). A detailed comparison of advantages and disadvantages for each test method is presented in the corresponding table in ASTM document. Certain properties can be evaluated through multiple test methods with various specimen shapes and specifications. While ASTM D4762 covers the most commonly utilized and applicable ASTM standards, it does not comprehensively include all possible test methods that are applicable to evaluate continuous-fiber reinforced polymer matrix composites.

As mentioned in research objectives, this study is to investigate and evaluate the mechanical performance of the resulting composites with different weave patterns and viscosity of composite constituents, and the incorporation of carbon nanotube. Continuous-fiber reinforced polymer matrix composites are typically evaluated using their tensile strength to indicate their mechanical performance. Following the recommendation of ASTM D4762, ASTM D3039 is the Standard Test Method for Tensile Properties of Polymer Matrix Composite Materials that provides standardized testing procedures for evaluating the tensile properties of continuous-fiber reinforced polymer matrix composites. In accordance with ASTM D3039, static in-plane tensile tests were conducted on the CFRP composites fabricated in this study. Tensile tests were utilized to measure the tensile strength and illustrate the tensile behavior of the CFRP composites with the aid of a stress-strain curve. The modulus of elasticity and Poisson's ratio could be derived from the tensile data collected during the test to assess the stiffness and deformation in the transverse direction of the CFRP composites (ASTM International, 2017). The fabrication quality of CFRP composites could be evaluated by analyzing the failure mode of the specimen after the tensile test. The failure mode represents the type, area and location of the failure when the specimen fractures under stress during the tensile test. Potential causes, such as voids or dry spots, which affect the fabrication quality can be identified by analyzing the failure modes.

In addition to tensile properties, short-beam strength serves as an indicator of the bonding compatibility between the reinforcement phase and the matrix phase, which is a characteristic closely correlated to the mechanical performance of the composites. Following the recommendation of ASTM D4762, ASTM D2344 is the Standard Test Method for Short-Beam Strength of Polymer Matrix Composite Materials and Their Laminates, which provides standardized testing procedures for evaluating the short-beam properties of continuous-fiber reinforced polymer matrix composites. In accordance with ASTM D2344, static out-of-plane short-beam shear tests were conducted on the CFRP composites fabricated in this study. Short-beam shear tests were utilized to measure the short-beam strength and identify the short-beam failure behavior of the CFRP composites. The short-beam failure mode indicates the interfacial interaction at the reinforcement-matrix interface of the CFRP composites that is the extent to which the matrix phase is bonded to the reinforcement phase. The details of testing conditions and the specification of apparatus used in this research study will be discussed in the following sections.

3.3.1 *Tensile properties evaluation*

ASTM D3039 is preferred over ASTM D5083 for the standard of tensile testing of polymer matrix composite materials due to its widely applicable configurations, requirements, and guidance. While both standards utilize the same test specimen geometry, ASTM D3039 offers more flexibility. However, ASTM D3039 is limited to balanced and symmetric laminates in the test direction. Additionally, tabbed configuration requires extra specimen preparation and cautious adhesive selection. ASTM D3039 was employed to assess the ultimate tensile properties, modulus of elasticity, Poisson's ratio, and failure mode of the CFRP composites fabricated in this research study. The modulus of elasticity, an in-plane tensile property, serves as an indicator of the elastic stress-strain response in the test direction of the composite. Stress-strain response refers to the elongation of the composite when subjected to external stress. The ultimate tensile properties are the tensile stress and strain at the point of failure of the specimen. Failure modes in tensile testing provide insights into the ways of tensile energy dissipation during composite failure. Poisson's ratio is utilized to quantify the transverse strain response in relation to the tensile strain observed in the test direction.

The testing procedure involved a thin, flat specimen with a uniform rectangular cross-section which was securely positioned within the grips of a universal testing machine. The specimen is subjected to a sustained tension loading process, and the corresponding force readings were continuously recorded. Tensile strain was monitored using a strain gauge or an extensometer adhered to the specimen surface. Force readings from the testing machine and the elongation readings from the strain gauge or extensometer throughout the tensile test can be plotted into a stress-strain curve. Modulus of elasticity and Poisson's ratio can be derived from the stress-strain curve to assess the stress-strain response of the specimen. The ultimate tensile stress and ultimate tensile strain of the specimen are the force reading and the elongation reading at the failure point (ASTM International, 2017). Each batch of test conditions should contain at least five specimens to ensure the accuracy of the results. To obtain statistically significant data, the tensile test is recommended to be conducted by following the procedures outlined in ASTM E122 Standard Practice for Calculating Sample Size to Estimate, With Specified Precision, the Average for a Characteristic of a Lot or Process.

Apparatus

Universal testing machine should be equipped with a stationary head and a movable head. The drive mechanism should be capable of controlling the velocity of the movable head relative to the stationary head and maintaining a consistent rate of movement. The force sensing device in the universal testing machine should not be affected by the inertia lag at any specified head moving rate. The force sensing device should be able to indicate the total force borne by the test specimen with ±1% accuracy. A grip should be installed on both the stationary head and the movable head respectively to hold the test specimen during the test. The grip installation should ensure the force application direction is coincident with the longitudinal axis of the specimen. Sufficient gripping force should be applied by the grips to apply lateral pressure on the test specimen, thereby preventing slippage between the grips and the specimen surface. Rotationally self-aligning grips are preferred to minimize bending stresses in the test specimen. The universal testing machine and its components should be calibrated according to the ASTM E4 Standard Practices for Force Calibration and Verification of Testing Machines to ensure their alignment and accuracy.

A strain-indicating device such as a strain gauge or an extensometer should be selected based on the material type of test specimens and the required active gauge length. Active gauge length should be at least 3 mm, and most materials are recommended to have an active gauge length of 6 mm. For woven fabric laminates, the active gauge length should cover at least a repeating unit of the weave pattern along the longitudinal direction. The attachment of a strain-indicating device should not cause any damage to the specimen surface. For evaluating Poisson's ratio, two strain-indicating devices should be installed on the specimen to measure the strain in both longitudinal and lateral directions. For evaluating modulus of elasticity, an additional strain-indicating device should be positioned on the opposite face of the specimen to simultaneously measure the strain in longitudinal direction, which enables data correction when specimen is subjected to bending motion.

The INSTRON 5982 electromechanical universal testing machine (UTM) was utilized to assess the tensile properties of CFRP composites fabricated in this study as shown in Figure 3.26. The INSTRON 5982 UTM was equipped with a load cell or force sensing unit capable of withstanding a maximum load of 100 kN and a drive mechanism that controlled the rate of head displacement ranging from 0.00005 to 1016 mm/minute. The accuracy of INSTRON 5982 UTM was ±0.5% in load measurement and ±0.1% in displacement. The UTM was manufactured in United States and its components were calibrated in accordance with the ASTM E4 standard practice.

The INSTRON 5982 UTM was equipped with an integrated strain measurement system known as the advanced video extensometer (AVE). The AVE could detect the white dots on the test specimen, which had been marked with a specific marking tool before the tensile test, as shown in Figure 3.25. The AVE was capable of simultaneously measuring both longitudinal and lateral strain without any direct contact with the specimen. The digital image correlation (DIC) could work with AVE to provide precise strain readings and enable the calculation of accurate modulus of elasticity and Poisson's ratio of the specimen. Figure 3.27 shows the AVE positioned at the left bottom area of the UTM, facing towards the test specimen.

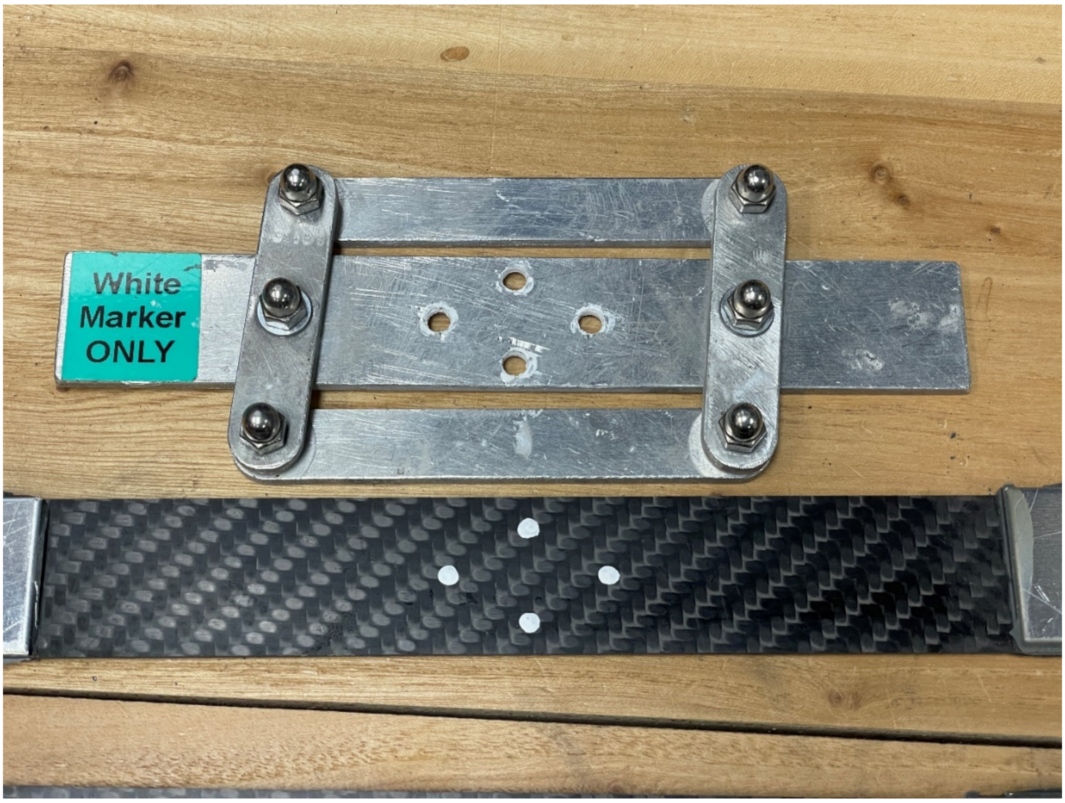

Figure 3.25 Tensile specimen marked with white dots and the specific marking tool

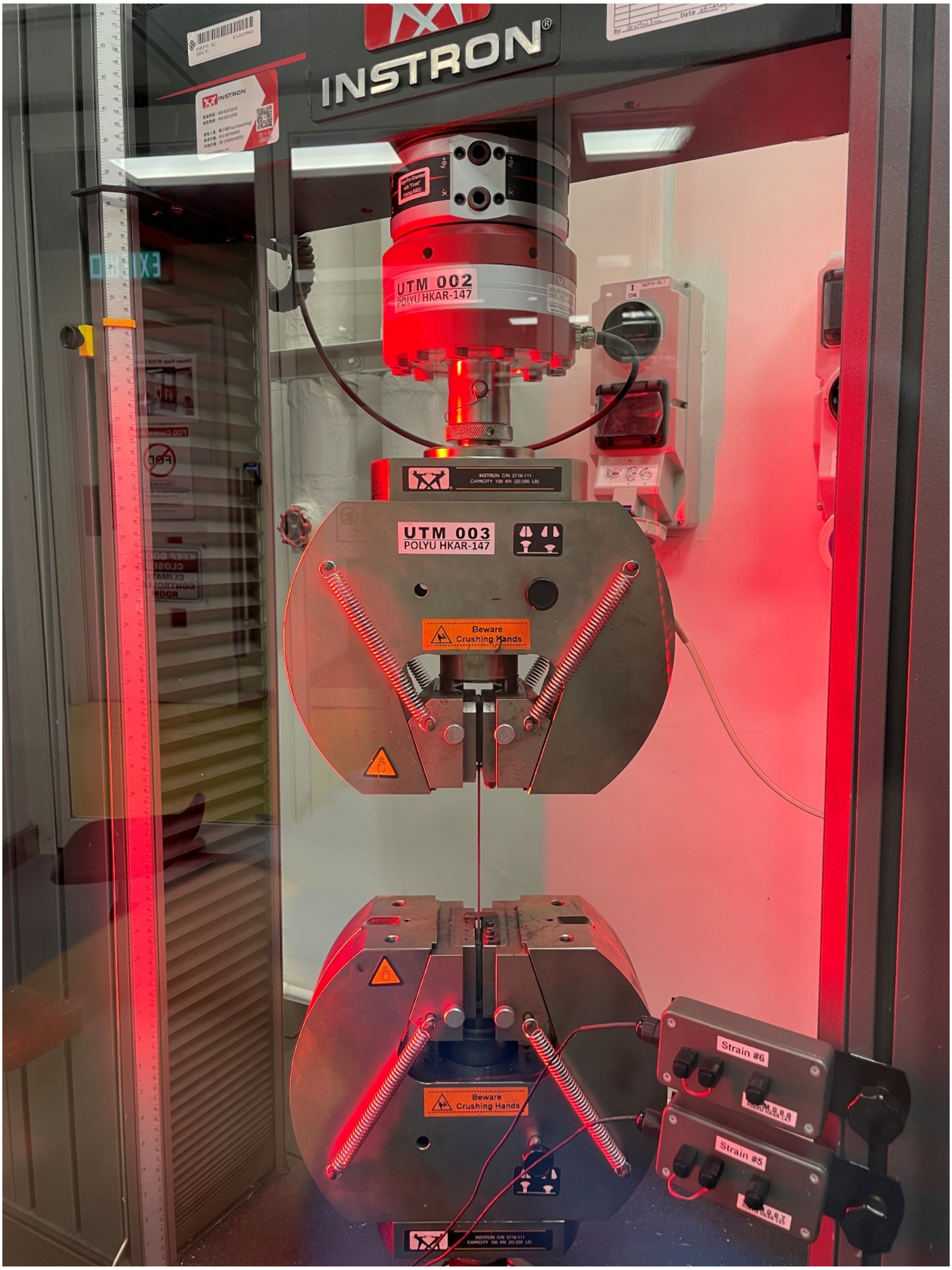

Figure 3.26 INSTRON 5982 electromechanical universal testing machine (UTM)

Figure 3.27 AVE facing towards the test specimen.

A micrometer or caliper can be used to measure the final dimensions of specimens. For instrumental measurement of a typical specimen geometry, thickness measurement should have an accuracy of ±0.0025 mm, while width measurement should have an accuracy of ±0.025 mm. Additionally, other measuring tools with a reading accuracy within 1% of the dimension being measured can also be used.

Specimen preparation

Specimens should have a consistent rectangular cross-section, with a minimum length that equals to the sum of gripping length, twice the width and the gauge length. Different fiber orientations require different specimen dimensions. For balanced and symmetric fiber orientation, the specimen should have a dimension of 25 mm (width) by 250 mm (length). During specimen fabrication, fiber alignment is crucial, as improper alignment can result in reduced measurement accuracy. Tabbed configuration is recommended to protect the specimen from gripping damage.

To avoid delamination, undercuts, and notches on the edges or surfaces of the specimen, the appropriate machining method should be employed. All test specimens must be appropriately labeled to ensure the traceability of knowing the production batch or raw materials used, and each specimen should be distinguished from others. Each test configuration should include a minimum of five specimens within the test batch to obtain valid results. Additionally, all test specimens should be conditioned in a laboratory atmosphere at a temperature of 23 ± 3°C and a relative humidity of 50 ± 10% for at least 24 hours.

Testing condition

Dimensions of each test specimen should be measured with a micrometer or a caliper and documented. Measurements of width and thickness should be taken from the mid-section of the test specimens, which is the gauge length area. The test should be conducted under a laboratory atmosphere that is same as the conditioning environment. There are two methods for conducting tensile testing: strain-controlled testing and constant head-speed testing. In strain-controlled testing, the strain rate must be maintained at 0.01 per minute. In constant head-speed testing, the rate of head displacement must be maintained at 2 mm per minute. If a strain gauge is available on the testing machine, strain-controlled testing is preferred. Although AVE is available on INSTRON 5982 UTM, the strain measuring setup does not conform with ASTM D3039 testing standard. Therefore, constant head-speed testing was conducted to evaluate the CFRP composites fabricated in this research study.

Specimens were positioned with the end-tabs placed inside the grips. The longitudinal axis of the specimen was aligned with the center line of the grips. The grips were tightened and a constant rate of head displacement was applied to the specimen while data of both the applied load and the displacement of the head were simultaneously recorded. The data should be recorded at a rate of three samples per second until the specimen ruptures or over 100 data points are collected. The ultimate tensile loading which was the final load before the test was terminated and any significant disruption were recorded.

Each specimen was examined, and its failure mode was identified. Failure mode could be identified based on three characteristics: type, area, and location. Figure 3.28 illustrates the typical failure modes and the corresponding characteristic coding that can be observed from the specimen.

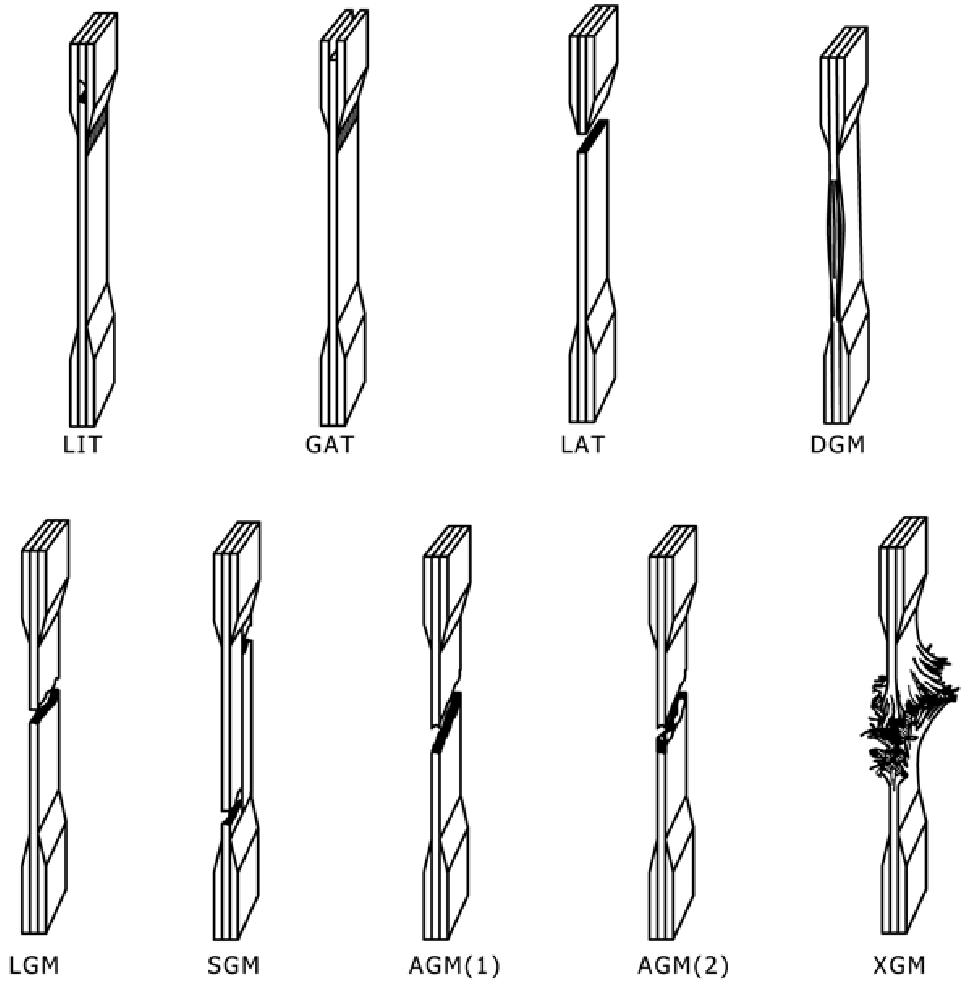

First Character

Failure Type	Code
Angled	A
edge Delamination	D
Grip/tab	G
Lateral	L
Multi-mode	M(xyz)
long. Splitting	S
eXplosive	X
Other	O

Second Character

Failure Area	Code
Inside grip/tab	I
At grip/tab	A
<1W from grip/tab	W
Gage	G
Multiple areas	M
Various	V
Unknown	U

Third Character

Failure Location	Code
Bottom	B
Top	T
Left	L
Right	R
Middle	M
Various	V
Unknown	U

Figure 3.28 Example and legend of tensile test three-part failure mode code (ASTM International, 2017)

Calculation

$$F^{tu} = P^{max}/A$$

$$\sigma_i = P_i/A$$

Equation 3.1 Tensile strength and tensile stress

Where,

F^{tu} = ultimate tensile strength (MPa)

P^{max} = maximum force before failure (N)

σ_i = tensile stress at *i*th data point (MPa)

P_i = force at *i*th data point (N)

A = average cross-sectional area (mm^2)

$$\varepsilon_i = \delta_i/L_g$$

Equation 3.2 Tensile strain

Where,

ε_i = tensile strain at *i*th data point

δ_i = extensometer displacement at *i*th data point (mm)

L_g = extensometer gage length (mm)

$$E = \Delta\sigma/\Delta\varepsilon$$

Equation 3.3 Modulus of elasticity

Where,

E = tensile strain at *i*th data point

$\Delta\sigma$ = extensometer displacement at ith data point (mm)

$\Delta\varepsilon$ = extensometer gage length (mm)

$$\nu = -\Delta\varepsilon_t / \Delta\varepsilon_l$$

Equation 3.4 Poisson's ratio

Where,

ν = Poisson's ratio

$\Delta\varepsilon_t$ = difference in lateral strain between the two longitudinal strain points

$\Delta\varepsilon_l$ = difference between the two longitudinal strain points

$$\overline{x} = \left(\sum_{i=1}^{n} x_i\right) \Big/ n$$

$$s_{n-1} = \sqrt{\left(\sum_{i=1}^{n} x_i^2 - n(\overline{x})^2\right) \Big/ (n-1)}$$

$$CV = 100 \times s_{n-1} / \overline{x}$$

Equation 3.5 Statistical parameters of tensile properties

Where,

$\overline{x}$ = sample mean

s_{n-1} = sample standard deviation

CV = sample coefficient of variation (%)

n = number of specimens

x_i = value of the measured property

The modulus of elasticity and Poisson's ratio are typically calculated using the chord method which determines the tensile properties of a specimen within a specific longitudinal strain range. For calculating these properties, the longitudinal strain used in the chord method is usually ranged from 0.001 to 0.003. This strain range is suggested by ASTM to ensure the materials show linear elasticity. Strain below 0.001 may be inconsistent due to initial alignment and slack in the tensile test setup. For strain beyond 0.003 some materials may undergo plastic deformation and begin to experience micro-cracking and creeping which lead to non-linear behavior. (ASTM International, 2017; Vlach et al., 2022). If the specimen fails with an ultimate tensile strain below 0.006, it is recommended to use 25% to 50% of the ultimate tensile strain as the strain range in the chord method. Any other defined strain range used in the calculation should be specified. All calculation results should be reported in three significant figures.

3.3.2 *Short-beam properties evaluation*

ASTM D2344 was employed to assess the short-beam strength and short-beam failure mode of CFRP composites fabricated in this research study. Short-beam strength, an out-of-plane shear property, serves as a quality comparison between composites with the same short-beam failure mode. The quality comparison of composite specimens in short-beam testing indicates the adhesive bonding between the reinforcement sizing resin and the matrix utilized in composite fabrication. Failure modes observed during short-beam test can indicate the bonding condition at the reinforcement-matrix interface which lies between the reinforcement phase and the matrix phase of the composite. While short-beam strength is a type of out-of-plane shear property, and it cannot be directly correlated with any individual material property.

ASTM D2344 is applicable for measuring the short-beam strength of curved or flat laminate up to a thickness of 6 mm with continuous or discontinuous fiber reinforcement. The laminate arrangement within the composite should be balanced and the elastic properties should be balanced or symmetric with respect to the longitudinal axis of the specimens. In this research study, composite specimens were fabricated using continuous fiber reinforcement with high-modulus carbon fiber. The laminate configurations for the composite specimens were either four or eight plies with balanced and symmetric fiber orientations which result in quasi-isotropic elastic properties. The thickness of the composite specimens was approximately 2 mm for the eight-ply configuration and 1 mm for the four-ply configuration.

Apparatus

Similar to the requirements specified in ASTM D3039, the universal testing machine should be equipped with a stationary head and a movable head. The drive mechanism should be able to control the velocity of the movable head relative to the stationary head at a consistent rate of movement with the force sensing device unaffected by the inertia lag at any specified head moving rate. The force sensing device should be able to accurately measure the force applied to the test specimen, with an error of less than ±1%. The three-point flexure fixtures are comprised of a loading nose with a 6 mm (± 0.5 mm) diameter cylinder and two side supports with 3 mm (± 0.4 mm) diameter cylinders, as shown in Figure 3.29. All cylinders within the flexure fixtures should have 60-62 HRC hardness with finely grounded and free of indentation surfaces. The universal testing machine and its components should undergo calibration in accordance with the ASTM E4 standard practices to ensure their alignment and accuracy.

The INSTRON 5982 electromechanical universal testing machine (UTM) was utilized to assess the short-beam properties of CFRP composites fabricated in this study. The INSTRON 5982 UTM is equipped with a load cell or force sensing unit capable of withstanding a maximum load of 100 kN and a drive mechanism that capable to control the rate of head displacement ranging from 0.00005 to 1016 mm/minute. A three-point flexure fixture that complies with the apparatus requirements of ASTM D2344 was mounted on the heads of INSTRON 5982 UTM.

The UTM and its components were calibrated in accordance with the ASTM E4 standard practice.

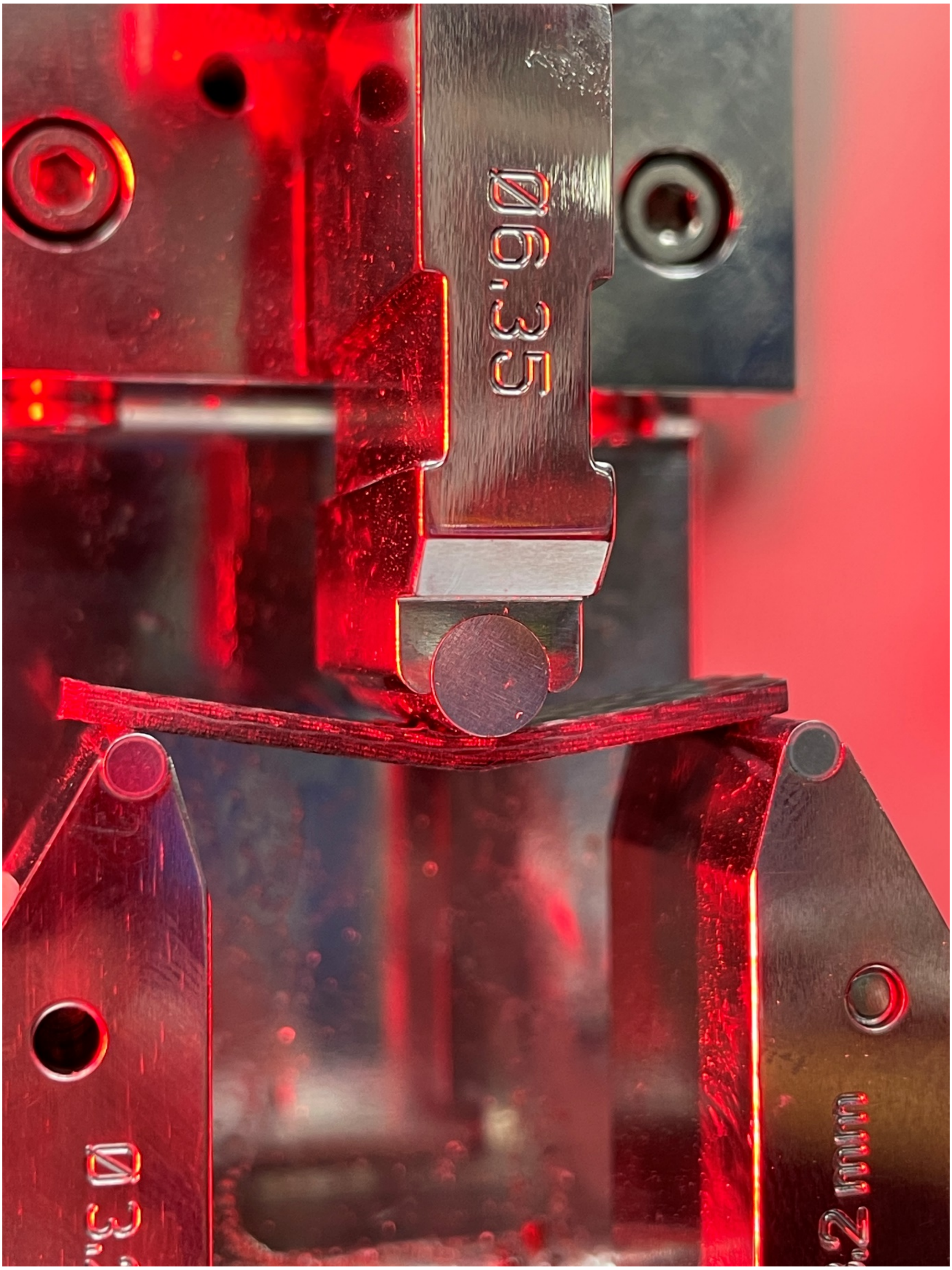

Figure 3.29 Three-point flexure fixtures for ASTM D2344 with a loading nose cylinder and two side supports cylinders

A micrometer or caliper can be used to measure the final dimensions of specimens. For the instrument that measures a typical specimen geometry, width or thickness, it should have an accuracy of ±0.0025 mm. While for length measurement, it should have an accuracy of ±0.025 mm. Additionally, other measuring tools with a reading accuracy within 1% of the dimension being measured can also be used.

Specimen preparation

The dimensions of a flat short-beam test specimen should be 40 mm (width) by 12 mm (length). For other dimensions, ASTM D2344 recommends adhering to the following relationship:

$$\text{Specimen length} = \text{thickness} \times 6$$
$$\text{Specimen width} = \text{thickness} \times 20$$

Equation 3.6 Short-beam specimen dimension

The appropriate machining method should be employed to obtain specimens from composite plates so as to avoid having delamination, undercuts, and notches on any edges or surfaces of the specimens. All test specimens have to be appropriately labeled to ensure the traceability for knowing the production batch, the utilized raw materials and distinguish the specimens from each other. Each test configuration should include a minimum of five specimens within the test batch to obtain valid results. All test specimens should be conditioned under a laboratory setting at a temperature of 23 ± 3°C and a relative humidity of 50 ± 10% for at least 24 hours. As all the composite specimens in this study are in flat plate form, configuration and specification information regarding curved specimens are not included.

Testing condition

Dimensions of each test specimen should be measured with a micrometer or a caliper and documented. Measurement of width and thickness was taken from the mid-section of the test specimens. The test was conducted in a laboratory atmosphere same as the conditioning environment. The rate of head displacement was set at 1.0 mm/min, and the specimen was inserted into the three-point flexure fixture between the loading nose and side supports. The span length between the supports at two sides should be four times the measured specimen thickness, with a tolerance of ±0.3 mm. Specimen was aligned with its longitudinal axis (spanwise direction) perpendicular to the loading nose and side supports. Specimen was centered in the middle of all three fixture cylinders with the cylinders being overhung at least 2 mm from the spanwise edges of the specimen. The specimen ends should overhang at both sides from the center of the side support, with at least the measured thickness of the specimen. The loading nose was positioned in the middle of the two side supports. Figure 3.30 shows the placement of specimen in the fixtures.

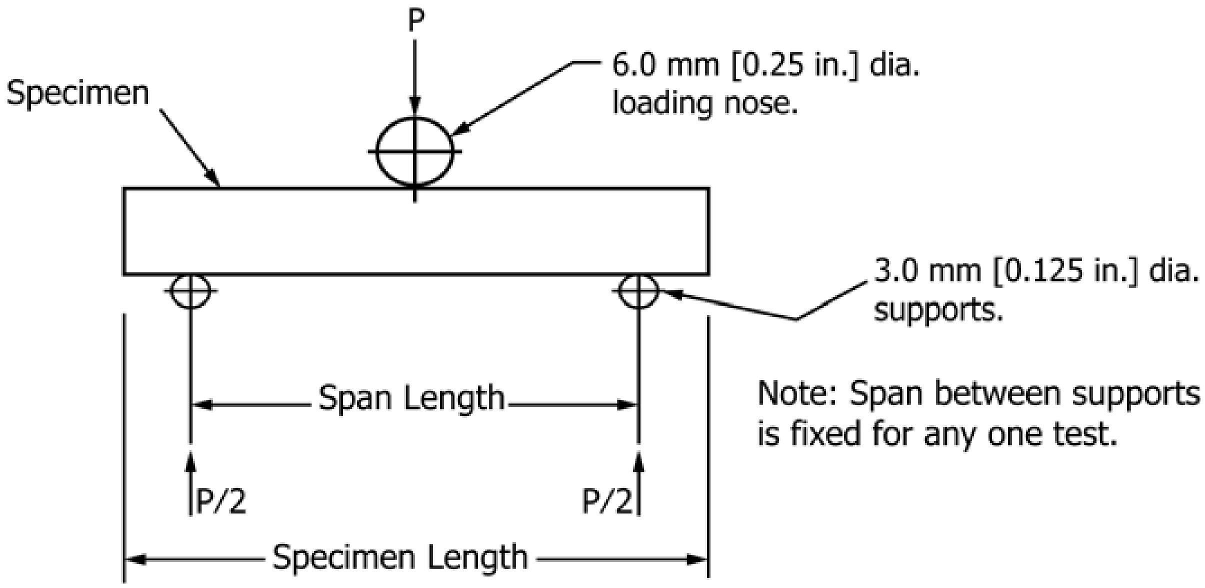

Figure 3.30 Specimen placement in three point flexure fixtures for horizontal shear load on flat laminate (ASTM International, 2016)

The testing process commenced by applying a constant rate of head displacement to the specimen. Data recording should run concurrently with the test process until any of the following conditions occurred: the load applied to the specimen decreased by more than 30%, the specimen fractured into two pieces, or the cumulative head displacement exceeded the specimen thickness. The test data should record both the applied load and the displacement of the head simultaneously. The ultimate tensile loading, which was the final load before the test was terminated, and any significant disruption were recorded.

Each specimen was examined, and its failure mode was identified. Figure 3.31 illustrates the typical failure modes that can be observed from the side view of the specimen. Some failures may not be visible on the specimen surface, such as localized damage in the center of the specimen. Additionally, some specimens may have a combination of failure modes.

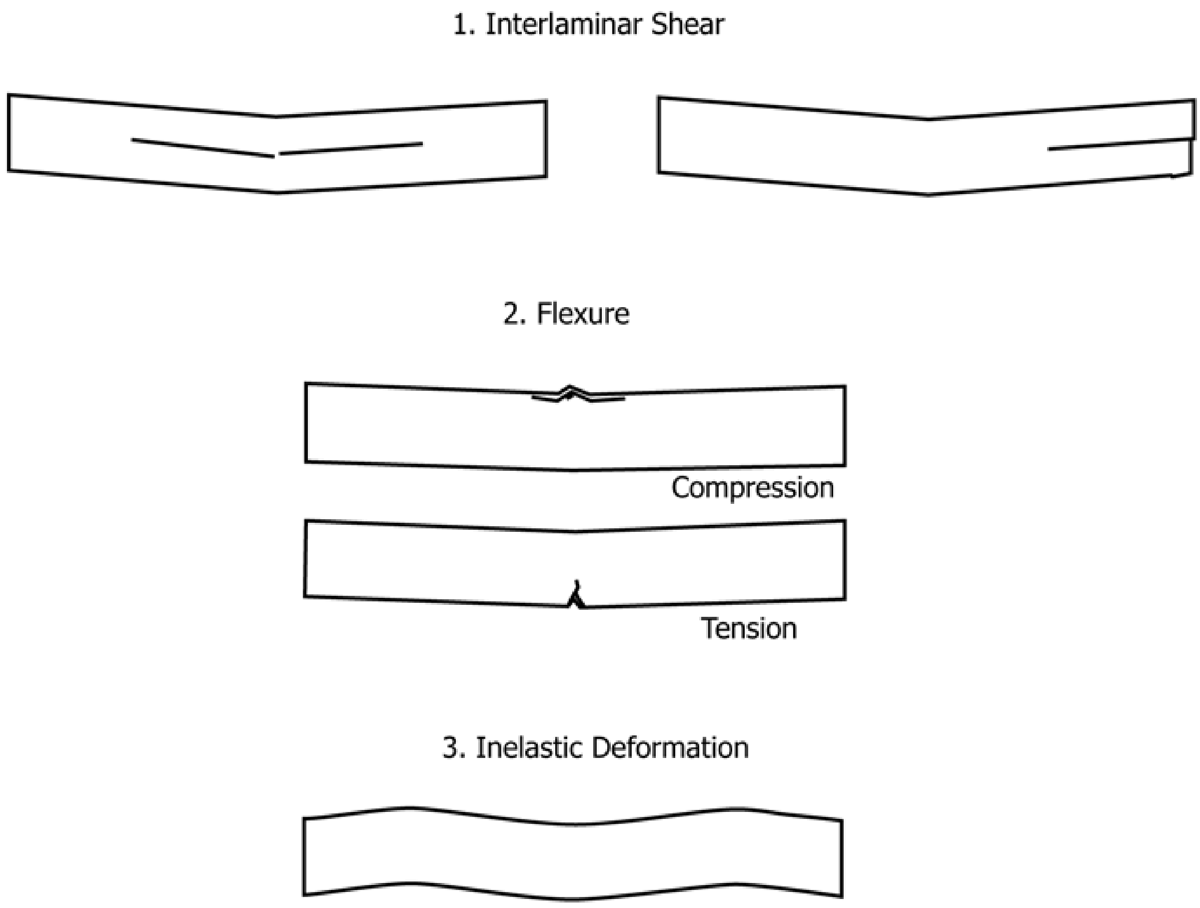

Figure 3.31 Typical failure modes of short-beam test specimens (ASTM International, 2016)

Calculation

$$F^{sbs} = 0.75 \times \frac{P_m}{b \times h}$$

Equation 3.7 Short-beam strength

Where,

F^{sbs} = short-beam strength (MPa)

P_m = maximum loading (N)

b = measured specimen width (mm)

h = measured specimen thickness (mm)

$$\overline{x} = \left(\sum_{i=1}^{n} x_i\right) \Big/ n$$

$$s_{n-1} = \sqrt{\left(\sum_{i=1}^{n} x_i^2 - n(\overline{x})^2\right) \Big/ (n-1)}$$

$$CV = 100 \times s_{n-1}/\overline{x}$$

Equation 3.8 Statistical parameters of short-beam strength

Where,

$\overline{x}$ = sample mean

s_{n-1} = sample standard deviation

CV = sample coefficient of variation (%)

n = number of specimens

x_i = value of the measured property

Chapter 4 Specimens characterization and observation

Specimens fabricated in this study are code according to their materials specifications and fabrication conditions. Table 4.1 shows the notation of different materials specifications and fabrication conditions and the nomenclature of each batch of specimens.

Table 4.1 Nomenclature of specimen batches

Specimen batch code	Resin system	Weave pattern	Ply stack configuration	CNT additive	Over-curing
WSTW4P01	WS105/209	Twill	Four-ply	-	-
WSTW4P02	WS105/209	Twill	Four-ply	-	-
WSTW4P03	WS105/209	Twill	Four-ply	-	-
WSTW8P04	WS105/209	Twill	Eight-ply	-	-
WSTW8P05	WS105/209	Twill	Eight-ply	-	-
WSTW8P06	WS105/209	Twill	Eight-ply	-	-
MLTW4P07	ML812A/B	Twill	Four-ply	-	-
MLTW4P08	ML812A/B	Twill	Four-ply	-	-
MLTW4P09	ML812A/B	Twill	Four-ply	-	-
MLTW8P10	ML812A/B	Twill	Eight-ply	-	-
MLTW8P11	ML812A/B	Twill	Eight-ply	-	-
MLTW8P12	ML812A/B	Twill	Eight-ply	-	-
IATW8P13	IN2/AT30S	Twill	Eight-ply	-	-
IATW8P14	IN2/AT30S	Twill	Eight-ply	-	-
IATW8P15	IN2/AT30S	Twill	Eight-ply	-	-
WSPW8P16	WS105/209	Plain	Eight-ply	-	-
WSTW8PCNT19	WS105/209	Twill	Eight-ply	0.1%wt	-
WSTW8POC21	WS105/209	Twill	Eight-ply	-	T_g + 25%
WSTW8PCNTOC23	WS105/209	Twill	Eight-ply	0.1%wt	T_g + 25%

Each batch of carbon fiber-reinforced polymer (CFRP) composite fabrication consists of eight specimens for each ASTM test. Each data set collected comprises the results of seven specimens in each batch of ASTM test, leaving one specimen as a spare in the event of an invalid result during testing. Specimens are coded with a number immediately following the batch code. The number ranged from 01 to 16 indicating the 16 specimens cut from the same composite plate. Specimen numbers 01 to 08 are the eight tensile specimens for ASTM D3039 while 09 to 16 are the eight short-beam specimens for ASTM D2344.

In the initial phase of this research study, CFRP composites with a four-ply laminate configuration were fabricated to investigate the impact of matrix viscosities and reinforcement weave patterns on CFRP composites. However, the first batch of CFRP composite specimens with the WS105/209 resin system shows multiple failure locations in most of the specimens after the tensile test. To ascertain whether this was an exceptional case, two additional batches of specimens with identical fabrication conditions were subjected to the same tensile testing. The tensile test results for all three batches of CFRP composite specimens with the WS105/209 resin system have multiple failure locations which indicates that the first batch specimen results were not exceptional. With the same ply configuration and weave pattern, three batches of CFRP composite specimens with ML812A/B resin system were fabricated and subjected to tensile testing to further investigate the causes of multiple failure locations. All three batches of CFRP composite specimens with the ML812A/B resin system show multiple failure locations in the tensile test results. This indicates that the resin systems are not the cause of the specimens having multiple failure locations. Therefore, an additional investigation on the ply configuration of CFRP composites was incorporated into the initial phase of this research study.

4.1 Influence of ply stack configurations on CFRP composites

A comparative evaluation of four-ply and eight-ply CFRP composite specimens is presented in this section. Both four-ply and eight-ply CFRP composites were fabricated using two distinct epoxy resin systems to eliminate any potential material bias. Furthermore, under each fabrication condition, three composite plates had been fabricated to mitigate any manufacturing-related errors.

Figure 4.1, Figure 4.2 and Figure 4.3 present the stress-strain characteristic of the three four-ply twill-weaved CFRP composite plates with WS105/209 resin system. Each graph consists of seven stress-strain curves which corresponds to a batch of seven test specimens from the same composite plate and subjected to the ASTM D3039 tensile test. Figure 4.1 illustrates the stress-strain curves of specimens from the WSTW4P01 composite plate. Some of the curves are non-linear and not overlapping with each other. Figure 4.2 illustrates the stress-strain curves of specimens from the WSTW4P02 composite plate. Most of the curves are fairly linear and mostly overlapping with each other except the WSTW4P02-01 specimen. Figure 4.3 illustrates the stress-strain curves of specimens from the WSTW4P03 composite plate. All curves are fairly linear and mostly overlapping with each other.

The deviation observed in the stress-strain curves may indicate an inconsistent quality throughout the composite plate. Specimens from the same composite plate should have similar properties which their stress-strain curves should be comparable with each other. Furthermore, the stress-strain behavior of composite material should show elasticity between the strain range of 0.001 to 0.003 and the stress-strain curve should be straight and linear within this strain range. The inconsistency in slope along the stress-strain curve may be caused by the following factors: 1) local failure occurs in certain laminate, 2) slippage between the grips and end tabs, or 3) slippage between the end tabs and composite (De Baere, Van Paepegem, & Degrieck, 2009; Karimi, Rahmatabadi, & Baghani, 2024). Comparing the stress-strain curves in Figure 4.1, Figure 4.2 and Figure 4.3, the stress-strain behavior is fairly consistent throughout the specimens in the WSTW4P02 and WSTW4P03 composite plates. Only WSTW4P02-01 specimen is slightly deviated from other specimens in the WSTW4P02 composite plate and its stress-strain behavior fluctuated along the curve. This indicates that the composite fabrication of plates WSTW4P02 and WSTW4P03 have a fairly constant quality and uniform properties across the plate. However, the stress-strain curves of specimens in the WSTW4P01 composite plate are fluctuating and deviated from each other which indicates the quality of the composite plate maybe uneven, resulting in the occurrence of local failures during the tensile test (Karimi, Rahmatabadi, & Baghani, 2024).

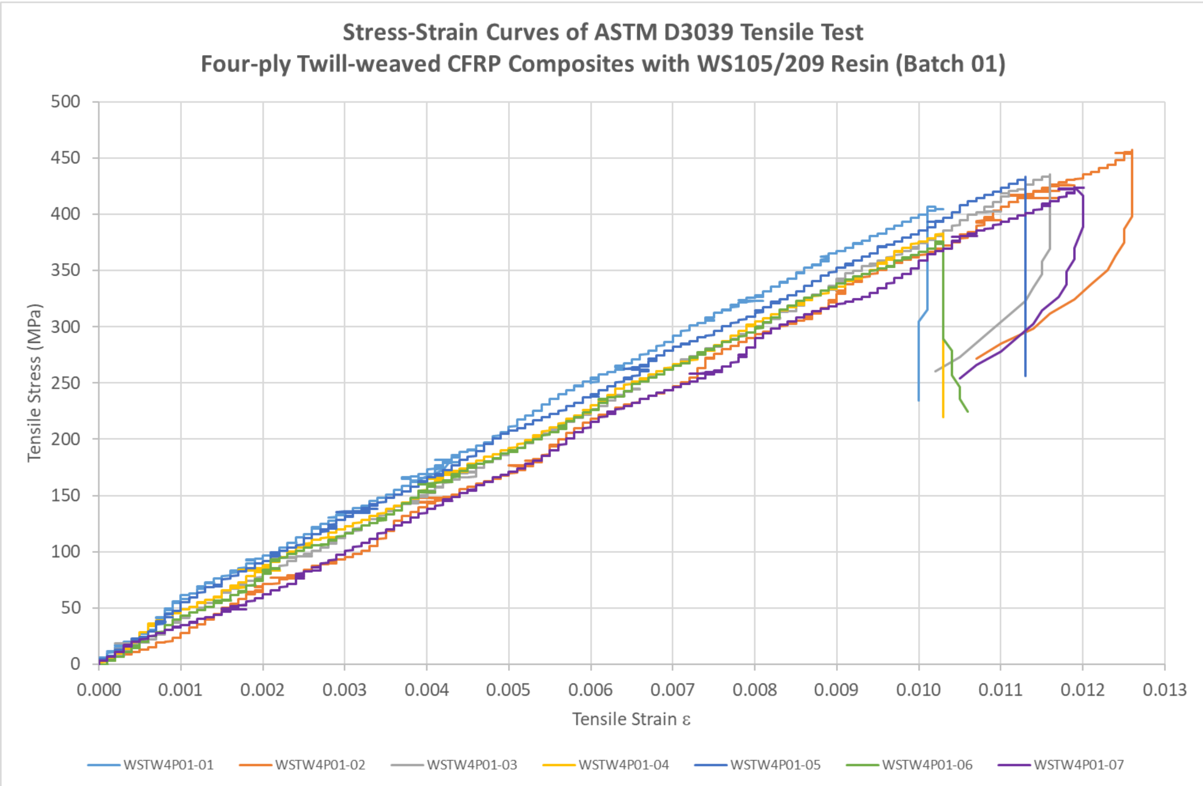

Figure 4.1 Stress-strain curve of four-ply twill-weaved CFRP composites with WS105/209 resin system (Batch 01)

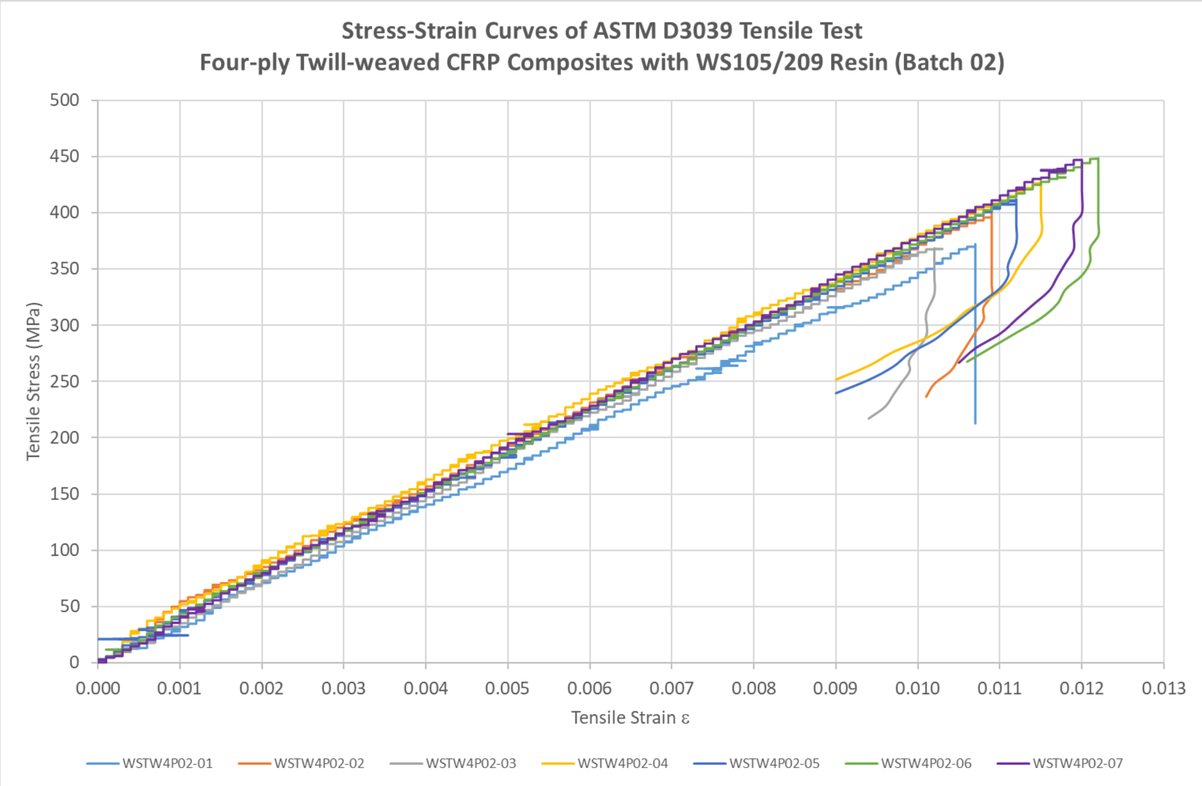

Figure 4.2 Stress-strain curve of four-ply twill-weaved CFRP composites with WS105/209 resin system (Batch 02)

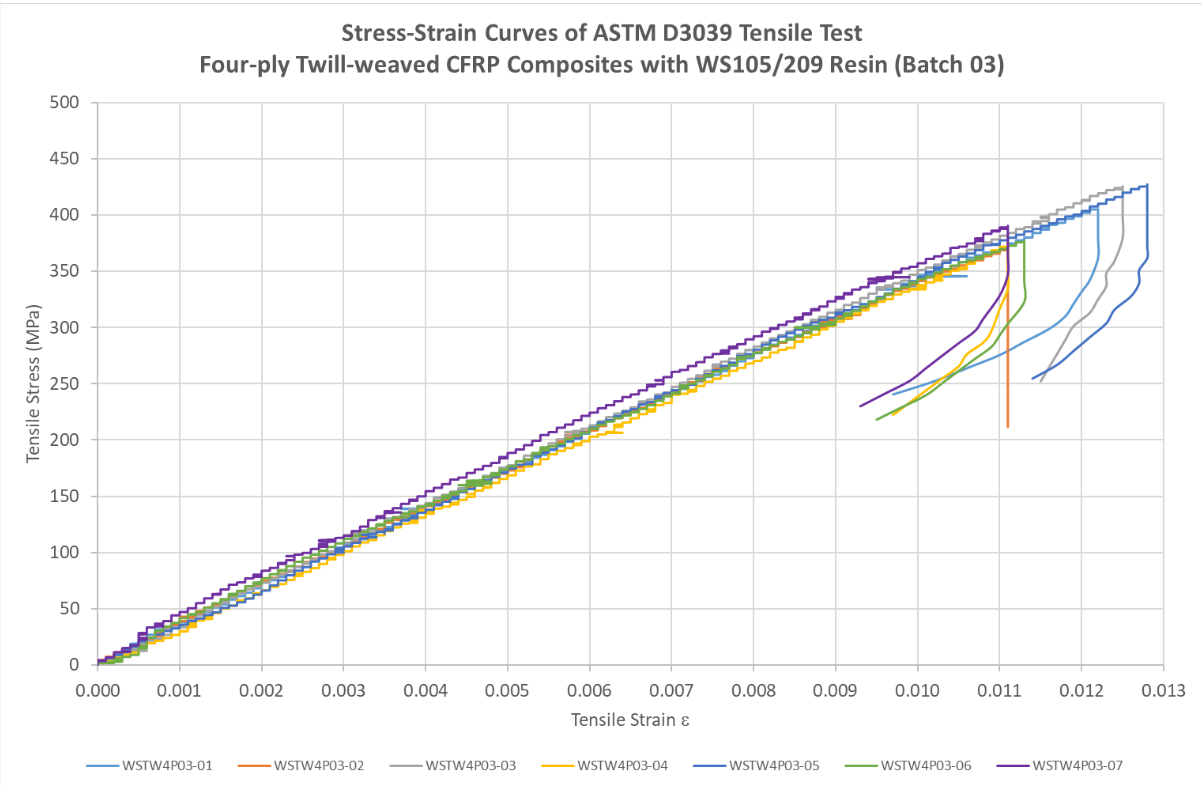

Figure 4.3 Stress-strain curve of four-ply twill-weaved CFRP composites with WS105/209 resin system (Batch 03)

Figure 4.4, Figure 4.5 and Figure 4.6 present the stress-strain characteristic of the three eight-ply twill-weaved CFRP composite plates with WS105/209 resin system. Figure 4.4 illustrates the stress-strain curves of specimens from the WSTW8P07 composite plate. All the curves are mostly overlapping with each other. None of the curves have significant deviation and they are mostly linear. A slight oscillation is found in the stress-strain curves of both WSTW8P07-03 and WSTW8P07-05 specimens but it does affect the overall trend and behavior of these two curves. Figure 4.5 illustrates the stress-strain curves of specimens from the WSTW8P08 composite plate. Most of the curves are linear and mostly overlapping with each other except the WSTW8P08-02 specimen. Oscillations and inconsistent slope are found in the stress-strain curves of WSTW8P08-02 specimen. Figure 4.6 illustrates the stress-strain curves of specimens from the WSTW8P09 composite plate. All the curves are mostly straight and linear but slightly deviated from each other. Slight oscillations are found in the stress-strain curves of WSTW8P09-01, WSTW8P09-05 and WSTW8P09-07 specimens.

All the stress-strain curves of eight-ply composite plates show relatively consistent and steady curves compared to those of four-ply composite plates. Notably, the stress-strain curves of eight-ply composite plates have comparable stress-strain behavior to the WSTW4P03 composite plate. Although the stress-strain curves of specimens from the WSTW8P09 composite plate are barely overlapping with each other, all curves maintain a straight and linear pattern. The stress-strain curves of specimens from the WSTW8P07 and WSTW8P08 composites plates demonstrate consistent stress-strain behavior and uniform quality throughout the composite plates.

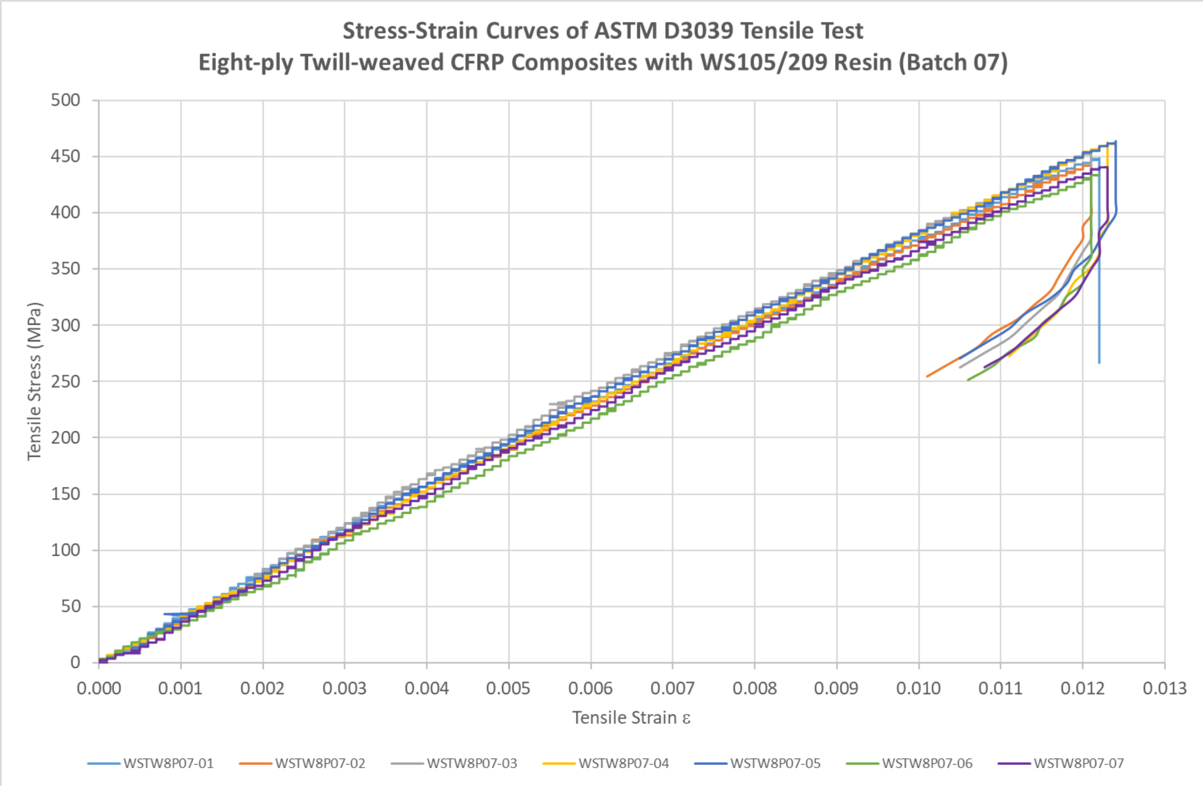

Figure 4.4 Stress-strain curve of eight-ply twill-weaved CFRP composites with WS105/209 resin system (Batch 07)

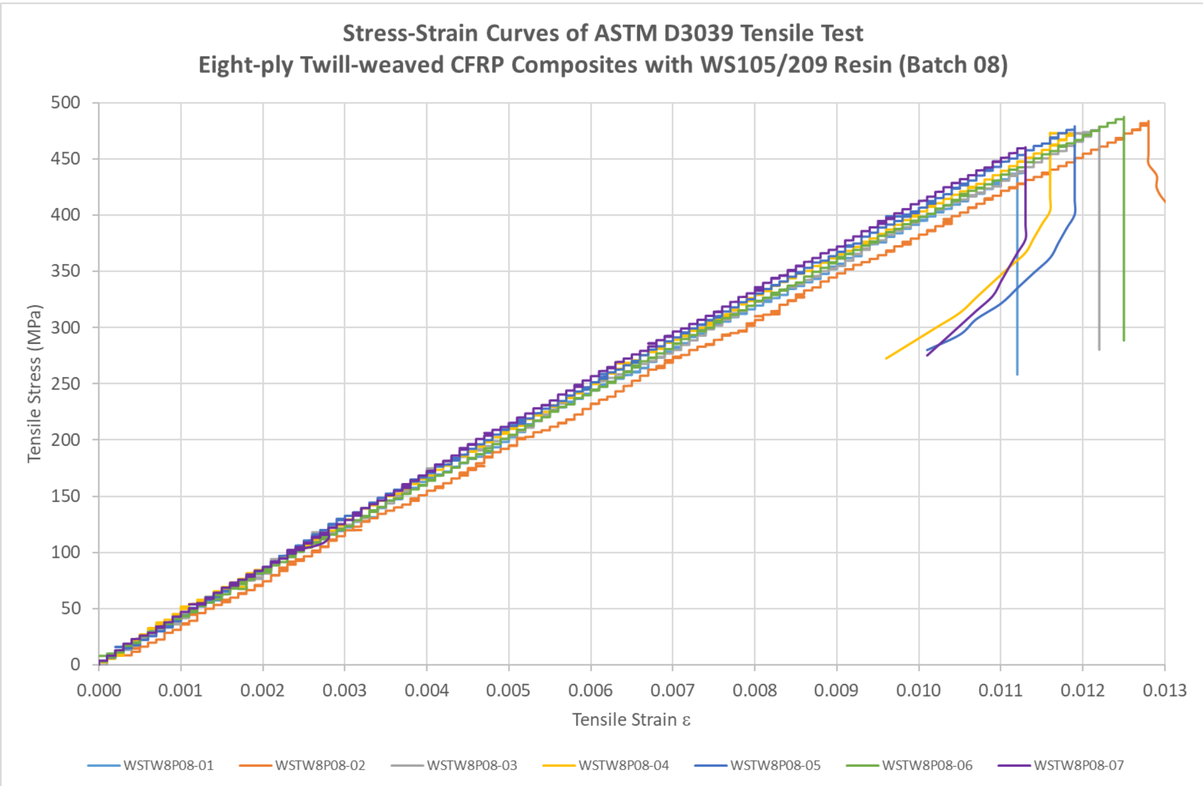

Figure 4.5 Stress-strain curve of eight-ply twill-weaved CFRP composites with WS105/209 resin system (Batch 08)

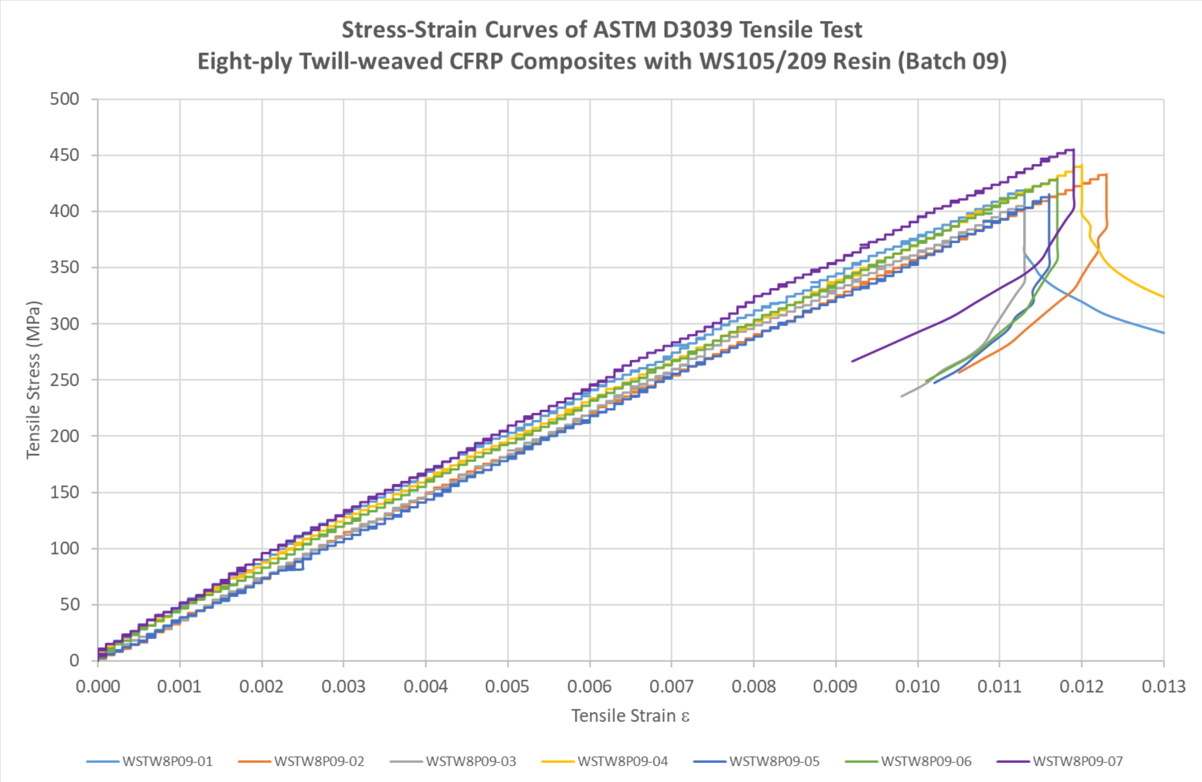

Figure 4.6 Stress-strain curve of eight-ply twill-weaved CFRP composites with WS105/209 resin system (Batch 09)

The inconsistent stress-strain behavior observed across the four-ply twill-weaved CFRP composites with the WS105/209 resin system can be attributed to the uneven quality of the matrix phase. During the fabrication of the composite plate, the resin mixture was drawn into the lay-up using vacuum force. The infusion rate of the resin mixture was influenced by the viscosity of the resin system and the composition of the lay-up, including the ply configuration of the reinforcement phase. By comparing the stress-strain curves of four-ply and eight-ply twill-weaved CFRP composites with the WS105/209 resin system, it is obvious that eight-ply composite plates show a more consistent stress-strain behavior compared to four-ply composite plates. Therefore, the inconsistent stress-strain behavior observed in four-ply specimens can be avoid by increasing the number of ply used to fabricate the composites.

In addition to the stress-strain curves, the ultimate tensile stress and ultimate tensile strain indicate the maximum force that the composite can withstand before failure and the elongation of specimen at failure respectively. Table 4.2 presents a comparison of ultimate tensile stress between four-ply and eight-ply twill-weaved CFRP composites with WS105/209 resin system. The overall mean ultimate tensile stress of four-ply composite specimens is 408 MPa, while eight-ply composite specimens is 450 MPa. The ultimate tensile stresses of four-ply composite specimens have an overall standard deviation of 28.9 MPa and an overall coefficient of variation of 7.10 %. The ultimate tensile stresses of eight-ply composite specimens have an overall standard deviation of 23.2 MPa and an overall coefficient of variation of 5.15 %. Therefore, eight-ply composite specimens have an 10.3 % increase in the overall mean ultimate tensile stress than four-ply composite specimens, with a 1.95 % decrease in the overall coefficient of variation.

Table 4.3 presents a comparison of ultimate tensile strain between four-ply and eight-ply twill-weaved CFRP composites with WS105/209 resin system. The overall mean ultimate tensile strain of four-ply composite specimens is 0.0114, while eight-ply composite specimens is 0.0120. The ultimate tensile strains of four-ply composite specimens have an overall standard deviation of 0.0008 and an overall coefficient of variation of 7.13 %. The ultimate tensile strains of eight-ply composite specimens have an overall standard deviation of 0.0004 and an overall coefficient of variation of 3.71 %. Therefore, eight-ply composite specimens have an 5.26 % increase in the overall mean ultimate tensile strain than four-ply composite specimens, with a 3.42 % decrease in the overall coefficient of variation.

The mean per composite plate is calculated by averaging the data of the seven specimens from the corresponding composite plate. All eight-ply composite plates show lower standard deviations (SD) than those of four-ply composite plates in both ultimate properties. With a higher mean and lower standard deviation than four-ply composite plates in both ultimate properties, the coefficients of variation (CV) of eight-ply composite plates are significantly lower. Since the means of the three composite plates with the same fabrication condition are quite distinct in both ultimate properties, the data of all 21 specimens from the three composite plates with the same fabrication condition are averaged for further comparison. The results show that the eight-ply fabrication condition consistently demonstrates a higher mean and lower standard deviation in both ultimate properties. The coefficient of variation for the eight-ply fabrication condition demonstrates a satisfactory repeatability in collecting ultimate properties data.

Table 4.2 Comparison of ultimate tensile stress between four-ply and eight-ply twill-weaved CFRP composites with WS105/209 resin system

Ultimate Tensile Stress						
	per composite plate			per fabrication condition		
	Mean (MPa)	SD (MPa)	CV	Mean (MPa)	SD (MPa)	CV
WSTW4P01	416	29.7	7.13	408	28.9	7.10
WSTW4P02	411	32.8	7.99			
WSTW4P03	396	23.8	6.02			
WSTW8P07	450	11.6	2.57	450	23.2	5.15
WSTW8P08	472	16.7	3.53			
WSTW8P09	429	17.0	3.96			

Table 4.3 Comparison of ultimate tensile strain between four-ply and eight-ply twill-weaved CFRP composites with WS105/209 resin system

Ultimate Tensile Strain						
	per composite plate			per fabrication condition		
	Mean	SD	CV	Mean	SD	CV
WSTW4P01	0.0112	0.0010	8.53	0.0114	0.0008	7.13
WSTW4P02	0.0112	0.0007	6.35			
WSTW4P03	0.0117	0.0007	6.36			
WSTW8P07	0.0122	0.0001	0.995	0.0120	0.0004	3.71
WSTW8P08	0.0119	0.0006	5.07			
WSTW8P09	0.0117	0.0004	3.14			

To have a better understanding of the statistic presented in Table 4.2 and Table 4.2, the ultimate properties of each specimen are visually represented by marking the highest points of each stress-strain curve, which is the failure point of each specimen. Figure 4.7 and Figure 4.8 illustrate the ultimate properties of four-ply and eight-ply twill-weaved CFRP composites with WS105/209 resin system respectively. Failure points in Figure 4.7 is more scattered when compared to failure points in Figure 4.8. Therefore, eight-ply twill-weaved composite specimens have a higher consistency in ultimate tensile properties then eight-ply specimens.

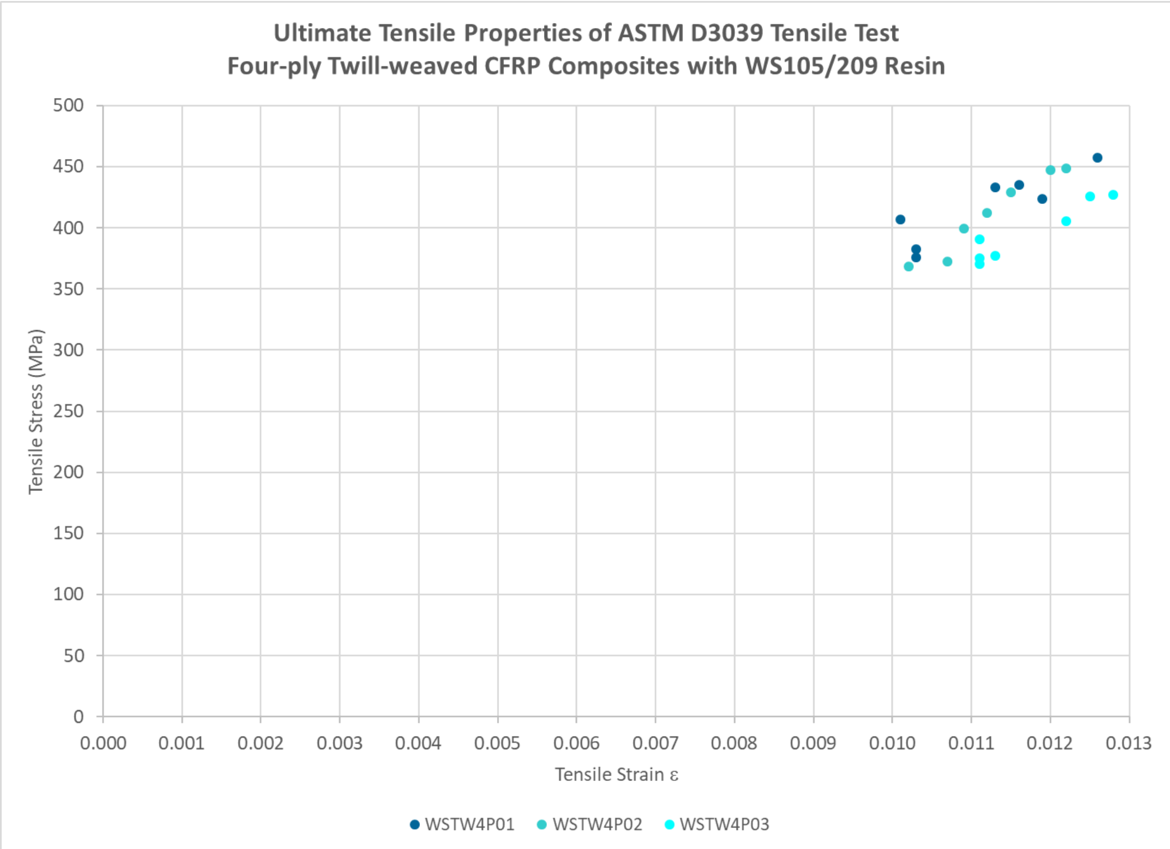

Figure 4.7 Ultimate tensile properties of four-ply twill-weaved CFRP composites with WS105/209 resin system

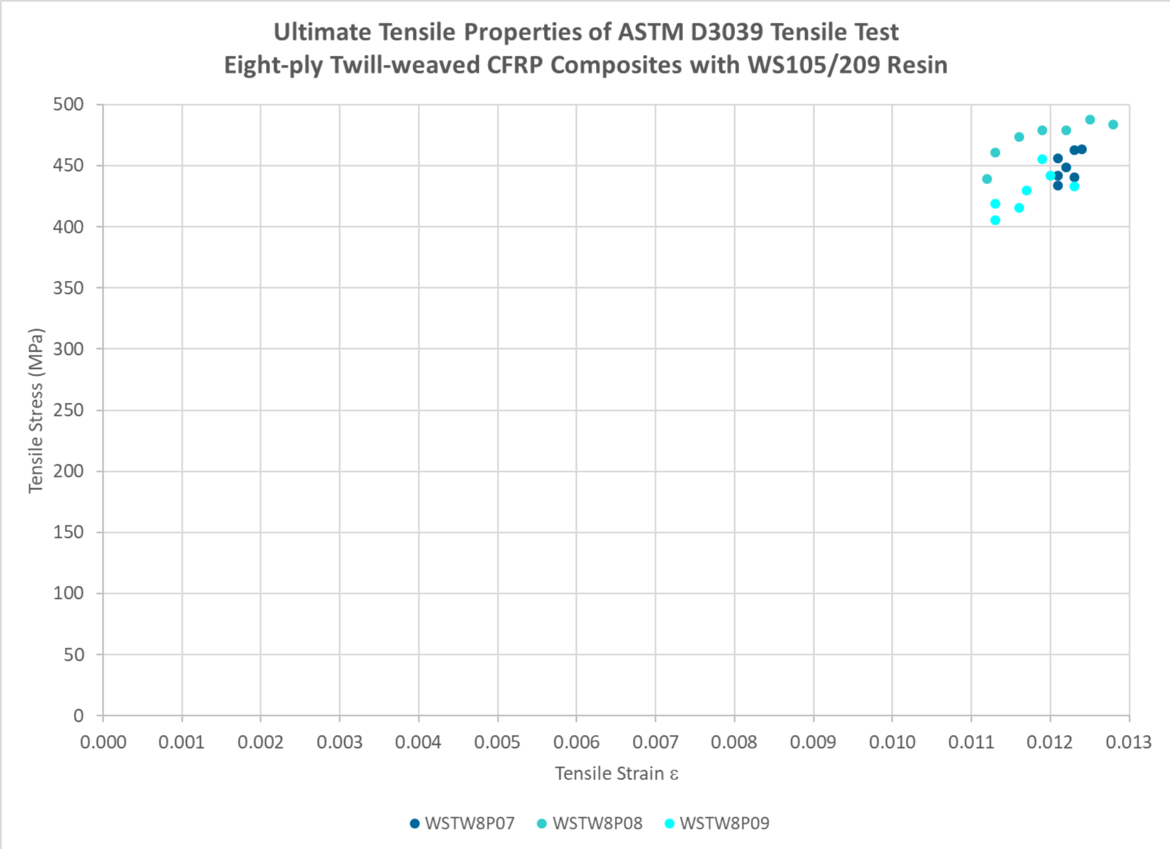

Figure 4.8 Ultimate tensile properties of eight-ply twill-weaved CFRP composites with WS105/209 resin system

Linear regression analysis was conducted on 18 random sets of ultimate tensile stress and ultimate tensile strain data from 21 specimens of both four-ply and eight-ply twill-weaved CFRP composites with WS105/209 resin system. For optimizing a linear regression model, several fundamental requirements should ideally be met. However, a linear regression model can often be generated from a data set even if some of these conditions are only partially satisfied. (Norusis, 1999). Both dependent and independent variables are continuous and a linear relationship should be observed between them. One-way ANOVA was conducted to determine the significance of the model. A significance level (Sig-value) of less than 0.05 indicates that the linear regression model is statistically significant and the independent variable is related to the dependent variable. A normal probability-probability plot of regression standardized residuals is a plot that indicates the normality of the residuals. Data points closely follow the diagonal line suggest a normal distribution of the residuals. A scatterplot of regression standardized residuals against regression standardized predicted values was used to indicate the homoscedasticity of the data. Randomly scattered data points forming a rectangular shape suggest consistent variance across the data set (Field, 2018; Tabachnick & Fidell, 2013). A Durbin-Watson statistic test was conducted to assess the autocorrelation between data errors. The Durbin-Watson value, which ranges from 0 to 4, is considered acceptable when it falls between 1.5 and 2.5 indicating no obvious autocorrelation in the data set (Tabachnick & Fidell, 2013). Tensile stress and tensile strain are continuous variables with a linear relationship as shown in Figure 4.1 to Figure 4.6. The ultimate tensile data used in linear regression also shows no obvious outliers in Figure 4.7 and Figure 4.8.

For four-ply twill-weaved specimens with WS105/209 resin system, the significance value of one-way ANOVA is 0.001. Figure 4.9 and Figure 4.10 show the normal probability-probability plot and scatterplot respectively. The residuals of the data follow a normal distribution and the variance is consistent. However, the Durbin-Watson value is 1.001 indicating a slight negative autocorrelation between data errors. Figure 4.11 presents the statistical result of a linear regression model with the following equation to demonstrate the relationship between tensile stress and tensile strain.

$$ultimate\ tensile\ stress = 127.863 + (24{,}522.359 \times ultimate\ tensile\ strain)$$

Equation 4.1 Linear regression model for ultimate tensile properties of four-ply twill-weaved specimens with WS105/209 resin system

The R-squared value of the linear regression model is 0.511, indicating that 51.1% of the variation in tensile stress is related to tensile strain. This model is then used to predict the ultimate tensile stress of the remaining three specimens. The predicted ultimate tensile stresses are compared with the measured ultimate tensile stresses of the three specimens to validate the linear regression model. Table 4.4 shows the comparison between the predicted and measured ultimate tensile stresses of the three specimens. The predicted ultimate tensile stresses deviate from the measured values by approximately 5%.

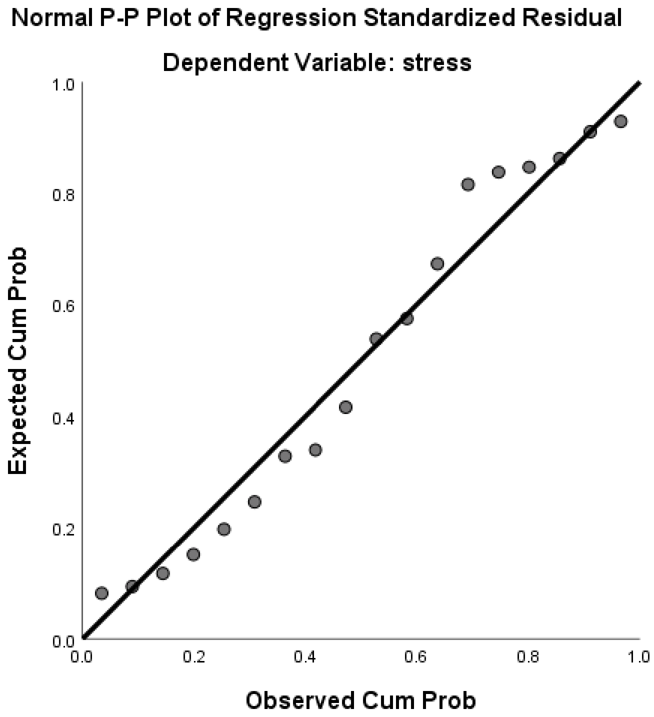

Figure 4.9 Normal probability-probability plot of regression standardized residuals of four-ply twill-weaved specimens with WS105/209 resin system

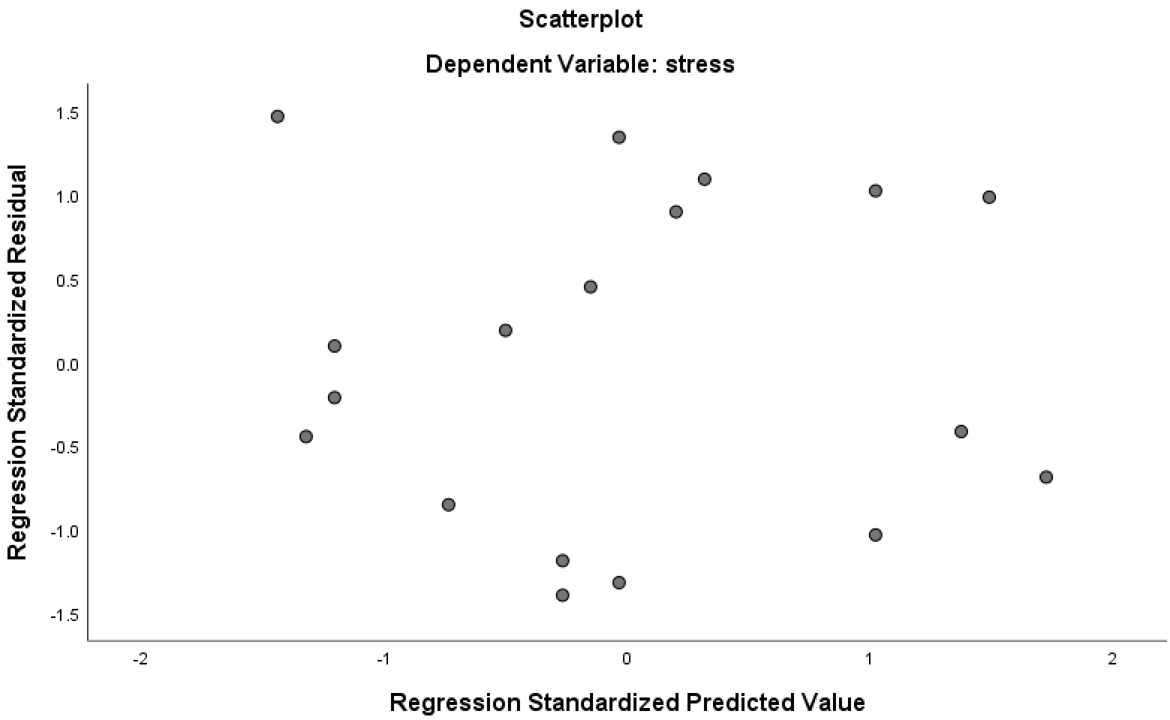

Figure 4.10 Scatterplot of regression standardized residuals against regression standardized predicted values of four-ply twill-weaved specimens with WS105/209 resin system

Model Summary[b]

Model	R	R Square	Adjusted R Square	Std. Error of the Estimate	Durbin-Watson
1	.715[a]	.511	.481	21.0855402	1.001

a. Predictors: (Constant), long_strain

b. Dependent Variable: stress

ANOVA[a]

Model		Sum of Squares	df	Mean Square	F	Sig.
1	Regression	7442.326	1	7442.326	16.739	.001[b]
	Residual	7113.600	16	444.600		
	Total	14555.926	17			

a. Dependent Variable: stress

b. Predictors: (Constant), long_strain

Coefficients[a]

Model		Unstandardized Coefficients		Standardized Coefficients	t	Sig.
		B	Std. Error	Beta		
1	(Constant)	127.863	68.077		1.878	.079
	long_strain	24522.359	5993.667	.715	4.091	.001

a. Dependent Variable: stress

Figure 4.11 Linear regression model results of four-ply twill-weaved specimens with WS105/209 resin system

Table 4.4 Comparison between predicted and actual ultimate tensile stress of four-ply twill-weaved specimens with WS105/209 resin system

Specimens	Actual ultimate tensile strain	Predicted ultimate tensile stress	Actual ultimate tensile stress	Deviation
WSTW4P01-07	0.0119	419.6791	423.9336	-1.00%
WSTW4P02-07	0.0120	422.1313	447.0986	-5.58%
WSTW4P03-07	0.0111	400.0611	390.4890	2.45%

For eight-ply twill-weaved specimens with WS105/209 resin system, the significance value of one-way ANOVA is 0.003. Figure 4.12 and Figure 4.13 show the normal probability-probability plot and scatterplot respectively. The residuals of the data follow a normal distribution and the variance is consistent. However, the Durbin-Watson value is 0.752 indicating a negative autocorrelation between data errors. Figure 4.14 presents the statistical result of a linear regression model with the following equation to demonstrate the relationship between tensile stress and tensile strain.

$$ultimate\ tensile\ stress = 13.324 + (36{,}426.311 \times ultimate\ tensile\ strain)$$

Equation 4.2 Linear regression model for ultimate tensile properties of eight-ply twill-weaved specimens with WS105/209 resin system

The R-squared value of the linear regression model is 0.425, indicating that 42.5% of the variation in tensile stress is related to tensile strain. This model is then used to predict the ultimate tensile stress of the remaining three specimens. The predicted ultimate tensile stresses are compared with the measured ultimate tensile stresses of the three specimens to validate the linear regression model. Table 4.5 shows the comparison between the predicted and measured ultimate tensile stresses of the three specimens. The predicted ultimate tensile stresses deviate from the measured values by approximately 7%.

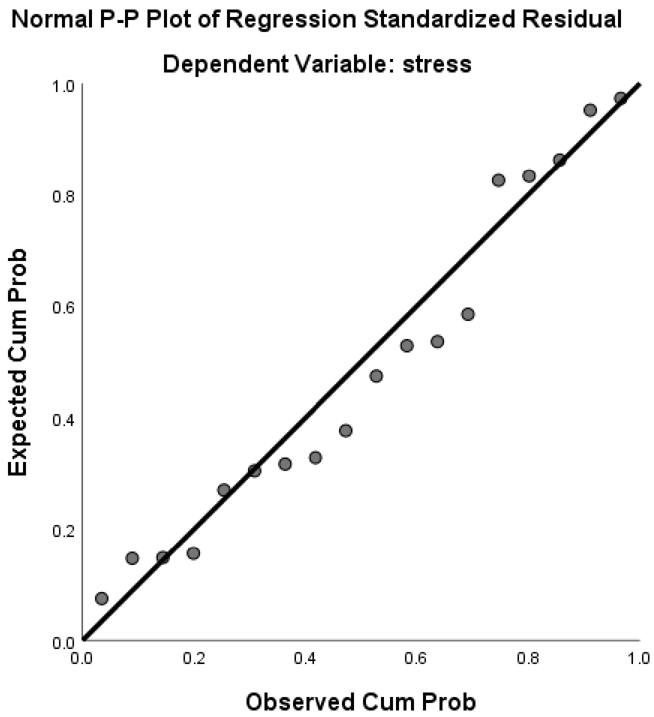

Figure 4.12 Normal probability-probability plot of regression standardized residuals of eight-ply twill-weaved specimens with WS105/209 resin system

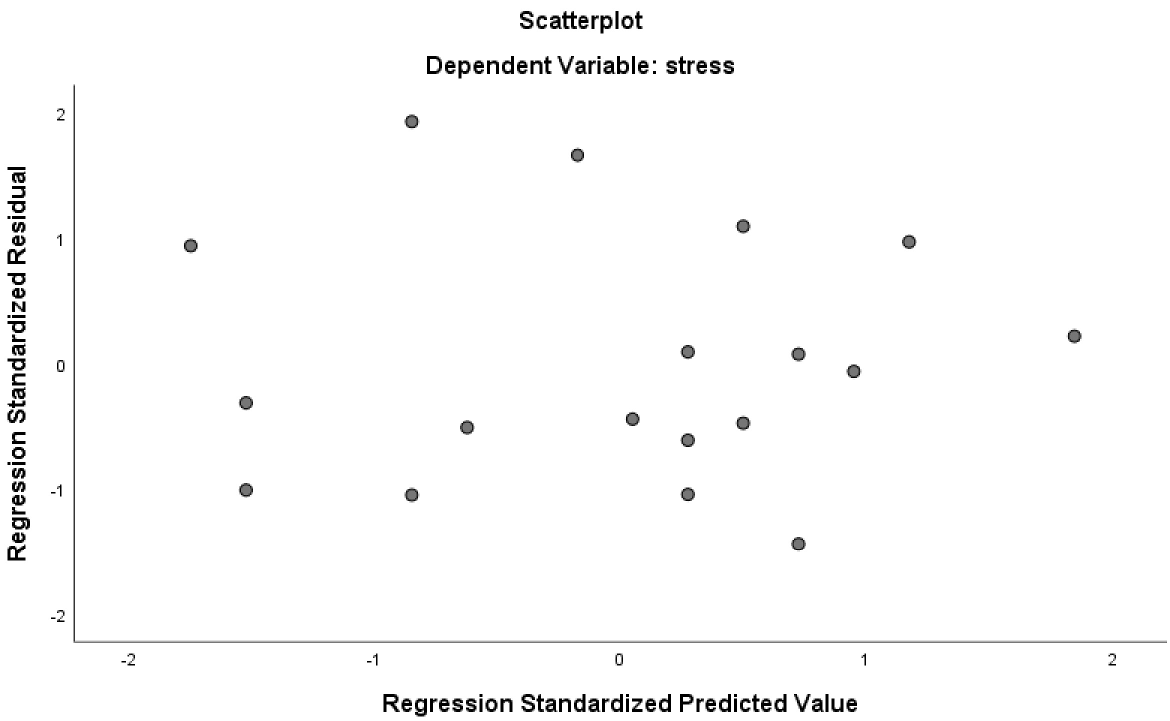

Figure 4.13 Scatterplot of regression standardized residuals against regression standardized predicted values of eight-ply twill-weaved specimens with WS105/209 resin system

Model Summary[b]

Model	R	R Square	Adjusted R Square	Std. Error of the Estimate	Durbin-Watson
1	.652[a]	.425	.389	19.4615028	.752

a. Predictors: (Constant), long_strain

b. Dependent Variable: stress

ANOVA[a]

Model		Sum of Squares	df	Mean Square	F	Sig.
1	Regression	4473.047	1	4473.047	11.810	.003[b]
	Residual	6060.001	16	378.750		
	Total	10533.048	17			

a. Dependent Variable: stress

b. Predictors: (Constant), long_strain

Coefficients[a]

Model		Unstandardized Coefficients		Standardized Coefficients	t	Sig.
		B	Std. Error	Beta		
1	(Constant)	13.324	127.043		.105	.918
	long_strain	36426.311	10599.609	.652	3.437	.003

a. Dependent Variable: stress

Figure 4.14 Linear regression model results of eight-ply twill-weaved specimens with WS105/209 resin system

Table 4.5 Comparison between predicted and actual ultimate tensile stress of eight-ply twill-weaved specimens with WS105/209 resin system

Specimens	Actual ultimate tensile strain	Predicted ultimate tensile stress	Actual ultimate tensile stress	Deviation
WSTW8P07-07	0.0123	461.3676	440.6750	4.70%
WSTW8P08-07	0.0113	424.9413	460.4770	-7.72%
WSTW8P09-07	0.0119	446.7971	455.3835	-1.89%

By comparing Equation 4.1 and Equation 4.2, the differences in ultimate tensile stress behavior between four-ply and eight-ply twill-weaved specimens with the WS105/209 resin system can be identified. The ultimate tensile stress of eight-ply specimens is highly dependent on the ultimate tensile strain whereas that of four-ply specimens has a larger base value with a smaller influence from ultimate tensile strain.

Apart from the ultimate properties that indicate the failure point on the stress-strain curve, modulus of elasticity represents the slope of stress-strain curve at the strain range between 0.0001 and 0.0003. Modulus of elasticity, also known as Young's modulus, measures the material stiffness and resistance to elastic deformation of the composite specimen. Table 4.6 presents a comparison of modulus of elasticity between four-ply and eight-ply twill-weaved CFRP composites with WS105/209 resin system. The overall mean modulus of elasticity of four-ply composite specimens is 36.7 GPa, while eight-ply composite specimens is 40.0 GPa. The modulus of elasticity of four-ply composite specimens have an overall standard deviation of 2.79 GPa and an overall coefficient of variation of 7.59 %. The modulus of elasticity of eight-ply composite specimens have an overall standard deviation of 1.99 GPa and an overall coefficient of variation of 4.98 %. Therefore, eight-ply composite specimens have an 8.99 % increase in the overall mean modulus of elasticity than four-ply composite specimens, with a 2.61 % decrease in the overall coefficient of variation.

Eight-ply composite specimens have a slightly lower standard deviations and a slightly higher mean values than four-ply composite specimens. As a result, some of the coefficients of variation of eight-ply composite plates are slightly lower than those of four-ply composite plates. All data from the composite plates with the same fabrication condition is further averaged for comparison and statistical analysis. The eight-ply fabrication condition demonstrates a higher mean and lower standard deviation in modulus of elasticity compared to the four-ply fabrication condition. The coefficient of variation of the eight-ply fabrication condition indicates a slightly better consistency in material stiffness.

Table 4.6 Comparison of modulus of elasticity between four-ply and eight-ply twill-weaved CFRP composites with WS105/209 resin system

Modulus of Elasticity						
	per composite plate			per fabrication condition		
	Mean (GPa)	SD (GPa)	CV	Mean (GPa)	SD (GPa)	CV
WSTW4P01	36.9	2.67	7.24	36.7	2.79	7.59
WSTW4P02	38.5	2.92	7.59			
WSTW4P03	34.6	0.993	2.87			
WSTW8P07	39.7	1.25	3.14	40.0	1.99	4.98
WSTW8P08	41.2	2.09	5.07			
WSTW8P09	39.1	2.15	5.50			

Another tensile property that shows the deformation of the material under tensile loading is Poisson's ratio. Poisson's ratio is the ratio of transverse strain to longitudinal strain. Table 4.7shows the comparison of Poisson's ratio between four-ply and eight-ply twill-weaved CFRP composites with WS105/209 resin system.

The overall mean Poisson's ratio of four-ply composite specimens is 0.328, while eight-ply composite specimens is 0.370. The Poisson's ratio of four-ply composite specimens have an overall standard deviation of 0.0552 and an overall coefficient of variation of 16.8 %. The Poisson's ratio of eight-ply composite specimens have an overall standard deviation of 0.0670 and an overall coefficient of variation of 18.1 %. Therefore, eight-ply composite specimens have an 12.8 % increase in the overall mean Poisson's ratio than four-ply composite specimens, with an 1.3 % increase in the overall coefficient of variation.

Eight-ply composite specimens have a slightly higher Poisson's ratio than four-ply composite specimens and there is no obvious difference between the statistical data of four-ply composites and eight-ply composites. The coefficient of variation of Poisson's ratio are higher than other tensile properties regardless of the data sets or sample size, which indicates that the ratio of material deformation in transverse direction to longitudinal direction are not consistent regardless of the composite fabrication configuration.

Table 4.7 Comparison of Poisson's ratio between four-ply and eight-ply twill-weaved CFRP composites with WS105/209 resin system

Poisson's Ratio						
	per composite plate			per fabrication condition		
	Mean	SD	CV	Mean	SD	CV
WSTW4P01	0.338	0.0518	15.3	0.328	0.0552	16.8
WSTW4P02	0.354	0.0622	17.6			
WSTW4P03	0.291	0.0331	11.4			
WSTW8P07	0.370	0.0650	17.6	0.370	0.0670	18.1
WSTW8P08	0.363	0.0560	15.4			
WSTW8P09	0.377	0.0864	22.9			

Furthermore, the failure mode guideline in ASTM D3039 tensile test can help determine the possible failure causes by categorizing the types, areas, and location of fracture on the specimen. Figure 4.15, Figure 4.16 and Figure 4.17 illustrate the failure modes of the four-ply twill-weaved CFRP composites with WS105/209 resin system. The failure types observed in specimens from three composite plate are presented in Figure 4.15. For WSTW4P01 composite plate, all seven specimens are fractured in lateral manner. For WSTW4P02 composite plate, five specimens are fractured in angled manner and two specimens are fractured in lateral manner. For WSTW4P03 composite plate, two specimens are fractured in lateral manner and five specimens are fractured in multi-mode. The failure areas observed in specimens from three composite plate are presented in Figure 4.16. For WSTW4P01 composite plate, all seven specimens are fractured in multiple areas. For WSTW4P02 composite plate, one specimen is fractured in gage area and six specimens are fractured in multiple areas. For WSTW4P03 composite plate, two specimens are fractured in gage area and five specimens are fractured in multiple areas. The failure locations observed in specimens from three composite plate are presented in Figure 4.17. For WSTW4P01 composite plate, all seven specimens are fractured in various locations. For WSTW4P02 composite plate, one specimen is fractured in the middle and six specimens are fractured in various locations. For WSTW4P03 composite plate, two specimens are fractured in the middle and five specimens are fractured in various locations.

The failure modes of specimens from the WSTW4P01 composite plate show consistent patterns, with all seven specimens having the same failure types, areas, and locations. In contrast, the failure modes of specimens from the WSTW4P02 and WSTW4P03 composite plates show some diversity. Most of the specimens of four-ply twill-weaved CFRP composites have multiple failure areas and various failure locations. The presence of multiple failure areas indicates that each specimen experienced more than one failure, while the various failure locations suggest that these failures occurred in different segments of the specimens. Furthermore, the presence of multi-mode failure types indicates that each specimen experienced more than one failure type, such as lateral and angled manner. Specimens with multi-mode failure types typically have multiple failure areas and various failure locations. All the failure types in specimens of four-ply twill-weaved CFRP composites with WS105/209 resin system are either in lateral or angled manner, as the multi-mode failure types specimens are all having a combination of lateral and angled manner in two or more areas. A high-speed camera reveals that multiple fracture locations are created due to the shockwave from the primary fracture. Half of the four-ply twill-weaved specimens have a lateral failure type. The occurrence of multi-mode failure type in four-ply twill-weaved specimens may also be attributed to the shockwave.

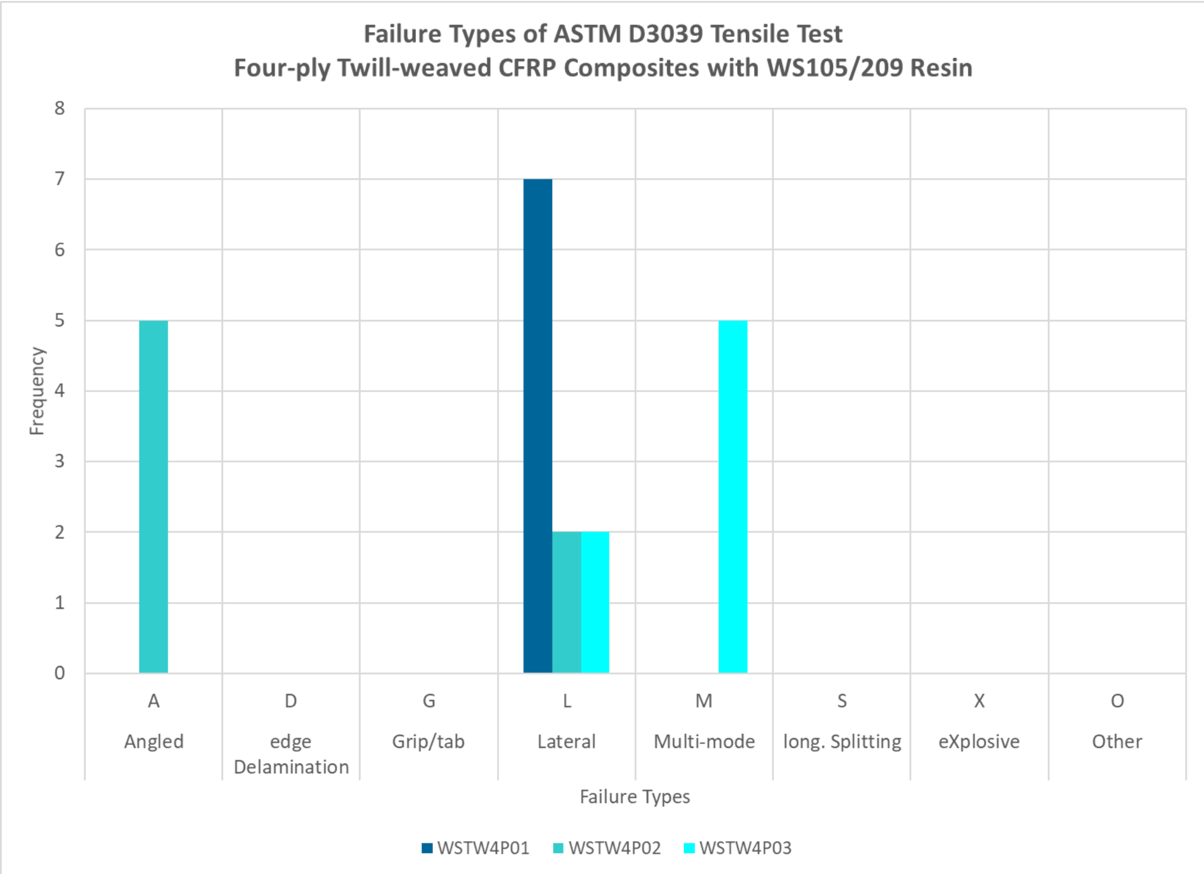

Figure 4.15 ASTM D3039 failure types of four-ply twill-weaved CFRP composites with WS105/209 resin system

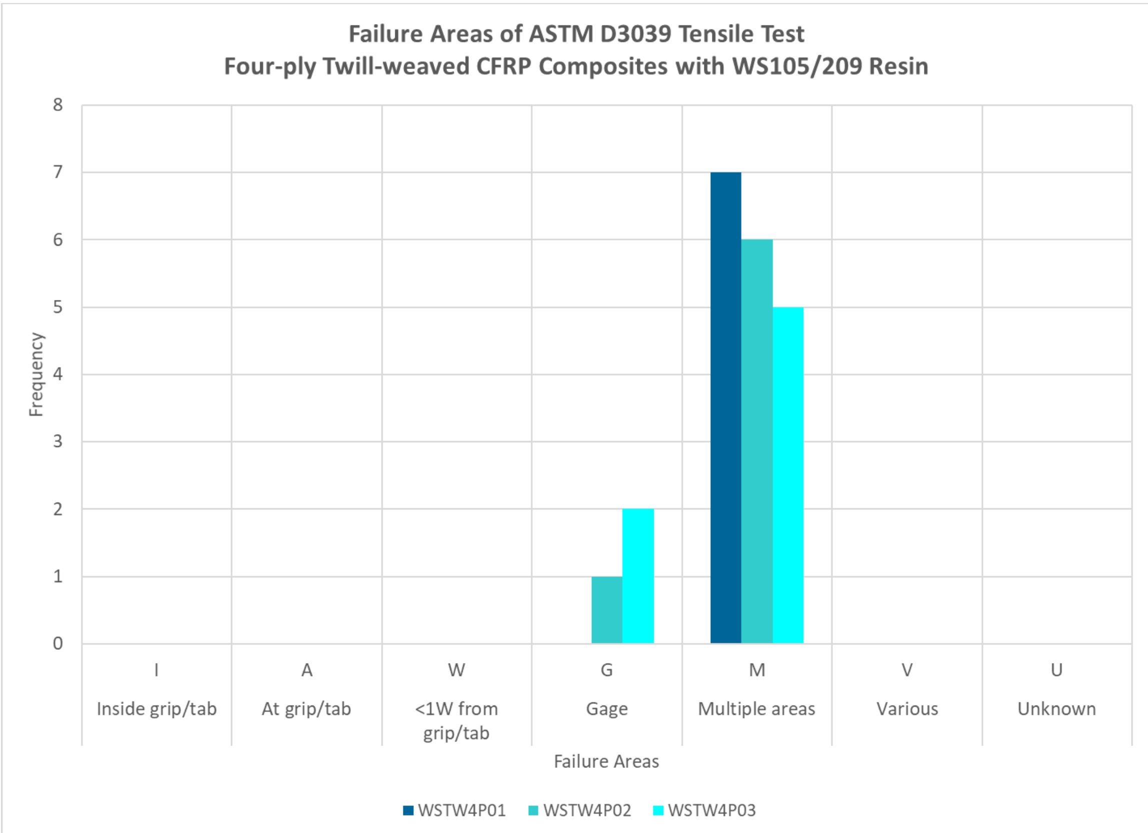

Figure 4.16 ASTM D3039 failure areas of four-ply twill-weaved CFRP composites with WS105/209 resin system

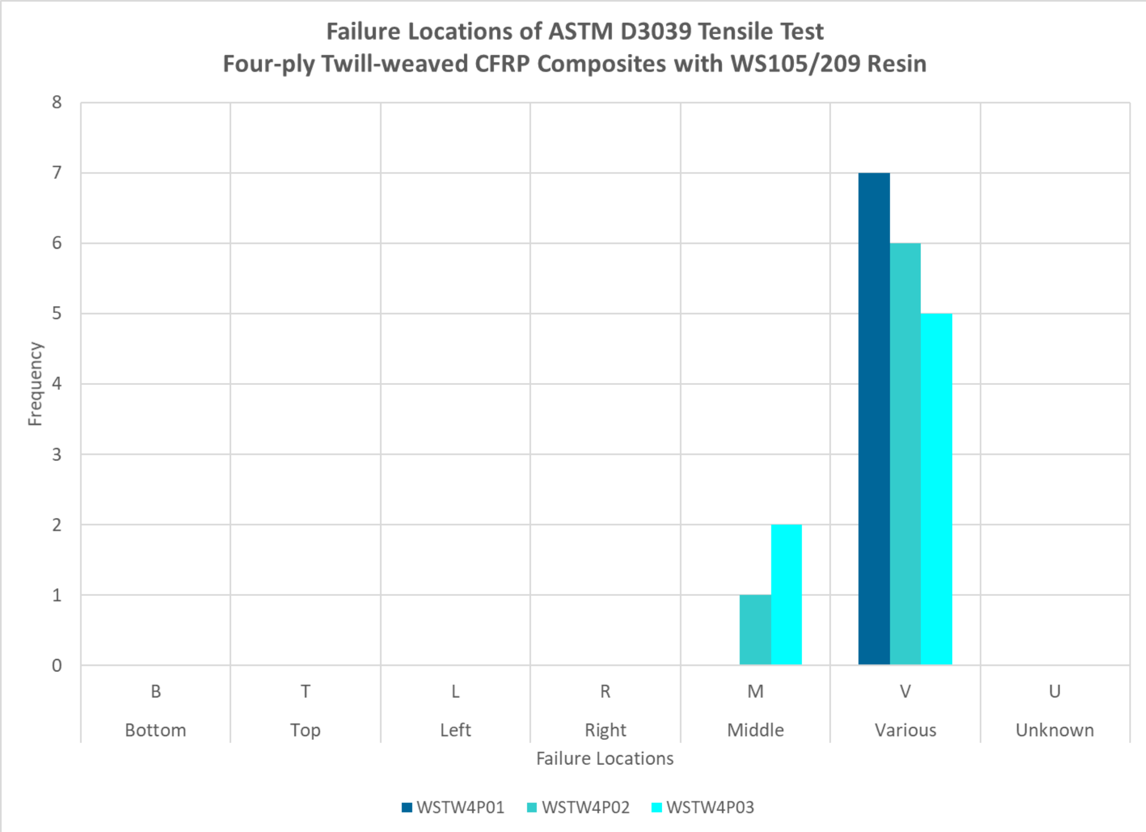

Figure 4.17 ASTM D3039 failure locations of four-ply twill-weaved CFRP composites with WS105/209 resin system

Specimens of four-ply twill-weaved CFRP composites with WS105/209 resin system are generally fractured in four failure mode combinations: L M V (Lateral type, Multiple areas, Various location), M M V (Multi-mode type, Multiple areas, Various locations), L G M (Lateral type, Gage area, Middle location), and A M V (Angled type, Multiple areas, Various locations). Figure 4.18 shows lateral fracture at both the top and bottom of the specimen. Figure 4.19 shows the multi-mode fracture with lateral manner at the bottom (B) and angled manner at the top (T) of the specimen. Figure 4.20 shows the lateral fracture at gage area which is one specimen width (yellow squares) away from the end tabs and an illustration of failure mode - L G M in ASTM D3039 is shown for reference. Figure 4.21 shows the angled manner failure at both the top and bottom of the specimen, and the bottom failure is not completely fractured.

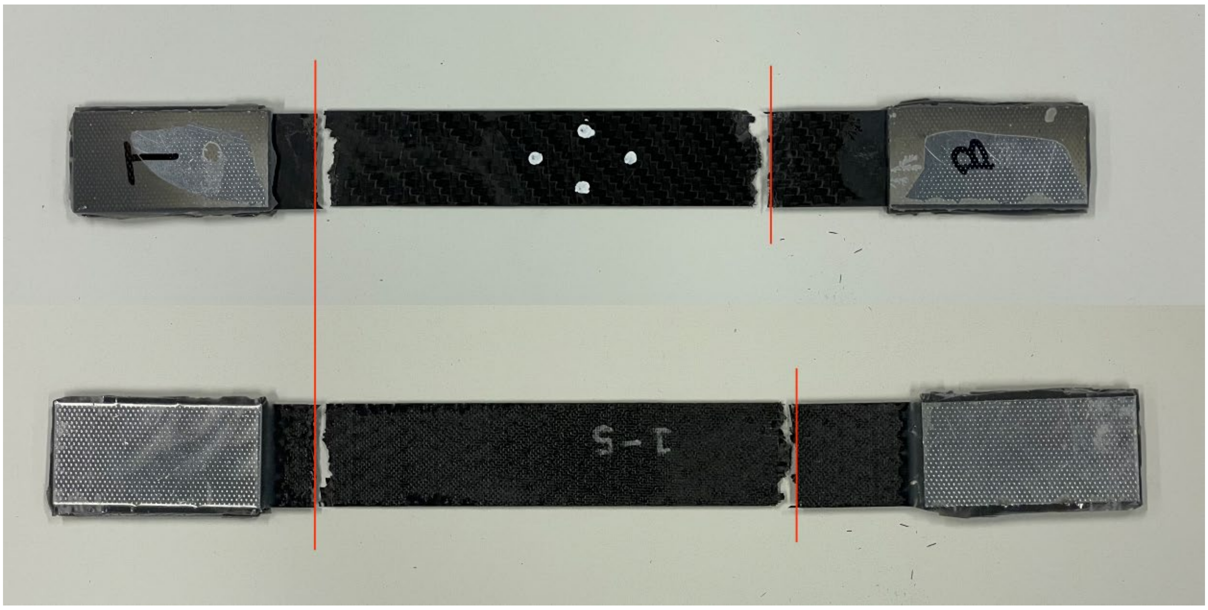

Figure 4.18 Specimen with failure mode – L M V (Lateral type, Multiple areas, Various locations)

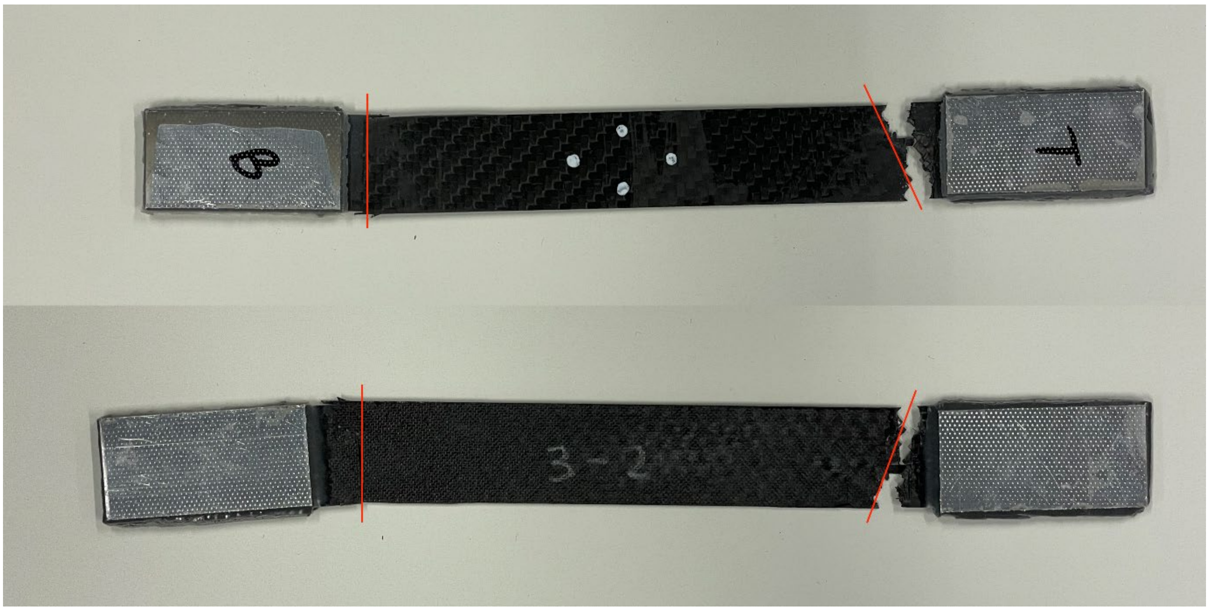

Figure 4.19 Specimen with failure mode - M M V (Multi-mode type: lateral+angled, Multiple areas, Various locations)

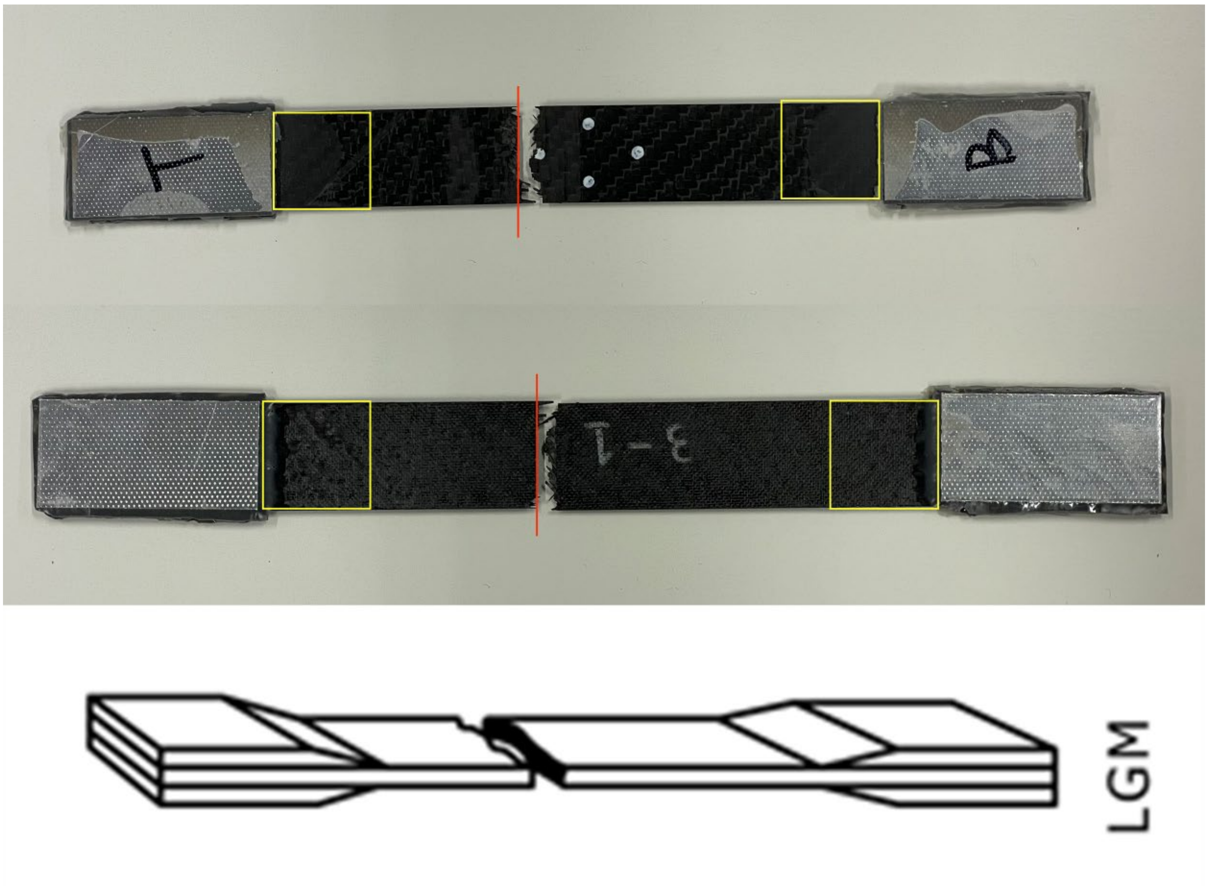

Figure 4.20 Specimen with failure mode - L G M (Lateral type, Gage area, Middle location)

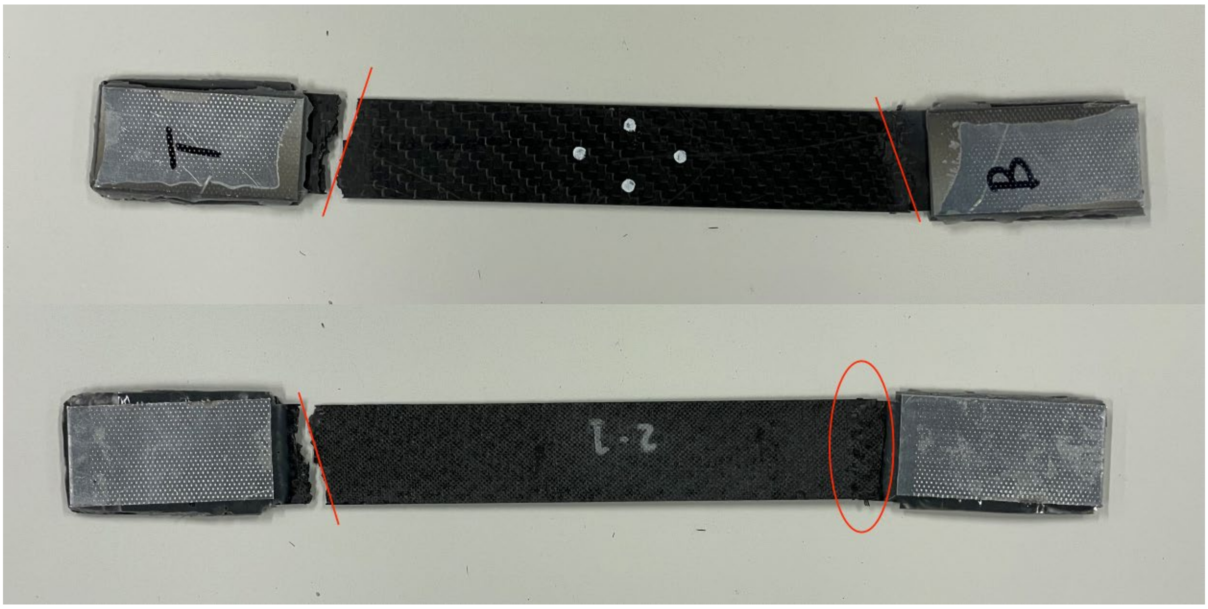

Figure 4.21 Specimen with failure mode - A M V (Angled type, Multiple areas, Various locations)

Figure 4.22, Figure 4.23 and Figure 4.24 shows the failure types, failure areas and failure locations of the eight-ply twill-weaved composites with the WS105/209 resin system respectively. The failure types of specimens from three composite plate are shown in Figure

4.22. For WSTW8P07 composite plate, five specimens are fractured in lateral manner and two specimens are fractured in multi-mode. For WSTW8P08 composite plate, four specimens are fractured in lateral manner and three specimens are fractured in multi-mode. For WSTW8P09 composite plate, all seven specimens are fractured in lateral manner. The failure areas of specimens from three composite plate are shown in Figure 4.23. For WSTW8P07 composite plate, one specimen is fractured within one width from grip/tab, four specimens are fractured in gage area and two specimens are fractured in multiple areas. For WSTW8P08 composite plate, three specimens are fractured in gage areas and four specimens are fractured in multiple areas. For WSTW8P09 composite plate, three specimens are fractured within one width from grip/tab and four specimens are fractured in gage area. The failure locations of specimens from three composite plate are shown in Figure 4.24. For WSTW8P07 composite plate, one specimen is fractured at the bottom, four specimens are fractured in the middle and two specimens are fractured in various locations. For WSTW8P08 composite plate, three specimens are fractured in the middle and four specimens are fractured in various locations. For WSTW8P09 composite plate, two specimens are fractured at the bottom, one specimen is fractured at the top and four specimens are fractured in the middle.

Unlike the failure mode of specimens from four-ply composites, specimens from eight-ply twill-weaved CFRP composites with the WS105/209 resin system do not have many specimens fractured in multiple areas at various locations. This indicated that a thicker specimen can lower the impacts of fracture reaction force and reveal the fracture behavior of the specimens. Although none of the eight-ply composite plates have a consistent failure mode, most of their specimens fractured in lateral manner, gage area and in the middle which is the ideal failure mode that tensile test intended to have.

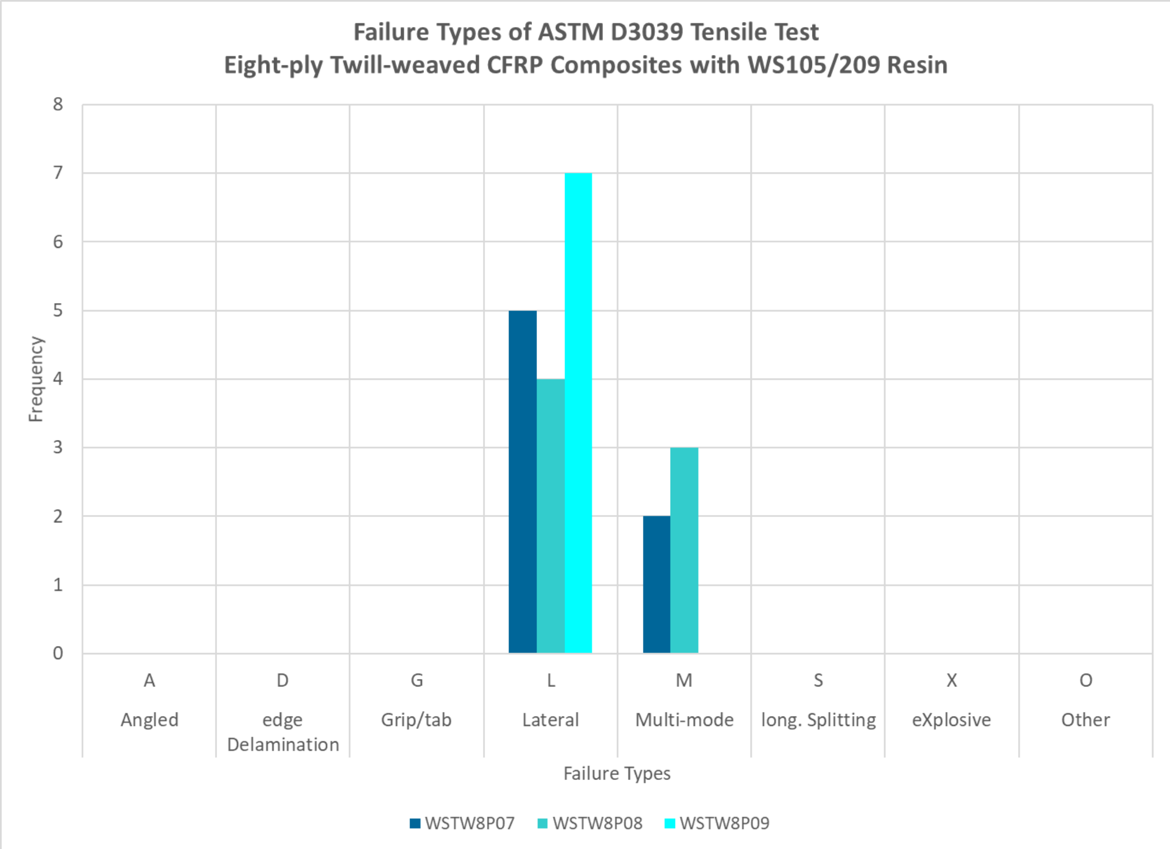

Figure 4.22 ASTM D3039 failure types of eight-ply twill-weaved CFRP composites with WS105/209 resin system

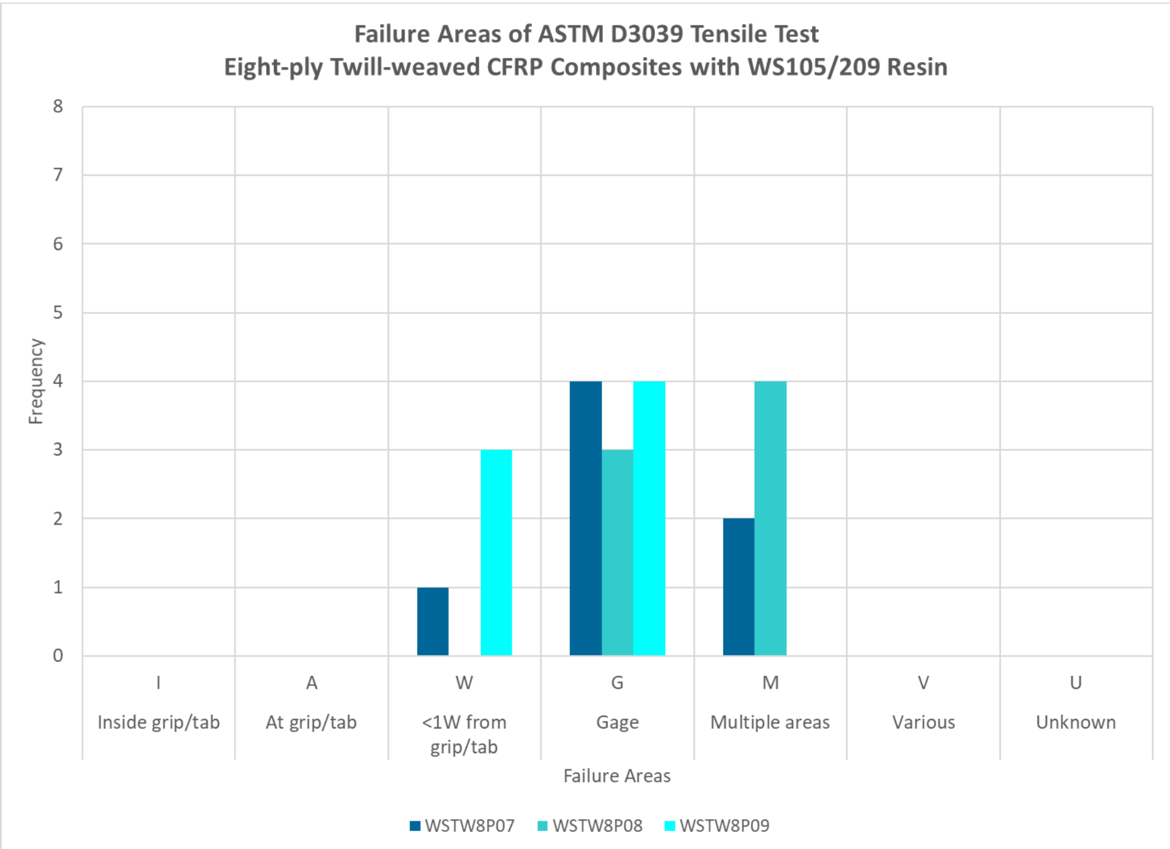

Figure 4.23 ASTM D3039 failure areas of eight-ply twill-weaved CFRP composites with WS105/209 resin system

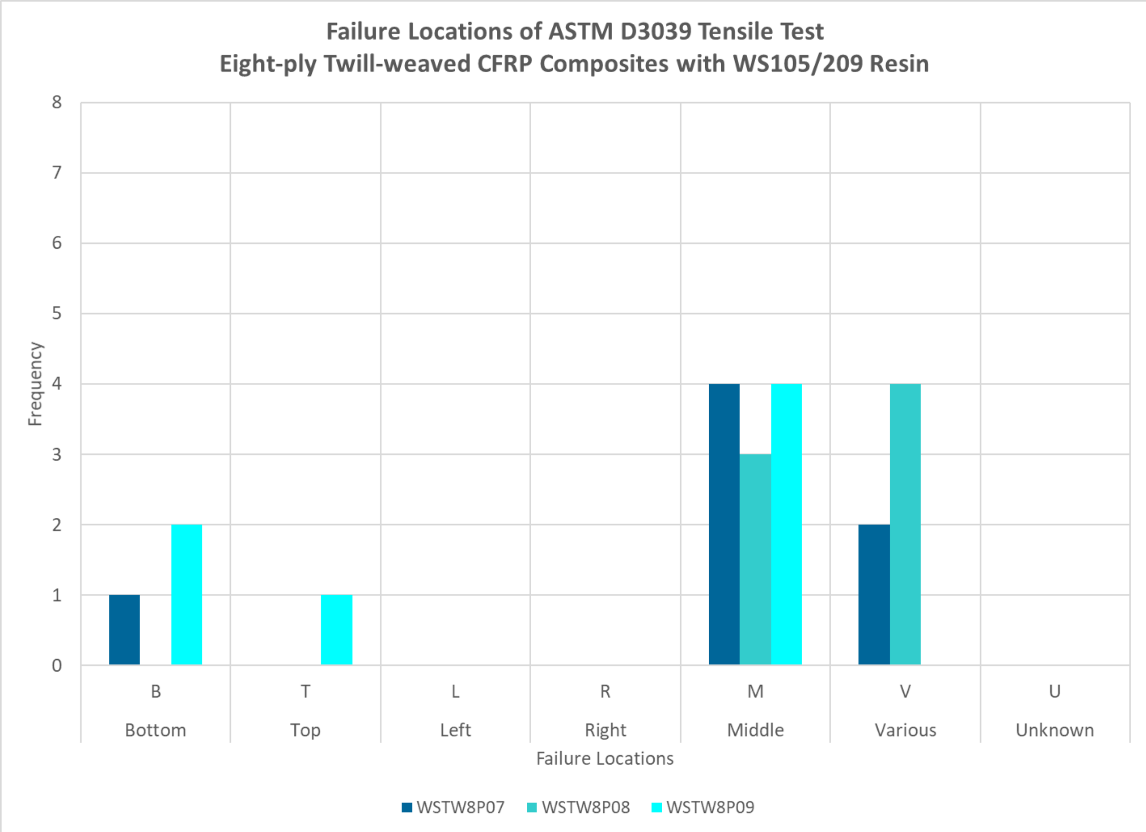

Figure 4.24 ASTM D3039 failure locations of eight-ply twill-weaved CFRP composites with WS105/209 resin system

Specimens for eight-ply twill-weaved CFRP composites with WS105/209 resin system are fractured in five failure mode combinations: L M V, M M V, L G M, L W B (Lateral type, <1 Width from grip/tab area, Bottom location), and L W T (Lateral type, <1 Width from grip/tab area, Top location). For the first three failure modes, example can be found in failure modes of specimens from WSTW4P composite plates. Figure 4.25 shows the fracture take place in one specimen width (yellow squares) from the end tabs at the bottom of the specimen and Figure 4.26 shows the fracture at the top of the specimen.

Figure 4.25 Specimen with failure mode - L W B (Lateral type, <1 Width from grip/tab area, Bottom location)

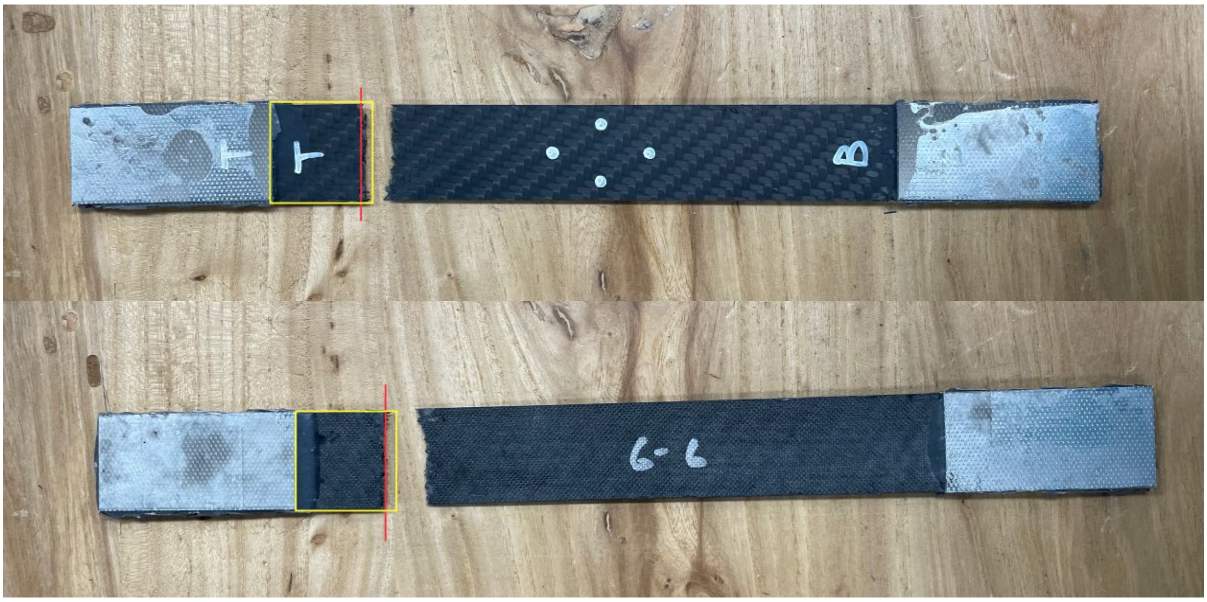

Figure 4.26 Specimen with failure mode - L W T (Lateral type, <1 Width from grip/tab area, Top location)

The failure mode of ASTM D2344 short-beam test provides a quality control on resin and interlaminar properties which indicates the compatibility between the matrix phase and the sizing of the reinforcement phase. Figure 4.27 and Figure 4.28 show the ASTM D2344 failure mode of four-ply and eight-ply twill-weaved CFRP composites with WS105/209 resin system. All specimens from four-ply and eight-ply composites show a flexure tension failure mode, which means the resin is well bonded with the carbon fiber and the stress can be effectively transferred between them.

The results between four-ply and eight-ply twill-weaved CFRP composites with WS105/209 resin system can be concluded as eight-ply configuration gives a better repeatability on data collection and creates a more reliable control group for data comparison. However, since a specific resin system may be favorable to a particular ply configuration, a four-ply and eight-ply twill-weaved CFRP composites comparison is also conducted with ML812A/B resin system.

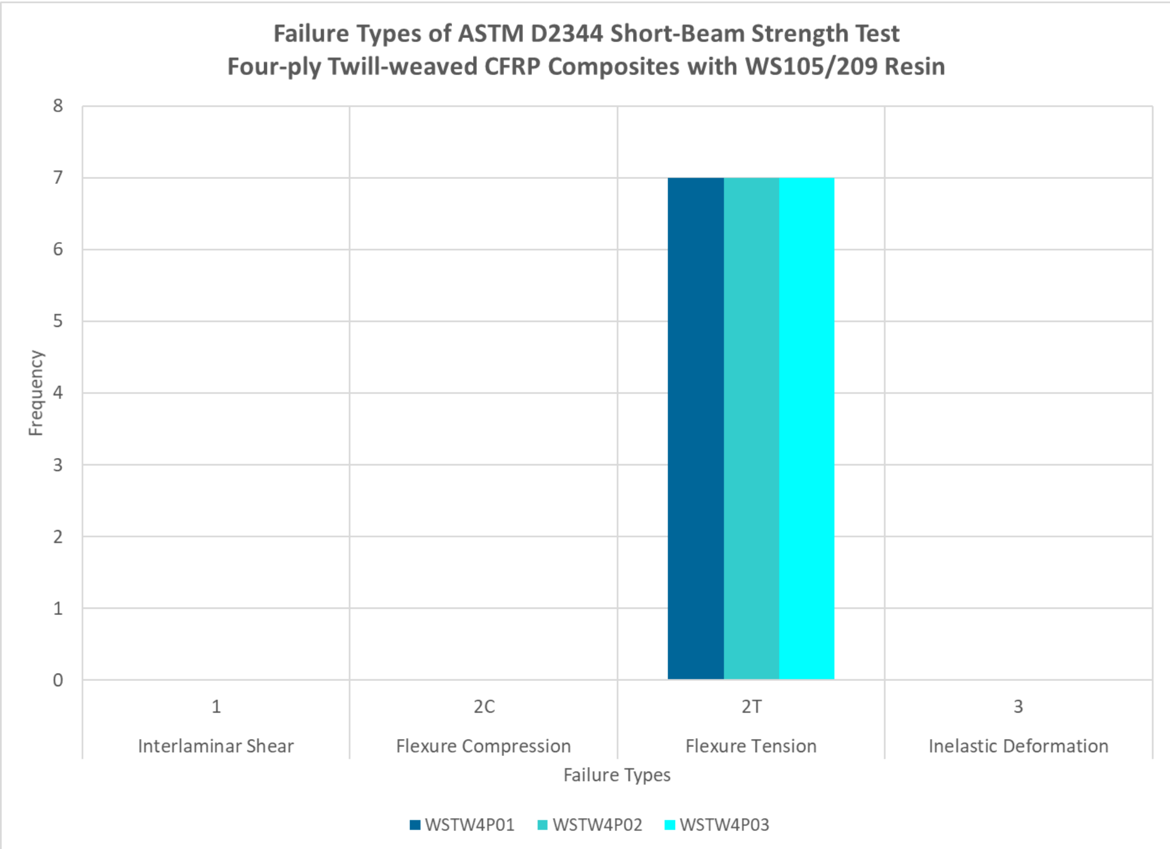

Figure 4.27 ASTM D2344 failure modes of four-ply twill-weaved CFRP composites with WS105/209 resin system

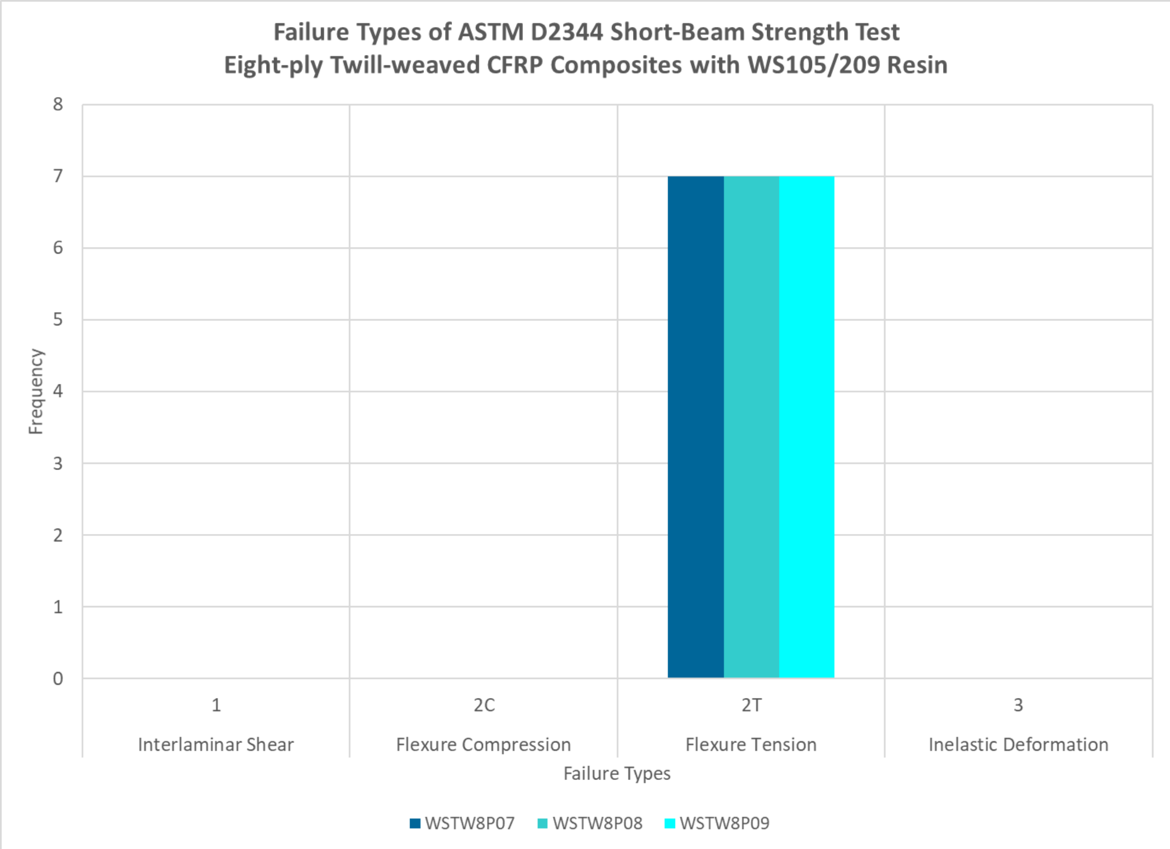

Figure 4.28 ASTM D2344 failure modes of eight-ply twill-weaved CFRP composites with WS105/209 resin system

Figure 4.29, Figure 4.30 and Figure 4.31 present the stress-strain characteristic of the three four-ply twill-weaved CFRP composites plates with ML812A/B resin system. Figure 4.29 presents the stress-strain curves of specimens from the MLTW4P04 composite plate. Most of the curves show a linear trend and they are close to each other, while MLTW4P04-01 specimen is significantly deviated from other curves. The curve of MLTW4P04-04 specimen oscillates at approximately 200 MPa tensile stress. Figure 4.30 presents the stress-strain curves of specimens from the MLTW4P-05 composite plate. Most of the curves are fairly linear and overlapping with each other in the beginning of the curves. All curves show slight deviations from one another beyond 200 MPa tensile stress. Curves of MLTW4P05-04 and MLTW4P05-06 specimens deviate from the other curves at the beginning of tensile loading. Figure 4.31 present the stress-strain curves of specimens from the MLTW4P06 composite plate. Similar to MLTW4P05 composite plate, most of the curves are fairly linear but slightly deviated after 200

MPa. MLTW4P06-05 and MLTW4P06-06 specimens have a non-zero tensile stress at the starting point of the curve and separated from the main trend.

The deviation observed in the stress-strain curve of MLTW4P04-01 specimen is likely caused by the dislocation of carbon fiber laminate. Manufacturing defects may result in interlaminar bond failures, which may lead to elongation without any increase in tensile stress (Karimi, Rahmatabadi, & Baghani, 2024). The deviation in stress-strain curves under high tensile stress observed in MLTW4P05 and MLTW4P06 composite plates suggests the possibility of microscopic deformation or failure that has altered their stress-strain behaviors. A new phenomenon is observed in the MLTW4P06 composite plate, which is a non-zero tensile stress starting. Residue stress induced during the fabrication of the composite plate is likely responsible for the offset of the stress-strain curves from the origin. Residue stress inside the specimen needs to be compensated by the external stress before the specimen start to elongate. Usually, pre-loading is applied to straighten the specimen at the beginning of tensile test, however the residue stress of MLTW4P06-05 and MLTW4P06-06 specimens maybe much larger than the pre-loading, causing the stress-strain curve to start from non-zero tensile stress. The residue stress may be attributed to the uneven curing of the matrix phase or entanglement of the reinforcement phase. Although the composite plates evaluated in this research study were fabricated according to a set of standard fabrication procedures which aims to eliminate any errors or bias, occurrence of unanticipated conditions, which could not be controlled during the fabrication process, are still possible. The stress-strain behavior of four-ply twill-weaved CFRP composites plates with ML812A/B resin system are fairly consistent with a few outliers.

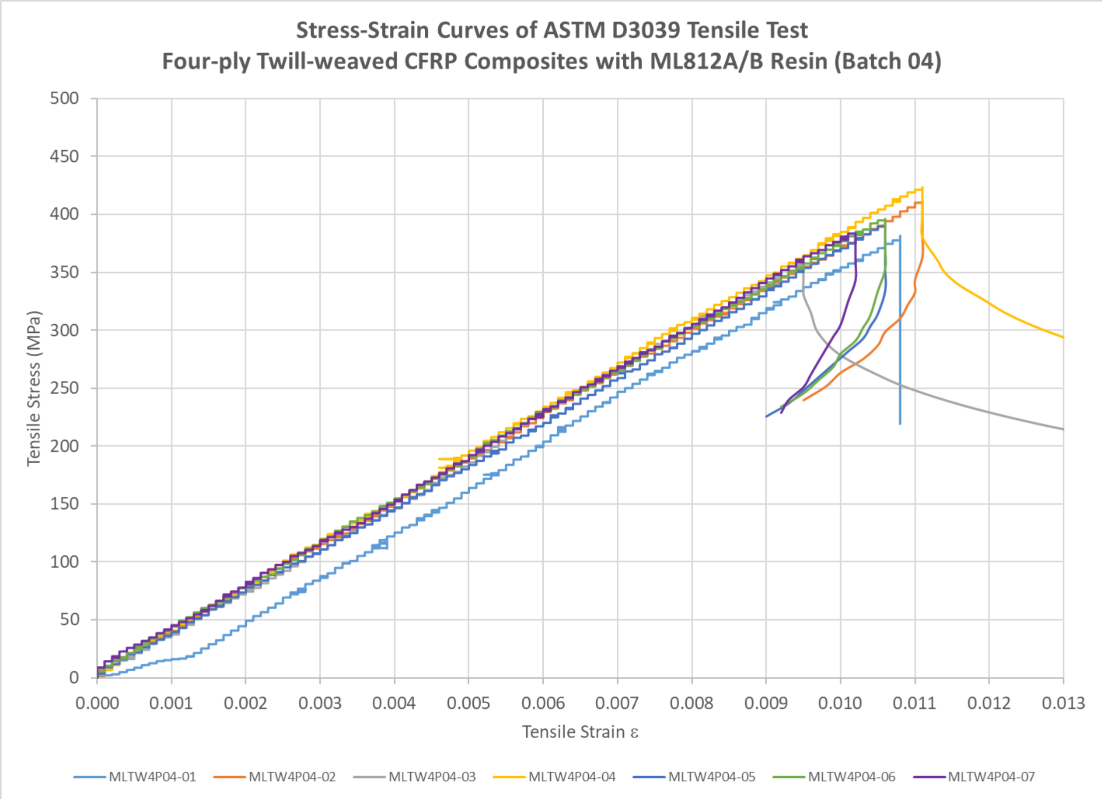

Figure 4.29 Stress-strain curve of four-ply twill-weaved CFRP composites with ML812A/B resin system (Batch 04)

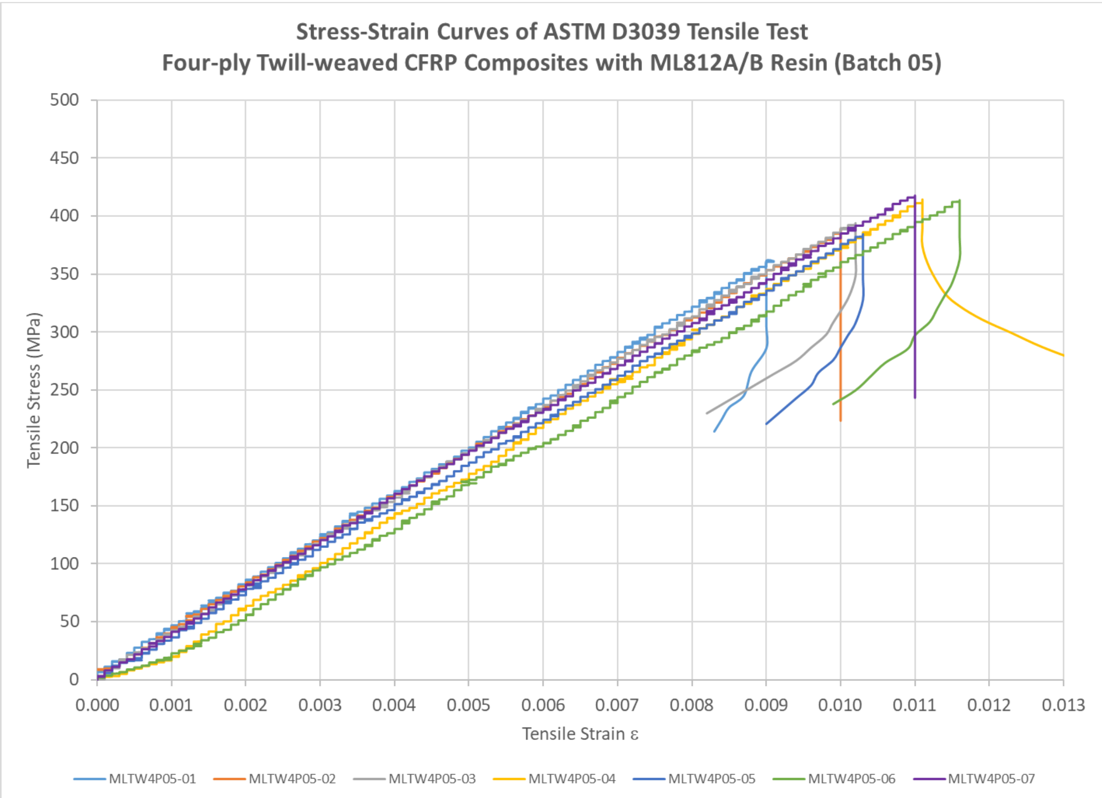

Figure 4.30 Stress-strain curve of four-ply twill-weaved CFRP composites with ML812A/B resin system (Batch 05)

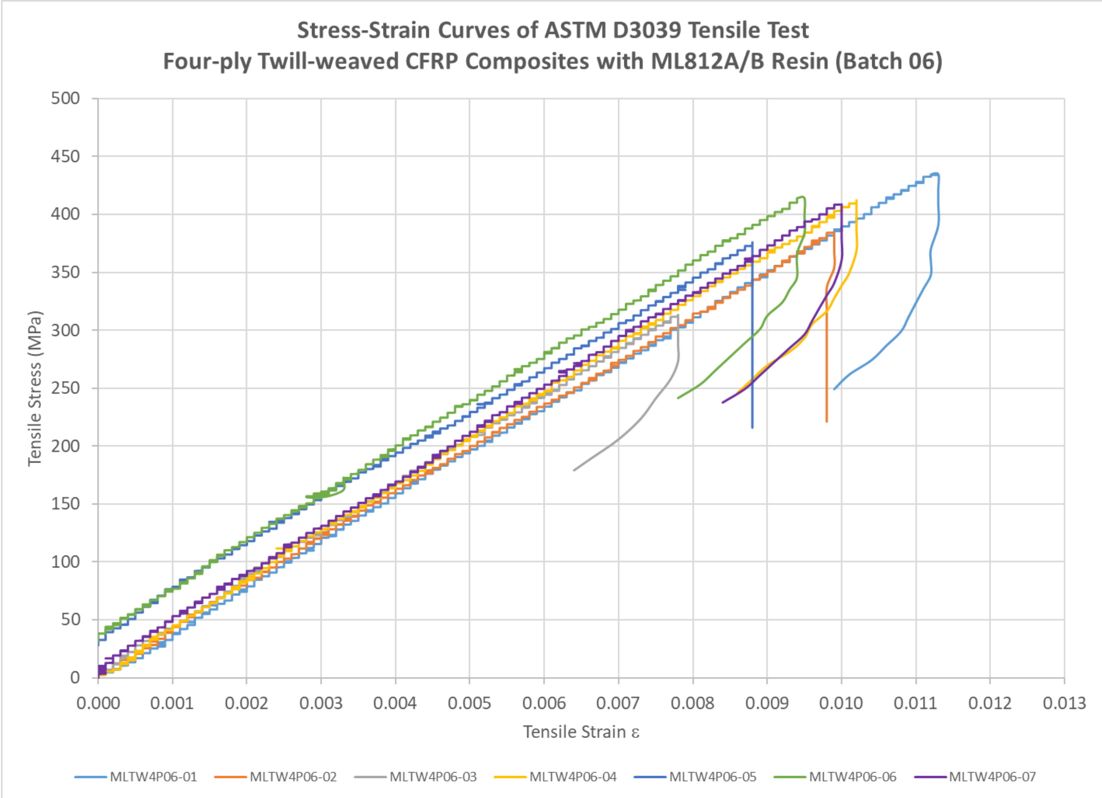

Figure 4.31 Stress-strain curve of four-ply twill-weaved CFRP composites with ML812A/B resin system (Batch 06)

Figure 4.32, Figure 4.33 and Figure 4.34 present the stress-strain characteristic of the three eight-ply twill-weaved CFRP composite plates with ML812A/B resin system. Figure 4.32 illustrates the stress-strain curves of specimens from the MLTW8P10 composite plate. All the curves are not linear and mostly deviated from each other. Oscillation and inconsistency of slope are found in every curves. Figure 4.33 illustrates the stress-strain curves of specimens from the MLTW8P11 composite plate. All the curves are not linear but the curves are not as deviated as the stress-strain curves of specimens from the MLTW8P10 composite plate. Only MLTW8P11-01 specimen is greatly deviated from other curves. Oscillations are found in most of the curves at the first half of the graph and large fluctuation is found in MLTW8P11-03 and MLTW8P11-07 specimens. Figure 4.34 illustrates the stress-strain curves of specimens from the MLTW8P12 composite plate. All the curves are not linear and have an inconsistent slope but they overlap more compare with the stress-strain curves of specimens from the MLTW8P10 and MLTW8P11 composite plates.

All the stress-strain curves of eight-ply composite plates show relatively inconsistency and fluctuation compared to those of four-ply composite plates. The stress-strain curves of eight-ply composite plates have comparable stress-strain behavior to the WSTW4P01 composite plate. In normal case, composite experiences elastic deformation between the strain range of 0.001 to 0.003 and the stress-strain curve should be straight and linear within this strain range, however, most of the curves of the eight-ply composites have oscillation between the range. Particularly, the stress-strain curve of MLTW8P12-06 specimen has possible local failure occurring in certain laminae when tensile strain is around 0.001 and 0.003. Some of the specimens from MLTW8P12 composite plate have stress-strain curves starting from non-zero tensile stress.

Overall, the stress-strain curves of specimens from eight-ply twill-weaved CFRP composites with ML812A/B resin system demonstrate an inconsistent stress-strain behavior when compared to those from four-ply composite plates. However, the specimens from four-ply composite plates also have outlier which makes ML812A/B resin system questionable for producing a composite with consistent stress-strain behavior across the whole plate.

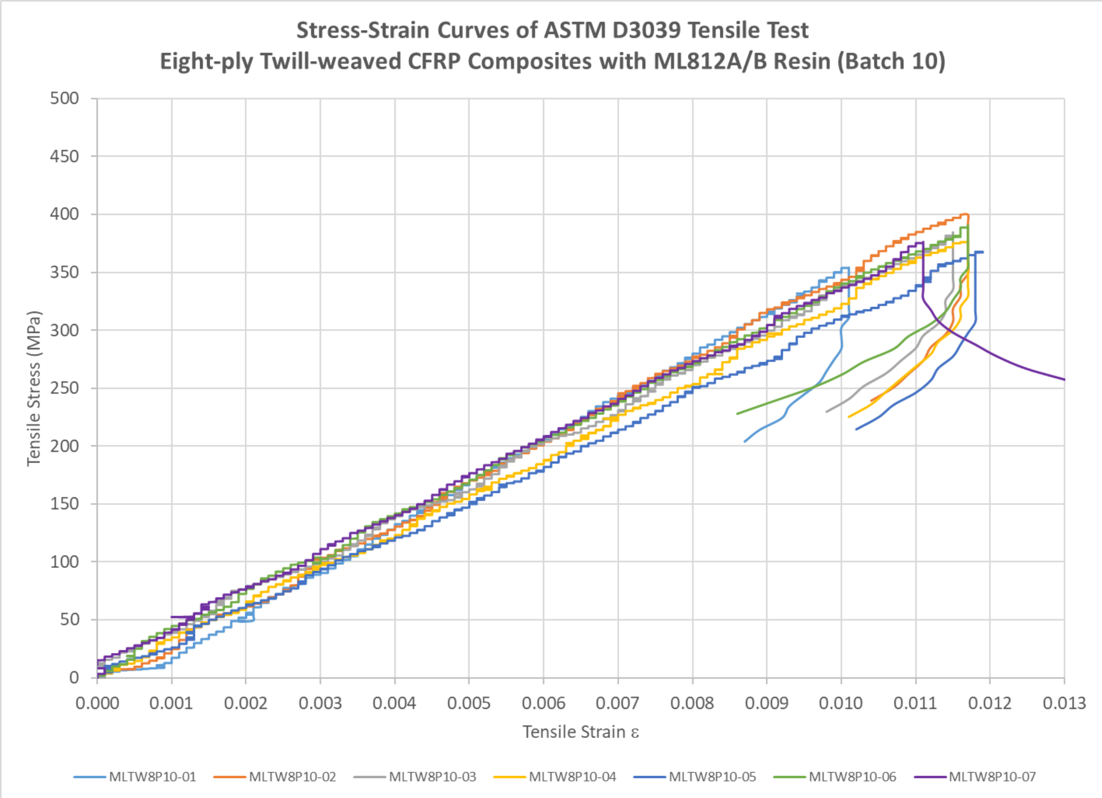

Figure 4.32 Stress-strain curve of eight-ply twill-weaved CFRP composites with ML812A/B resin system (Batch 10)

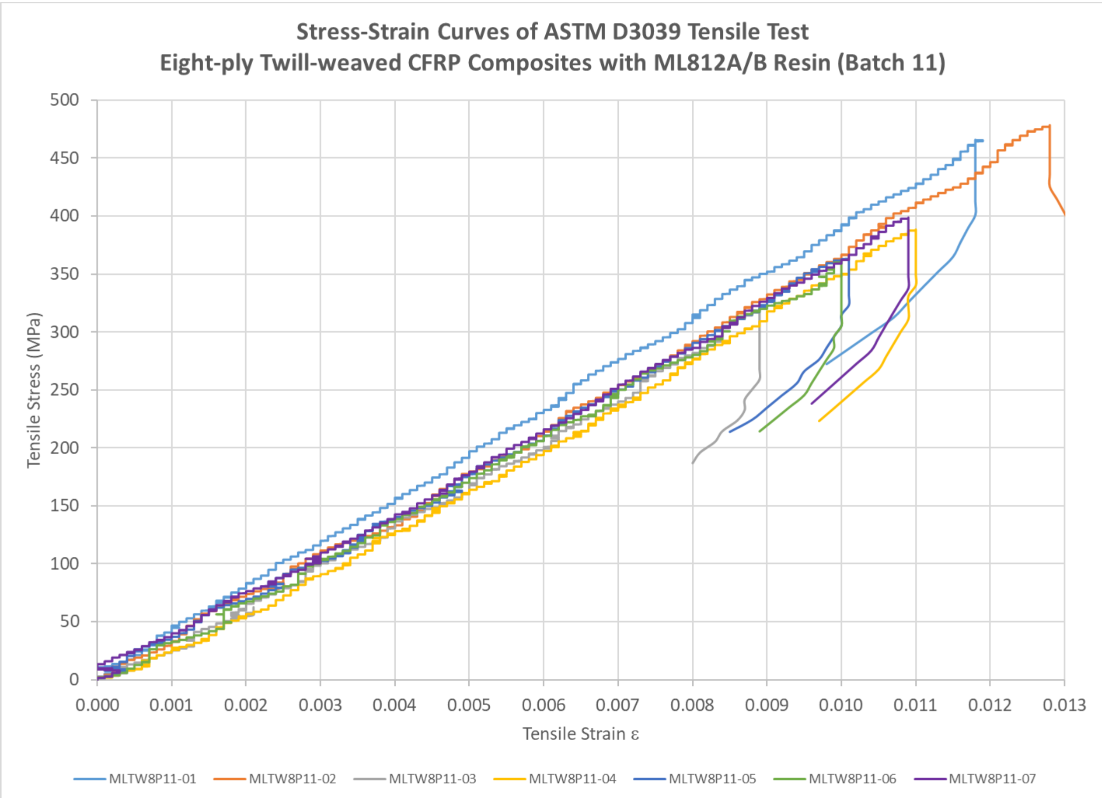

Figure 4.33 Stress-strain curve of eight-ply twill-weaved CFRP composites with ML812A/B resin system (Batch 11)

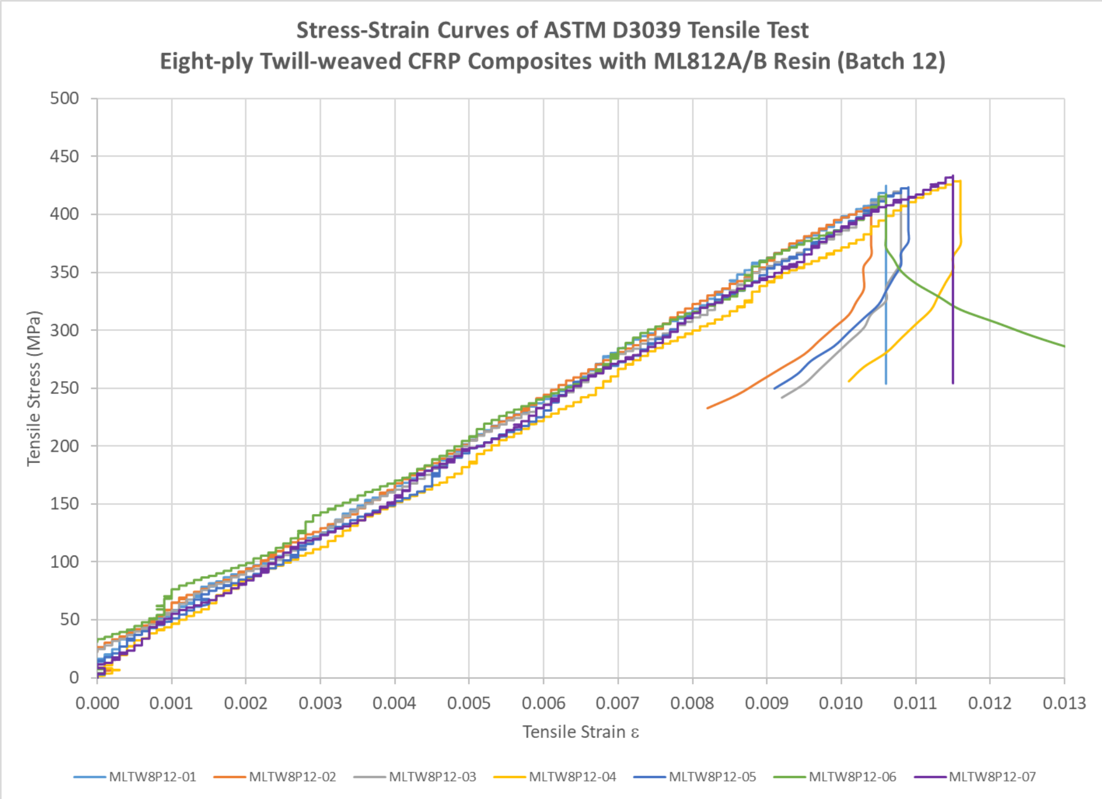

Figure 4.34 Stress-strain curve of eight-ply twill-weaved CFRP composites with ML812A/B resin system (Batch 12)

Further looking into the ultimate properties, Table 4.8 presents comparisons of ultimate tensile stress between four-ply and eight-ply twill-weaved CFRP composites with ML812A/B resin system. The overall mean ultimate tensile stress of four-ply composite specimens is 393 MPa, while eight-ply composite specimens is 399 MPa. The ultimate tensile stresses of four-ply composite specimens have an overall standard deviation of 27.2 MPa and an overall coefficient of variation of 6.91 %. The ultimate tensile stresses of eight-ply composite specimens have an overall standard deviation of 37.5 MPa and an overall coefficient of variation of 9.38 %. Therefore, eight-ply composite specimens have an 1.53 % increase in the overall mean ultimate tensile stress than four-ply composite specimens, with an 2.47 % increase in the overall coefficient of variation.

Table 4.9 presents comparisons of ultimate tensile strain between four-ply and eight-ply twill-weaved CFRP composites with ML812A/B resin system. The overall mean ultimate tensile strain of four-ply composite specimens is 0.0102, while eight-ply composite specimens is 0.0110. The ultimate tensile strains of four-ply composite specimens have an overall standard deviation of 0.0009 and an overall coefficient of variation of 9.08 %. The ultimate tensile strains of eight-ply composite specimens have an overall standard deviation of 0.0009 and an overall coefficient of variation of 7.76 %. Therefore, eight-ply composite specimens have an 7.84 % increase in the overall mean ultimate tensile strain than four-ply composite specimens, with a 1.32 % decrease in the overall coefficient of variation.

Both four-ply and eight-ply composite plates show inconsistent ultimate properties, with significant differences in standard deviation and coefficient of variation. Some of the composite plates have exceptionally high coefficients of variation which are few times large than those of other composite plates with the same fabrication condition. This indicates that the quality of composite plates is inconsistent even if the fabrication condition remains constant. After further averaging the data from composite plates with the same fabrication condition, distant statistics are noticed between ultimate tensile stress and ultimate tensile strain. Four-ply composite plates have higher consistency in ultimate tensile stress, while eight-ply composite plates have higher consistency in ultimate tensile strain.

Table 4.8 Comparison of ultimate tensile stress between four-ply and eight-ply twill-weaved CFRP composites with ML812A/B resin system

Ultimate Tensile Stress						
	per composite plate			per fabrication condition		
	Mean (MPa)	SD (MPa)	CV	Mean (MPa)	SD (MPa)	CV
MLTW4P04	392	21.2	5.40	393	27.2	6.91
MLTW4P05	396	20.5	5.17			
MLTW4P06	392	39.8	10.1			
MLTW8P10	379	15.0	3.96	399	37.5	9.38
MLTW8P11	397	57.2	14.4			
MLTW8P12	422	9.05	2.14			

Table 4.9 Comparison of ultimate tensile strain between four-ply and eight-ply twill-weaved CFRP composites with ML812A/B resin system

Ultimate Tensile Strain						
	per composite plate			per fabrication condition		
	Mean	SD	CV	Mean	SD	CV
MLTW4P04	0.0106	0.0006	5.33	0.0102	0.0009	9.08
MLTW4P05	0.0105	0.0009	8.22			
MLTW4P06	0.0096	0.0011	11.5			
MLTW8P10	0.0114	0.0006	5.34	0.0110	0.0009	7.76
MLTW8P11	0.0108	0.0013	11.8			
MLTW8P12	0.0109	0.0005	4.25			

The ultimate properties of four-ply and eight-ply twill-weaved CFRP composites with ML812A/B resin system are visually presented in Figure 4.35 and Figure 4.36 respectively. Both four-ply and eight-ply composite plates have a wide spectrum of failure points, and the failure points are even more scattered than that of the four-ply twill-weaved CFRP composite plates with WS105/209 resin system. Therefore, in terms of stress-strain curves and ultimate properties, composite plates with ML812A/B resin system have a lower consistency of tensile properties when compared to composite plates with WS105/209 resin system and give no preference to the ply configuration.

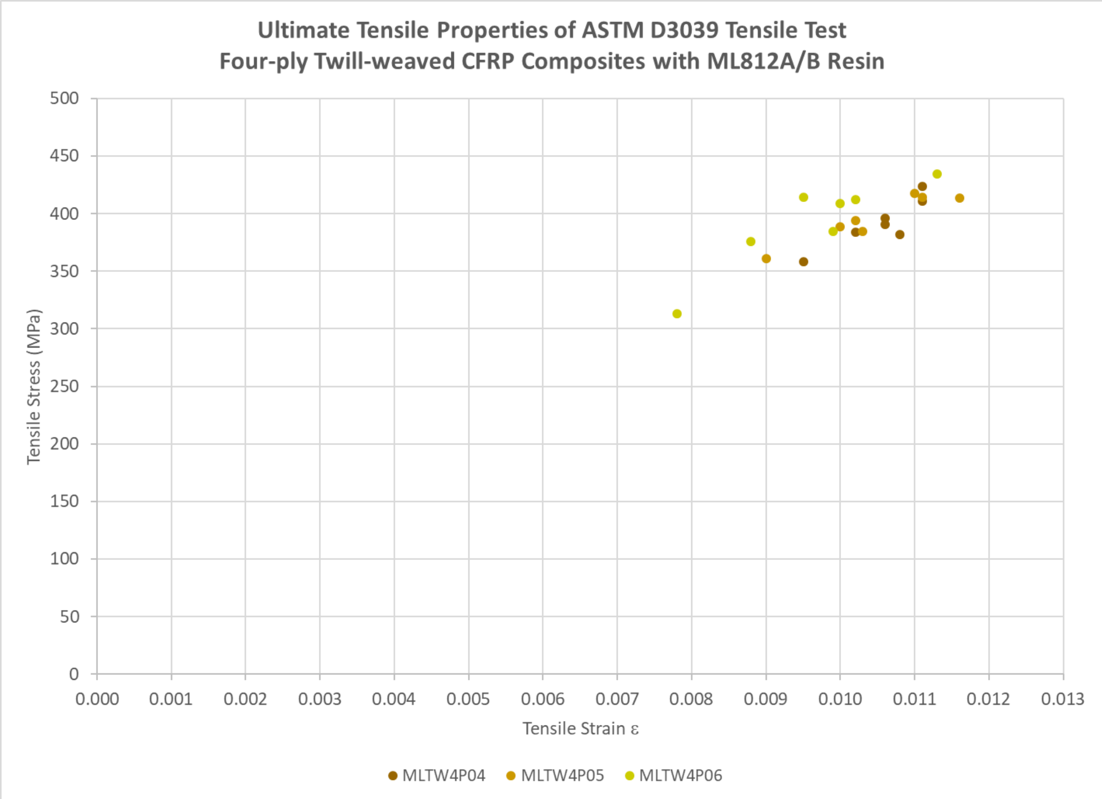

Figure 4.35 Ultimate tensile properties of four-ply twill-weaved CFRP composites with ML812A/B resin system

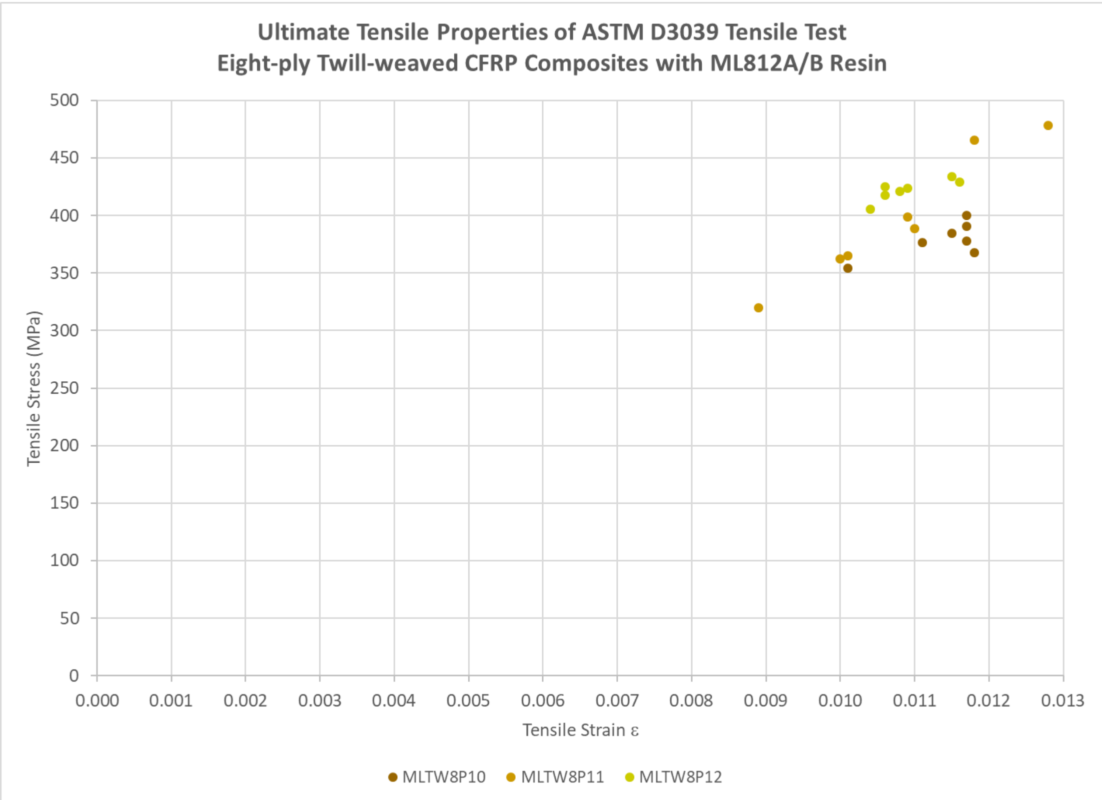

Figure 4.36 Ultimate tensile properties of eight-ply twill-weaved CFRP composites with ML812A/B resin system

Linear regression analysis was conducted on 18 random sets of ultimate tensile stress and ultimate tensile strain data from 21 specimens of both four-ply and eight-ply twill-weaved CFRP composites with ML812A/B resin system. Tensile stress and tensile strain are continuous variables with a linear relationship as shown in Figure 4.29 to Figure 4.34. The ultimate tensile data used in linear regression also shows no obvious outliers in Figure 4.35 and Figure 4.36.

For four-ply twill-weaved specimens with ML812A/B resin system, the significance value of one-way ANOVA is below 0.001. Figure 4.37 and Figure 4.38 show the normal probability-probability plot and scatterplot respectively. The residuals of the data follow a normal distribution and the variance is consistent. However, the Durbin-Watson value is 1.318 indicating a slight negative autocorrelation between data errors. Figure 4.39 presents the statistical result of a linear regression model with the following equation to demonstrate the relationship between tensile stress and tensile strain.

$$ultimate\ tensile\ stress = 147.971 + (23{,}928.525 \times ultimate\ tensile\ strain)$$

Equation 4.3 Linear regression model for ultimate tensile properties of four-ply twill-weaved specimens with ML812A/B resin system

The R-squared value of the linear regression model is 0.686, indicating that 68.6% of the variation in tensile stress is related to tensile strain. This model is then used to predict the ultimate tensile stress of the remaining three specimens. The predicted ultimate tensile stresses are compared with the measured ultimate tensile stresses of the three specimens to validate the linear regression model. Table 4.10 shows the comparison between the predicted and measured ultimate tensile stresses of the three specimens. The predicted ultimate tensile stresses deviate from the measured values by approximately 5%.

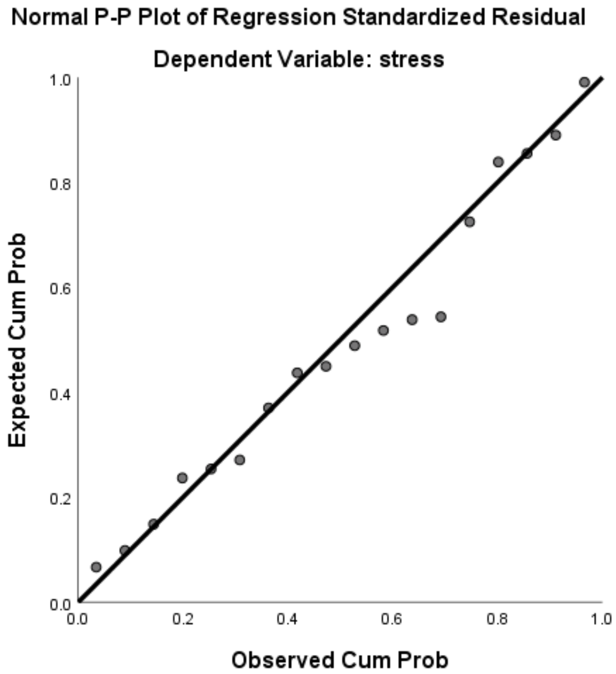

Figure 4.37 Normal probability-probability plot of regression standardized residuals of four-ply twill-weaved specimens with ML812A/B resin system

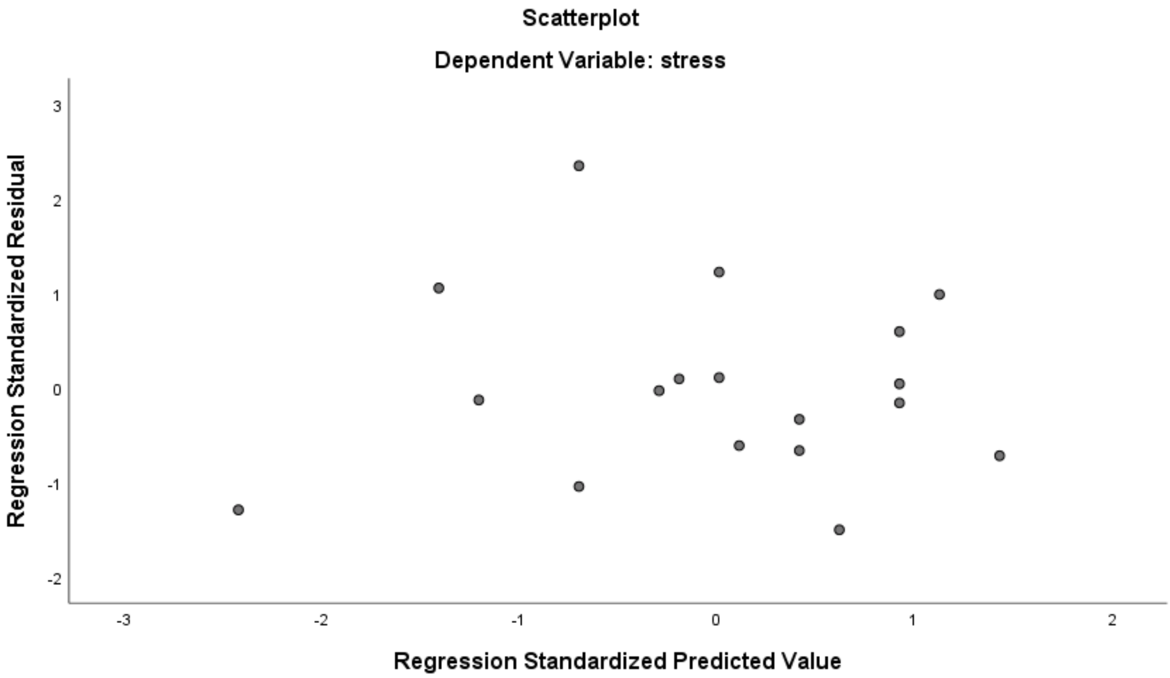

Figure 4.38 Scatterplot of regression standardized residuals against regression standardized predicted values of four-ply twill-weaved specimens with ML812A/B resin system

Model Summary[b]

Model	R	R Square	Adjusted R Square	Std. Error of the Estimate	Durbin-Watson
1	.828[a]	.686	.666	16.4691590	1.318

a. Predictors: (Constant), long_strain

b. Dependent Variable: stress

ANOVA[a]

Model		Sum of Squares	df	Mean Square	F	Sig.
1	Regression	9480.558	1	9480.558	34.954	.000[b]
	Residual	4339.731	16	271.233		
	Total	13820.289	17			

a. Dependent Variable: stress

b. Predictors: (Constant), long_strain

Coefficients[a]

Model		Unstandardized Coefficients		Standardized Coefficients	t	Sig.
		B	Std. Error	Beta		
1	(Constant)	147.971	41.420		3.572	.003
	long_strain	23928.525	4047.347	.828	5.912	.000

a. Dependent Variable: stress

Figure 4.39 Linear regression model results of four-ply twill-weaved specimens with ML812A/B resin system

Table 4.10 Comparison between predicted and actual ultimate tensile stress of four-ply twill-weaved specimens with ML812A/B resin system

Specimens	Actual ultimate tensile strain	Predicted ultimate tensile stress	Actual ultimate tensile stress	Deviation
MLTW4P04-07	0.0102	392.0420	383.8022	2.15%
MLTW4P05-07	0.0110	411.1848	417.6977	-1.56%
MLTW4P06-07	0.0100	387.2563	408.7100	-5.25%

For eight-ply twill-weaved specimens with WS105/209 resin system, the significance value of one-way ANOVA is 0.003. Figure 4.40 and Figure 4.41 show the normal probability-probability plot and scatterplot respectively. The residuals of the data follow a normal distribution and the variance is consistent. However, the Durbin-Watson value is 0.786 indicating a negative autocorrelation between data errors. Figure 4.42 presents the statistical result of a linear regression model with the following equation to demonstrate the relationship between tensile stress and tensile strain.

$$ultimate\ tensile\ stress = 86.244 + (28{,}399.877 \times ultimate\ tensile\ strain)$$

Equation 4.4 Linear regression model for ultimate tensile properties of eight-ply twill-weaved specimens with ML812A/B resin system

The R-squared value of the linear regression model is 0.439, indicating that 43.9% of the variation in tensile stress is related to tensile strain. This model is then used to predict the ultimate tensile stress of the remaining three specimens. The predicted ultimate tensile stresses are compared with the measured ultimate tensile stresses of the three specimens to validate the linear regression model. Table 4.11 shows the comparison between the predicted and measured ultimate tensile stresses of the three specimens. The predicted ultimate tensile stresses deviate from the measured values by approximately 6%.

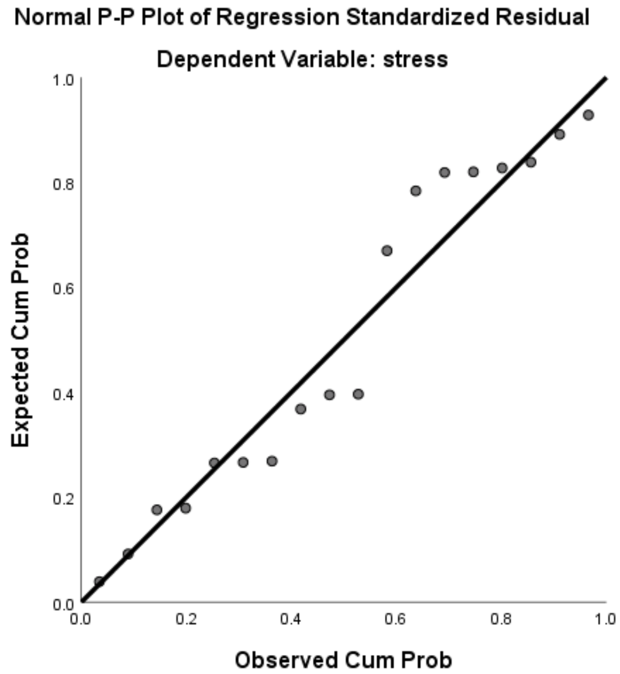

Figure 4.40 Normal probability-probability plot of regression standardized residuals of eight-ply twill-weaved specimens with ML812A/B resin system

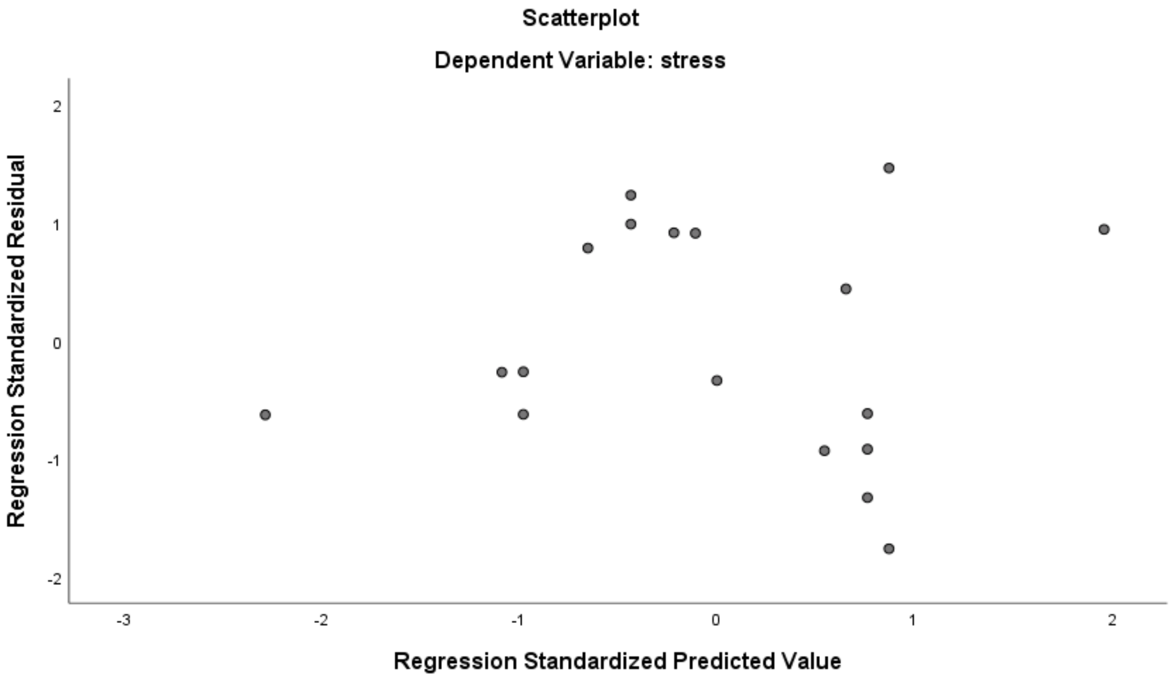

Figure 4.41 Scatterplot of regression standardized residuals against regression standardized predicted values of eight-ply twill-weaved specimens with ML812A/B resin system

Model Summary[b]

Model	R	R Square	Adjusted R Square	Std. Error of the Estimate	Durbin-Watson
1	.663[a]	.439	.404	30.3869508	.786

a. Predictors: (Constant), long_strain

b. Dependent Variable: stress

ANOVA[a]

Model		Sum of Squares	df	Mean Square	F	Sig.
1	Regression	11582.102	1	11582.102	12.543	.003[b]
	Residual	14773.868	16	923.367		
	Total	26355.970	17			

a. Dependent Variable: stress

b. Predictors: (Constant), long_strain

Coefficients[a]

Model		Unstandardized Coefficients		Standardized Coefficients	t	Sig.
		B	Std. Error	Beta		
1	(Constant)	86.244	88.497		.975	.344
	long_strain	28399.877	8018.810	.663	3.542	.003

a. Dependent Variable: stress

Figure 4.42 Linear regression model results of eight-ply twill-weaved specimens with ML812A/B resin system

Table 4.11 Comparison between predicted and actual ultimate tensile stress of eight-ply twill-weaved specimens with ML812A/B resin system

Specimens	Actual ultimate tensile strain	Predicted ultimate tensile stress	Actual ultimate tensile stress	Deviation
MLTW8P10-07	0.0111	401.4826	376.3104	6.69%
MLTW8P11-07	0.0109	395.8027	398.7436	-0.74%
MLTW8P12-07	0.0115	412.8426	433.5883	-4.78%

By comparing Equation 4.3 and Equation 4.4, the differences in ultimate tensile stress behavior between four-ply and eight-ply twill-weaved specimens with the ML812A/B resin system can be identified. The ultimate tensile stress of eight-ply specimens is closely related with the ultimate tensile strain whereas that of four-ply specimens has a slightly larger base value with a smaller influence from ultimate tensile strain. Further comparison of linear regression models to specimens with the WS105/209 resin system shows that eight-ply specimens achieve a higher ultimate tensile stress with the same ultimate tensile strain compared to four-ply specimens in both resin systems.

Table 4.12 further compares the modulus of elasticity between four-ply and eight-ply twill-weaved CFRP composites with ML812A/B resin system. The overall mean modulus of elasticity of four-ply composite specimens is 38.7 GPa, while eight-ply composite specimens is 34.4 GPa. The modulus of elasticity of four-ply composite specimens have an overall standard deviation of 2.10 GPa and an overall coefficient of variation of 5.43 %. The modulus of elasticity of eight-ply composite specimens have an overall standard deviation of 2.64 GPa and an overall coefficient of variation of 7.65 %. Therefore, eight-ply composite specimens have a 11.1 % decrease in the overall mean modulus of elasticity than four-ply composite specimens, with an 2.22 % increase in the overall coefficient of variation. Four-ply composite plates show relatively constant coefficients of variation across the three plates, whereas the coefficients of variation of eight-ply composite plates vary from 3.4 to 10.5, having a threefold difference. When comparing the modulus of elasticity per fabrication condition, four-ply fabrication condition shows a more consistent result than eight-ply with a lower coefficient of variation.

Table 4.12 Comparison of modulus of elasticity between four-ply and eight-ply twill-weaved CFRP composites with ML812A/B resin system

Modulus of Elasticity						
	per composite plate			per fabrication condition		
	Mean (GPa)	SD (GPa)	CV	Mean (GPa)	SD (GPa)	CV
MLTW4P04	36.2	1.09	3.02	38.7	2.10	5.43
MLTW4P05	39.2	0.527	1.35			
MLTW4P06	40.6	1.04	2.55			
MLTW8P10	33.7	3.53	10.5	34.4	2.64	7.65
MLTW8P11	35.4	2.74	7.74			
MLTW8P12	34.2	1.17	3.40			

Table 4.13 shows the comparison of Poisson's ratio between four-ply and eight-ply twill-weaved CFRP composites with ML812A/B resin. The overall mean Poisson's ratio of four-ply composite specimens is 0.359, while eight-ply composite specimens is 0.259. The Poisson's ratio of four-ply composite specimens have an overall standard deviation of 0.0796 and an overall coefficient of variation of 22.2 %. The Poisson's ratio of eight-ply composite specimens have an overall standard deviation of 0.132 and an overall coefficient of variation of 51.0 %. Therefore, eight-ply composite specimens have a 27.9 % decrease in the overall mean Poisson's ratio than four-ply composite specimens, with an 28.8 % increase in the overall coefficient of variation. Composite plates with ML812A/B resin system have relatively unstable Poisson ratio with the coefficients of variation ranging from 5.82 to 72.3, which is 12 times difference. Further averaging the data from composite plates with the same fabrication condition, it is noticed that the coefficients of variation of composite plates with ML812A/B resin are much higher when compared to composite plates with WS105/209 resin. The results of Poisson's ratio are fluctuating and cannot be used as base or control sample to compare any changes in fabrication condition.

Table 4.13 Comparison of Poisson's ratio between four-ply and eight-ply twill-weaved CFRP composites with ML812A/B resin system

Poisson's Ratio						
	per composite plate			per fabrication condition		
	Mean	SD	CV	Mean	SD	CV
MLTW4P04	0.306	0.118	38.4	0.359	0.0796	22.2
MLTW4P05	0.367	0.0213	5.82			
MLTW4P06	0.404	0.0333	8.25			
MLTW8P10	0.272	0.114	41.7	0.259	0.132	51.0
MLTW8P11	0.363	0.0743	20.5			
MLTW8P12	0.140	0.101	72.3			

Given the significant discrepancy observed in the data collected, the failure mode of ASTM D3039 tensile test may provide explanations for this phenomenon. Figure 4.43, Figure 4.44 and Figure 4.45 illustrate the failure modes of the four-ply twill-weaved CFRP composites with ML812A/B resin system. The failure types observed in specimens from three composite plate are presented in Figure 4.43. For MLTW4P04 composite plate, two specimens are fractured in lateral manner and five specimens are fractured in multi-mode. Both MLTW4P05 and MLTW4P06 composite plates have six specimens fractured in lateral manner and one specimen fractured in multi-mode. The failure areas observed in specimens from three composite plate are presented in Figure 4.44. For MLTW4P04 composite plate, one specimen is fractured in gage area and six specimens are fractured in multiple areas. For MLTW4P05 composite plate, all seven specimens are fractured in multiple areas. For MLTW4P06 composite plate, one specimen is fractured at grip or tab and six specimens are fractured in multiple areas. The failure locations observed in specimens from three composite plate are presented in Figure 4.45. For MLTW4P04 composite plate, one specimen is fractured at the top and six specimens are fractured in various locations. For MLTW4P05 composite plate, all seven specimens are fractured in various locations. For MLTW4P06 composite plate, one specimen is fractured in the middle and six specimens are fractured in various locations.

The failure modes of specimens from four-ply twill-weaved CFRP composite plates with ML812A/B resin system have a consistent pattern. Specimens are mainly fractured in multiple areas at various locations which mean the specimen is experiencing there are multiple failure occurrences during the tensile test. Multiple failure on a specimen can be the same or different failure types. All specimens with multi-mode failure type are having a combination of lateral and angled failure type. Therefore, all specimens from MLTW4P composite plates are mainly fractured in lateral manner.

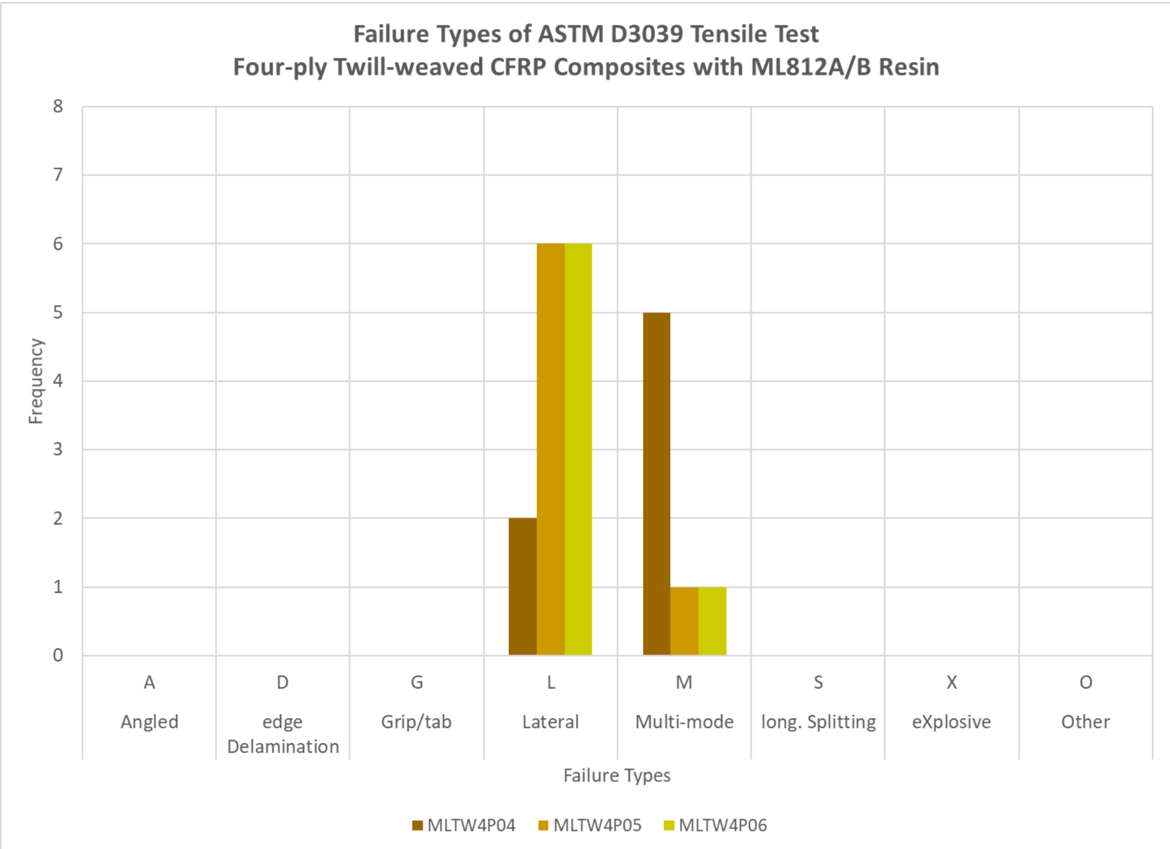

Figure 4.43 ASTM D3039 failure types of four-ply twill-weaved CFRP composites with ML812A/B resin system

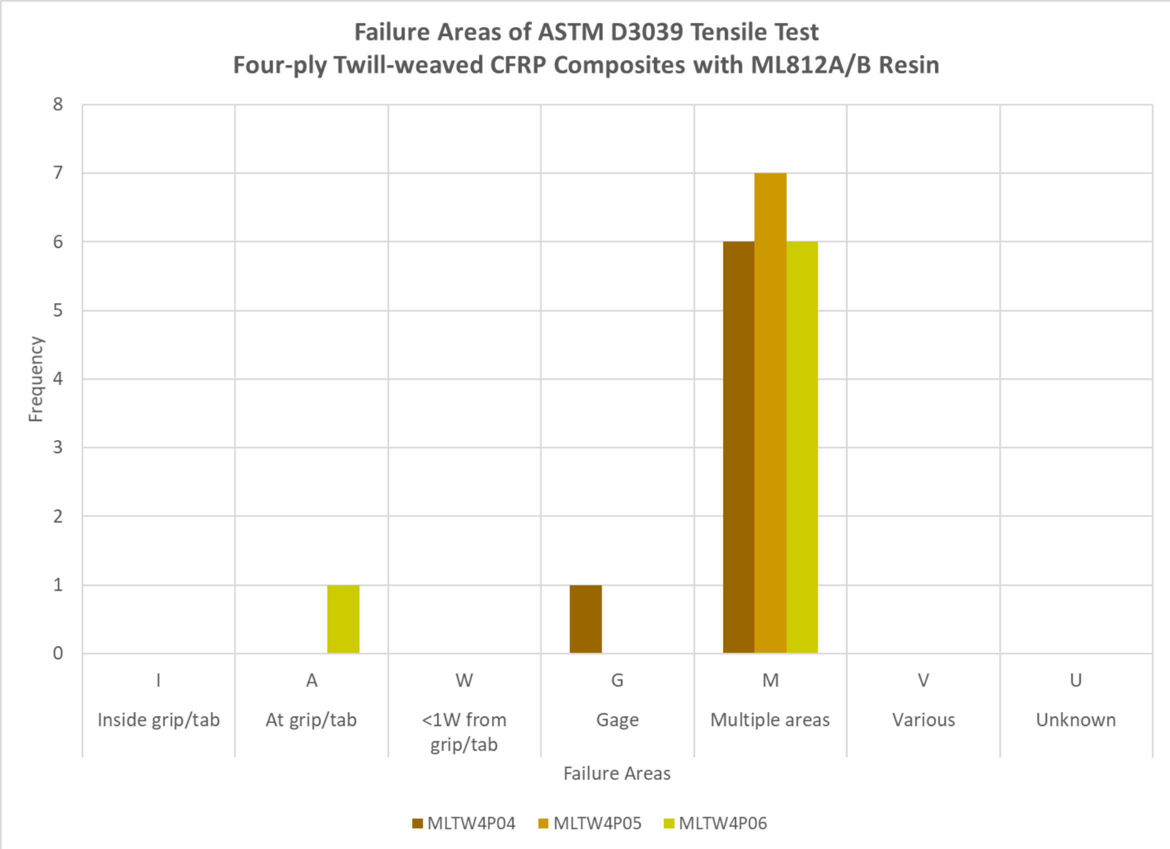

Figure 4.44 ASTM D3039 failure areas of four-ply twill-weaved CFRP composites with ML812A/B resin system

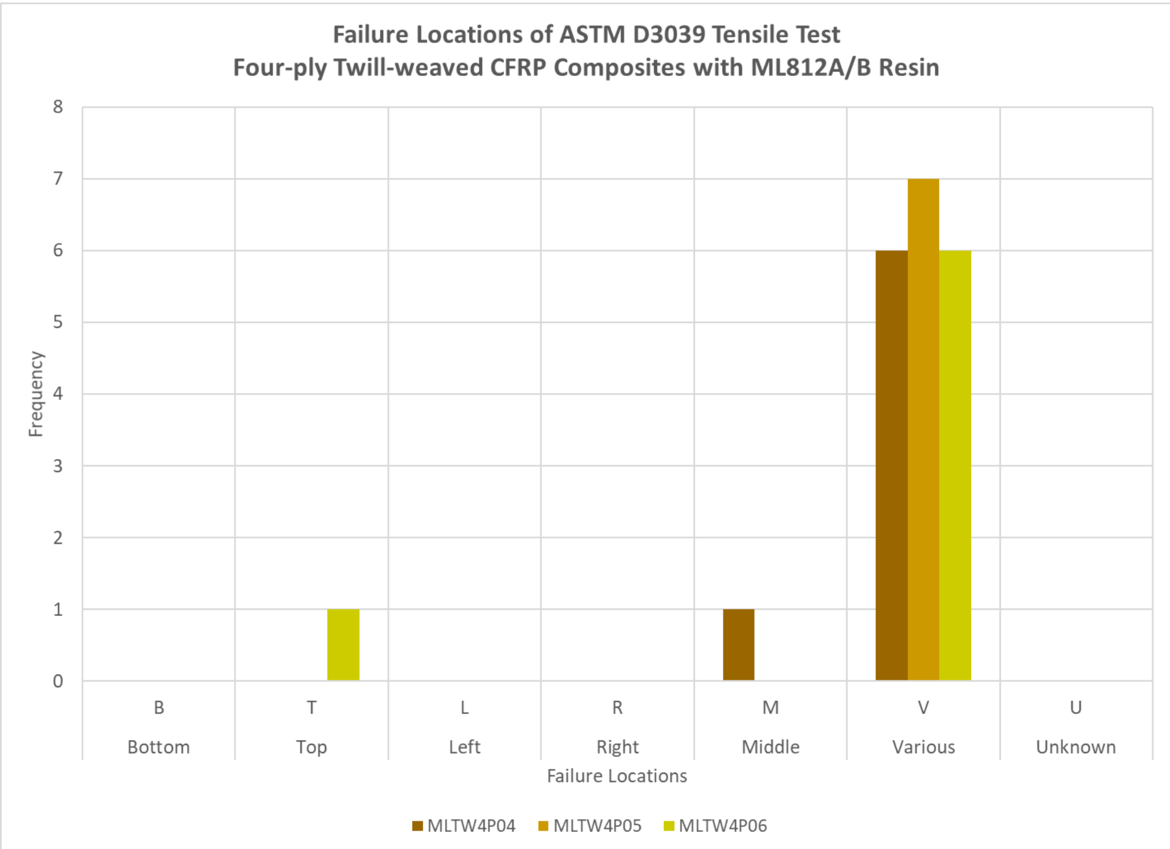

Figure 4.45 ASTM D3039 failure locations of four-ply twill-weaved CFRP composites with ML812A/B resin system

Specimen for four-ply twill-weaved CFRP composites with ML812A/B resin system are fractured in four failure mode combinations: L M V, M M V, L G M, and L A T (Lateral type, At grip/tab area, Top location). For the first three failure modes, example can be found in failure modes of specimens from WSTW4P composite plates. Figure 4.46 shows the fracture take place at the edge of the top end tab and an illustration of failure mode - L A T in ASTM D3039 is shown for reference.

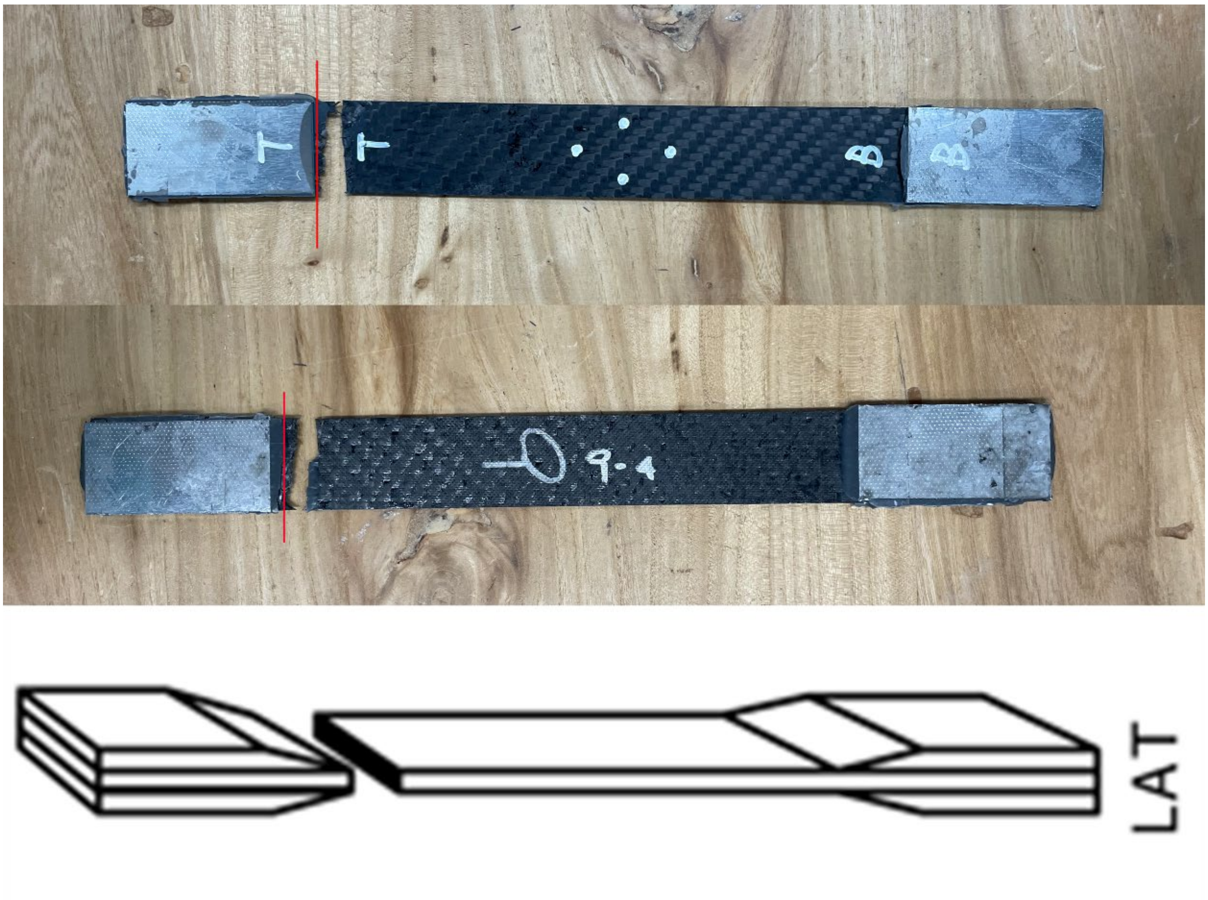

Figure 4.46 Specimen with failure mode - L A T (Lateral type, At grip/tab area, Top location)

Figure 4.47, Figure 4.48 and Figure 4.49 illustrate the failure modes of the eight-ply twill-weaved CFRP composites with ML812A/B resin system. The failure types observed in specimens from three composite plate are presented in Figure 4.47. For MLTW8P10 composite plate, all seven specimens are fractured in lateral manner. For MLTW8P11 composite plate, one specimen is fractured in multi-mode and six specimens are fractured in lateral manner. For

MLTW8P12 composite plate, one specimen is fractured in angled manner, three specimens are fractured in lateral manner and three specimens are fractured in multi-mode. The failure areas observed in specimens from three composite plate are presented in Figure 4.48. For MLTW8P10 composite plate, one specimen is fractured within one width from grip/tab, five specimens are fractured at gage areas and one specimen is fractured in multiple areas. For MLTW8P11 composite plate, two specimens are fractured at grip/tab, three specimens are fractured within one width from grip/tab, one specimen is fractured at gage areas and one specimen is fractured in multiple areas. For MLTW8P12 composite plate, three specimens are fractured at gage areas and four specimens are fractured in multiple areas. The failure locations observed in specimens from three composite plate are presented in Figure 4.49. For MLTW8P10 composite plate, one specimen is fractured at the top, five specimens are fractured in the middle and one specimen is fractured in various location. For MLTW8P11 composite plate, four specimens are fractured at the bottom, one specimen is fractured at the top, one specimen is fractured in the middle and one specimen is fractured in various locations. For MLTW8P12 composite plate, three specimens are fractured in the middle and four specimens are fractured in various locations.

Compare the failure mode of specimens from eight-ply twill-weaved CFRP composite plates with the failure mode of specimens from four-ply, four-ply specimens show a higher incidence of multi-mode failure type, multiple failure area, and various failure location. These failure modes are attributed to the fracture shockwave as proved by the high-speed camera footage. Eight-ply specimens are not affected by the fracture shockwave, however, their failure modes are not uniform and distributed across different failure areas and failure locations.

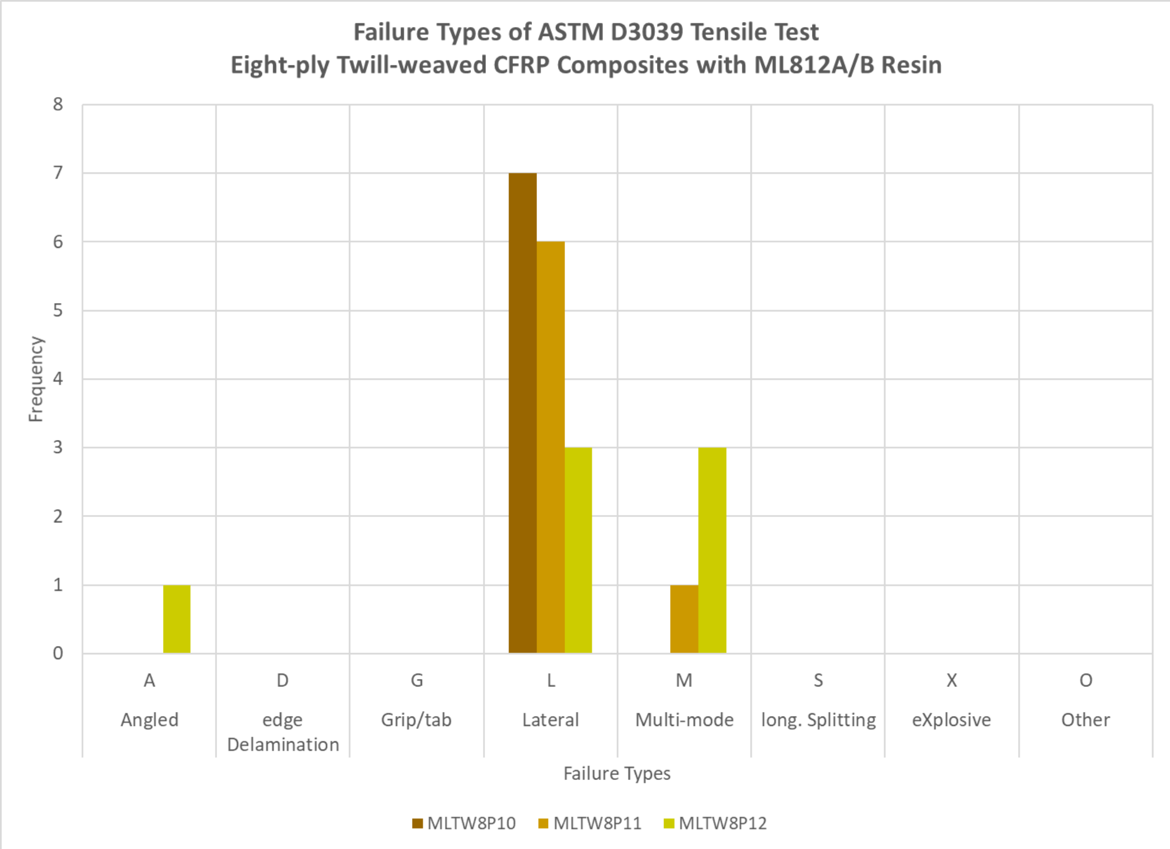

Figure 4.47 ASTM D3039 failure types of eight-ply twill-weaved CFRP composites with ML812A/B resin system

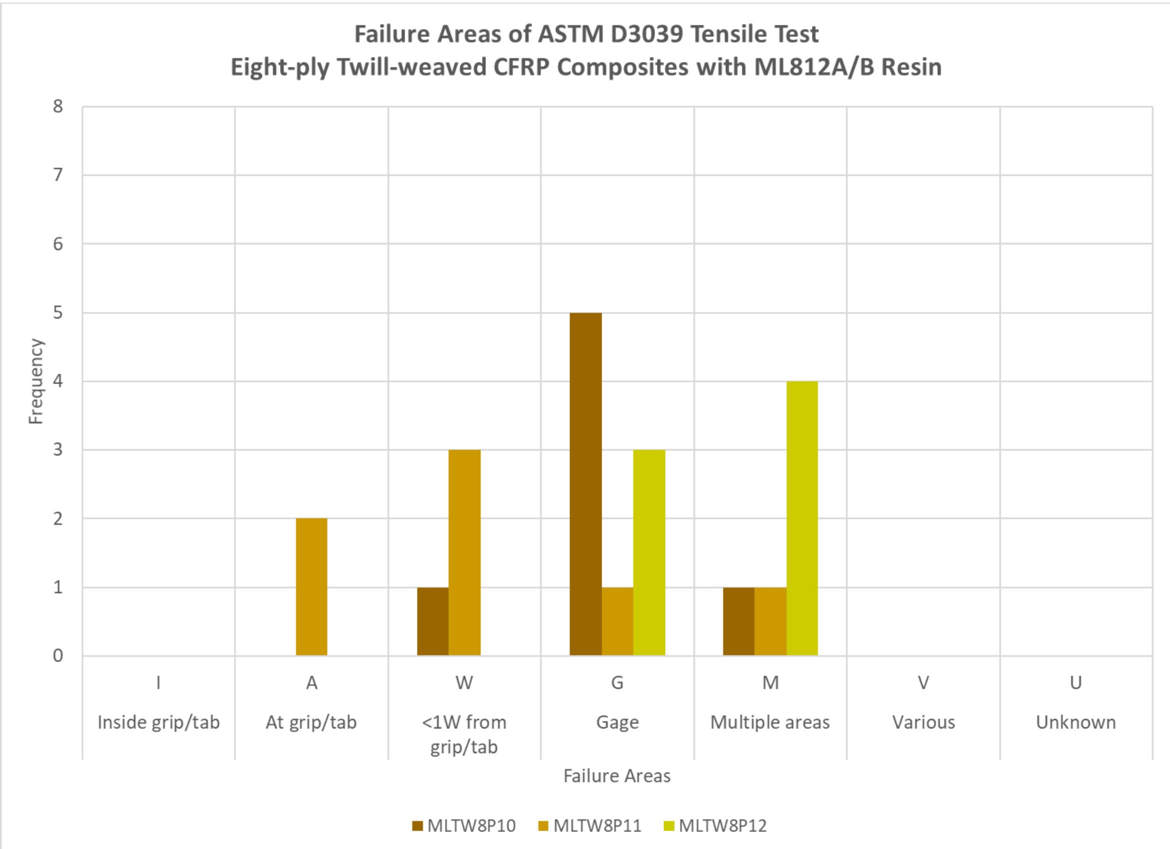

Figure 4.48 ASTM D3039 failure areas of eight-ply twill-weaved CFRP composites with ML812A/B resin system

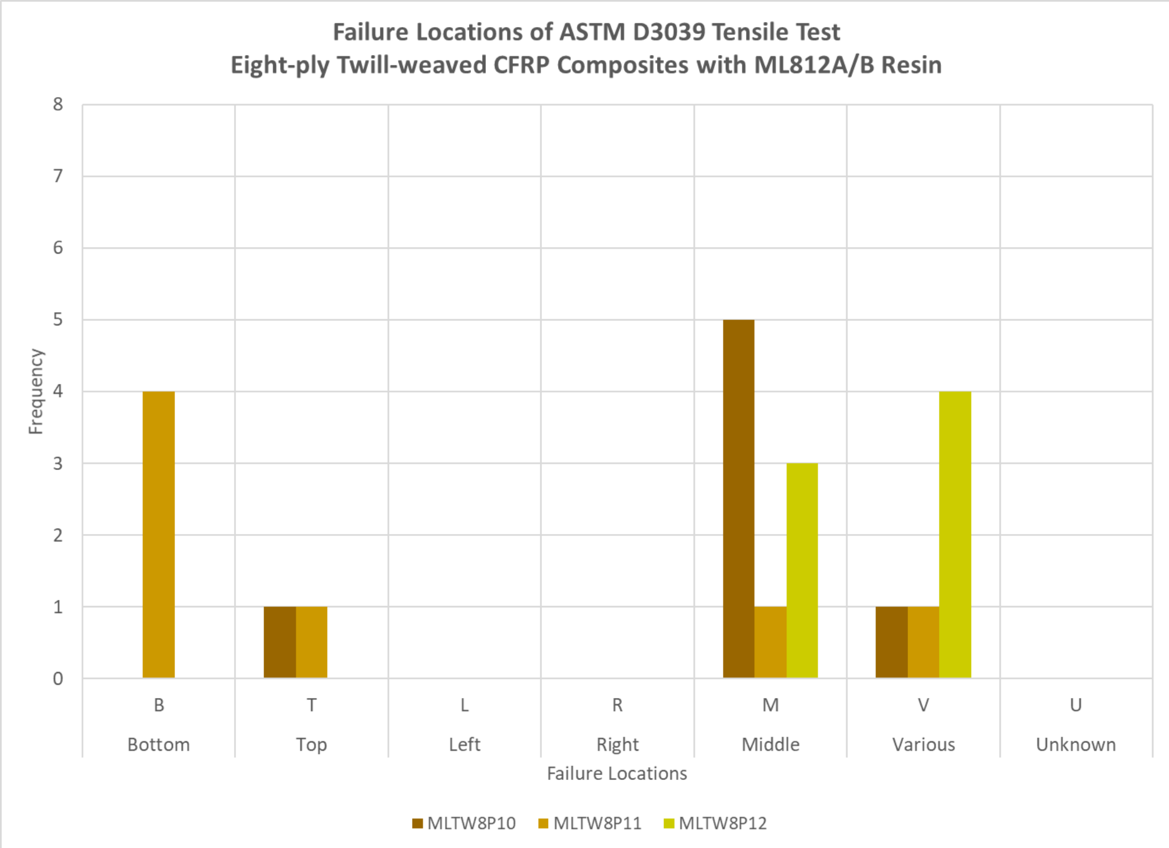

Figure 4.49 ASTM D3039 failure locations of eight-ply twill-weaved CFRP composites with ML812A/B resin system

Specimens for eight-ply twill-weaved CFRP composites with ML812A/B resin system are fractured in seven failure mode combinations: L M V, M M V, L G M, L W B, L W T, L A B (Lateral type, At grip/tab area, Bottom location), and A G M (Angled type, Gage area, Middle location). For the first three failure modes, example can be found in failure modes of specimens from WSTW4P composite plates. The fourth and fifth failure modes, example can be found in failure modes of specimens from WSTW8P composite plates. Figure 4.50 shows a lateral fracture take place at the edge of the bottom end tab of the specimen. Figure 4.51 shows an angled fracture at gage area which is one specimen width (yellow squares) away from the end tabs and an illustration of failure mode - A G M in ASTM D3039 is shown for reference.

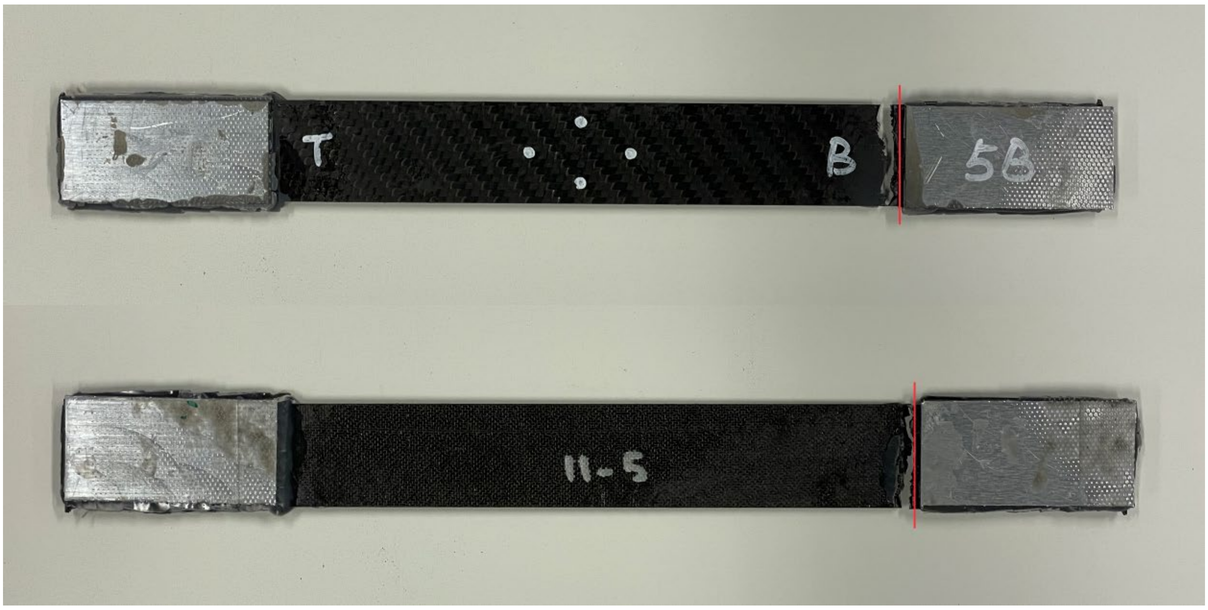

Figure 4.50 Specimen with failure mode - L A B (Lateral type, At grip/tab area, Bottom location)

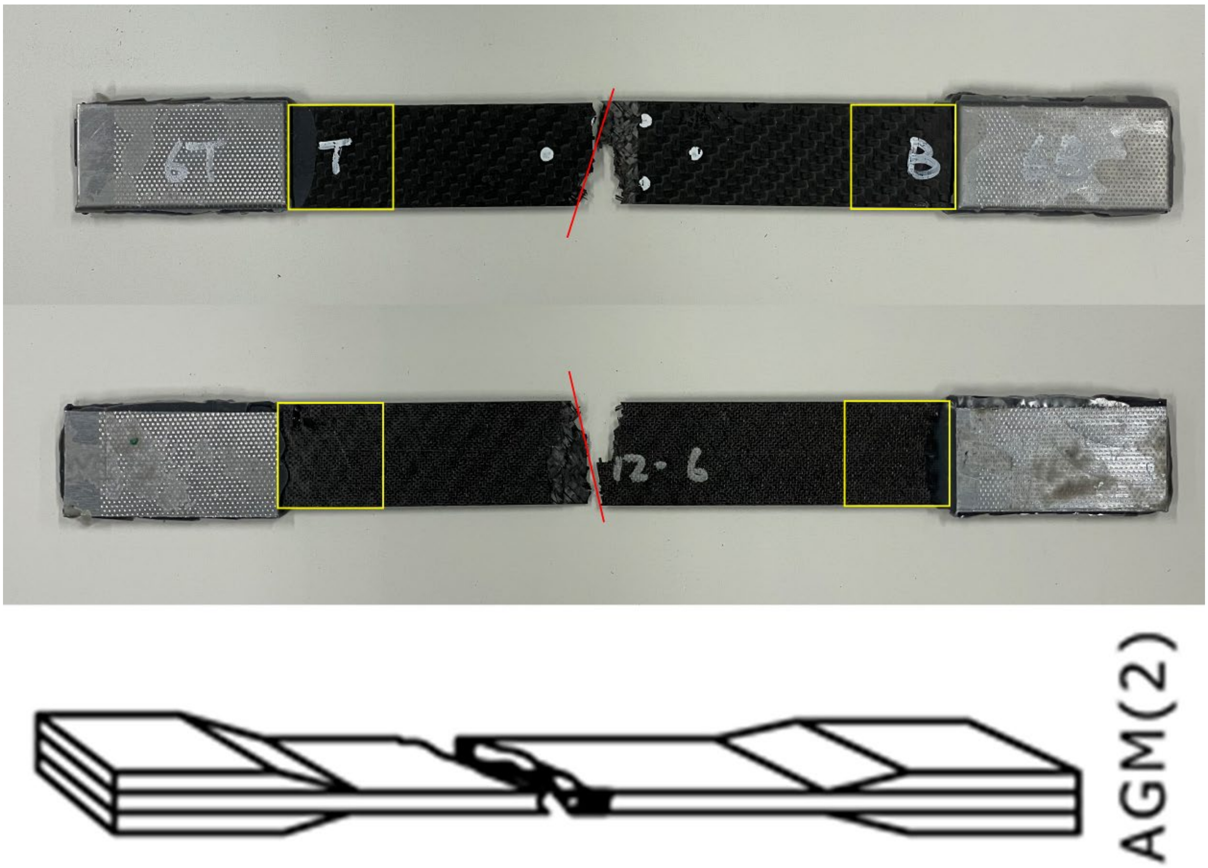

Figure 4.51 Specimen with failure mode - A G M (Angled type, Gage area, Middle location)

Figure 4.52 and Figure 4.53 illustrate the ASTM D2344 failure modes of four-ply and eight-ply twill-weaved CFRP composites with ML812A/B resin. One of the specimens of MLTW4P05 composite plate was destroyed in the waterjet machining process, while the results were not affected by the missing data. Both four-ply and eight-ply specimens show flexure tension failure modes, which are consistent with the failure mode observed in the specimens with WS105/209 resin system. This observation suggests a favorable compatibility between the matrix phase and the reinforcement phase, enabling effective stress transfer between them.

In conclusion, the fracture shockwave experienced by four-ply specimens may affect the evaluation of tensile properties, regardless of the resin system employed. The tensile properties of composite plates fabricated with the WS105/209 resin system show a more consistent pattern compared to those produced with the ML812A/B resin system, regardless of the ply configuration. In composite plates with WS105/209 resin system, all tensile properties indicate that eight-ply specimens show more reliable results with a lower coefficient of variation compared to four-ply specimens. While, the statistical data obtained from composite plates with ML812A/B resin system does not show a consistent trend regarding the ply configuration. Therefore, as the results obtained from composite plates with WS105/209 resin system demonstrate higher repeatability on the data collected and a robust conclusion regarding ply configuration, the eight-ply configuration with this resin system was selected as the baseline for comparative analysis of other fabrication conditions.

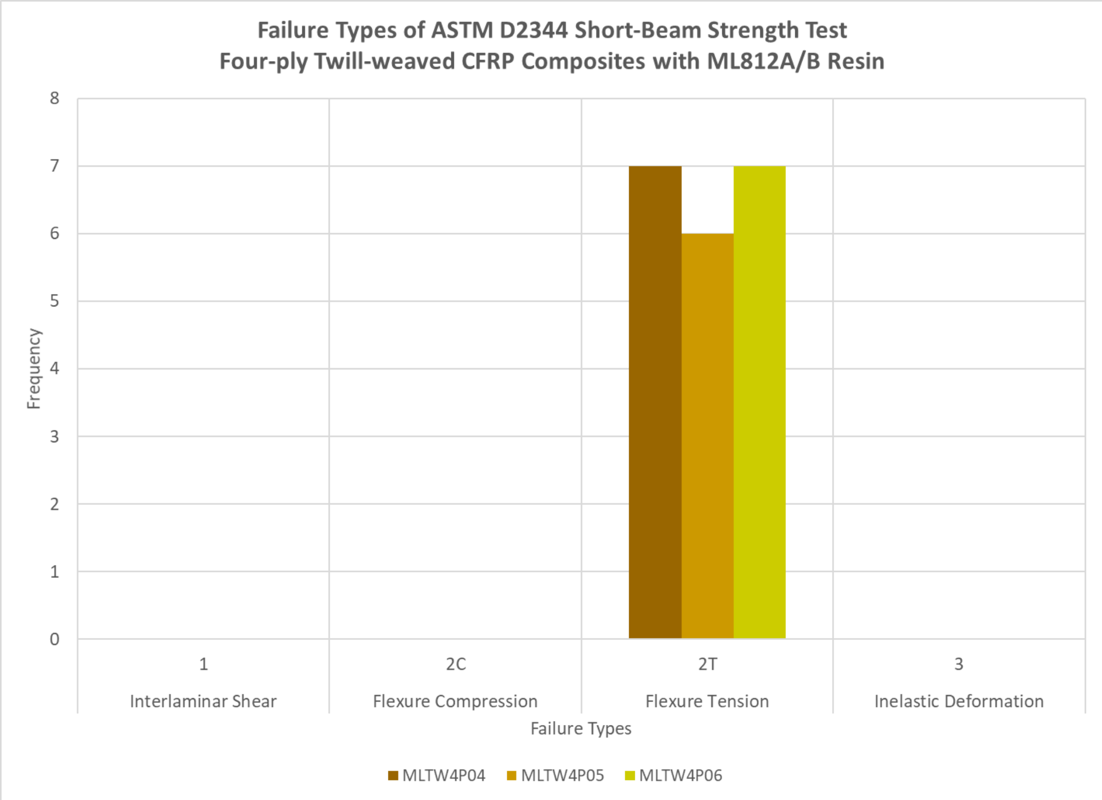

Figure 4.52 ASTM D2344 failure modes of four-ply twill-weaved CFRP composites with ML812A/B resin system

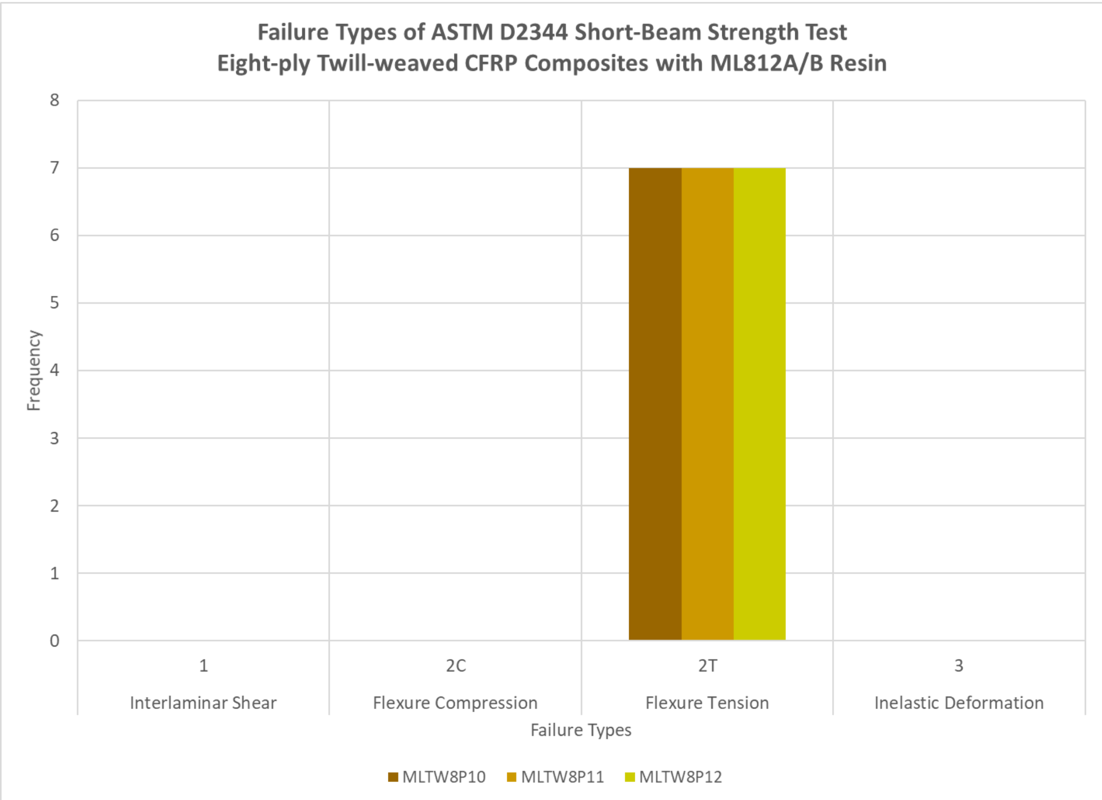

Figure 4.53 ASTM D2344 failure modes of eight-ply twill-weaved CFRP composites with ML812A/B resin system

4.2 Influence of matrix viscosity on CFRP composites

In Chapter 4.1, comparison of different ply configuration was done and eight-ply specimens show a consistent result in tensile properties evaluation. Using eight-ply configuration as a baseline, a comparative evaluation of CFRP composite specimens with different resin systems is presented in this section. The evaluation of tensile properties of eight-ply twill-weaved CFRP composites with WS105/209 and ML812A/B resin systems are presented in Chapter 4.1. Another matrix, IN2/AT30S resin system, was added into the comparison and three composite plates was fabricated to mitigate any manufacturing-related errors.

Figure 4.54, Figure 4.55 and Figure 4.56 present the stress-strain characteristic of the three eight-ply twill-weaved CFRP composites plates with IN2/AT30S resin system. Figure 4.54 presents the stress-strain curves of specimens from the IATW8P13 composite plate. Most of the curves are linear and overlapping with each other. IATW8P13-01 specimen is fluctuated when tensile stress is under 250 MPa. On the other hand, IATW8P13-03 specimen has a change in stress-strain behavior after 250 MPa tensile stress. Figure 4.55 presents the stress-strain curves of specimens from the IATW8P14 composite plate. All curves are straight and linear but some of the curves are slightly deviated and barely overlap with other curves. Figure 4.56 presents the stress-strain curves of specimens from the IATW8P15 composite plate. All curves show a slightly wavy pattern and they are not overlapping with each other. IATW8P15-05 specimen has a non-zero tensile stress at the start point of the curve. The change in stress-strain behavior observed in IATW8P13-03 specimen may attribute to the alignment of carbon fiber. The wavy pattern found in IATW8P15 composite plate and IATW8P13-01 specimen may also attribute to void content inside the matrix phase.

The stress-strain curves of eight-ply twill-weaved CFRP composites with ML812A/B resin system are the most unstable and fluctuating among these three resin systems. The stress-strain curves of eight-ply twill-weaved CFRP composites with IN2/AT30S resin system have a consistency similar to those with WS105/209 resin system. Although, the stress-strain curves of composite plates with WS105/209 resin system are diverged from each other, their stress-strain behavior keep constant as the curves are straight and linear. The wavy curves found in IATW8P15 composite plate and IATW8P13-01 specimen represent an unstable stress-strain behavior, therefore, the quality of eight-ply twill-weaved CFRP composites with WS105/209 resin system are more uniform than composite plates with ML812A/B and IN2/AT30S resin systems.

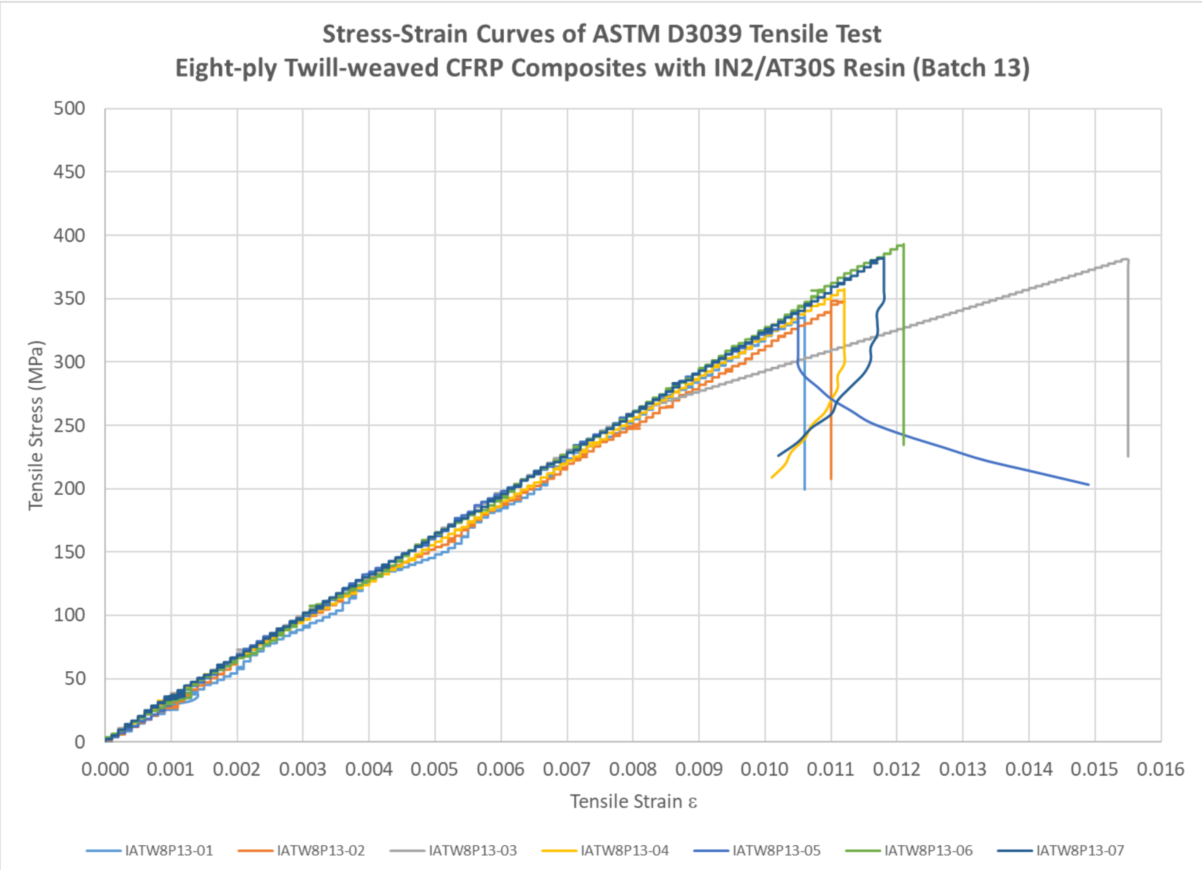

Figure 4.54 Stress-strain curve of eight-ply twill-weaved CFRP composites with IN2/AT30S resin system (Batch 13)

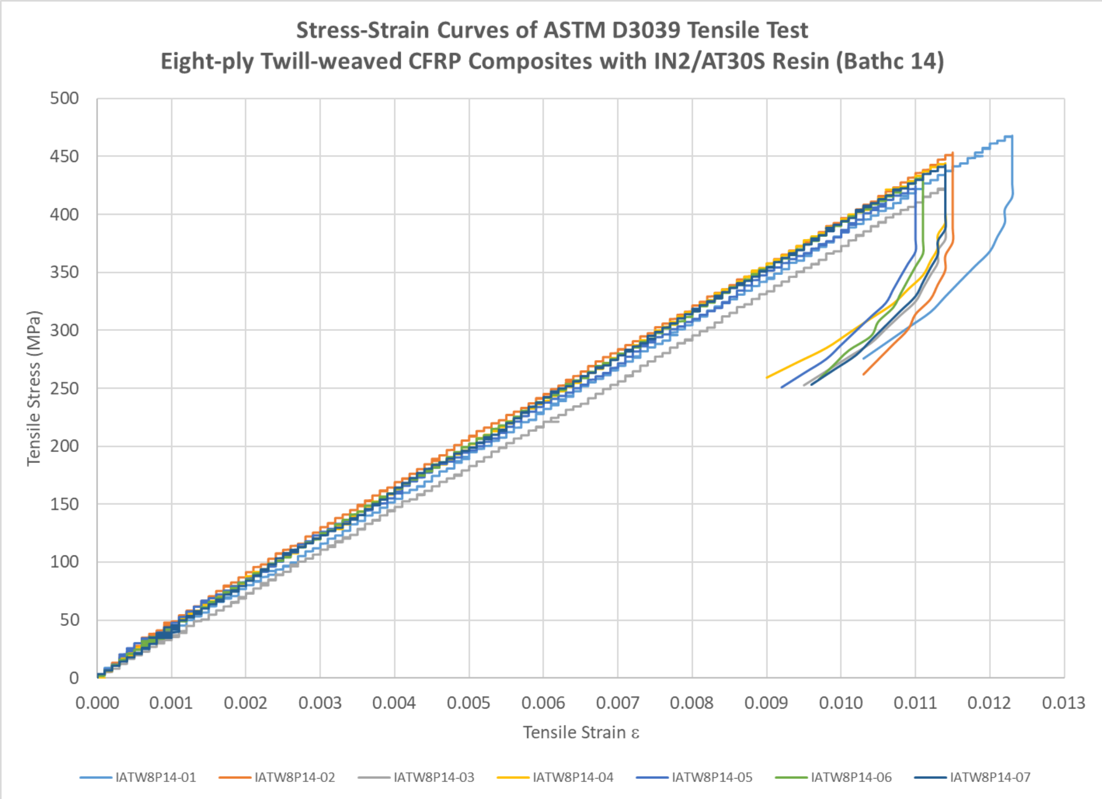

Figure 4.55 Stress-strain curve of eight-ply twill-weaved CFRP composites with IN2/AT30S resin system (Batch 14)

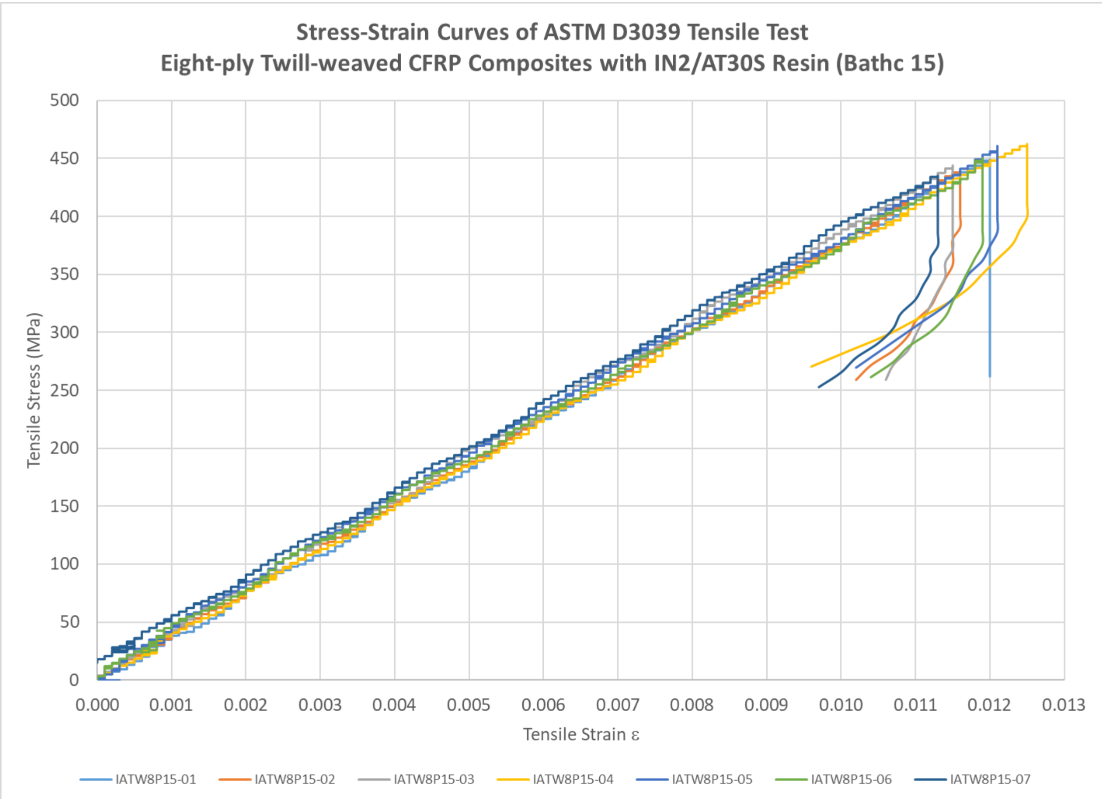

Figure 4.56 Stress-strain curve of eight-ply twill-weaved CFRP composites with IN2/AT30S resin system (Batch 15)

Table 4.14 and Table 4.15 presented a comparison of ultimate tensile stress and ultimate tensile strain of the eight-ply twill-weaved CFRP composite plates between three different resin systems. Composite plates with WS105/209 resin system have a relatively consistent coefficient of variation than those with other resin systems. Both ML812A/B and IN2/AT30S resin system have a high coefficient of variation in one of the data sets which indicates uneven quality across the plate. Further averaged the data with the same fabrication condition, ML812A/B and IN2/AT30S resin system show a relatively inconsistent quality among the composite plates as the coefficient of variation per fabrication condition is around double of that of WS105/209 resin system. The ultimate properties of eight-ply twill-weaved CFRP composites with IN2/AT30S resin system are visually presented in Figure 4.57. Compare Figure 4.57 with Figure 4.8, the ultimate properties of specimens with WS105/209 resin system are the least scattered among the three resin systems. Therefore, composite plates with WS105/209 resin system have a higher repeatability in collecting tensile properties data.

Table 4.14 Comparison of ultimate tensile stress of eight-ply twill-weaved CFRP composites between three resin systems

Ultimate Tensile Stress						
	per composite plate			per fabrication condition		
	Mean (MPa)	SD (MPa)	CV	Mean (MPa)	SD (MPa)	CV
WSTW8P07	450	11.6	2.57	450	23.2	5.15
WSTW8P08	472	16.7	3.53			
WSTW8P09	429	17.0	3.96			
MLTW8P10	379	15.0	3.96	399	37.5	9.38
MLTW8P11	397	57.2	14.4			
MLTW8P12	422	9.05	2.14			
IATW8P13	363	22.0	6.05	418	42.6	10.2
IATW8P14	441	16.0	3.63			
IATW8P15	449	10.5	2.34			

Table 4.15 Comparison of ultimate tensile strain of eight-ply twill-weaved CFRP composites between three resin systems

Ultimate Tensile Strain						
	per composite plate			per fabrication condition		
	Mean	SD	CV	Mean	SD	CV
WSTW8P07	0.0122	0.0001	0.995	0.0120	0.0004	3.71
WSTW8P08	0.0119	0.0006	5.07			
WSTW8P09	0.0117	0.0004	3.14			
MLTW8P10	0.0114	0.0006	5.34	0.0110	0.0009	7.76
MLTW8P11	0.0108	0.0013	11.8			
MLTW8P12	0.0109	0.0005	4.25			
IATW8P13	0.0118	0.0017	14.5	0.0117	0.0010	8.63
IATW8P14	0.0114	0.0004	3.67			
IATW8P15	0.0118	0.0004	3.44			

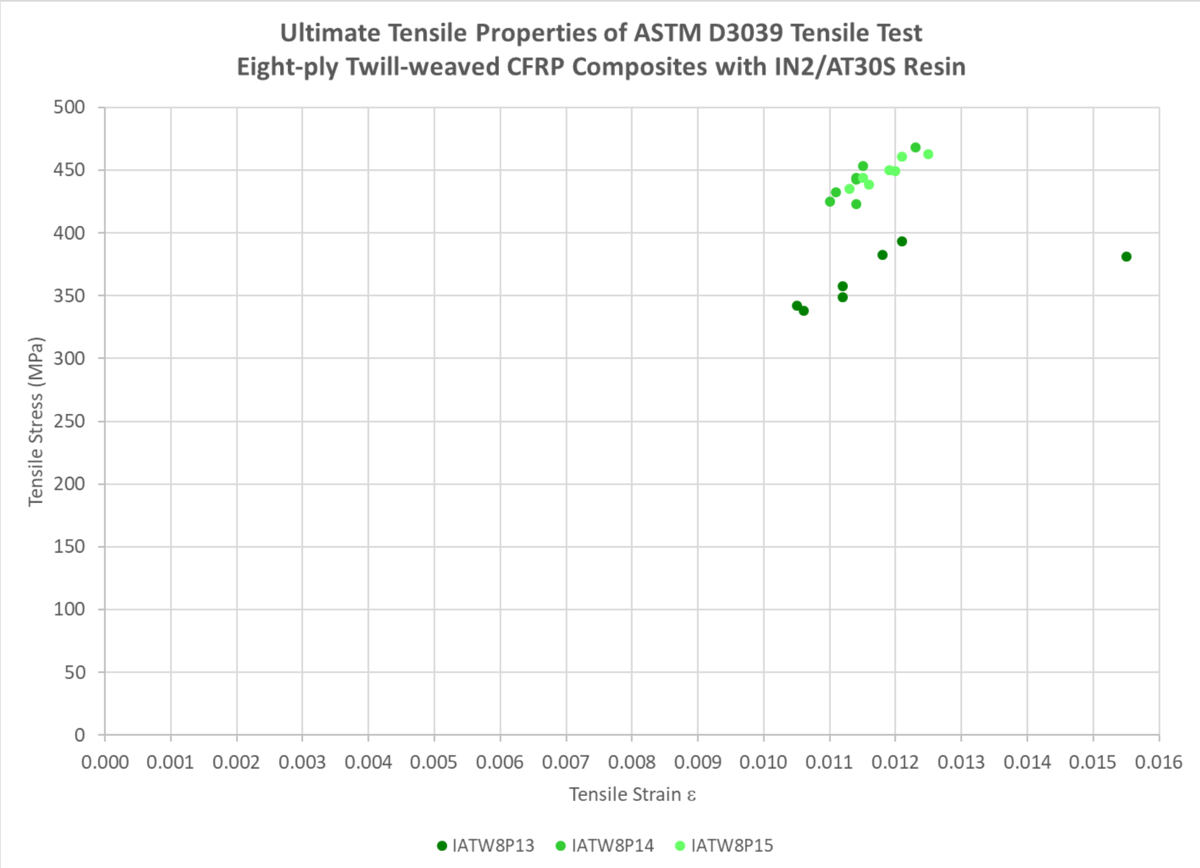

Figure 4.57 Ultimate tensile properties of eight-ply twill-weaved CFRP composites with IN2/AT30S resin system

Linear regression analysis was conducted on 18 random sets of ultimate tensile stress and ultimate tensile strain data from 21 specimens of eight-ply twill-weaved CFRP composites with IN2/AT30S resin system. Tensile stress and tensile strain are continuous variables with a linear relationship as shown in Figure 4.54 to Figure 4.56. The ultimate tensile data used in linear regression also shows an outlier in Figure 4.57.

For eight-ply twill-weaved specimens with IN2/AT30S resin system, the significance value of one-way ANOVA is 0.457 which is not significant. Figure 4.58 and Figure 4.59 show the normal probability-probability plot and scatterplot respectively. The residuals of the data follow a normal distribution and the variance is consistent. However, the Durbin-Watson value is 0.279 indicating a very negative autocorrelation between data errors. Figure 4.60 presents the statistical result of a linear regression model with the following equation to demonstrate the relationship between tensile stress and tensile strain.

$$ultimate\ tensile\ stress = 326.723 + (7719.49 \times ultimate\ tensile\ strain)$$

Equation 4.5 Linear regression model for ultimate tensile properties of eight-ply twill-weaved specimens with IN2/AT30S resin system

The R-squared value of the linear regression model is 0.035, indicating that 3.5% of the variation in tensile stress is related to tensile strain. This model is then used to predict the ultimate tensile stress of the remaining three specimens. The predicted ultimate tensile stresses are compared with the measured ultimate tensile stresses of the three specimens to validate the linear regression model. Table 4.16 shows the comparison between the predicted and measured ultimate tensile stresses of the three specimens. The predicted ultimate tensile stresses deviate from the measured values by approximately 10%.

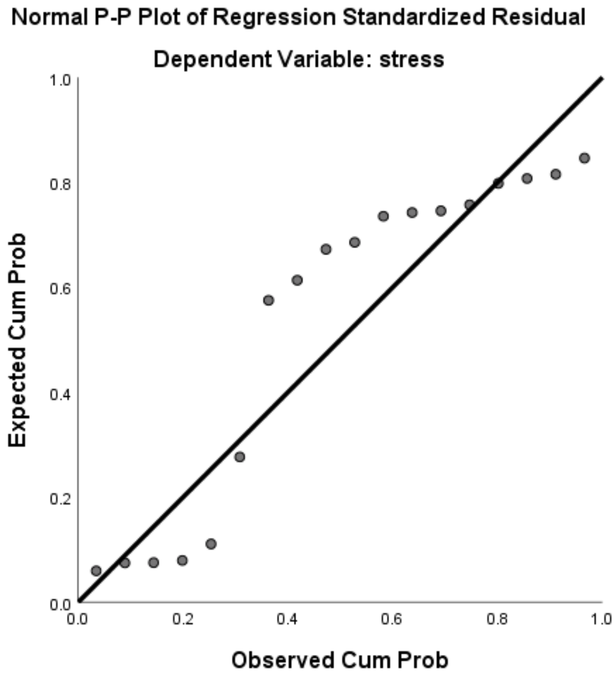

Figure 4.58 Normal probability-probability plot of regression standardized residuals of eight-ply twill-weaved specimens with IN2/AT30S resin system

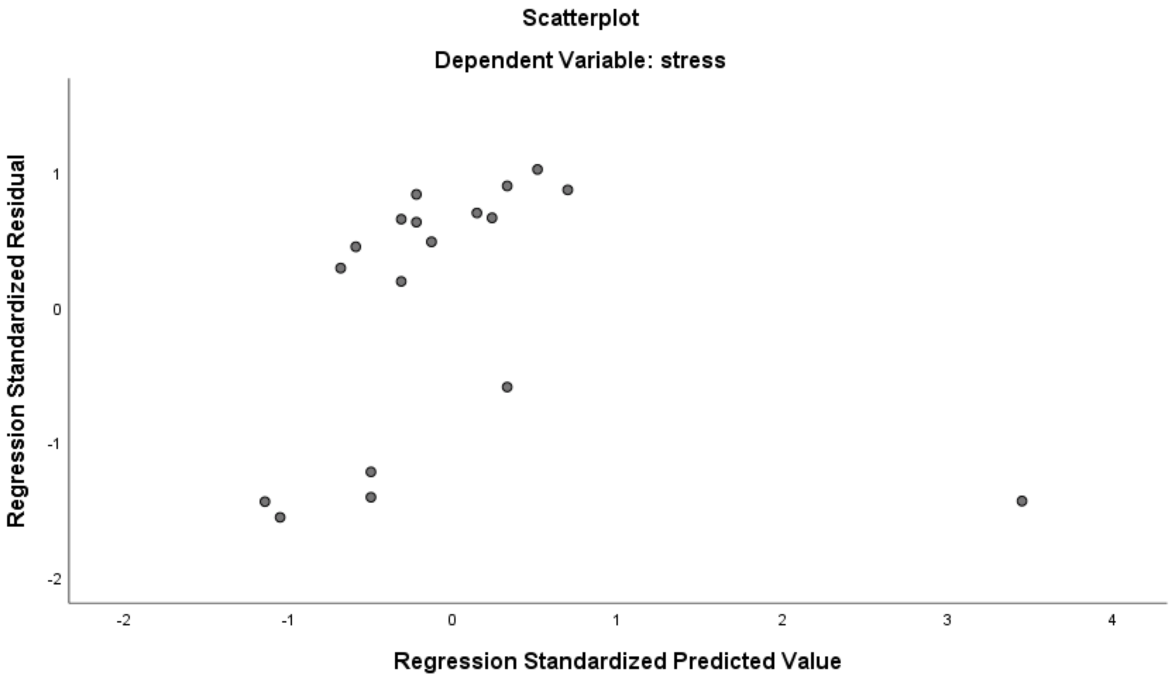

Figure 4.59 Scatterplot of regression standardized residuals against regression standardized predicted values of eight-ply twill-weaved specimens with IN2/AT30S resin system

Model Summary[b]

Model	R	R Square	Adjusted R Square	Std. Error of the Estimate	Durbin-Watson
1	.187[a]	.035	-.025	45.4174563	.279

a. Predictors: (Constant), long_strain

b. Dependent Variable: stress

ANOVA[a]

Model		Sum of Squares	df	Mean Square	F	Sig.
1	Regression	1198.294	1	1198.294	.581	.457[b]
	Residual	33003.925	16	2062.745		
	Total	34202.220	17			

a. Dependent Variable: stress

b. Predictors: (Constant), long_strain

Coefficients[a]

Model		Unstandardized Coefficients		Standardized Coefficients	t	Sig.
		B	Std. Error	Beta		
1	(Constant)	326.723	119.384		2.737	.015
	long_strain	7716.490	10124.203	.187	.762	.457

a. Dependent Variable: stress

Figure 4.60 Linear regression model results of eight-ply twill-weaved specimens with IN2/AT30S resin system

Table 4.16 Comparison between predicted and actual ultimate tensile stress of eight-ply twill-weaved specimens with IN2/AT30S resin system

Specimens	Actual ultimate tensile strain	Predicted ultimate tensile stress	Actual ultimate tensile stress	Deviation
IATW8P13-07	0.0118	417.7776	382.3642	9.26%
IATW8P14-07	0.0114	414.6910	442.5545	-6.30%
IATW8P15-07	0.0113	413.9193	435.1921	-4.89%

The linear regression model of eight-ply twill-weaved specimens with the IN2/AT30S resin system is not as significant as the models in Chapter 4.1. The low R-squared value suggests the model unable to accurately predict the ultimate tensile stress resulting in a significant deviation from the actual value.

Table 4.17 presented a comparison of modulus of elasticity of the eight-ply twill-weaved CFRP composite plates between three resin systems. Composite plates with WS105/209 and IN2/AT30S resin system show a relatively consistent coefficient of variation than those with ML812A/B resin system. However, when the data further averaged as per fabrication condition, the coefficient of variation shows an obvious difference between three resin systems and the composite plates with WS105/209 resin system shows a higher consistency in modulus of elasticity among the three resin systems.

Table 4.18 presented a comparison of Poisson's ratio of the eight-ply twill-weaved CFRP composite plates between three resin systems. The Poisson's ratios of composite with ML812A/B resin system show extremely high coefficients of variation. The Poisson's ratios of composite with WS105/209 resin system show relatively consistent coefficients of variation among the three composite plates when compare to those with IN2/AT30S resin system. However, the coefficient of variation per fabrication condition shows that composite plates with IN2/AT30S resin system have a slightly better consistency in the data collected then those with WS105/209 resin system.

Table 4.17 Comparison of modulus of elasticity of eight-ply twill-weaved CFRP composites between three resin systems

Modulus of Elasticity						
	per composite plate			per fabrication condition		
	Mean (GPa)	SD (GPa)	CV	Mean (GPa)	SD (GPa)	CV
WSTW8P07	39.7	1.25	3.14	40.0	1.99	4.98
WSTW8P08	41.2	2.09	5.07			
WSTW8P09	39.1	2.15	5.50			
MLTW8P10	33.7	3.53	10.5	34.4	2.64	7.65
MLTW8P11	35.4	2.74	7.74			
MLTW8P12	34.2	1.17	3.40			
IATW8P13	32.2	1.34	4.18	36.3	3.40	9.37
IATW8P14	39.1	2.12	5.43			
IATW8P15	37.6	1.39	3.69			

Table 4.18 Comparison of Poisson's ratio of eight-ply twill-weaved CFRP composites between three resin systems

Poisson's Ratio						
	per composite plate			per fabrication condition		
	Mean	SD	CV	Mean	SD	CV
WSTW8P07	0.370	0.0650	17.6	0.370	0.0670	18.1
WSTW8P08	0.363	0.0560	15.4			
WSTW8P09	0.377	0.0864	22.9			
MLTW8P10	0.272	0.114	41.7	0.259	0.132	51.0
MLTW8P11	0.363	0.0743	20.5			
MLTW8P12	0.140	0.101	72.3			
IATW8P13	0.368	0.0230	6.25	0.385	0.0523	13.6
IATW8P14	0.395	0.0652	16.5			
IATW8P15	0.393	0.0618	15.7			

Further compare the failure mode of ASTM D3039 tensile test, Figure 4.61, Figure 4.62 and Figure 4.63 illustrate the failure types, failure areas, and failure locations of the eight-ply twill-weaved CFRP composites with IN2/AT30S resin respectively. Compare Figure 4.61, Figure 4.62, Figure 4.63 to Figure 4.22, Figure 4.23, Figure 4.24, Figure 4.47, Figure 4.48 and Figure 4.49 with WS105/209 resin and ML812A/B resin systems, IN2/AT30S resin system shows the highest incidence of lateral failure type and WS105/209 resin system shows the highest incidence of gauge failure area and middle failure location. Lateral failure type, gage failure area, and middle failure location indicate no stress concentration or weak points due to fabrication error or fabrication configuration. Therefore, specimens with WS105/209 resin system have a relatively standard failure mode than other two resin systems.

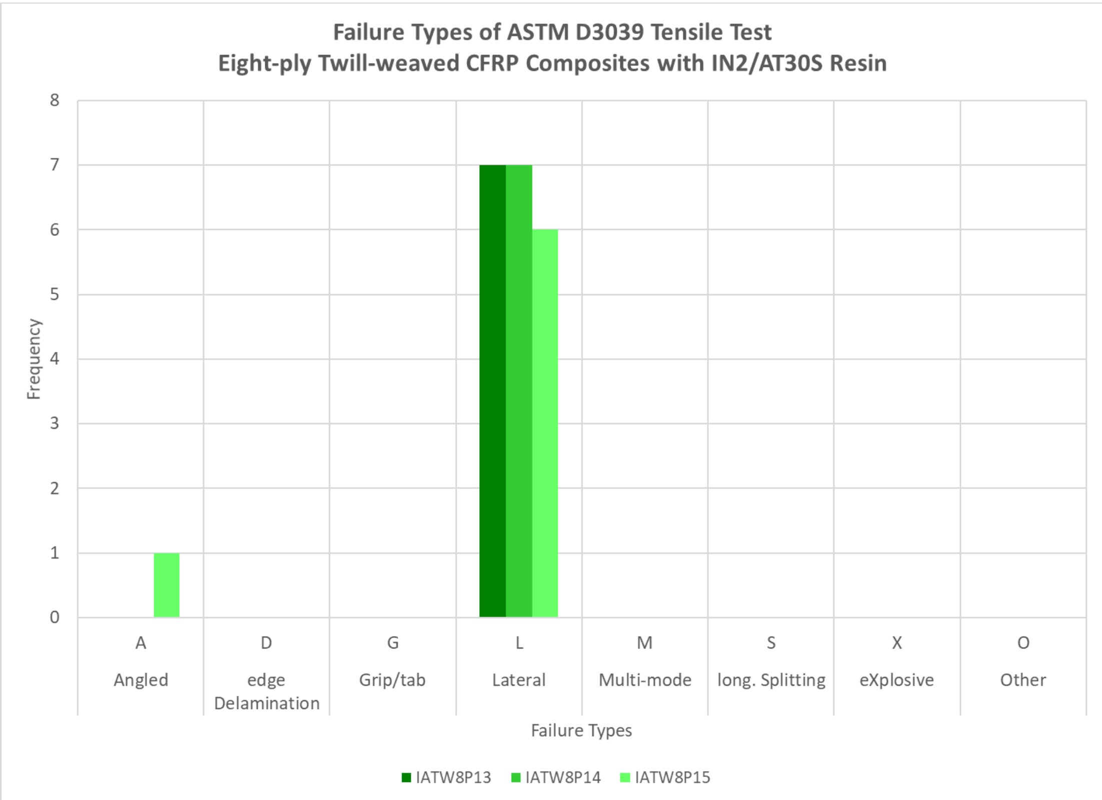

Figure 4.61 ASTM D3039 failure types of eight-ply twill-weaved CFRP composites with IN2/AT30S resin system

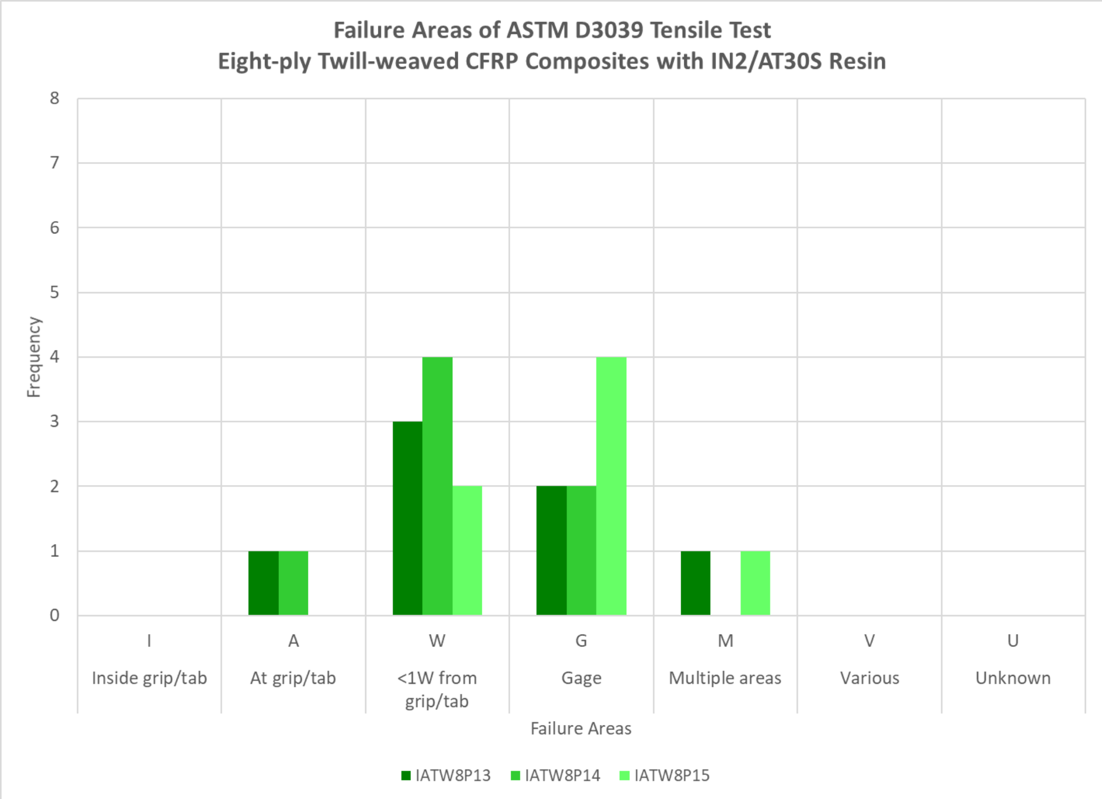

Figure 4.62 ASTM D3039 failure areas of eight-ply twill-weaved CFRP composites with IN2/AT30S resin system

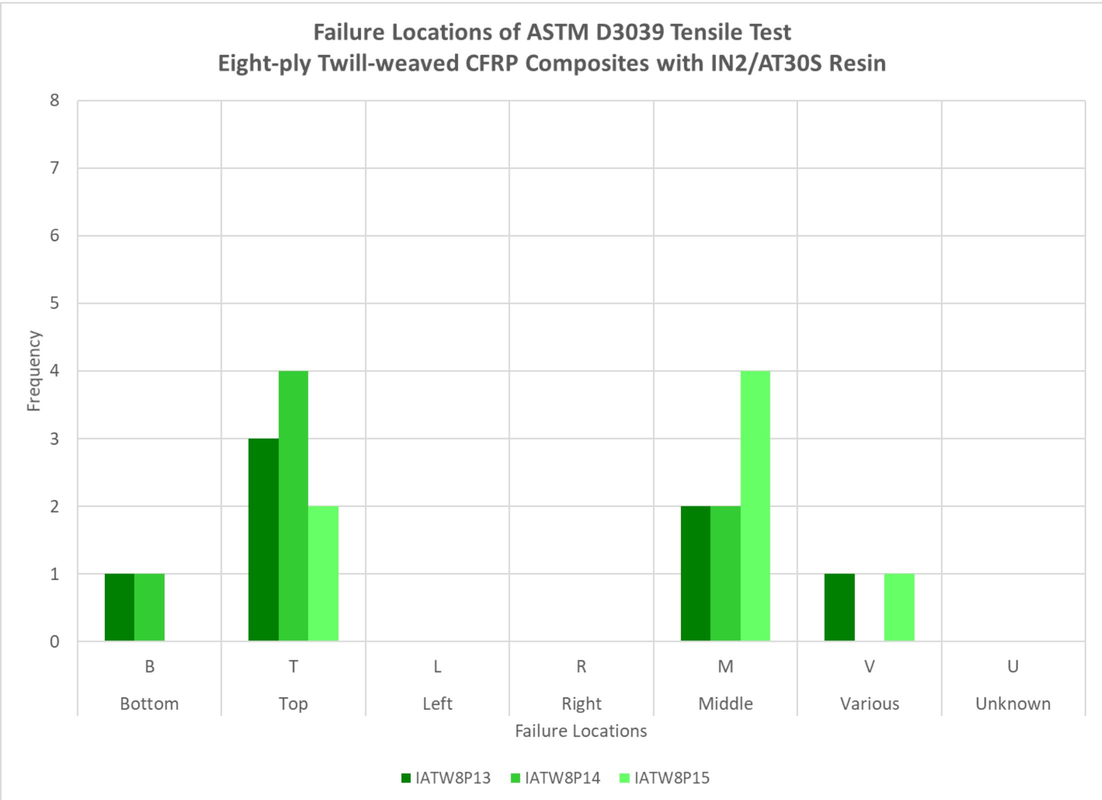

Figure 4.63 ASTM D3039 failure locations of eight-ply twill-weaved CFRP composites with IN2/AT30S resin system

Specimens for eight-ply twill-weaved CFRP composites with IN2/AT30S resin system are fractured in six failure mode combinations: L M V, L G M, L W B, L W T, L A T, and A G M. For the first two failure modes, example can be found in failure modes of specimens from WSTW4P composite plates. The third and fourth failure modes, example can be found in failure modes of specimens from WSTW8P composite plates. The fifth failure mode, example can be found in failure modes of specimens from MLTW4P composite plates. The sixth failure mode, example can be found in failure modes of specimens from MLTW8P composite plates.

For the compatibility between the matrix phase and the sizing of the reinforcement phase, Figure 4.64 shows the ASTM D2344 failure mode of eight-ply twill-weaved CFRP composites with IN2/AT30S resin system. Compare Figure 4.64 with Figure 4.28 and Figure 4.53, all three resin systems show a flexure tension failure mode which means the resin is well bonded with the carbon fiber and the stress can effectively transfer between them.

Conclude the results from different tensile properties, composite plates with WS105/209 resin system show the highest reliability among the three resin systems. Referring to the resin properties, the WS105/209 resin system has a mixed viscosity of 650 mPa·s, while the ML812A/B resin system has a mixed viscosity of 400 mPa·s, and IN2/AT30S resin system has a mixed viscosity of 200 mPa·s. By cross-referencing the tensile properties results with the resin properties, a higher viscosity of the resin mixture results in a more uniform quality of the composite plate.

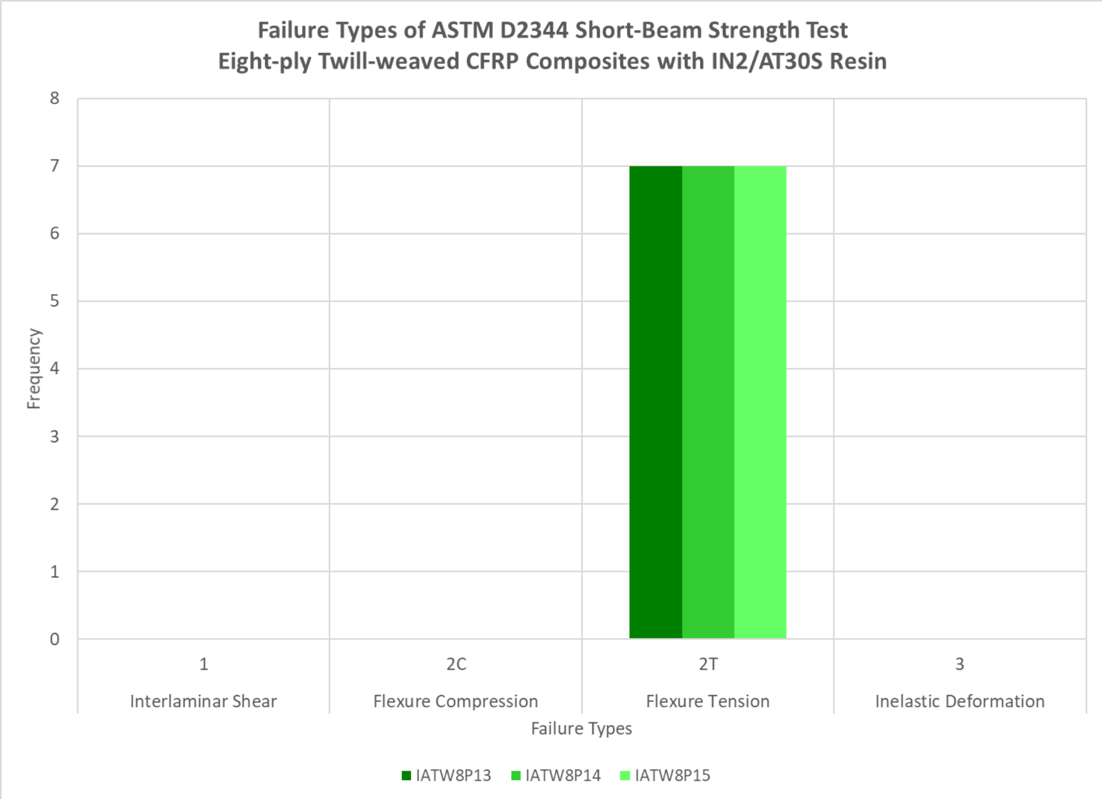

Figure 4.64 ASTM D2344 failure modes of eight-ply twill-weaved CFRP composites with IN2/AT30S resin system

4.3 Influence of reinforcement weave pattern on CFRP composites

With the conclusion from the previous chapters, composites with eight-ply configuration and WS105/209 resin system have the most stable and consistent tensile behavior compared to those with other fabrication conditions. This creates a common ground for reliable data collection to compare other fabrication condition. Therefore, only one composite plate was fabricated per fabrication condition in the upcoming comparison for easier data processing. If the comparison involves data from previous chapter, the average of three composite plates with the same fabrication conditions was used. As the composite plates examined in the previous chapters were all fabricated using twill-weaved carbon fiber reinforcement, the influence of weave pattern of the reinforcement phase is investigated in this chapter. Tensile properties of twill-weaved and plain-weaved reinforcements are evaluated based on eight-ply configuration and the WS105/209 resin system.

Figure 4.65 presents the stress-strain curves of the eight-ply plain-weaved CFRP composites plates with WS105/209 resin system and designated as WSPW8P16. It is observed that all stress-strain curves show irregularities when tensile stress exceeds 250 MPa. During the tensile testing, all specimens with plain-weaved reinforcement show cracking sounds in the latter stages of the test. This phenomenon can be attributed to localized failure and stress is concentrated at the carbon fiber tows.

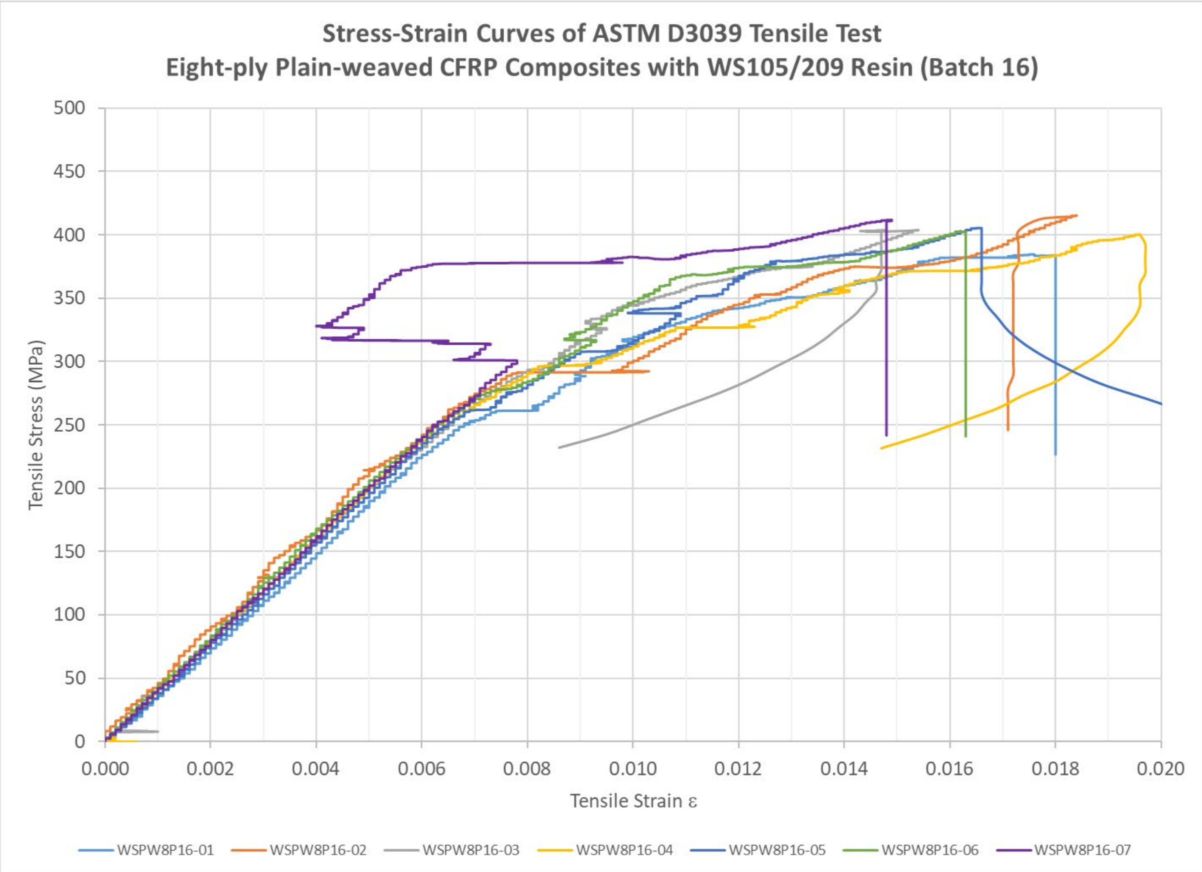

Figure 4.65 Stress-strain curve of eight-ply plain-weaved CFRP composites with WS105/209 resin system (Batch 16)

As the latter part of the stress-strain curves are irregular, the ultimate tensile properties of specimens maybe inconsistent. Table 4.19 and Table 4.20 show the comparison of ultimate tensile stress and ultimate tensile strain between twill-weaved and plain-weaved eight-ply CFRP composites with WS105/209 resin system. Plain-weaved composite plate shows a lower coefficient of variation in tensile stress but a higher in tensile strain when compared to twill-weaved composite plates. This indicated that the maximum stress carried by plain-weaved specimens is similar but the elongation of the specimens is inconsistent. The ultimate properties of eight-ply plain-weaved CFRP composites with WS105/209 resin system are visually presented in Figure 4.66. The failure points are scattered in a line shape with tensile stress at around 400 MPa and a wide range of tensile strain due to unpredictable stress-strain behavior.

Table 4.19 Comparison of ultimate tensile stress between twill-weaved and plain-weaved eight-ply CFRP composites with WS105/209 resin system

Ultimate Tensile Stress						
	per composite plate			per fabrication condition		
	Mean (MPa)	SD (MPa)	CV	Mean (MPa)	SD (MPa)	CV
WSTW8P07	450	11.6	2.57	450	23.2	5.15
WSTW8P08	472	16.7	3.53			
WSTW8P09	429	17.0	3.96			
WSPW8P16	404	9.85	2.44	404	9.85	2.44

Table 4.20 Comparison of ultimate tensile strain between twill-weaved and plain-weaved eight-ply CFRP composites with WS105/209 resin system

Ultimate Tensile Strain						
	per composite plate			per fabrication condition		
	Mean	SD	CV	Mean	SD	CV
WSTW8P07	0.0122	0.0001	0.995	0.0120	0.0004	3.71
WSTW8P08	0.0119	0.0006	5.07			
WSTW8P09	0.0117	0.0004	3.14			
WSPW8P16	0.0169	0.0017	9.91	0.0169	0.0017	9.91

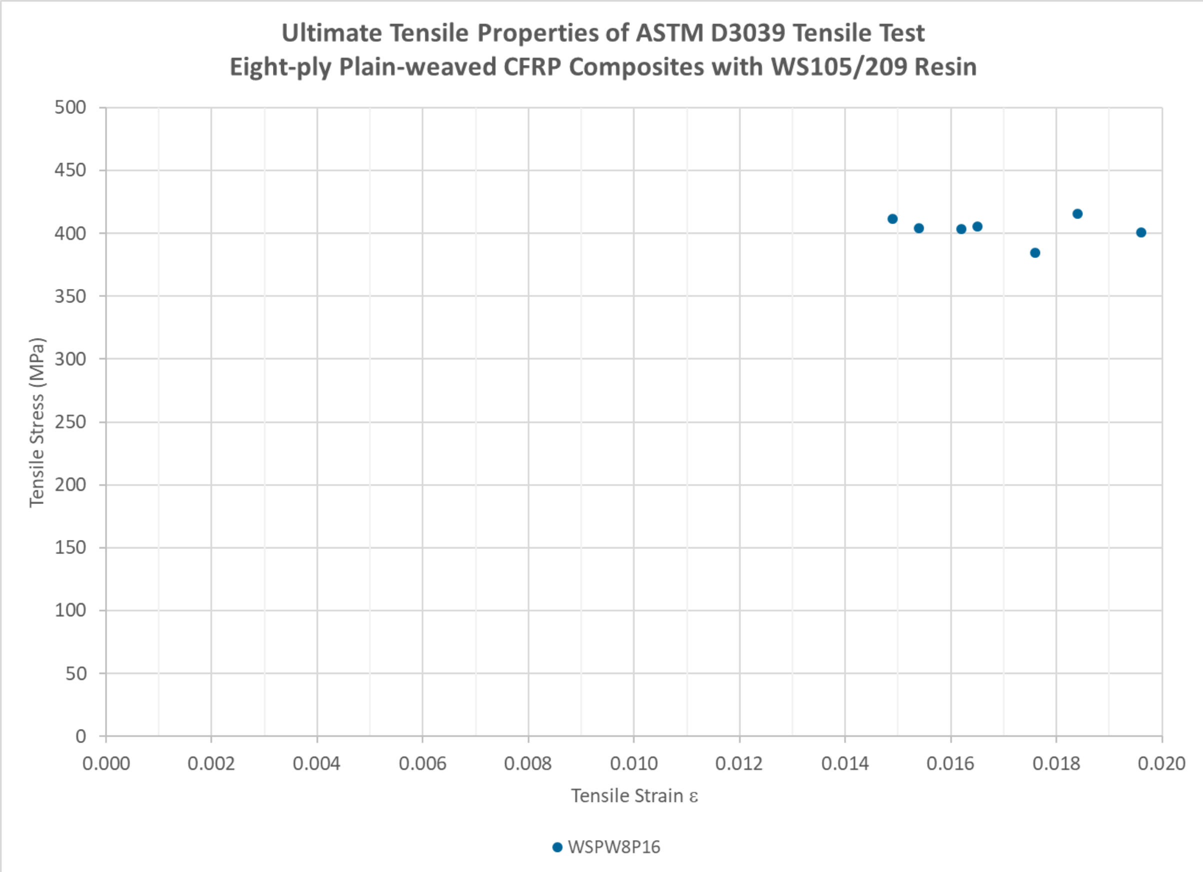

Figure 4.66 Ultimate tensile properties of eight-ply plain-weaved CFRP composites with WS105/209 resin system

Linear regression analysis was conducted on 6 random sets of ultimate tensile stress and ultimate tensile strain data from 7 specimens of eight-ply plain-weaved CFRP composites with WS105/209 resin system. Tensile stress and tensile strain are continuous variables as shown in Figure 4.65 and are expected to be linearly related. However, the stress-strain curves of WSPW8P specimens show non-linear behavior beyond 250 MPa. The ultimate tensile data used in linear regression also shows no obvious outlier in Figure 4.66.

For eight-ply plain-weaved specimens with WS105/209 resin system, the significance value of one-way ANOVA is 0.966 which is not significant. Figure 4.67 and Figure 4.68 show the normal probability-probability plot and scatterplot respectively. The residuals of the data follow a normal distribution and the variance is consistent. However, the Durbin-Watson value is 2.259 indicating no autocorrelation between data errors. Figure 4.69 presents the statistical result of a linear regression model with the following equation to demonstrate the relationship between tensile stress and tensile strain.

$$ultimate\ tensile\ stress = 404.722 + (-145..501 \times ultimate\ tensile\ strain)$$

Equation 4.6 Linear regression model for ultimate tensile properties of eight-ply plain-weaved specimens with WS105/209 resin system

The R-squared value of the linear regression model is 0.001, indicating that 0.1% of the variation in tensile stress is related to tensile strain. This model is then used to predict the ultimate tensile stress of the remaining specimen. The predicted ultimate tensile stress is compared with the measured ultimate tensile stress of the specimen to validate the linear regression model. Table 4.21 shows the comparison between the predicted and measured ultimate tensile stresses of the three specimens. The predicted ultimate tensile stress deviate from the measured value by approximately 2%.

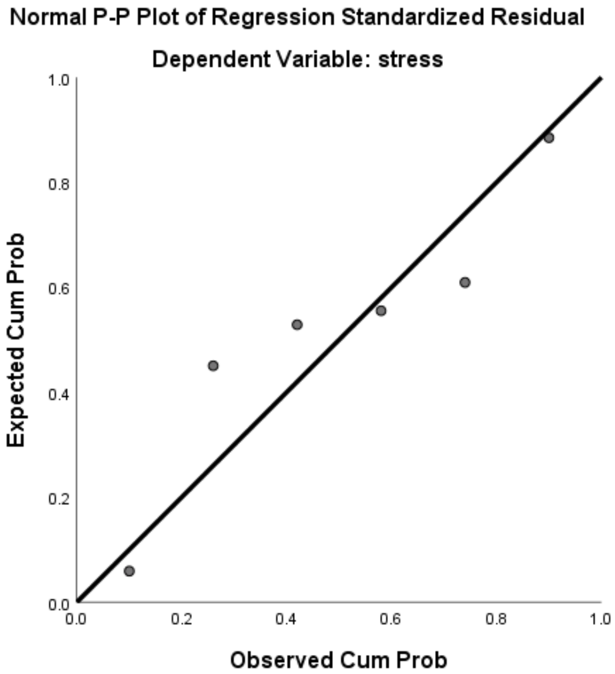

Figure 4.67 Normal probability-probability plot of regression standardized residuals of eight-ply plain-weaved specimens with WS105/209 resin system

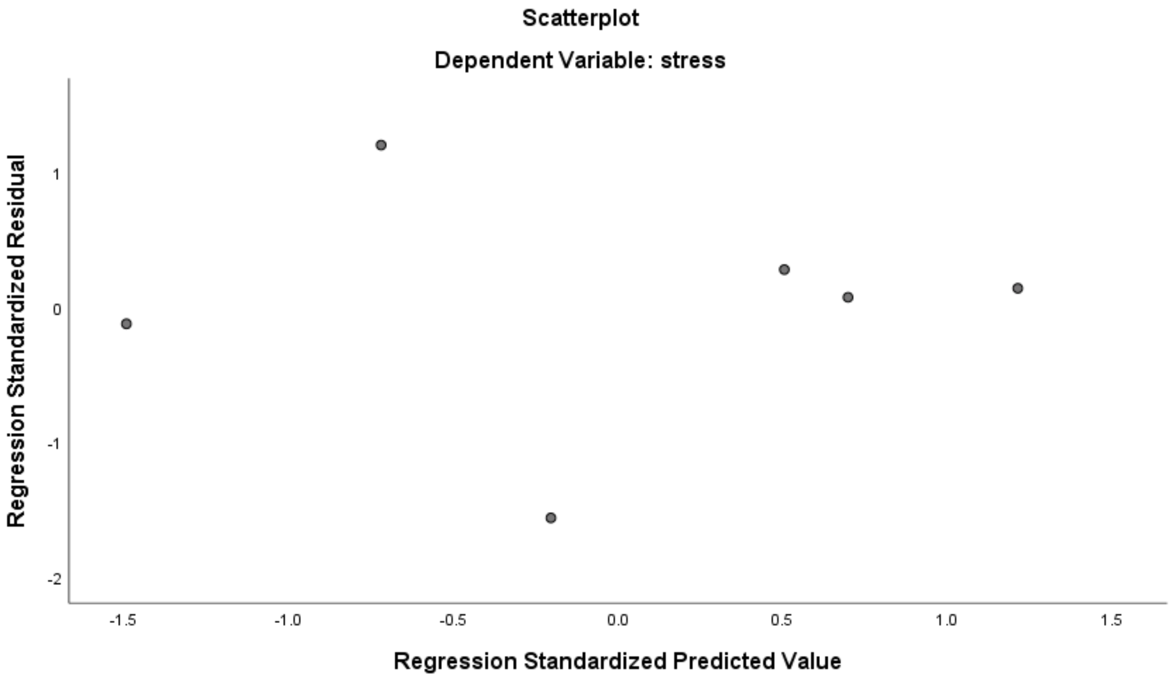

Figure 4.68 Scatterplot of regression standardized residuals against regression standardized predicted values of eight-ply plain-weaved specimens with WS105/209 resin system

Model Summary[b]

Model	R	R Square	Adjusted R Square	Std. Error of the Estimate	Durbin-Watson
1	.023[a]	.001	-.249	11.2164119	2.259

a. Predictors: (Constant), long_strain

b. Dependent Variable: stress

ANOVA[a]

Model		Sum of Squares	df	Mean Square	F	Sig.
1	Regression	.255	1	.255	.002	.966[b]
	Residual	503.232	4	125.808		
	Total	503.487	5			

a. Dependent Variable: stress

b. Predictors: (Constant), long_strain

Coefficients[a]

Model		Unstandardized Coefficients		Standardized Coefficients	t	Sig.
		B	Std. Error	Beta		
1	(Constant)	404.722	56.037		7.222	.002
	long_strain	-145.501	3231.398	-.023	-.045	.966

a. Dependent Variable: stress

Figure 4.69 Linear regression model results of eight-ply plain-weaved specimens with WS105/209 resin system

Table 4.21 Comparison between predicted and actual ultimate tensile stress of eight-ply plain-weaved specimens with WS105/209 resin system

Specimens	Actual ultimate tensile strain	Predicted ultimate tensile stress	Actual ultimate tensile stress	Deviation
WSPW8P16-07	0.0149	402.5540	411.8163	-2.25%

The linear regression model of eight-ply plain-weaved specimens with the WS105/209 resin system is not significant. The high significance value of the one-way ANOVA and the extremely low R-squared value make the model unreliable. Furthermore, the small sample size limits the predictive capability of the model.

Table 4.22 and Table 4.23 presented a comparison of modulus of elasticity and Poisson's ratio between twill-weaved and plain-weaved eight-ply CFRP composites with WS105/209 resin system. Plain-weaved composite plate shows a higher coefficient of variation than twill-weaved composite plates. Although the stiffness of the plain-weaved and twill-weaved composites are similar both at around 40 GPa, the specimens from plain-weaved composite show a larger fluctuation in their modulus of elasticity. Same phenomenon happens in Poisson's ratio, the ratios of material deformation in transverse direction to longitudinal direction have a larger variation in plain-weaved composite plates than twill-weaved composite plate.

Table 4.22 Comparison of modulus of elasticity between twill-weaved and plain-weaved eight-ply CFRP composites with WS105/209 resin system

Modulus of Elasticity						
	per composite plate			per fabrication condition		
	Mean (GPa)	SD (GPa)	CV	Mean (GPa)	SD (GPa)	CV
WSTW8P07	39.7	1.25	3.14	40.0	1.99	4.98
WSTW8P08	41.2	2.09	5.07			
WSTW8P09	39.1	2.15	5.50			
WSPW8P16	41.7	5.69	13.6	41.7	5.69	13.6

Table 4.23 Comparison of Poisson's ratio between twill-weaved and plain-weaved eight-ply CFRP composites with WS105/209 resin system

Poisson's Ratio						
	per composite plate			per fabrication condition		
	Mean	SD	CV	Mean	SD	CV
WSTW8P07	0.370	0.0650	17.6	0.370	0.0670	18.1
WSTW8P08	0.363	0.0560	15.4			
WSTW8P09	0.377	0.0864	22.9			
WSPW8P16	0.418	0.0980	23.4	0.418	0.0980	23.4

For the failure mode of ASTM D3039, Figure 4.70, Figure 4.71, and Figure 4.72 shows the failure types, failure areas and failure locations of the eight-ply plain-weaved CFRP composites with WS105/209 resin system respectively. The failure mode is surprisingly consistent in plain-weaved composite plate as all specimens are having explosive failure type, gauge failure area, and middle failure location. However, explosive failure type indicates the matrix phase and the reinforcement phase are having a different stress-strain behavior causing one of the constituents fail before another. The epoxy resin fails first and the carbon fibers are being straighten by the tensile stress as plain-weaved carbon fiber fabric has higher crimp than twill-weaved.

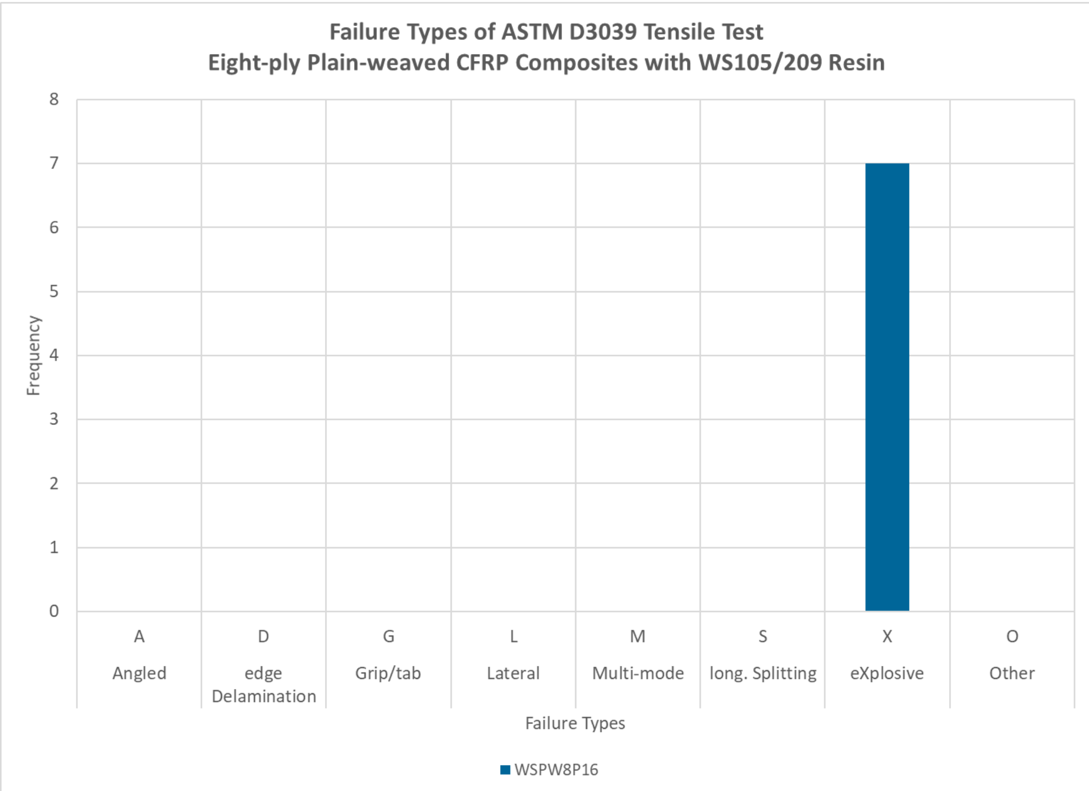

Figure 4.70 ASTM D3039 failure types of eight-ply plain-weaved CFRP composites with WS105/209 resin system

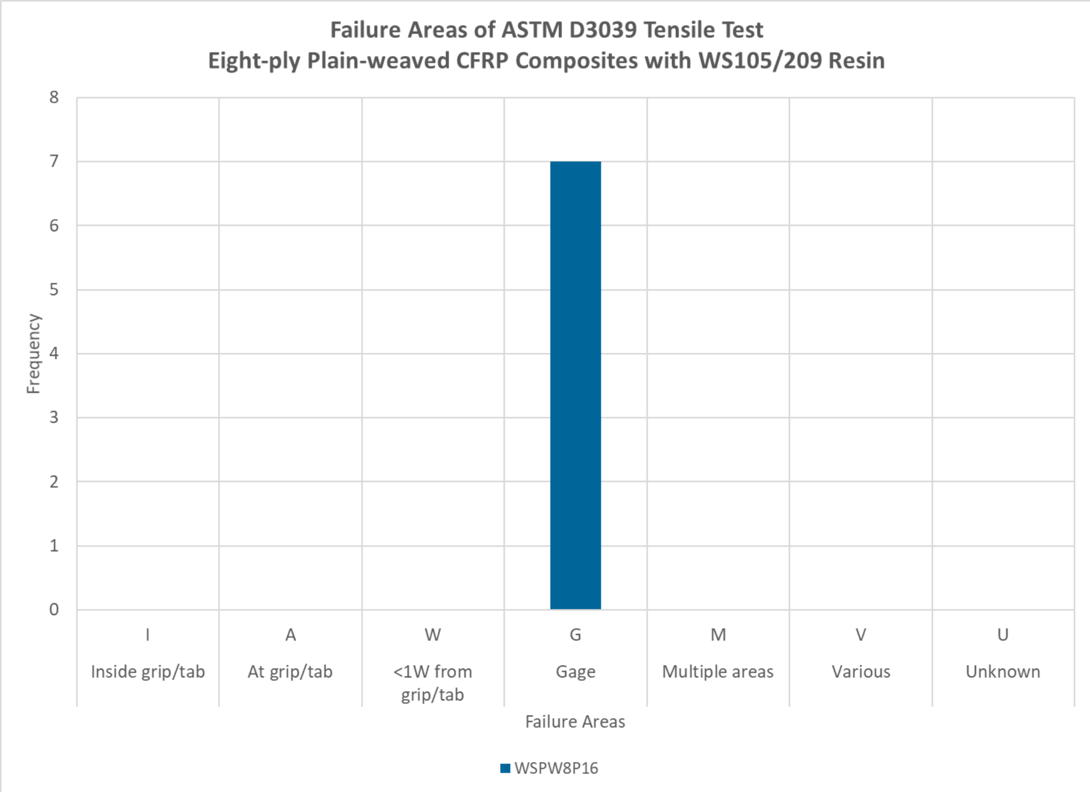

Figure 4.71 ASTM D3039 failure areas of eight-ply plain-weaved CFRP composites with WS105/209 resin system

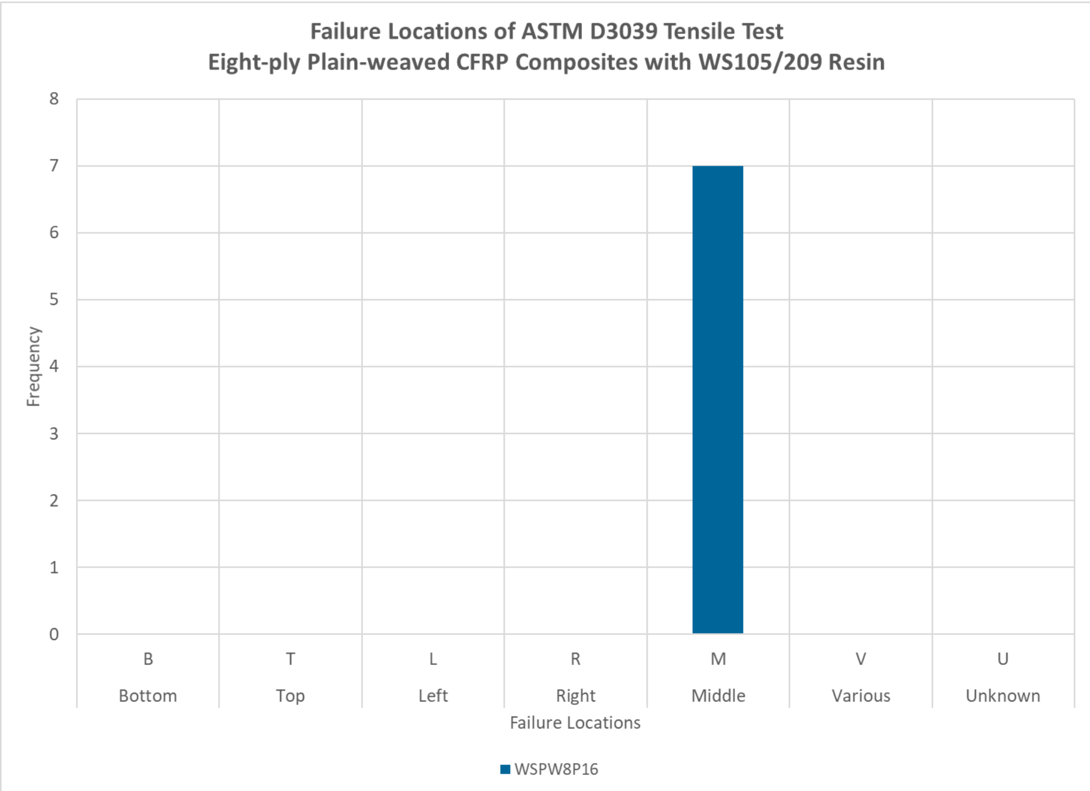

Figure 4.72 ASTM D3039 failure locations of eight-ply plain-weaved CFRP composites with WS105/209 resin system

Specimens for eight-ply plain-weaved CFRP composites with WS105/209 resin system are all fractured in one failure mode combination: X G M (eXplosive type, Gage area, Middle location). Figure 4.73 shows an explosive fracture at gage area which is one specimen width (yellow squares) away from the end tabs and an illustration of failure mode - X G M in ASTM D3039 is shown for reference.

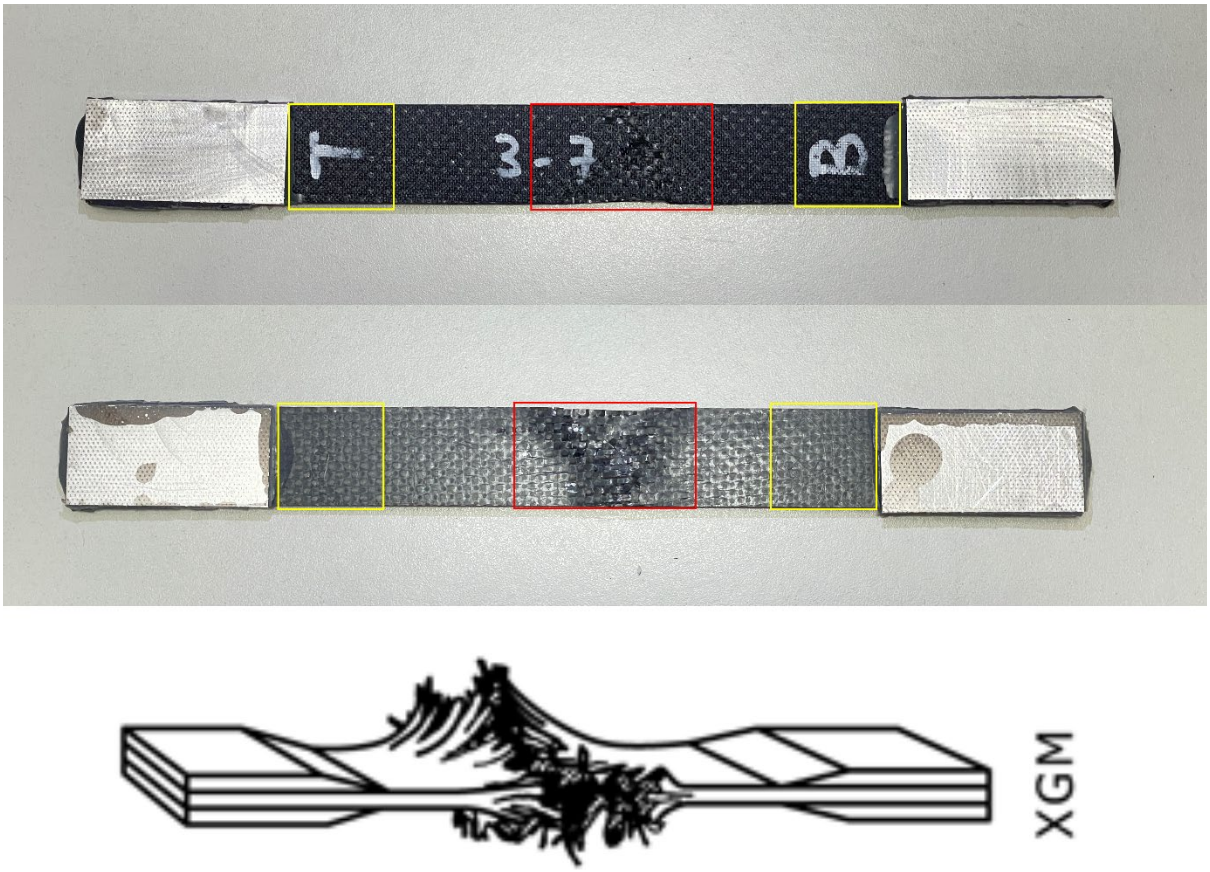

Figure 4.73 Specimen with failure mode - X G M (eXplosive type, Gage area, Middle location)

For the compatibility between the matrix phase and the sizing of the reinforcement phase, Figure 4.74 shows the ASTM D2344 failure mode of eight-ply plain-weaved CFRP composites with WS105/209 resin system. All specimens show a flexure compression failure mode which means the resin does not have a deformation consistent with the carbon fiber and the stress are not effectively transferred between them.

Summarizing the results from different tensile properties, the tensile behavior of plain-weaved composite plate is not consistent due to the incompatibility between the composite constituents. The eight-ply twill-weaved CFRP composite with WS105/209 resin system provides the most reliable and consistent tensile properties to be the control sample for comparing the mechanical performance of carbon nanotube incorporation.

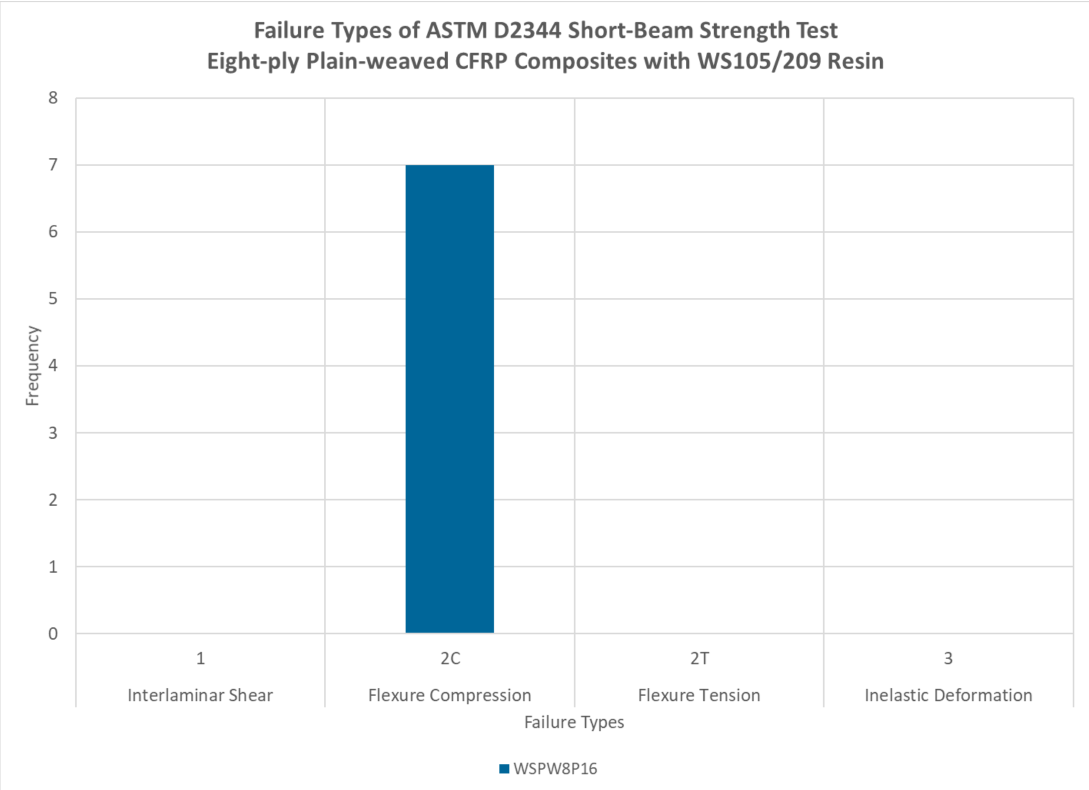

Figure 4.74 ASTM D2344 failure modes of eight-ply plain-weaved CFRP composites with WS105/209 resin system

4.4 Influence of carbon nanotube additive on CFRP composites

As the eight-ply twill-weaved CFRP composites with WS105/209 resin system provides reliable and consistent tensile properties results, the influence of CNT additive can be observed without any bias from other fabrication factors. CNT is added and well stirred into the WS105 resin before mixing with WS209 hardener and the rest of the fabrication steps are just the same as any eight-ply twill-weaved CFRP composite plates. In order to investigate the influence of CNT in thermal perspective, some specimens are being over-cured. Over-curing means the specimens were put in oven with a temperature higher than the curing temperature for a specific time after fabrication. In this study, the oven temperature was set to 25% above the glass transition temperature of the matrix phase, which is 72.5°C for WS105/209 resin system. Specimens were placed in the oven for 8 hours to ensure that the entire specimen was uniformly heated to the target temperature. Therefore, two batches of CNT specimens are fabricated and one batch of specimens is put in oven for over-curing. The results of these two batches of CNT specimens are compared to the control group which is the result of eight-ply twill-weaved CFRP composites with WS105/209 resin system from previous chapter and an addition batch for over-curing.

Figure 4.75 presents the stress-strain curves of specimens from the WSTW8PCNT19 composite plate. The stress-strain behavior of composite with CNT additive are more consistent than those in Figure 4.4, Figure 4.5, and Figure 4.6. All stress-strain curves of CNT specimens are almost collinear with each other. Figure 4.76 presents the stress-strain curves of specimens from the WSTW8POC21 composite plate. The stress-strain behavior of over-cured eight-ply twill-weaved CFRP composites with WS105/209 resin system are fluctuating than those without over-curing in Figure 4.4, Figure 4.5, and Figure 4.6. All stress-strain curves of over-cured specimens are wavy but a linear trend can still be observed. Figure 4.77 presents the stress-strain curves of specimens from the WSTW8PCNTOC23 composite plate. The stress-strain behavior of over-cured composite with CNT additive are similar to those without over-curing in Figure 4.75. All stress-strain curves of over-cured CNT specimens are straight and collinear with each other. Further compare the stress-strain behavior between the combination of over-curing and CNT additive, specimens with CNT additive show no changes between Figure 4.75 and Figure 4.77 after over-curing while specimens without CNT additive changed from consistent behavior to fluctuating behavior between Figure 4.4, Figure 4.5, Figure 4.6, and Figure 4.76. This indicated that CNT additive helps stabilize the composites during the over-curing process and keeps the stress-strain behavior unaffected from high temperature.

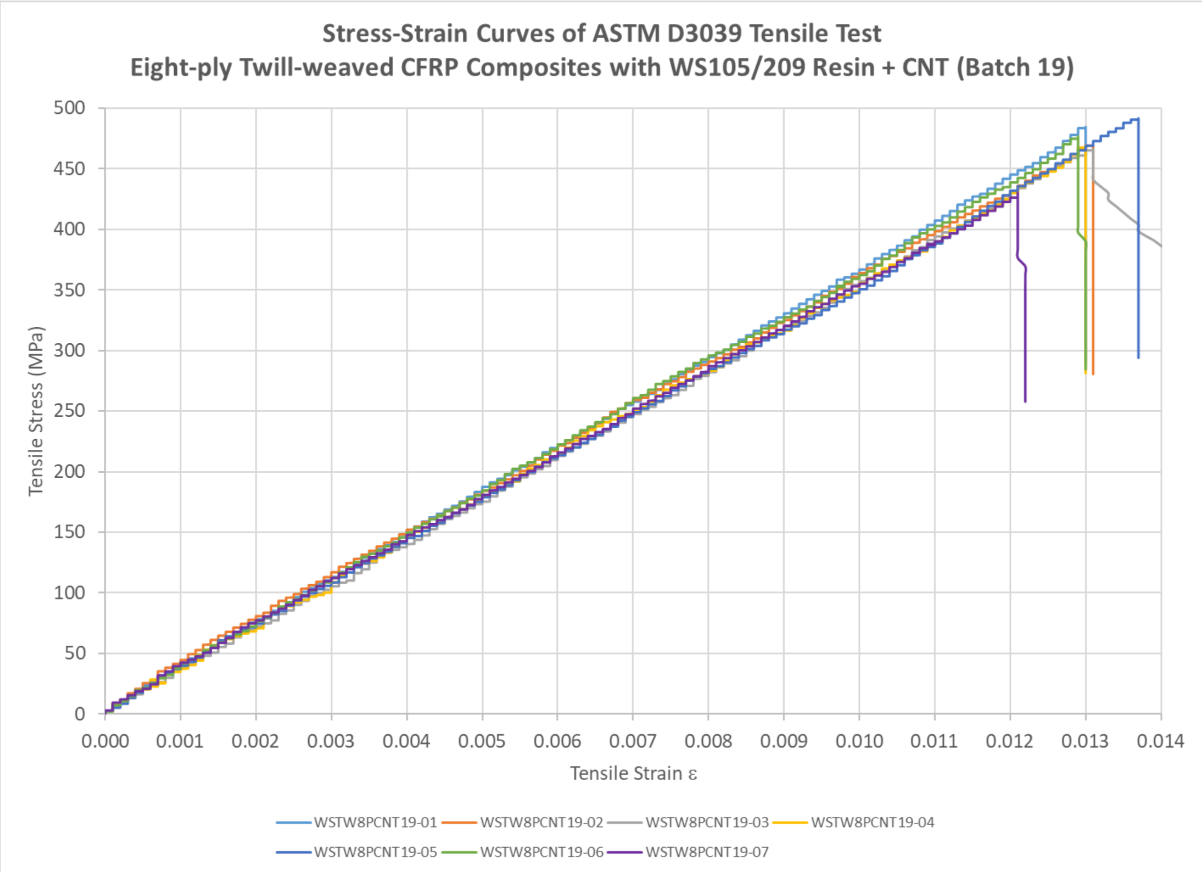

Figure 4.75 Stress-strain curve of eight-ply twill-weaved CFRP composites with WS105/209 resin system + CNT (Batch 19)

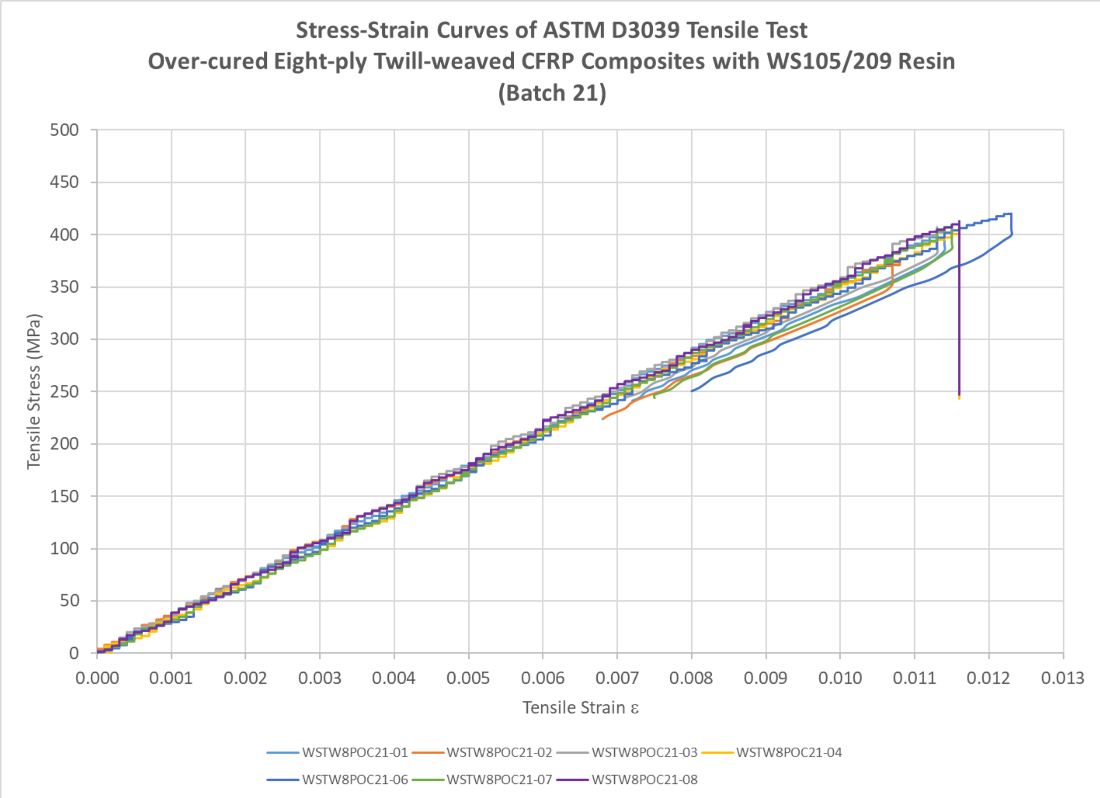

Figure 4.76 Stress-strain curve of over-cured eight-ply twill-weaved CFRP composites with WS105/209 resin system (Batch 21)

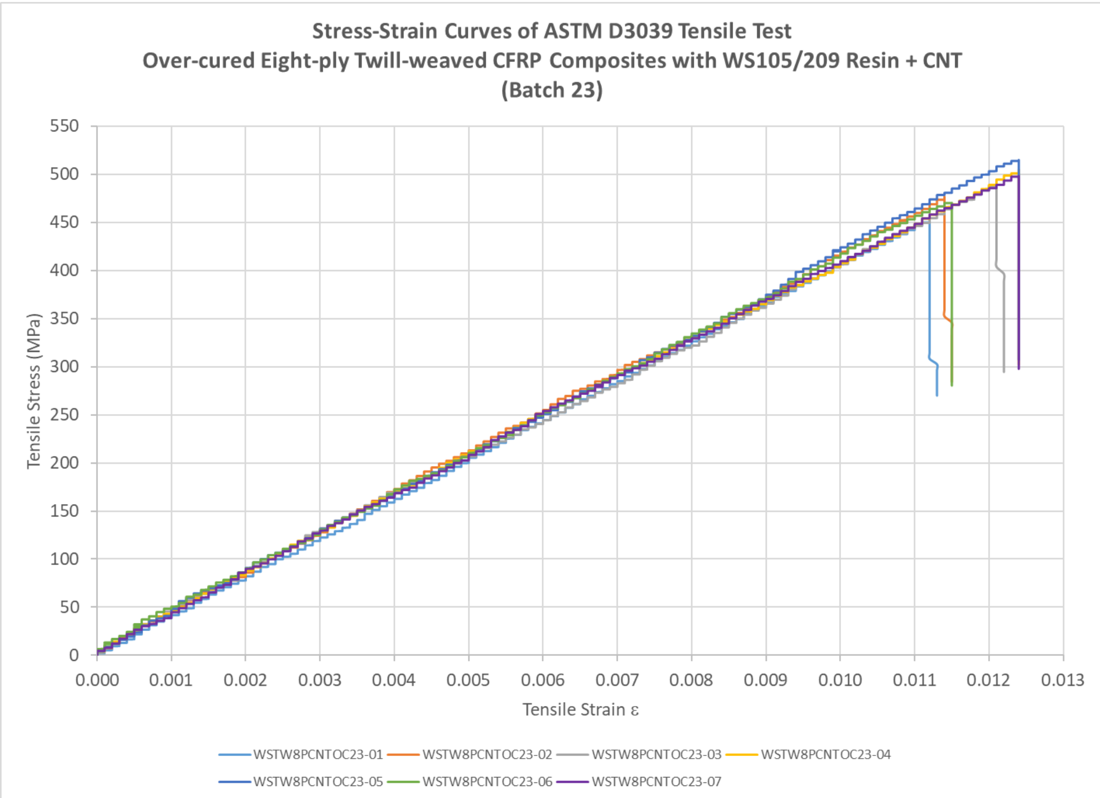

Figure 4.77 Stress-strain curve of over-cured eight-ply twill-weaved CFRP composites with WS105/209 resin system + CNT (Batch 23)

Table 4.24 and Table 4.26 show the comparison of ultimate tensile stress and ultimate tensile strain between the combination of over-curing and CNT additive. All fabrication conditions show similar consistency in the ultimate properties collected. Therefore, the dispersions of the failure points are similar when visualized in Figure 4.78, Figure 4.79, and Figure 4.80. Another interesting finding about the ultimate tensile stress is presented in Table 4.25. CNT was found enhancing the composites as there is a 4.44% increase in the maximum stress carried. Without CNT additive, composites experienced a 10% drop in ultimate tensile stress when over-cured. Surprisingly, composites with CNT additive experienced an increase of 3.62% in ultimate tensile stress instead of a decrease.

Table 4.24 Comparison of ultimate tensile stress between the combination of over-curing and CNT additive

Ultimate Tensile Stress						
	per composite plate			per fabrication condition		
	Mean (MPa)	SD (MPa)	CV	Mean (MPa)	SD (MPa)	CV
WSTW8P07	450	11.6	2.57	450	23.2	5.15
WSTW8P08	472	16.7	3.53			
WSTW8P09	429	17.0	3.96			
WSTW8PCNT19	470	19.6	4.18	470	19.6	4.18
WSTW8POC21	405	14.6	3.60	405	14.6	3.60
WSTW8PCNTOC23	487	21.7	4.45	487	21.7	4.45

Table 4.25 Percentage changes of ultimate tensile stress between the combination of over-curing and CNT additive

Ultimate Tensile Stress (MPa)			
WSTW8P	Without Over-curing	Over-cured	
without CNT	450	405	- 10%
with CNT	470	487	+ 3.62%
	+ 4.44%	+ 20.2%	

Table 4.26 Comparison of ultimate tensile strain between the combination of over-curing and CNT additive

Ultimate Tensile Strain						
	per composite plate			per fabrication condition		
	Mean	SD	CV	Mean	SD	CV
WSTW8P07	0.0122	0.0001	0.995	0.0120	0.0004	3.71
WSTW8P08	0.0119	0.0006	5.07			
WSTW8P09	0.0117	0.0004	3.14			
WSTW8PCNT19	0.0130	0.0005	3.62	0.0130	0.0005	3.62
WSTW8POC21	0.0115	0.0004	3.89	0.0115	0.0004	3.89
WSTW8PCNTOC23	0.0119	0.0005	4.45	0.0119	0.0005	4.45

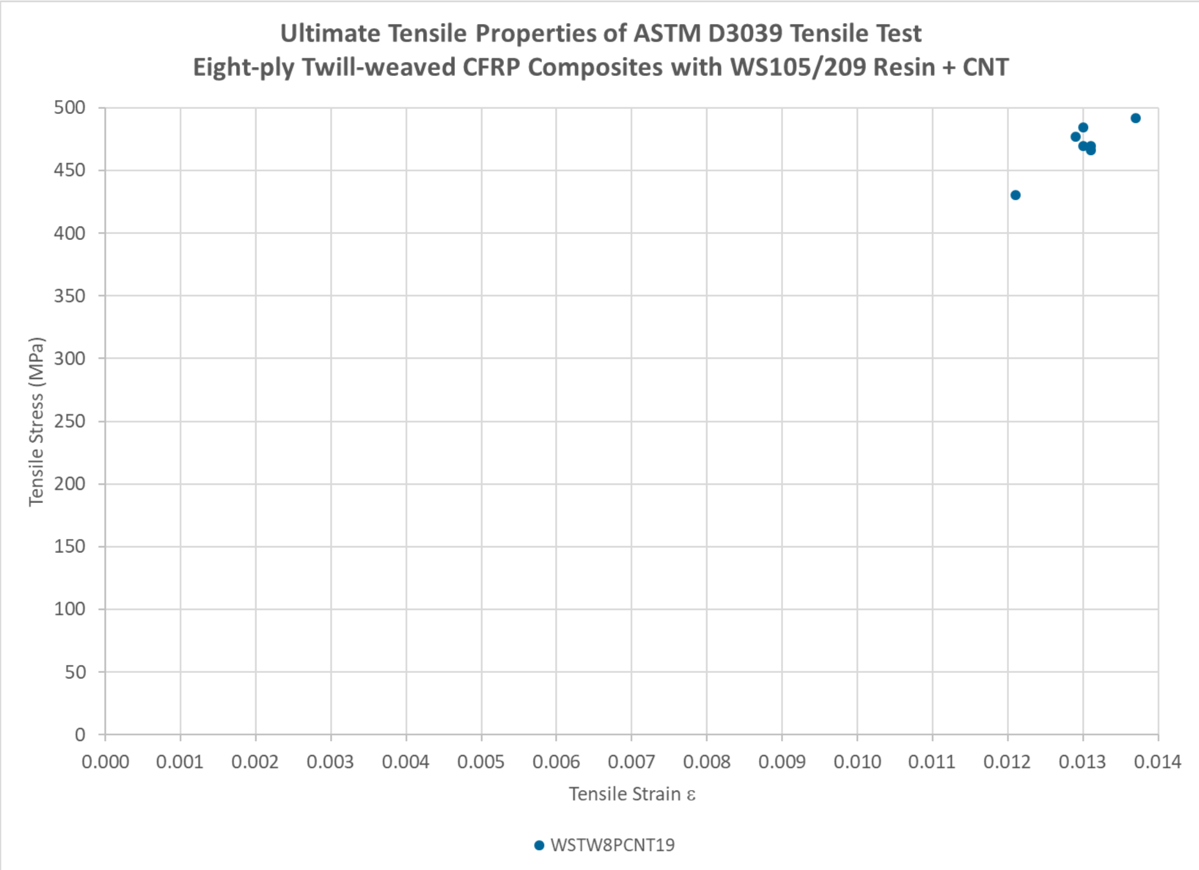

Figure 4.78 Ultimate tensile properties of eight-ply twill-weaved CFRP composites with WS105/209 resin system + CNT

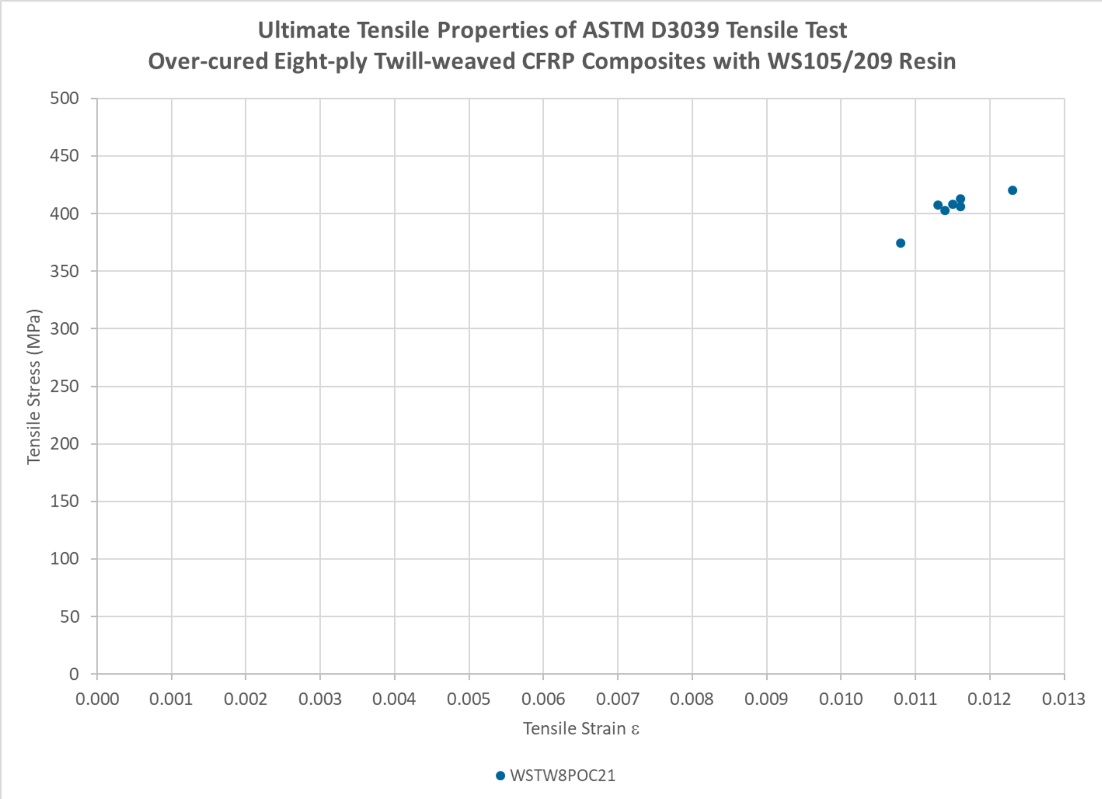

Figure 4.79 Ultimate tensile properties of over-cured eight-ply twill-weaved CFRP composites with WS105/209 resin system

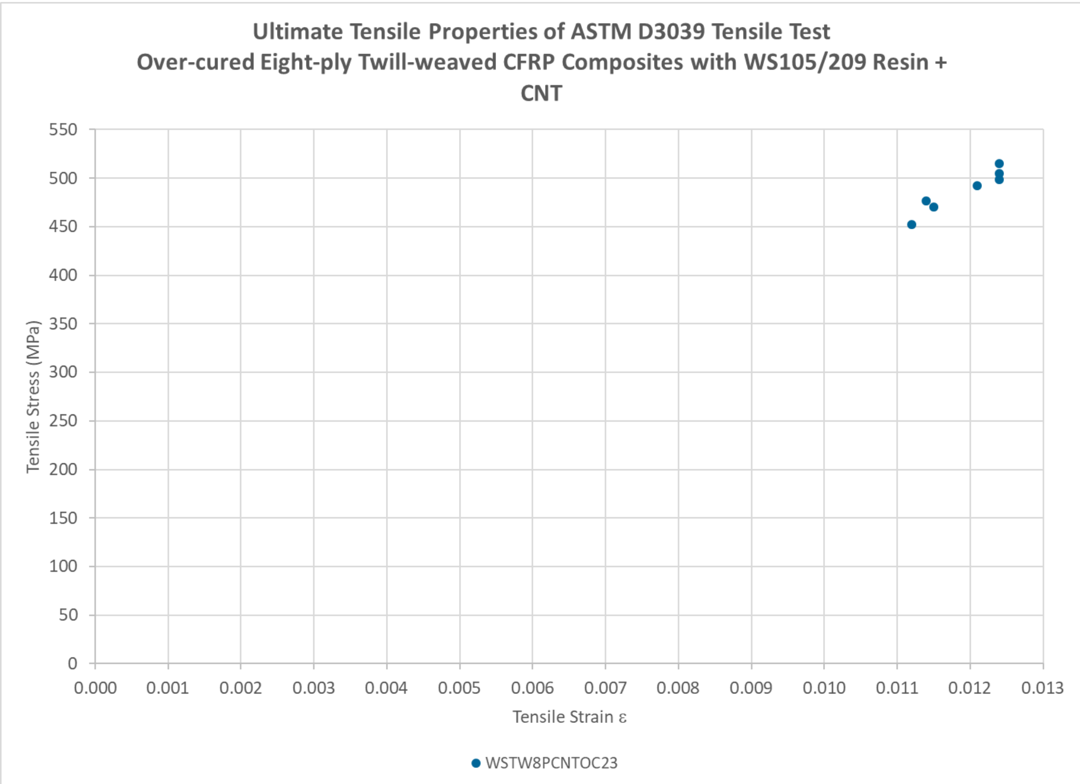

Figure 4.80 Ultimate tensile properties of over-cured eight-ply twill-weaved CFRP composites with WS105/209 resin system + CNT

Linear regression analysis was conducted on 6 random sets of ultimate tensile stress and ultimate tensile strain data from 7 specimens of WSTW8POC, WSTW8PCNT, and WSTW8PCNTOC. Tensile stress and tensile strain are continuous variables with a linear relationship as shown in Figure 4.75 to Figure 4.77. The ultimate tensile data used in linear regression also shows no obvious outliers in Figure 4.78 to Figure 4.80.

For eight-ply twill-weaved specimens with WS105/209 resin system and CNT additive, the significance value of one-way ANOVA is 0.184 which is not significant. Figure 4.81 and Figure 4.82 show the normal probability-probability plot and scatterplot respectively. The residuals of the data follow a normal distribution and the variance is consistent. However, the Durbin-Watson value is 1.263 indicating a slightly negative autocorrelation between data errors. Figure 4.83 presents the statistical result of a linear regression model with the following equation to demonstrate the relationship between tensile stress and tensile strain.

$$ultimate\ tensile\ stress = 191.826 + (21{,}663.597 \times ultimate\ tensile\ strain)$$

Equation 4.7 Linear regression model for ultimate tensile properties of eight-ply twill-weaved specimens with WS105/209 resin system +CNT

The R-squared value of the linear regression model is 0.391, indicating that 39.1% of the variation in tensile stress is related to tensile strain. This model is then used to predict the ultimate tensile stress of the remaining specimen. The predicted ultimate tensile stress is compared with the measured ultimate tensile stress of the specimen to validate the linear regression model. Table 4.27 shows the comparison between the predicted and measured ultimate tensile stresses of the three specimens. The predicted ultimate tensile stress deviate from the measured value by approximately 5%.

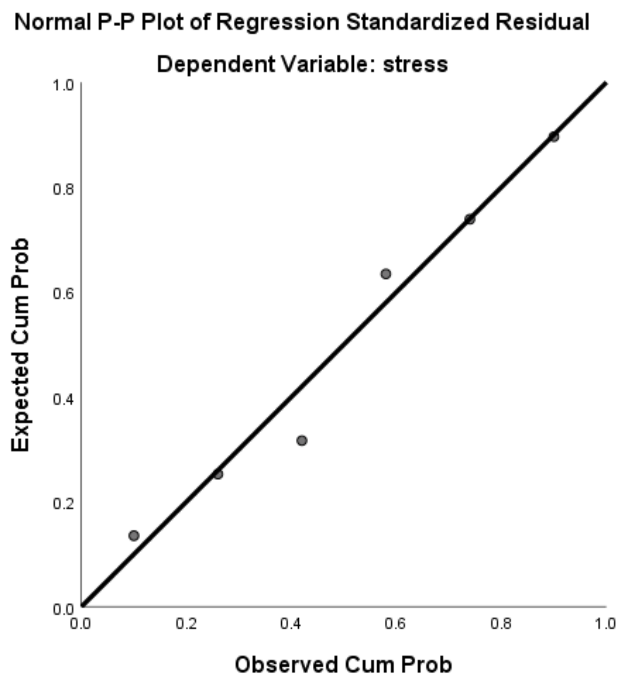

Figure 4.81 Normal probability-probability plot of regression standardized residuals of eight-ply twill-weaved specimens with WS105/209 resin system + CNT

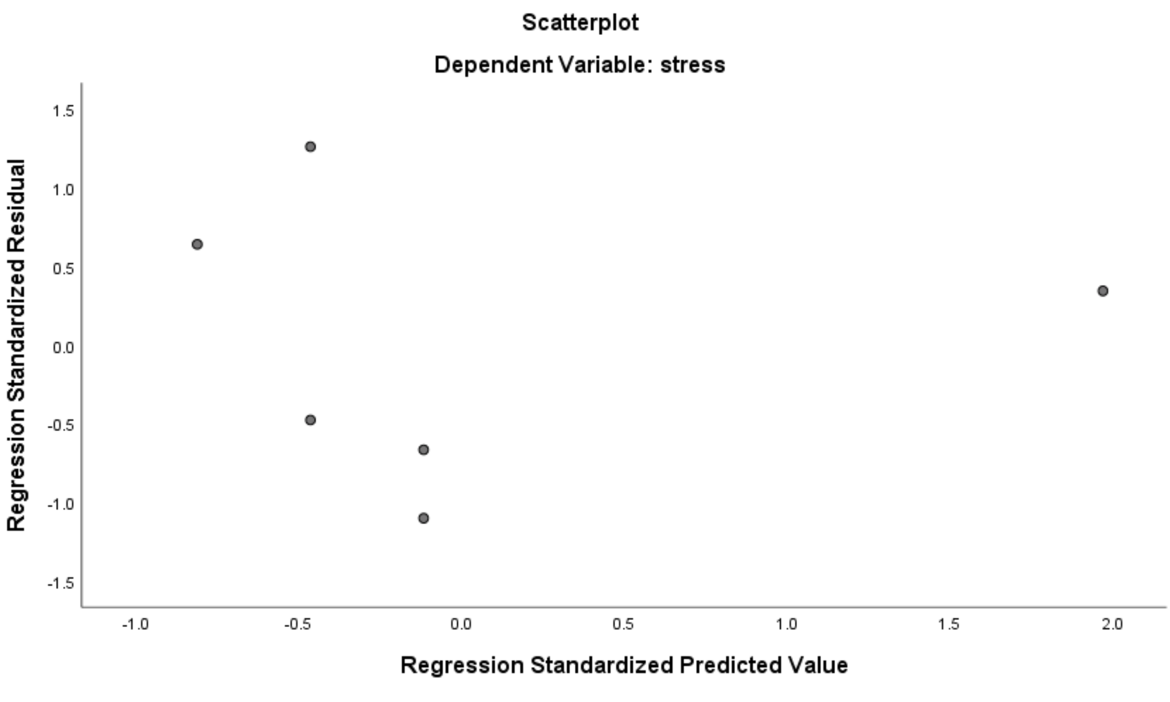

Figure 4.82 Scatterplot of regression standardized residuals against regression standardized predicted values of eight-ply twill-weaved specimens with WS105/209 resin system + CNT

Model Summary[b]

Model	R	R Square	Adjusted R Square	Std. Error of the Estimate	Durbin-Watson
1	.625[a]	.391	.239	8.6878577	1.263

a. Predictors: (Constant), long_strain

b. Dependent Variable: stress

ANOVA[a]

Model		Sum of Squares	df	Mean Square	F	Sig.
1	Regression	193.982	1	193.982	2.570	.184[b]
	Residual	301.915	4	75.479		
	Total	495.898	5			

a. Dependent Variable: stress

b. Predictors: (Constant), long_strain

Coefficients[a]

Model		Unstandardized Coefficients		Standardized Coefficients	t	Sig.
		B	Std. Error	Beta		
1	(Constant)	191.826	177.511		1.081	.341
	long_strain	21663.597	13513.333	.625	1.603	.184

a. Dependent Variable: stress

Figure 4.83 Linear regression model results of eight-ply twill-weaved specimens with WS105/209 resin system + CNT

Table 4.27 Comparison between predicted and actual ultimate tensile stress of eight-ply twill-weaved specimens with WS105/209 resin system + CNT

Specimens	Actual ultimate tensile strain	Predicted ultimate tensile stress	Actual ultimate tensile stress	Deviation
WSTW8PCNT 19-07	0.0121	453.9555	430.2623	5.51%

For over-cured eight-ply twill-weaved specimens with WS105/209 resin system, the significance value of one-way ANOVA is 0.016. Figure 4.84 and Figure 4.85 show the normal probability-probability plot and scatterplot respectively. The residuals of the data follow a normal distribution and the variance is consistent. However, the Durbin-Watson value is 3.028 indicating a positive autocorrelation between data errors. Figure 4.86 presents the statistical result of a linear regression model with the following equation to demonstrate the relationship between tensile stress and tensile strain.

$$ultimate\ tensile\ stress = 78.621 + (28{,}257.783 \times ultimate\ tensile\ strain)$$

Equation 4.8 Linear regression model for ultimate tensile properties of over-cured eight-ply twill-weaved specimens with WS105/209 resin system

The R-squared value of the linear regression model is 0.799, indicating that 79.9% of the variation in tensile stress is related to tensile strain. This model is then used to predict the ultimate tensile stress of the remaining specimen. The predicted ultimate tensile stress is compared with the measured ultimate tensile stress of the specimen to validate the linear regression model. Table 4.28 shows the comparison between the predicted and measured ultimate tensile stresses of the three specimens. The predicted ultimate tensile stress deviate from the measured value by approximately 2%.

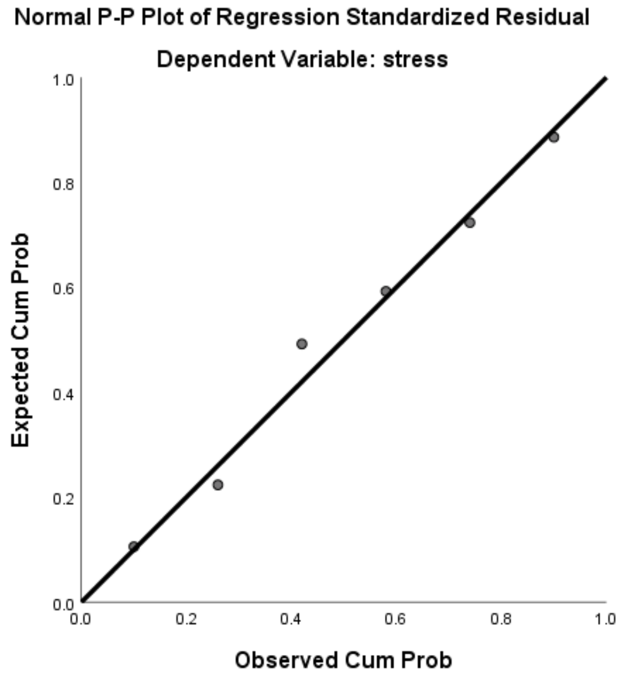

Figure 4.84 Normal probability-probability plot of regression standardized residuals of over-cured eight-ply twill-weaved specimens with WS105/209 resin system

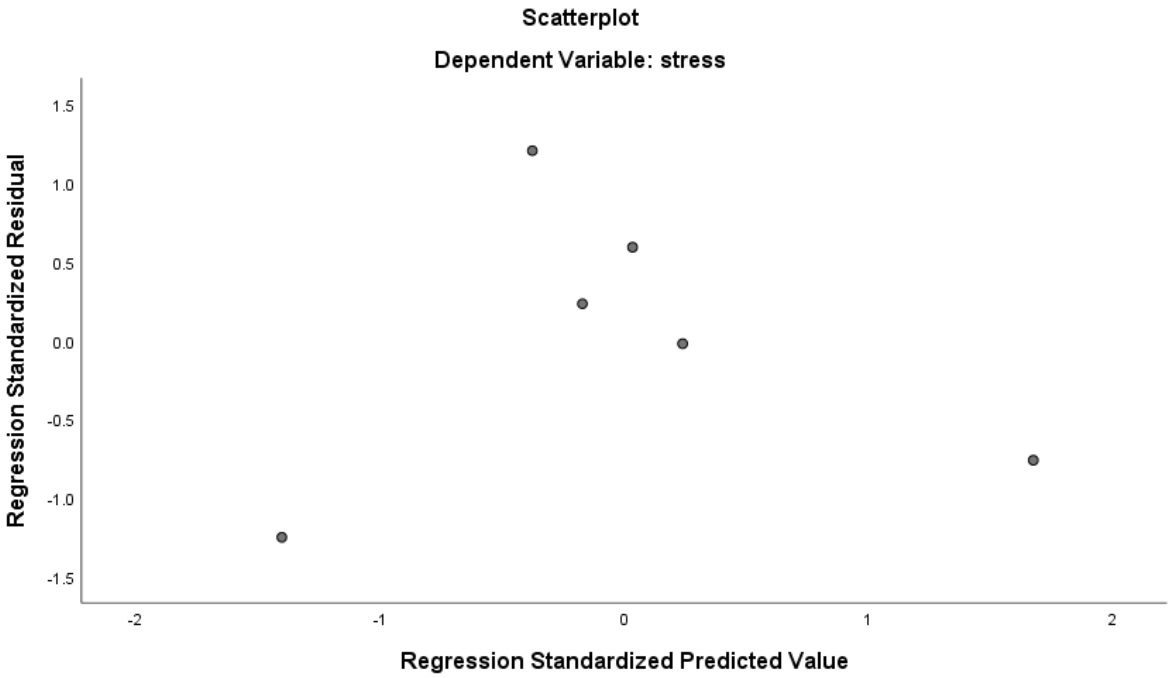

Figure 4.85 Scatterplot of regression standardized residuals against regression standardized predicted values of over-cured eight-ply twill-weaved specimens with WS105/209 resin system

Model Summary[b]

Model	R	R Square	Adjusted R Square	Std. Error of the Estimate	Durbin-Watson
1	.894[a]	.799	.748	7.7353085	3.028

a. Predictors: (Constant), long_strain

b. Dependent Variable: stress

ANOVA[a]

Model		Sum of Squares	df	Mean Square	F	Sig.
1	Regression	948.887	1	948.887	15.858	.016[b]
	Residual	239.340	4	59.835		
	Total	1188.227	5			

a. Dependent Variable: stress

b. Predictors: (Constant), long_strain

Coefficients[a]

Model		Unstandardized Coefficients		Standardized Coefficients	t	Sig.
		B	Std. Error	Beta		
1	(Constant)	78.621	81.546		.964	.390
	long_strain	28257.783	7095.917	.894	3.982	.016

a. Dependent Variable: stress

Figure 4.86 Linear regression model results of over-cured eight-ply twill-weaved specimens with WS105/209 resin system

Table 4.28 Comparison between predicted and actual ultimate tensile stress of over-cured eight-ply twill-weaved specimens with WS105/209 resin system

Specimens	Actual ultimate tensile strain	Predicted ultimate tensile stress	Actual ultimate tensile stress	Deviation
WSTW8POC 21-08	0.0116	406.4113	413.1313	-1.63%

For over-cured eight-ply twill-weaved specimens with WS105/209 resin system and CNT additive, the significance value of one-way ANOVA is 0.002. Figure 4.87 and Figure 4.88 show the normal probability-probability plot and scatterplot respectively. The residuals of the data follow a normal distribution and the variance is consistent. However, the Durbin-Watson value is 2.921 indicating a slightly positive autocorrelation between data errors. Figure 4.89 presents the statistical result of a linear regression model with the following equation to demonstrate the relationship between tensile stress and tensile strain.

$$ultimate\ tensile\ stress = -9.385 + (41{,}798.517 \times ultimate\ tensile\ strain)$$

Equation 4.9 Linear regression model for ultimate tensile properties of over-cured eight-ply twill-weaved specimens with WS105/209 resin system + CNT

The R-squared value of the linear regression model is 0.922, indicating that 92.2% of the variation in tensile stress is related to tensile strain. This model is then used to predict the ultimate tensile stress of the remaining specimen. The predicted ultimate tensile stress is compared with the measured ultimate tensile stress of the specimen to validate the linear regression model. Table 4.29 shows the comparison between the predicted and measured ultimate tensile stresses of the three specimens. The predicted ultimate tensile stress deviate from the measured value by approximately 2%.

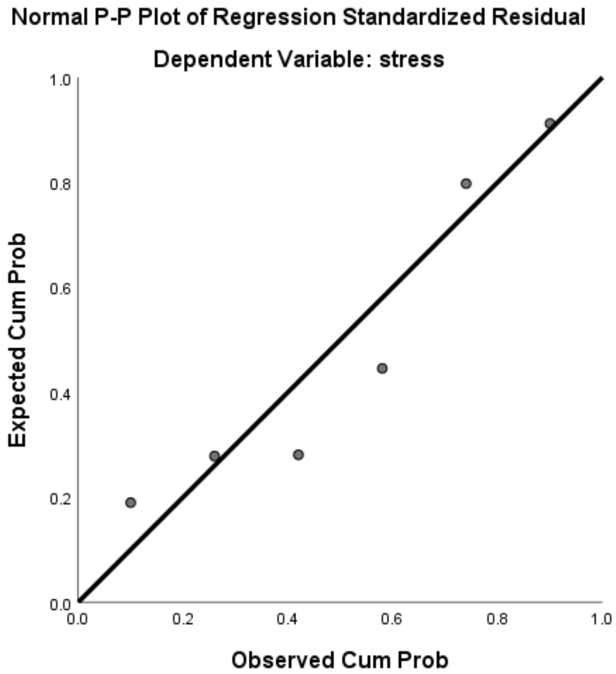

Figure 4.87 Normal probability-probability plot of regression standardized residuals of over-cured eight-ply twill-weaved specimens with WS105/209 resin system + CNT

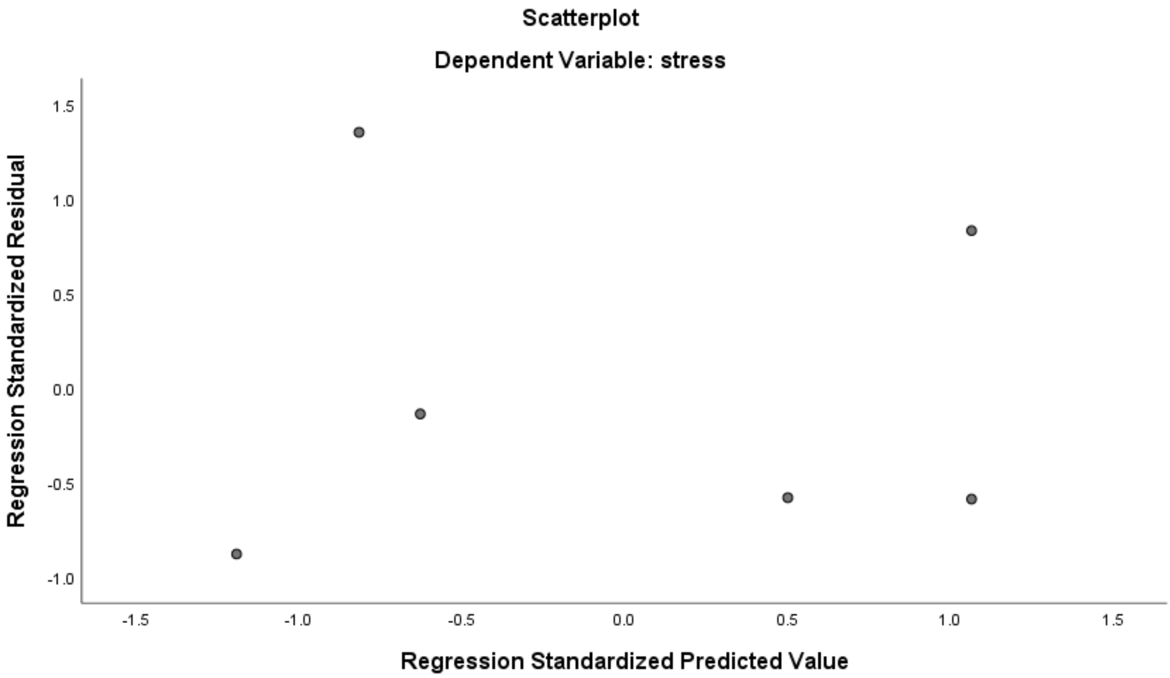

Figure 4.88 Scatterplot of regression standardized residuals against regression standardized predicted values of over-cured eight-ply twill-weaved specimens with WS105/209 resin system + CNT

Model Summary[b]

Model	R	R Square	Adjusted R Square	Std. Error of the Estimate	Durbin-Watson
1	.960[a]	.922	.903	7.2143965	2.921

a. Predictors: (Constant), long_strain

b. Dependent Variable: stress

ANOVA[a]

Model		Sum of Squares	df	Mean Square	F	Sig.
1	Regression	2469.257	1	2469.257	47.442	.002[b]
	Residual	208.190	4	52.048		
	Total	2677.447	5			

a. Dependent Variable: stress

b. Predictors: (Constant), long_strain

Coefficients[a]

Model		Unstandardized Coefficients		Standardized Coefficients	t	Sig.
		B	Std. Error	Beta		
1	(Constant)	-9.385	71.870		-.131	.902
	long_strain	41798.517	6068.449	.960	6.888	.002

a. Dependent Variable: stress

Figure 4.89 Linear regression model results of over-cured eight-ply twill-weaved specimens with WS105/209 resin system + CNT

Table 4.29 Comparison between predicted and actual ultimate tensile stress of over-cured eight-ply twill-weaved specimens with WS105/209 resin system + CNT

Specimens	Actual ultimate tensile strain	Predicted ultimate tensile stress	Actual ultimate tensile stress	Deviation
WSTW8PCNT OC23-07	0.0124	508.9166	498.2193	2.15%

The linear regression model of WSTW8PCNT has a slightly higher significance value of one-way ANOVA and a low R-square value. The dependency on ultimate tensile strain is not as high as Equation 4.2. For linear regression models of WSTW8POC and WSTW8PCNTOC, both models have parameters positively indicating their significance and accuracy. Despite the small sample size, the predicted ultimate tensile stresses are consistent with actual values.

Table 4.30 and Table 4.31 further compares the modulus of elasticity and Poisson's ratio between the combination of over-curing and CNT additive. All fabrication conditions show similar consistency in the modulus of elasticity. WSTW8PCNT19 and WSTW8POC21 composite plates show a lower mean modulus of elasticity than eight-ply twill-weaved CFRP composites with WS105/209 resin system. WSTW8PCNT19 composite plate show a higher consistency in Poisson's ratio than other composite plates. All fabrication conditions have a similar mean Poisson's ratio.

Table 4.30 Comparison of modulus of elasticity between the combination of over-curing and CNT additive

Modulus of Elasticity						
	per composite plate			per fabrication condition		
	Mean (GPa)	SD (GPa)	CV	Mean (GPa)	SD (GPa)	CV
WSTW8P07	39.7	1.25	3.14	40.0	1.99	4.98
WSTW8P08	41.2	2.09	5.07			
WSTW8P09	39.1	2.15	5.50			
WSTW8PCNT19	34.6	1.30	3.77	34.6	1.30	3.77
WSTW8POC21	34.5	2.01	5.83	34.5	2.01	5.83
WSTW8PCNTOC23	41.2	1.83	4.44	41.2	1.83	4.44

Table 4.31 Comparison of Poisson's ratio between the combination of over-curing and CNT additive

Poisson's Ratio						
	per composite plate			per fabrication condition		
	Mean	SD	CV	Mean	SD	CV
WSTW8P07	0.370	0.0650	17.6	0.370	0.0670	18.1
WSTW8P08	0.363	0.0560	15.4			
WSTW8P09	0.377	0.0864	22.9			
WSTW8PCNT19	0.382	0.0331	8.67	0.382	0.0331	8.67
WSTW8POC21	0.392	0.0481	12.3	0.392	0.0481	12.3
WSTW8PCNTOC23	0.355	0.0579	16.3	0.355	0.0579	16.3

For the failure mode of ASTM D3039, Figure 4.90, Figure 4.93 and Figure 4.96 shows the failure types, failure areas and failure locations of WSTW8PCNT19 composites specimens. Figure 4.91, Figure 4.94 and Figure 4.97 shows the failure types, failure areas and failure locations of WSTW8POC21 composites specimens. Figure 4.92, Figure 4.95 and Figure 4.98 shows the failure types, failure areas and failure locations of WSTW8PCNTOC23 composites specimens. Together with Figure 4.22, Figure 4.23 and Figure 4.24 from Chapter 4.1, the failure modes does not show a particular failure pattern on whether the specimens are over-cured or have CNT additive.

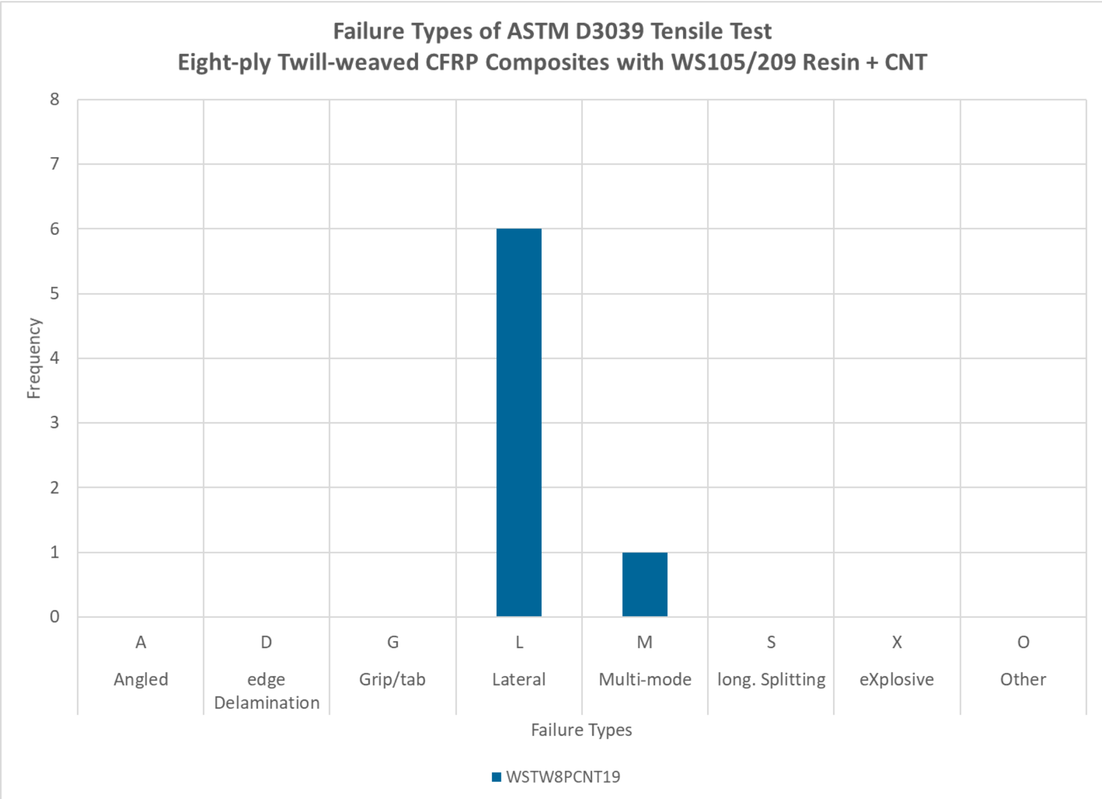

Figure 4.90 ASTM D3039 failure types of eight-ply twill-weaved CFRP composites with WS105/209 resin system + CNT

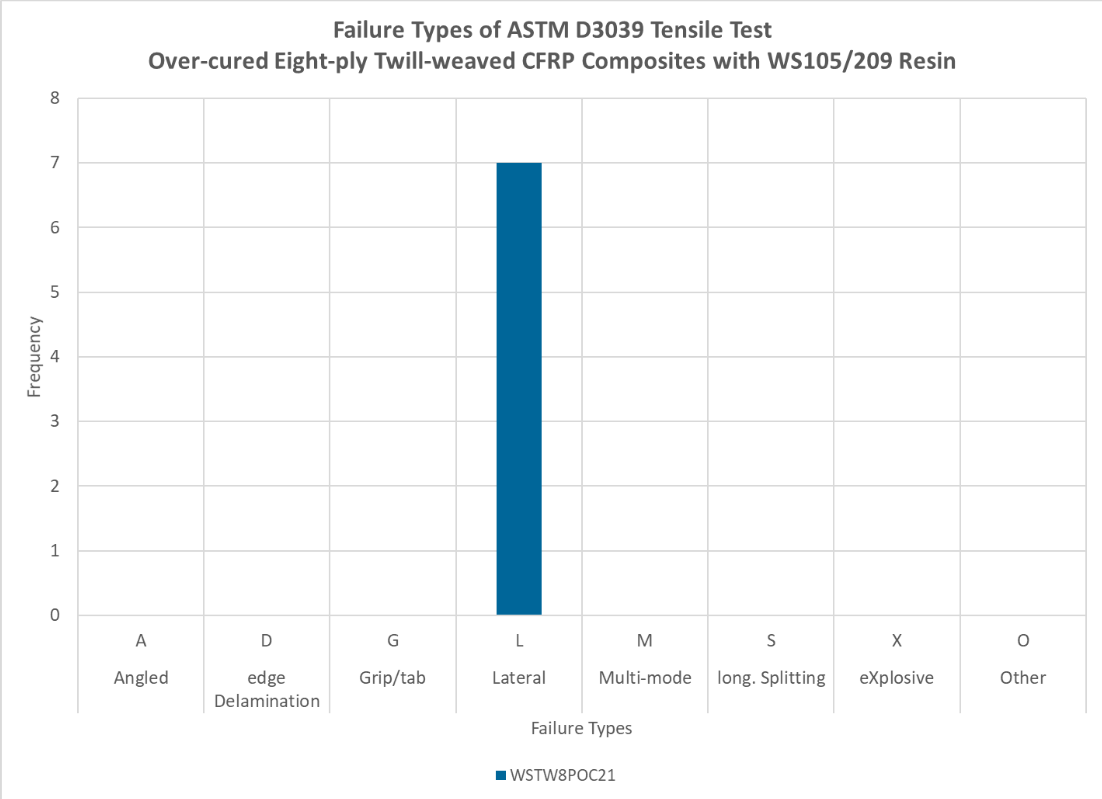

Figure 4.91 ASTM D3039 failure types of over-cured eight-ply twill-weaved CFRP composites with WS105/209 resin system

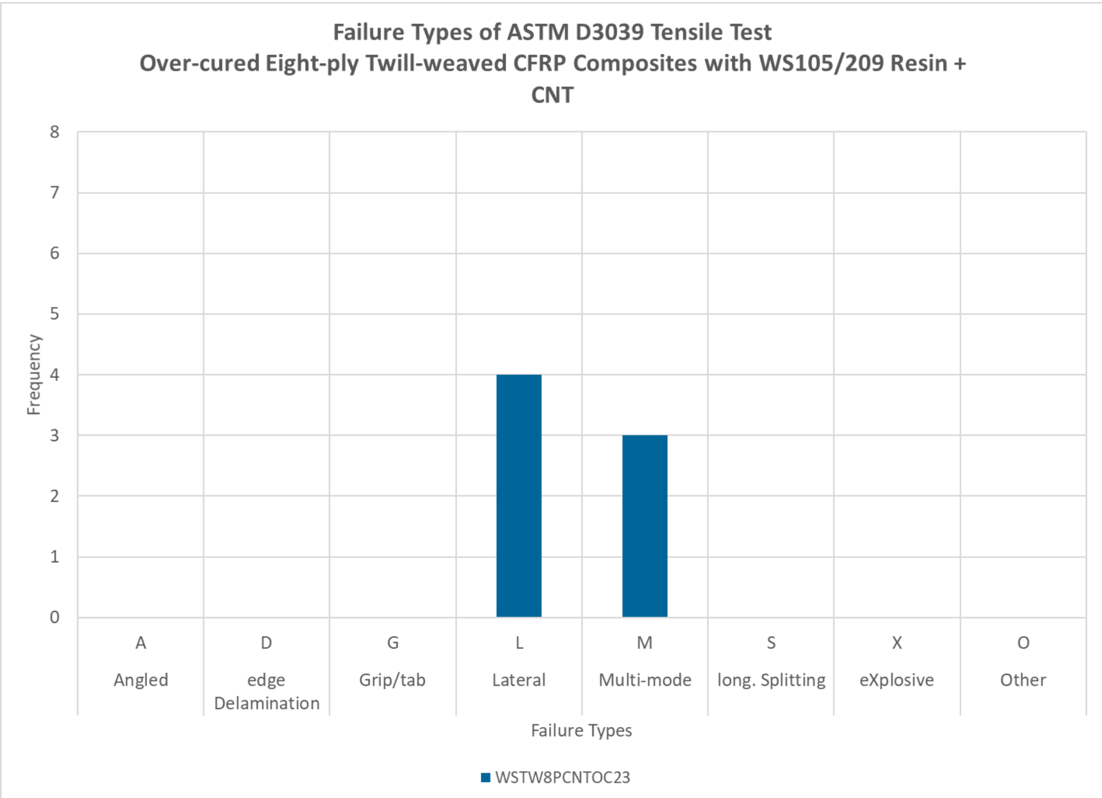

Figure 4.92 ASTM D3039 failure types of over-cured eight-ply twill-weaved CFRP composites with WS105/209 resin system + CNT

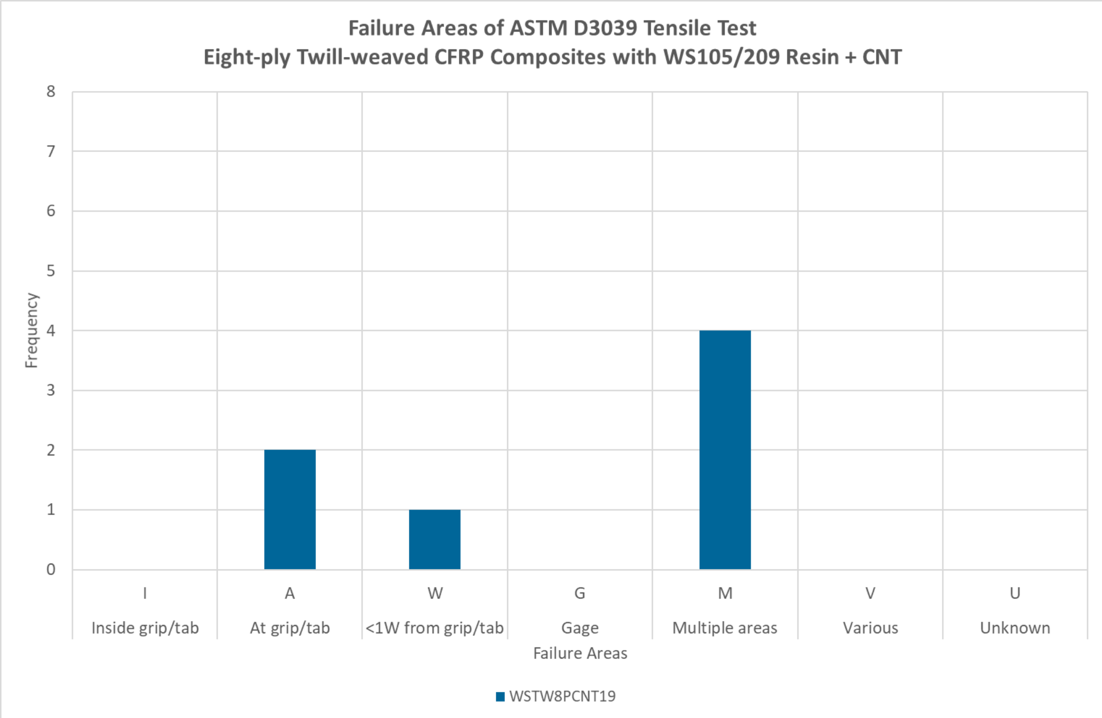

Figure 4.93 ASTM D3039 failure areas of eight-ply twill-weaved CFRP composites with WS105/209 resin system + CNT

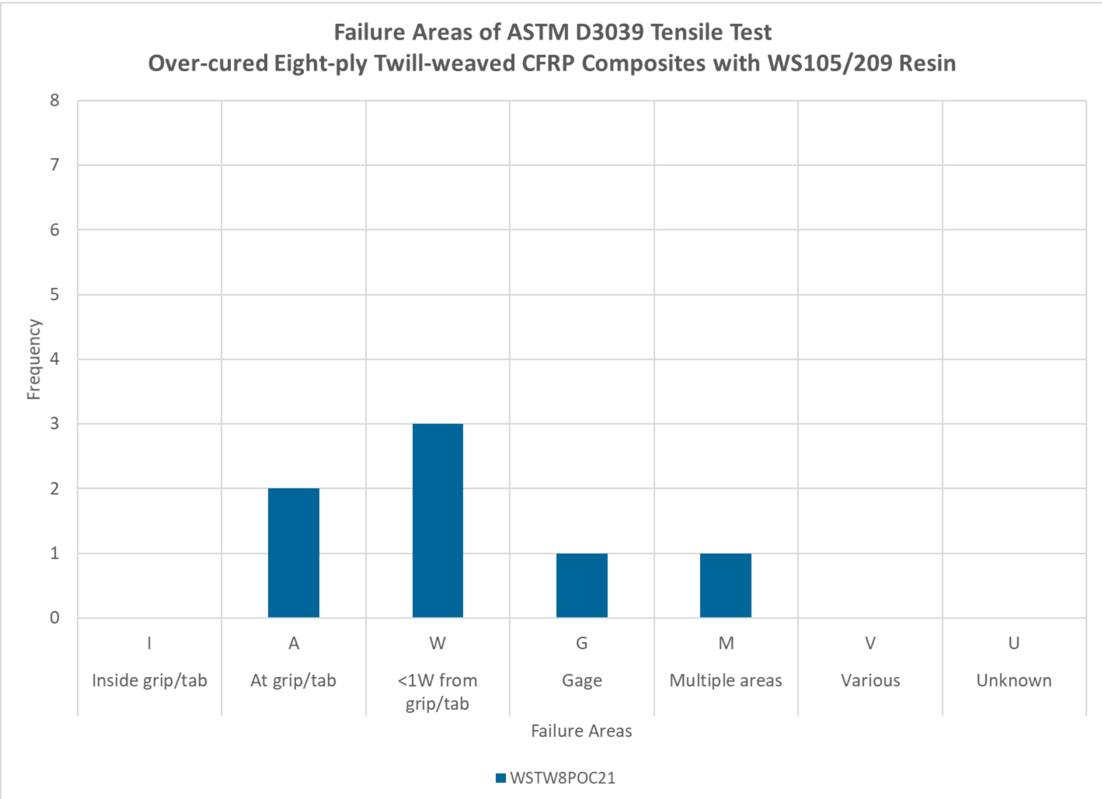

Figure 4.94 ASTM D3039 failure areas of over-cured eight-ply twill-weaved CFRP composites with WS105/209 resin system

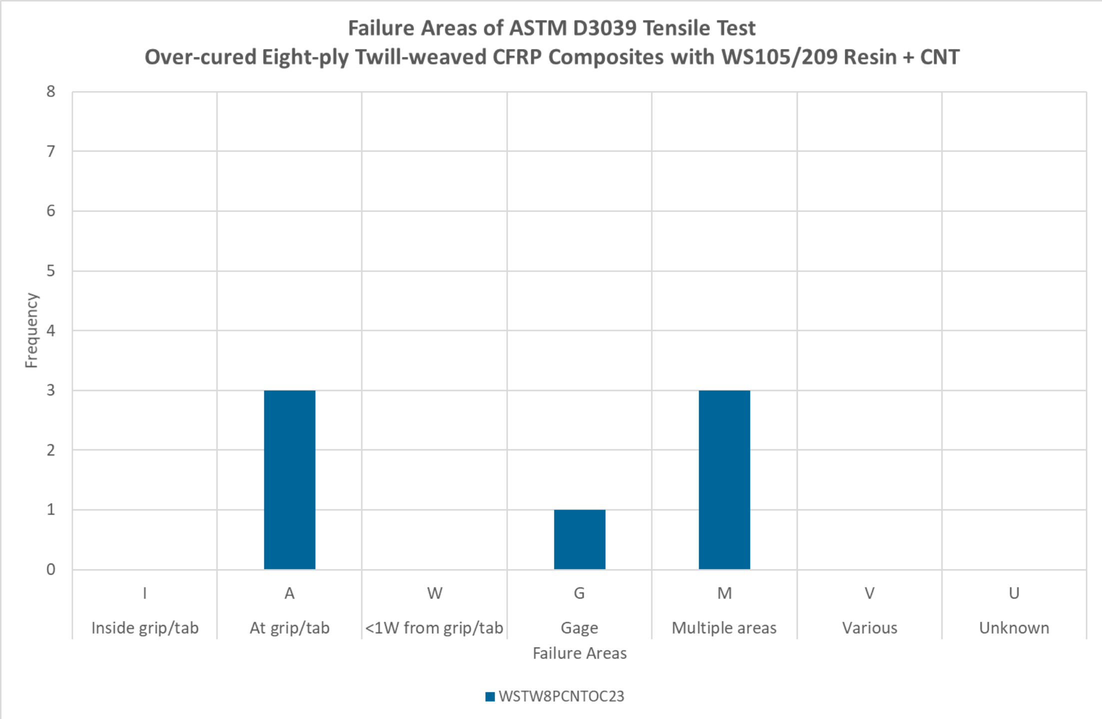

Figure 4.95 ASTM D3039 failure areas of over-cured eight-ply twill-weaved CFRP composites with WS105/209 resin system + CNT

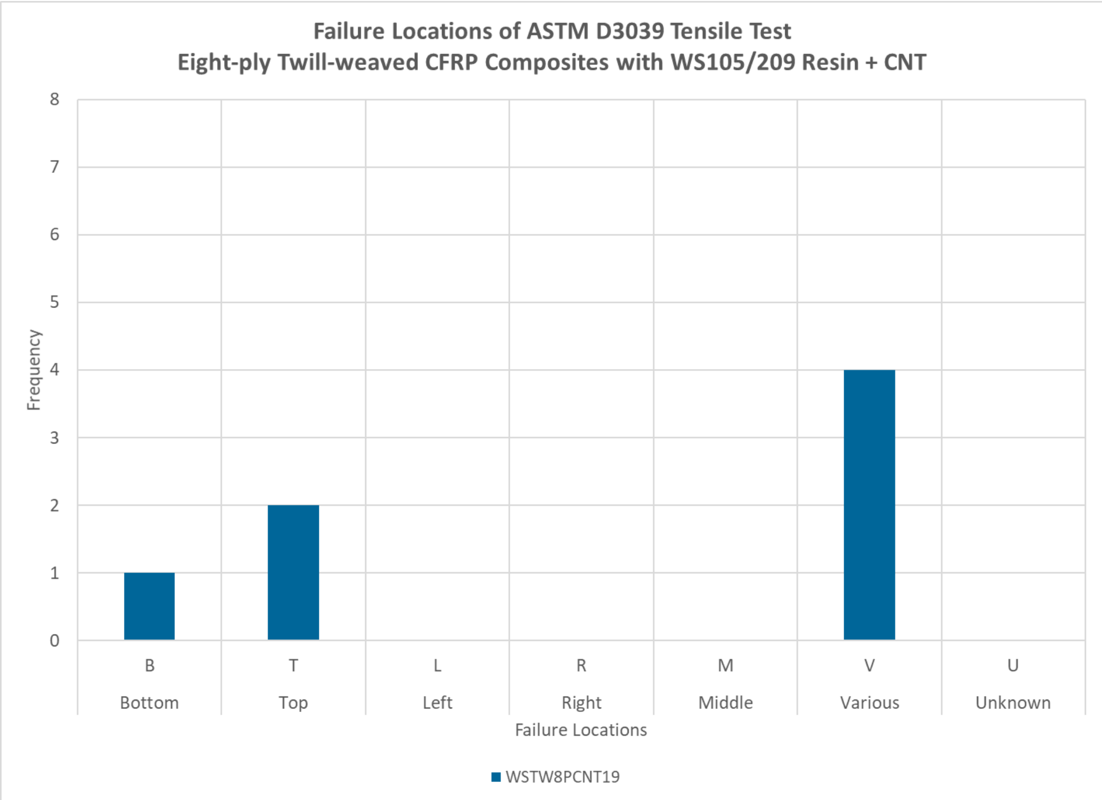

Figure 4.96 ASTM D3039 failure locations of eight-ply twill-weaved CFRP composites with WS105/209 resin system + CNT

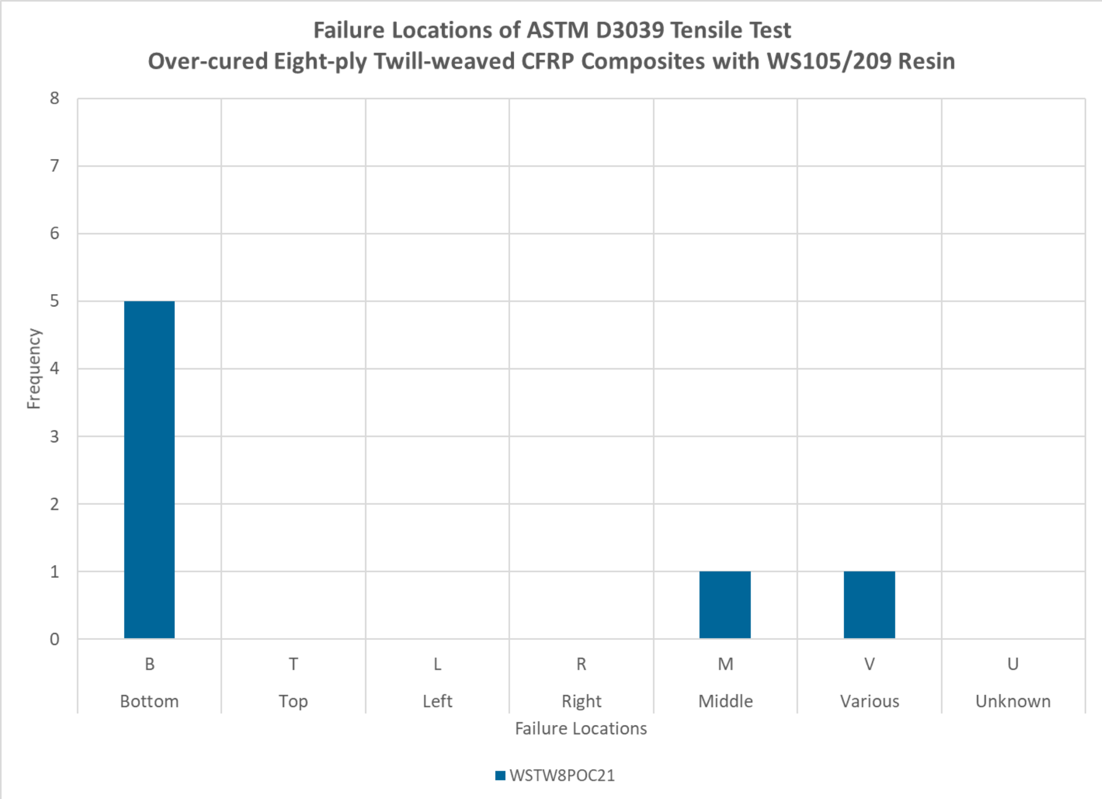

Figure 4.97 ASTM D3039 failure locations of over-cured eight-ply twill-weaved CFRP composites with WS105/209 resin system

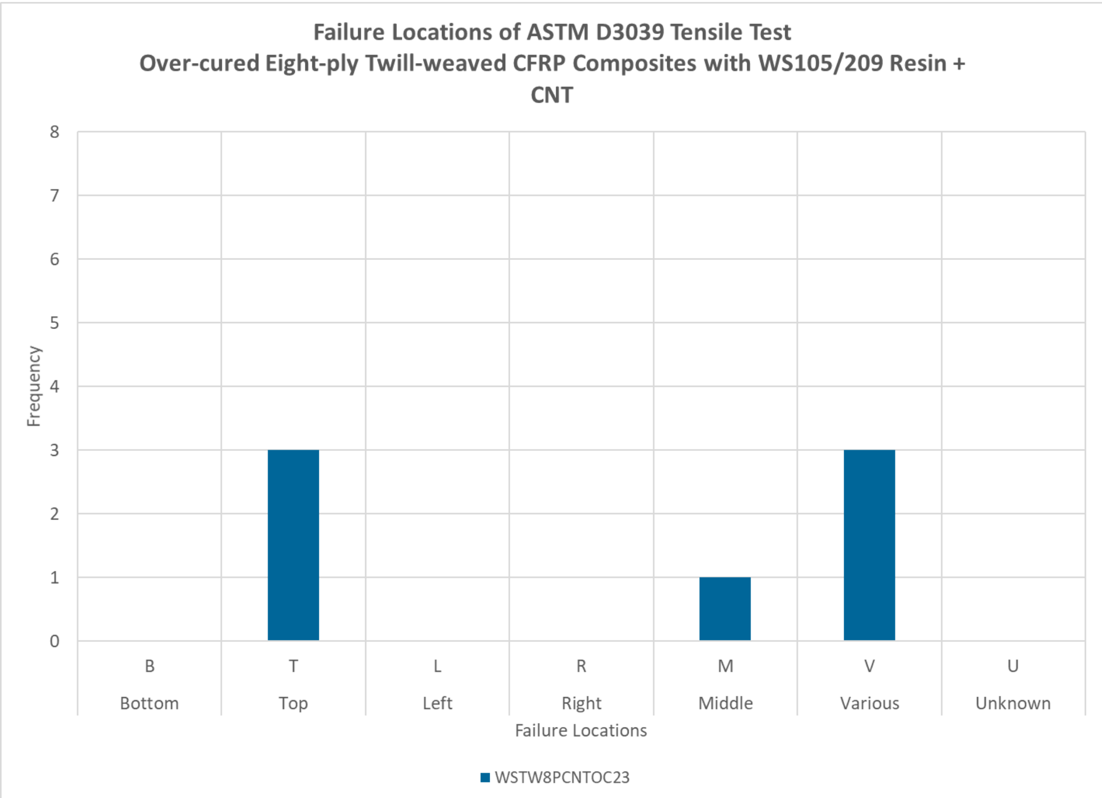

Figure 4.98 ASTM D3039 failure locations of over-cured eight-ply twill-weaved CFRP composites with WS105/209 resin system + CNT

Specimens for eight-ply twill-weaved CFRP composites with WS105/209 resin system and CNT additive are fractured in four failure mode combinations: L M V, M M V, L W B, and L A T. Specimens for over-cured eight-ply twill-weaved CFRP composites with WS105/209 resin system are fractured in four failure mode combinations: L M V, L G M, L W B, and L A B. Specimens for over-cured eight-ply twill-weaved CFRP composites with WS105/209 resin system and CNT additive are fractured in three failure mode combinations: M M V, L G M, and L A T. For L M V, M M V, and L G M failure modes, example can be found in failure modes of specimens from WSTW4P composite plates. For L W B failure modes, example can be found in failure modes of specimens from WSTW8P composite plates. For L A T failure modes, example can be found in failure modes of specimens from MLTW4P composite plates. For L A B failure modes, example can be found in failure modes of specimens from MLTW8P composite plates.

As a result of an accident occurring during the waterjet machining process, one of the composite plates with CNT additive shifted, causing the waterjet to operate in an incorrect trajectory. Immediately after the incident, the waterjet machining process was terminated, and the composite plate was repositioned to align with the original cutting path. However, due to the removal of some materials prior to the machine's shutdown, specimens for ASTM D2344 of the composite plates were destroyed. Due to limited resources for fabricating an additional batch of specimens with CNT additive, only one batch of ASTM D2344 specimens remained for testing the influence of over-curing. This situation gives no choice but to split the only batch of ASTM D2344 specimens with CNT additive into two, with four specimens allocated for over-curing and four serving as control samples. Figure 4.99, Figure 4.100 and Figure 4.101 show the ASTM D2344 failure modes of WSTW8PCNT19, WSTW8POC21, and WSTW8PCNTOC23 composite plates respectively. Specimens from WSTW8POC21 composite plate show a flexure compression failure mode. Compare with Figure 4.28 from

Chapter 4.1, over-cured specimens changed from flexure tension failure mode to compression. This indicated that the matrix phase can no longer transfer stress to or from reinforcement phase effectively. The over-curing process changed the stress-strain behavior of the matrix phase which makes the deformation of matrix phase inconsistent with the carbon fiber. For specimens with CNT additive, all specimens from WSTW8PCNT19 and WSTW8PCNTOC23 show a flexure tension failure mode. This indicated that the resin is still well bonded with the carbon fiber after the over-curing when CNT is added into the matrix phase.

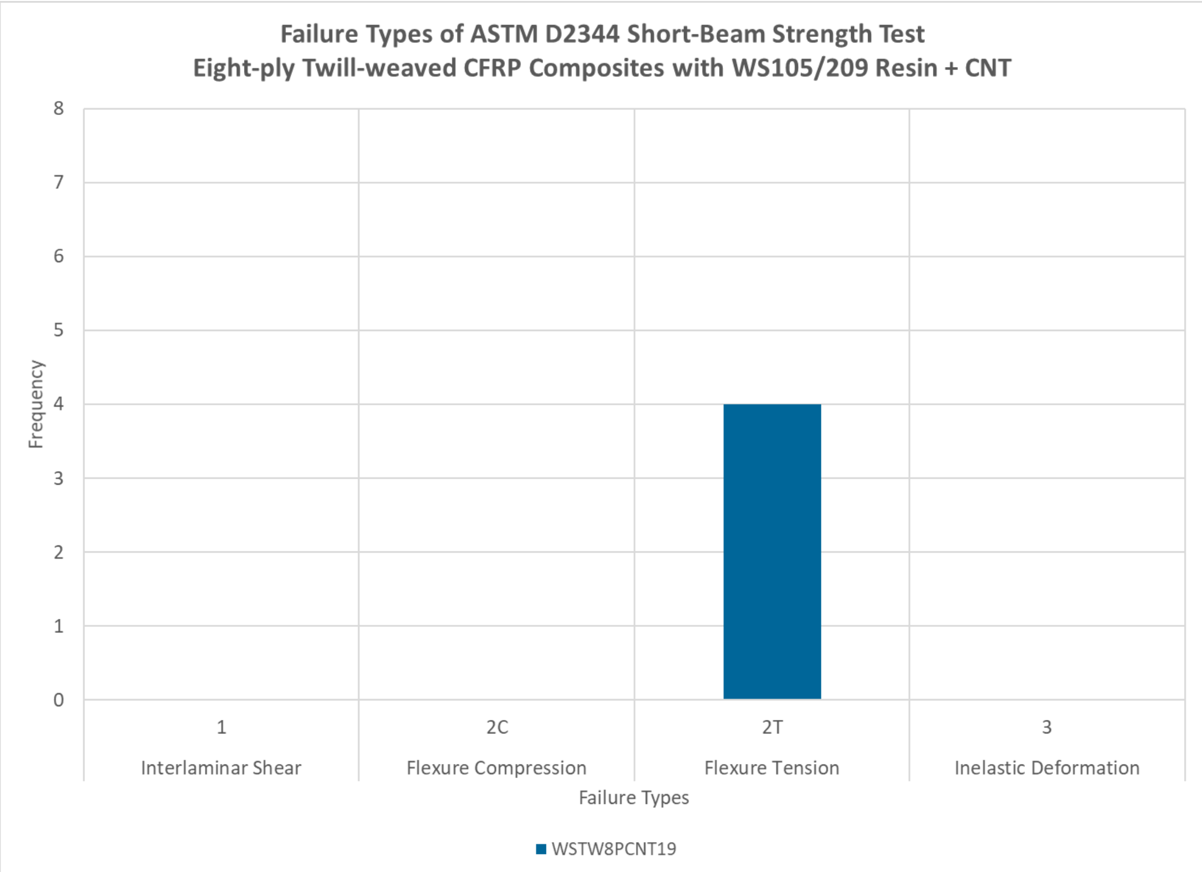

Figure 4.99 ASTM D2344 failure modes of eight-ply twill-weaved CFRP composites with WS105/209 resin system + CNT

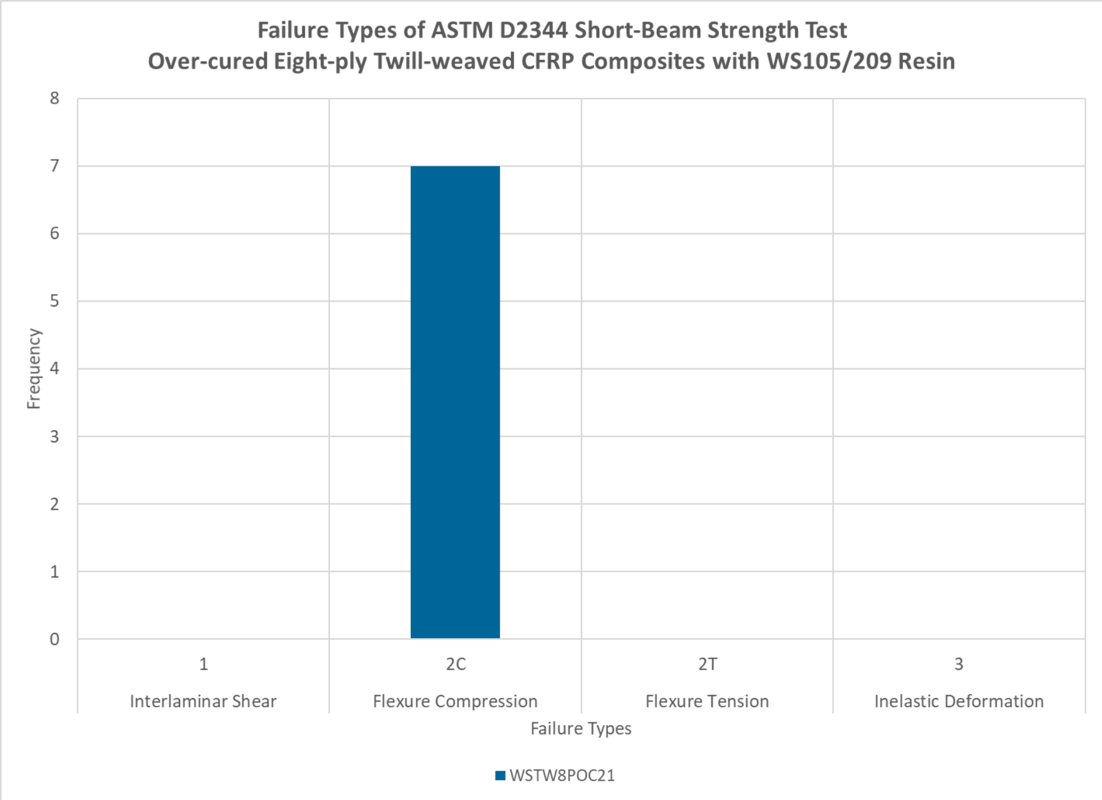

Figure 4.100 ASTM D2344 failure modes of over-cured eight-ply twill-weaved CFRP composites with WS105/209 resin system

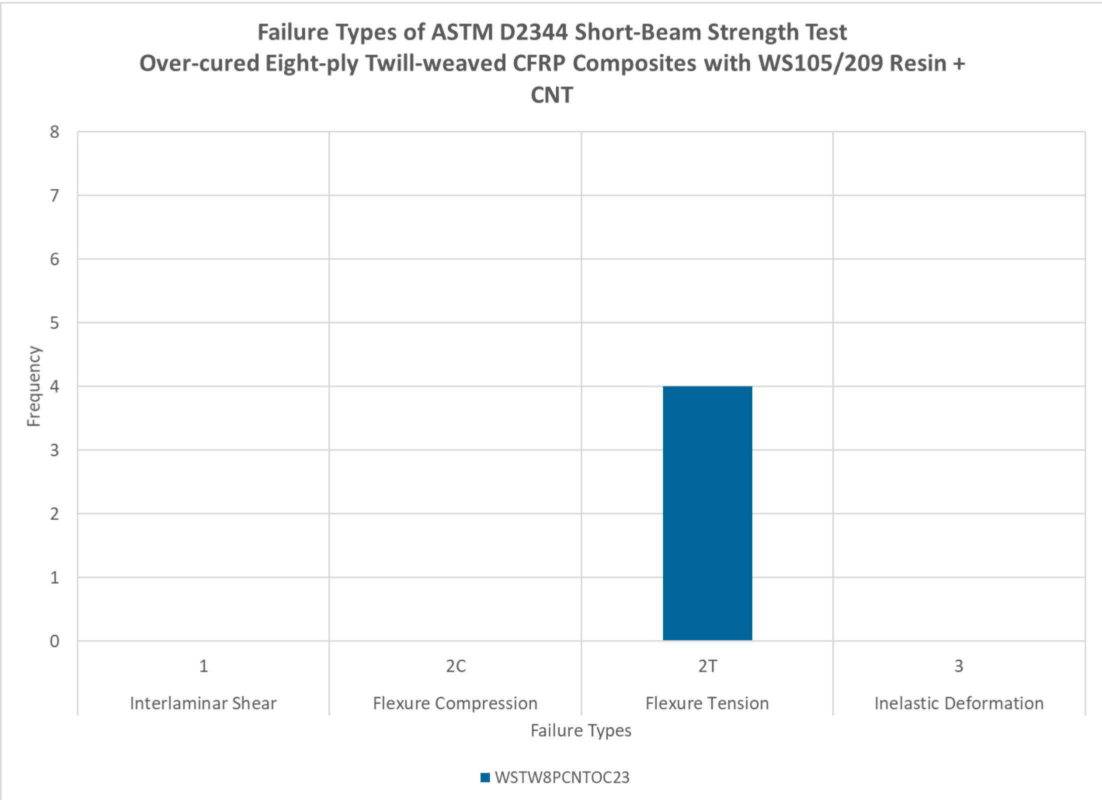

Figure 4.101 ASTM D2344 failure modes of over-cured eight-ply twill-weaved CFRP composites with WS105/209 resin system + CNT

In conclusion, ultimate tensile properties show an enhancement on the composites with CNT additives to withstand 4.44% higher stress without affecting other tensile properties. The stress-strain behavior become more consistent across the composite plate when CNT is incorporated as shown in the stress-strain curves. Furthermore, CNT improves the matrix phase of the composites to withstand a higher temperature without any degradation of tensile properties. This phenomenon is proved with the stress-strain curve, ultimate tensile stress, and the failure mode of ASTM D2344.

Chapter 5 Conclusions

Carbon fiber-reinforced polymer composites have different fabrication configurations with different constituents, including matrix, fiber weave patterns, and additives. This study conducted a comprehensive comparison of some configurations. In the initial phase, matrix with different viscosities were compared. In the first few batches of composite plates, the specimens show multiple failure locations due to fracture shockwaves. To ascertain whether the result was an exceptional case, more composite plates with the same fabrication configuration were produced and tested. Additionally, composite plates with different resin systems were evaluated to eliminate the possibility that specific type of matrix could be the potential cause of multiple failure locations. Eventually, the ply stack configuration was identified as the cause, as four-ply composites failed to withstand the fracture shockwave. Subsequently, specimens were fabricated using eight-ply carbon fiber laminate to compare the tensile performance of different resin systems. Three epoxy resin systems with different mixture viscosities were evaluated, and composites fabricated with higher matrix viscosities show higher consistency in the collected results. Possible void contents were suspected in composites fabricated with low matrix viscosities, and the stress-strain behavior of composites with void content is unstable. Stress concentration may occur in the specimens with voids as stress could not be evenly distributed between the matrix and reinforcement phases. Therefore, composites fabricated with the WS105/209 resin system, which has a higher matrix viscosity, show a more consistent tensile performance than other composite plates.

Employing the results obtained from ply stack configurations and matrix viscosities, eight-ply configuration and WS105/209 resin system were served as the foundation for evaluating different reinforcement weave patterns. The tensile performance of plain-weaved composites show unpredictability, as the crimp of carbon fiber fabric concentrated stress, resulting in localized failure that eventually decreased the stiffness of the composites. As a result, eight-ply twill-weaved composites with WS105/209 resin system have the most reliable results for investigating the influence of carbon nanotube additive.

Based on previous findings, carbon nanotubes (CNTs) were incorporated into the composites by mixing it with the matrix phase. The results of composites with CNT additive show high consistency and repeatability. It is observed that CNTs can enhance the tensile performance and thermal stability of the composites. Composite specimens with CNT additives show a 4.44% increase in ultimate tensile properties and a further 3.62% increase under over-cured conditions. Over-curing elevates the composite to a temperature exceeding the capability of the matrix phase material. Therefore, over-cured specimens are anticipated to experience a reduction in ultimate tensile properties similar to WSTW8POC specimens. With other fabrication conditions unchanged, composite with CNT additives incorporated can survive under a temperature exceeding the glass transition temperature of the matrix phase material. This is the result of CNT increasing the thermal stability of the composite. Furthermore, composites with CNT additive demonstrate an exceptional outcome with an further improvement on ultimate tensile properties after exposure to a high-temperature environment. The stress-strain behavior of over-cured composites with CNT additives is comparable to that of composites which have never been exposed to high temperatures. Therefore, CNTs are found to be beneficial to composites with better performances in several properties. This phenomenon may be related to the inherent properties of CNTs such as negative Poisson’s ratio.

Linear regression models were developed for various fabrication conditions. Some models, such as eight-ply twill-weaved composites with the IN2/AT30S resin system and eight-ply plain-weaved composites with the WS105/209 resin system, are unreliable due to data quality.

For specimens with CNT additive or over-curing treatment, their linear regression models can be used to predict ultimate tensile stresses in future studies.

Composite with improved tensile performance and thermal stability can be used as a choice for crafting features along fire escaping route and building structures or components with high operating temperature such as the in-cabin passageway and engine cowling of an aircraft. As composites have high specific strength and stiffness, broadening its applications can further reduce the structural weight of the product for lower energy consumption and higher economic values.

Chapter 6 Limitation and future research

There are two limitations in this study: combinations of composite constituents and over-curing conditions. First, regarding the composite constituents, there is a wide range of matrix and reinforcement phase materials available in the markets. Since there is considerable amount of combinations of different constituents, selected combinations were investigated in this study. For the weave patterns of reinforcement, there are various configurations, such as 2/2 twill-weaved pattern and 3/1 twill-weaved pattern. However, only 2/2 twill-weaved pattern was utilized in this study. Similarly, for matrix, there are different viscosities and curing conditions for a specific resin system with different hardeners, such as WS105 resin with WS205 fast hardener, WS206 slow hardener, or WS209 extra slow hardener. In this study, only WS209 hardener was employed. Every combination of resin and hardener has its own viscosity and glass transition temperature which are not able to be fabricated under the same molding method. Second, the over-curing process was conducted after the end-tab adhesion process, and the over-curing temperature was limited by the adhesive used to bond the end-tab. If the over-curing temperature exceeds the temperature that the adhesive can withstand, end-tab slippage will occur during the tensile test, compromising the evaluation of the tensile properties of specimens.

In future studies, larger varieties of composite constituents can be compared for a more robust conclusion. Fabrication methods can be adjusted to accommodate more configurations of composites such as using other molding methods for fabricating composite with higher resin viscosity. Furthermore, the composite can be evaluated in other perspective such as compression and fatigue performance in order to uncover the potential of CNT additive towards the enhancement of composite.

References

Aamir, M., Tolouei-Rad, M., Giasin, K., & Nosrati, A. (2019). Recent advances in drilling of carbon fiber–reinforced polymers for aerospace applications: A review. *International journal of advanced manufacturing technology, 105*(5-6), 2289-2308.

Akovali, G. (2001). *Handbook of composite fabrication*. Shawbury: Rapra.

Allaoui, A., & El Bounia, N. (2009). How carbon nanotubes affect the cure kinetics and glass transition temperature of their epoxy composites? – a review. *Express Polym. Lett., 3*(9), 588-594.

Amirkhosravi, M., Pishvar, M., & Altan, M. C. (2018). Fabricating high-quality vartm laminates by magnetic consolidation: Experiments and process model. *Composites Part A-Applied Science and Manufacturing, 114*, 398-406.

ASTM International. (2016). Standard test method for short-beam strength of polymer matrix composite materials and their laminates. In. West Conshohocken, PA: ASTM International.

ASTM International. (2017). Standard test method for tensile properties of polymer matrix composite materials. In. West Conshohocken, PA: ASTM International.

ASTM International. (2018). Standard guide for testing polymer matrix composite materials. In. West Conshohocken, PA: ASTM International.

Atkins, P. W. (2016). *Chemical principles : The quest for insight* (Seventh ed.). New York: W.H. Freeman : Macmillan Learning.

Ayatollahi, M. R., Isfahani, R. B., & Monfared, R. M. (2017). Effects of multi-walled carbon nanotube and nanosilica on tensile properties of woven carbon fabric-reinforced epoxy composites fabricated using varim. *Journal of Composite Materials, 51*(30), 4177-4188.

Bag, D. S. (2013). *Principles of polymers : An advanced book*. New York: Nova Publishers.

Balasubramanian, M. (2014). *Composite materials and processing*. Boca Raton, Fla.: CRC Press.

Beckwith, S. W., & Hyland, C. R. (1998). Resin transfer molding: A decade of technology advances. *SAMPE Journal, 34*(6), 7-19.

Berg, J. S., & Higgins, J. (2008). Vartm infusion: Processing large carbon/epoxy space structures out of the autoclave. *SAMPE Journal, 44*(6), 40-47.

Bodaghi, M., Costa, R., Gomes, R., Silva, J., Correia, N., & Silva, F. (2020). Experimental comparative study of the variants of high-temperature vacuum-assisted resin transfer moulding. *Composites Part A-Applied Science and Manufacturing, 129*, 17.

Carraher, C. E. (2018). *Carraher's polymer chemistry* (10th ed.). Boca Raton: CRC Press.

Chen, D. D., Arakawa, K., & Uchino, M. (2016). Effects of the addition of a cover mold on resin flow and the quality of the finished product in vacuum-assisted resin transfer molding. *Polymer Composites, 37*(5), 1435-1442.

Chen, D. D., Arakawa, K., & Xu, C. H. (2015). Reduction of void content of vacuum-assisted resin transfer molded composites by infusion pressure control. *Polymer Composites, 36*(9), 1629-1637.

Colicchia, C., & Strozzi, F. (2012). Supply chain risk management: A new methodology for a systematic literature review. *Supply Chain Management-an International Journal, 17*(4), 403-418.

De Baere, I., Van Paepegem, W., & Degrieck, J. (2009). On the design of end tabs for quasi-static and fatigue testing of fibre-reinforced composites. *Polymer Composites, 30*(4), 381-390.

Dean, D., Obore, A. M., Richmond, S., & Nyairo, E. (2006). Multiscale fiber-reinforced nanocomposites: Synthesis, processing and properties. *Composites Science and Technology, 66*(13), 2135-2142.

Dér, A., Dilger, N., Kaluza, A., Creighton, C., Kara, S., Varley, R., Herrmann, C., & Thiede, S. (2021). Modelling and analysis of the energy intensity in polyacrylonitrile (pan) precursor and carbon fibre manufacturing. *Journal of Cleaner Production, 303*, 127105.

Dogan, A., & Arman, Y. (2018). The effect of hygrothermal aging on the glass and carbon reinforced epoxy composites for different stacking sequences. *Mechanika, 24*(1), 19-25.

Dogan, A., Arman, Y., & Ozdemir, O. (2019). Experimental investigation of transverse loading on composite panels coated with different gelcoat colors subjected to uv radiation and hygrothermal aging. *Materials Research Express, 6*(2), 13.

Dogan, A., & Atas, C. (2016). Variation of the mechanical properties of e-glass/epoxy composites subjected to hygrothermal aging. *Journal of Composite Materials, 50*(5), 637-646.

Field, A. P. (2018). *Discovering statistics using ibm spss statistics* (5th edition. ed.). Los Angeles, California: SAGE Publications.

Fried, J. R. (2014). *Polymer science and technology* (3rd ed.). Upper Saddle River, NJ: Prentice Hall.

Gajjar, T., Shah, D. B., Joshi, S. J., & Patel, K. M. (2020). Experimental study of thickness gradient and flow simulation in vartm process. *Fibers and Polymers, 21*(2), 384-391.

Garcia, F. D., da Luz, F. S., Nascimento, L. F. C., Satyanarayana, K. G., Drelich, J. W., & Monteiro, S. N. (2020). Mechanical properties of boehmeria nivea natural fabric reinforced epoxy matrix composite prepared by vacuum-assisted resin infusion molding. *Polymers, 12*(6), 12.

Georgakilas, V., Otyepka, M., Bourlinos, A. B., Chandra, V., Kim, N., Kemp, K., Hobza, P., Zboril, R., & Kim, K. S. (2012). Functionalization of graphene: Covalent and non-covalent approaches, derivatives and applications. *Chem. Rev., 112*(11), 6156-6214.

Goren, A., & Atas, C. (2008). Manufacturing of polymer matrix composites using vacuum assisted resin infusion molding. *Archives of Materials Science and Engineering, 34*(2), 117-120.

Gu, Y. Z., Qin, X., Li, M., Zhang, K. M., & Zhang, Z. G. (2015). Temperature distribution and curing behaviour of carbon fibre/epoxy composite during vacuum assisted resin infusion moulding using rapid heating methods. *Polymers & Polymer Composites, 23*(1), 11-19.

Guo, Z., Zhuang, C., Li, Z., & Chen, Y. (2021). Mechanical properties of carbon fiber reinforced concrete (cfrc) after exposure to high temperatures. *Composite Structures, 256*.

Heider, D., & Gillespie, J. W. (2004). Automated vartm processing of large-scale composite structures. *Journal of Advanced Materials, 36*(4), 11-17.

Hossain, M. K., Chowdhury, M. M. R., Imran, K. A., Salam, M. B., Tauhid, A., Hosur, M., & Jeelani, S. (2014). Effect of low velocity impact responses on durability of conventional and nanophased cfrp composites exposed to seawater. *Polymer Degradation and Stability, 99*, 180-189.

Hosur, M. V., Adya, M., Alexander, J., Jeelani, S., Vaidya, U., & Mayer, A. (2003). Studies on impact damage resistance of affordable stitched woven carbon/epoxy composite laminates. *Journal of Reinforced Plastics and Composites, 22*(10), 927-952.

Hosur, M. V., Chowdhury, F., & Jeelani, S. (2007). Low-velocity impact response and ultrasonic nde of woven carbon/epoxy-nanoclay nanocomposites. *Journal of Composite Materials, 41*(18), 2195-2212.

Huang, X., Qi, X., Boey, F., & Zhang, H. (2012). Graphene-based composites. *Chem. Soc. Rev., 41*(2), 666-686.

Jones, F. R. (1994). *Handbook of polymer-fibre composites*. Burnt Mill, Harlow, Essex: Longman Scientific & Technical.

Karimi, A., Rahmatabadi, D., & Baghani, M. (2024). Various fdm mechanisms used in the fabrication of continuous-fiber reinforced composites: A review. *Polymers, 16*(6), 831.

Kaw, A. K. (1997). *Mechanics of composite materials*. Boca Raton, FL: CRC Press.

Kochan, C. (2020). An experimental investigation on mode-i fracture toughness of mussel shell/epoxy particle reinforced composites. *Pamukkale University Journal of Engineering Sciences-Pamukkale Universitesi Muhendislik Bilimleri Dergisi, 26*(4), 599-604.

Lengsfeld, H. (2020). *Carbon fibers: Production, applications, processing*. München: Hanser.

Li, W., Krehl, J., Gillespie, J. W., & Heider, D. (2004). Process and performance evaluation of the vacuum-assisted process. *Journal of Composite Materials, 38*(20), 1803-1814.

Liu, F., Deng, S. Q., & Zhang, J. N. (2017). Mechanical properties of epoxy and its carbon fiber composites modified by nanoparticles. *Journal of Nanomaterials, 2017*, 9.

Mallick, P. K. (2008). *Fiber-reinforced composites : Materials, manufacturing, and design* (3rd (expanded and rev.) ed.). Boca Raton, FL: CRC Press.

Mazumdar, S. K. (2002). *Composites manufacturing : Materials, product, and process engineering*. Boca Raton, FL: CRC Press.

Monfared, R. M., Ayatollahi, M. R., & Isfahani, R. B. (2018). Synergistic effects of hybrid mwcnt/nanosilica on the tensile and tribological properties of woven carbon fabric epoxy composites. *Theoretical and Applied Fracture Mechanics, 96*, 272-284.

Morgan, P. (2005). *Carbon fibers and their composites*. Boca Raton, FL: CRC Press.

Najmi, L., & Hu, Z. (2023). Effects of carbon nanotubes on thermal behavior of epoxy resin composites. *Journal of composites science, 7*(8), 313.

Ngai, E. W. T., Moon, K. K. L., Riggins, F. J., & Yi, C. Y. (2008). Rfid research: An academic literature review (1995-2005) and future research directions. *International Journal of Production Economics, 112*(2), 510-520.

Norusis, M. J. (1999). *Spss 9.0 guide to data analysis*. Upper Saddle River, N.J: Prentice Hall.

O'Donnell, A., Dweib, M. A., & Wool, R. P. (2004). Natural fiber composites with plant oil-based resin. *Composites Science and Technology, 64*(9), 1135-1145.

Or, I. K.-H., Lo, C. K.-Y., & Kan, C.-W. (2023). A systematic literature network analysis: Development of manufacturing, enhancement and sustainability of fiber-reinforced polymer composites (1998–2020) and future research agenda. *Fibers and Polymers, 24*(3), 789-800.

Park, S.-J. (2015). *Carbon fibers* (Vol. 210). Dordrecht: Springer.

Polowick, C. (2013). Optimizing vacuum assisted resin transfer moulding (vartm) processing parameters to improve part quality. In.

Rahaman, M. S. A., Ismail, A. F., & Mustafa, A. (2007). A review of heat treatment on polyacrylonitrile fiber. *Polymer Degradation and Stability, 92*(8), 1421-1432.

Ravikovich, Y., Arkhipov, A., Shakhov, A., & Erofeev, T. (2021). Application of composite materials in an upgraded engine low-pressure compressor for a regional passenger aircraft. *Inventions (Basel), 6*(3), 54.

Rudd, C. D., Long, A. C., Kendall, K. N., & Mangin, C. (1997). *Liquid moulding technologies - resin transfer moulding, structural reaction injection moulding and related processing techniques* (1 ed.). Chantilly: Woodhead Publishing.

Seemann, W. H. (1991). United States Patent No. US5052906 (A).

Shindo, A., Fujii, R., & Sengoku, T. (1962). Japan Patent No. 1962-4405.

Simacek, P., Eksik, O., Heider, D., Gillespie, J. W., & Advani, S. (2012). Experimental validation of post-filling flow in vacuum assisted resin transfer molding processes. *Composites Part A-Applied Science and Manufacturing, 43*(3), 370-380.

Strong, A. B. (2006). *Plastics : Materials and processing* (3rd ed.). Upper Saddle River, NJ: Pearson Prentice Hall.

Tabachnick, B. G., & Fidell, L. S. (2013). *Using multivariate statistics* (6th ed. ed.). Boston: Pearson Education.

Tafur, C. L., Mora, E. E., & Baracaldo, R. R. (2018). Effects of the vacuum moulding process on the mechanical properties of cotton/epoxy composite. *Fibres & Textiles in Eastern Europe, 26*(3), 93-97.

Takeda, F., Nishiyama, S., Hayashi, K., Komori, Y., Suga, Y., & Asahara, N. (2005). Research in the application of the vartm technique to the fabrication of primary aircraft composite structures. *Mitsubishi Heavy Industries, Ltd. Technical Review, 42*.

Tam, E. W. S., Yip, J., Fang, C., Lo, C. K. Y., Yick, K. L., & Ng, S. P. (2020). De quervain's tenosynovitis: A systematic and citation network analysis review. *Biomedical Journal of Scientific & Technical Research, 24*(5), 18674.

Uddin, M. F., & Sun, C. T. (2008). Strength of unidirectional glass/epoxy composite with silica nanoparticle-enhanced matrix. *Composites Science and Technology, 68*(7-8), 1637-1643.

Ullah, S., Palevicius, A., Vilutis, A., Fangueiro, R., & Janusas, G. (2026). Experimental and numerical assessment of fiber orientation effects in biaxial glass/vinyl ester laminates. *Polymers, 18*(2), 265.

van Eck, N. J., & Waltman, L. (2014). Citnetexplorer: A new software tool for analyzing and visualizing citation networks. *Journal of Informetrics, 8*(4), 802-823.

Vlach, J., Doubrava, R., Růžek, R., Raška, J., Horňas, J., & Kadlec, M. (2022). Strain-field modifications in the surroundings of impact damage of carbon/epoxy laminate. *Polymers, 14*(16), 3243.

Volponi, R., Spena, P., De Nicola, F., & Guadagno, L. (2019). Multiscale composites: Assessment of a feasible manufacturing process. *International Journal of Aerospace Engineering, 2019*, 8.

Wang, S., Liang, Z., Gonnet, P., Liao, Y. H., Wang, B., & Zhang, C. (2007). Effect of nanotube functionalization on the coefficient of thermal expansion of nanocomposites. *Adv. Funct. Mater., 17*(1), 87-92.

Williams, C., Summerscales, J., & Grove, S. (1996). Resin infusion under flexible tooling (rift): A review. *Composites. Part A, Applied science and manufacturing, 27*(7), 517-524.

Wong, S. H., Yip, J., Lo, C. K. Y., Cheung, K. M. C., Cheung, J. P. Y., Kwan, K. Y. H., Yick, K. L., & Ng, S. P. (2020). Non-invasive treatment of adolescent idiopathic scoliosis: Systematic literature review by using citation network analysis. *Spine and Surgery*, 1-9.

Yalcinkaya, M. A., Guloglu, G. E., Pishvar, M., Amirkhosravi, M., Sozer, E. M., & Altan, M. C. (2019). Pressurized infusion: A new and improved liquid composite molding process. *Journal of Manufacturing Science and Engineering-Transactions of the Asme, 141*(1), 12.

Yalcinkaya, M. A., Sozer, E. M., & Altan, M. C. (2017). Fabrication of high quality composite laminates by pressurized and heated-vartm. *Composites Part A-Applied Science and Manufacturing, 102*, 336-346.

Young, R. J. (2011). *Introduction to polymers* (3rd ed.). Boca Raton: CRC Press.

Zhang, H.-N., Fan, Y., & Shen, H.-S. (2023). Prediction of temperature-dependent mechanical properties for swcnt/cu nanocomposite metamaterials: A molecular dynamics study. *Nanomaterials (Basel, Switzerland), 13*(12), 1885.

Zhang, K., Gu, Y., Li, M., & Zhang, Z. (2014). Effect of rapid curing process on the properties of carbon fiber/epoxy composite fabricated using vacuum assisted resin infusion molding. *Materials & Design, 54*, 624.

Zhang, K. M., Gu, Y. Z., Wang, S. K., Li, M., & Zhang, Z. G. (2014). Effects of preheating temperature of the mould on the properties of rapid-curing carbon fibre composites fabricated by vacuum-assisted resin infusion moulding. *Polymers & Polymer Composites, 22*(9), 825-835.

Zhang, K. M., Gu, Y. Z., Zhang, J. L., Li, M., Wang, S. K., & Zhang, Z. G. (2016). Rapid curing vacuum-assisted resin infusion molding using silicone rubber sheet heater and the effect of cooling process on the properties of carbon fiber/epoxy composites. *Journal of Composite Materials, 50*(13), 1837-1850.